Thèse n° 10 494

Strong and micro lensing in distant quasars

Présentée le 24 novembre 2023

Faculté des sciences de base
Groupe SCI SB FC
Programme doctoral en physique

pour l'obtention du grade de Docteur ès Sciences

par

Eric Gérard Guy PAIC

Acceptée sur proposition du jury

Prof. M. Wyart, président du jury
Prof. F. Courbin, Dr G. Vernardos, directeurs de thèse
Prof. T. Anguita, rapporteur
Prof. M. O'dowd, rapporteur
Dr D. Harvey, rapporteur

École
polytechnique
fédérale
de Lausanne

2023

Images of broken light which dance before me like a million eyes. They call me on and on across the universe .

John Lennon

A ma famille, amis et à Diane …

Acknowledgements

Bien qu'il n'y ait qu'un seul nom sur la couverture, l'écriture de cette thèse n'aurait pas été possible sans l'aide de plusieurs personnes que j'aimerais remercier ici.

Tout d'abord, je suis reconnaissant envers Frédéric Courbin et Giorgos Vernardos pour leur supervision bienveillante au cours de ces quatres années, j'ai appris énormément sur l'astrophysique et sur la vie académique en général.

Le laboratoire d'astrophysique de l'EPFL regroupe des gens à la fois brillants, chaleureux et ... originaux. Cela créé une atmosphère idéale pour mener à bien des projets scientifiques aussi bien que pour susciter des discussions passionantes sur n'importe quel sujet allant de la science à la politique en passant par les particularités des voitures utilisées par Google dans chaque pays du monde pour créer la "Street View". J'aimerais particulièrement remercier Aymeric, Andrei, Cameron, Martin, Austin, Favio, Fred(dy), Javier, James, Jennifer, Robert et Utsav pour nos nombreux échanges enrichissants. Je remercie aussi Vivien qui m'a accueilli en stage quand je n'étais qu'un étudiant en Bachelor rêvant d'étoiles et m'a introduit à ce qui allait devenir mon domaine de recherche.

Malgré la pandémie, j'ai eu la chance de rencontrer des personnes hors de Suisse qui ont activement participé à la réussite de ce travail. Je pense notamment à Dominique, Simon, Sherry, Timo, Josh et Henry avec qui j'ai pu concrétiser des projets scientifiques ambitieux.

Cette quête d'un doctorat en astrophysique a commencé grâce à mon père et mon grand père qui, à travers des visites du CERN ou des nuits d'observations dans le jardin m'ont fait découvrir les phénomènes infiniment complexes et excitants qui répondent aux questions simples d'un enfant qui voit des points blancs dans le ciel noir. Je les remercie pour l'inspiration et l'exemple qu'ils m'ont donné de vouloir comprendre l'Univers qui nous entoure. Je remercie aussi ma mère qui m'a un jour soufflé de regarder France 3 à 17h30 (C'est pas sorcier !) et pour son soutien inébranlable tout au long de mes études. Comme on ne comprend jamais mieux quelque chose qu'en l'expliquant, je remercie ma soeur, Inès, pour sa curiosité qui m'a fait réaliser plus d'une fois que je ne savais pas autant que je pensais.

Après plus de dix ans passé à l'EPFL, les amitiés nouées sur fond d'aventures associatives, festives ou de "simples" bières à Satellite ont été une source intarissable de bons moments et de soutien. Je remercie Aymeric, Benoit et Etienne; je suis le dernier à finir cette fameuse "Road to PhD" mais je suis sûr que bien d'autres péripéties sportives et intellectuelles nous attendent et qu'on continuera à se tirer mutuellement vers le haut. Merci à Carla pour nos déjeuners de rires et de ragots. Merci à Stan et Guillaume avec qui l'aventure suisse a commencé quand on est parti de nos familles, alors à peine majeurs. Merci aussi à Laureline et Sévane pour les tours de lacs et d'Europe organisés et à Jérémie pour les dingueries de la coloc'. Evidement, je remercie mon chat, Spirou, de s'être assuré de multiples fois que les touches de mon clavier marchent toujours même après s'être assis dessus.

Enfin et surtout, je veux remercier ma femme, Diane, pour qui je n'ai pas été le meilleur conjoint ces derniers mois mais qui a toujours su trouver les mots pour me remotiver quand je ne voyais pas la fin de ce manuscrit.

Abstract

Most large galaxies host a Super Massive Black Hole at their center, attracting matter in its immediate vicinity and forming a swirling accretion disk that emits a wide range of electromagnetic radiations. These objects are called Active Galactic Nuclei. The brightest ones are known as quasars and are the most luminous objects in the Universe. Quasars' gravitational potential and energetic outflows have a significant impact on the morphology of their host galaxy, on their formation, and fate. By studying their structure, we can thus gain insight into the mechanisms behind galaxy evolution. In the past decade, various measurements of accretion disk radii have challenged the established accretion model, leading to an interest in alternative models and measurement methods.

As they are observable at large distances ($\sim 10^{10}$ light years), quasars can also be used as cosmological probes to measure the Hubble parameter, H_0: the Universe's current expansion rate. This tool is crucial to confirm the tension between early and late-Universe measurements of H_0, which could hint towards a different cosmological paradigm than the currently prevailing flat-ΛCDM model.

Gravitational lensing offers a way to tackle both problems. A strong gravitational lens system is observed when a massive object, such as a galaxy, lies between a quasar and the observer to create multiple magnified images of the same source. The multiple images are produced by the various paths light takes to reach us. As these optical paths are different in length and because they pass at different places in the gravitational well of the lens, the difference is seen in the arrival times of photons in each lensed image of the source. This so-called time delay gives us information about the cosmological distances between the source, the lens and the observer and allows us to measure H_0. This is called Time Delay Cosmography. In addition, stars within the lensing galaxy can magnify each image independently through the microlensing effect. The magnification partly depends on the light profile of the source, hence probing the quasar structure.

The goal of this thesis is double: 1- using microlensing to study the inner structure of quasars, with a focus on one of the most interesting objects in this field, namely QJ 0158−4325 and 2- measuring H_0 using the double-lensed quasar HE 1104−1805, the second doubly-imaged quasar available so far to do Time Delay Cosmography.

More specifically, I have shown that the reverberation of radiation from the accretion disk by the surrounding Broad Line Region (BLR) results in high-frequency features in the microlensing light curve that have been overlooked so far. Analyzing the microlensing light curves in the frequency domain has highlighted the importance of considering these features when measuring standard accretion disk size, as neglecting them can lead to systematic bias. This novel technique has also allowed me to accurately measure the size of the quasar's BLR, consistent with previous estimates. Furthermore, my work revealed that detecting unusually sustained periodic oscillations indicates that the quasar may host a Super Massive Binary Black Hole with a milli-parsec separation. The improbability of observing this kind of system right before they merge may indicate that their predicted coalescence time is underestimated and unknown mechanisms are

at play. In the context of imminent wide-field surveys that will observe thousands of lensed quasars, I led the development of a neural network that can quickly and efficiently identify pairs of quasar images undergoing microlensing events. By highlighting the relevant time window for complementary observations, this forecasting algorithm will maximize the scientific output of such events, with the potential to unveil features in quasar structure unseen so far.

The TDCOSMO collaboration aims at measuring H_0 with a 1% precision to assess the H_0 tension. As a contribution to this effort, I conducted the full analysis of HE 1104−1805, the second doubly imaged quasar in the sample. This involved measuring the time delay, the lens velocity dispersion in 2D, analyzing the line-of-sight and modelling the lens mass. Each step required handling a different data set and thoroughly investigating the measurement robustness. Despite the low number of images, the dimness of the lensed arc and the high number of perturbers, I could determine H_0 with a precision of 12%. This measurement will contribute to improving the precision of the H_0 measurement through the combined TDCOSMO sample and will be part of the next milestone H_0 measurement of the collaboration. Creating a sample of double-lensed quasars for H_0 measurement is crucial to identify any potential selection biases present in the current TDCOSMO sample, which is predominantly made up of quadruple-lensed quasars. Moreover, the population of doubly-imaged quasars outnumbers that of quadruples by a factor of 4. Using them to measure H_0 is thus crucial to fulfilling the TDCOSMO goal.

Key words: Quasars, Accretion disk, Broad Line Region, Microlensing, Strong Lensing, Time delay Cosmography, Hubble-Lemaitre constant.

Résumé

La plupart des galaxies massives abritent un trou noir supermassif en leur centre. Celui-ci attire la matière de son voisinage immédiat et forme un disque d'accrétion tourbillonnant qui émet une large gamme de rayonnements électromagnétiques. Ces objets sont appelés noyaux actifs de galaxies. Les plus brillants sont connus sous le nom de quasars et sont les objets les plus lumineux de l'Univers. Le potentiel gravitationnel et les écoulements énergétiques des quasars ont un impact significatif sur la morphologie de leur galaxie hôte, sur sa formation et sur son destin. En étudiant leur structure, nous pouvons donc obtenir des informations sur les mécanismes controlant l'évolution des galaxies. Au cours de la dernière décennie, différentes mesures des rayons des disques d'accrétion ont remis en question le modèle établi, suscitant un intérêt pour des modèles et des méthodes de mesure alternatifs.

Étant observables à de grandes distances ($\sim 10^{10}$ années-lumière), les quasars peuvent également être utilisés comme sondes cosmologiques pour mesurer le paramètre de Hubble, H_0 : le taux d'expansion actuel de l'Univers. Cet outil est crucial pour confirmer la tension entre les mesures du début et de la fin de l'Univers concernant H_0, ce qui pourrait provoquer un changement de paradigme cosmologique, différent du communément accepté ΛCDM.

L'effet de lentille gravitationnelle offre un moyen d'étudier ces deux problèmes. Un système de lentille gravitationnelle forte est observé lorsqu'un objet massif tel qu'une galaxie se trouve entre un quasar et l'observateur, créant ainsi plusieurs images mirages magnifiées de la même source. Les multiples images sont produites par les différents chemins empruntés par la lumière pour nous arriver. Comme ces chemins optiques ont des longueurs différentes et passent à des endroits différents du potentiel gravitationnel de la lentille, des différences sont observées dans les temps d'arrivée des photons de chaque image lentillée de la source. Ce délai temporel nous renseigne sur les distances cosmologiques entre la source, la lentille et l'observateur, et nous permet de mesurer H_0. Cela s'appelle la cosmographie par délai temporel. De plus, les étoiles à l'intérieur de la galaxie lentillée peuvent magnifier chaque image de manière indépendante grâce à l'effet de microlentille. L'agrandissement dépend en partie du profil lumineux de la source et sonde donc la structure du quasar.

L'objectif de cette thèse est double : 1) utiliser la microlentille pour étudier la structure interne des quasars, en mettant l'accent sur l'un des objets les plus intéressants dans ce domaine, à savoir QJ 0158−4325, et 2) mesurer H_0 en utilisant le quasar à double lentille HE 1104−1805, le second quasar doublement imagé disponible jusqu'à présent pour réaliser une cosmographie par délai temporel.

Plus précisément, j'ai montré que la variabilité de la micromagnification est affectée par la réverbération du rayonnement du disque d'accrétion par les nuages de gaz environnants (abbrégé BLR en anglais). Cela induit des variations à haute fréquence qui ont été négligées jusqu'à présent. L'analyse des courbes de variation de la micromagnification dans le domaine de la fréquence a souligné l'importance de prendre en compte ces caractéristiques lors de la mesure de la taille du disque d'accrétion, car les négliger peut entraîner un biais systématique. Cette nouvelle technique m'a également permis de mesurer avec précision

la taille de la BLR du quasar, en accord avec les estimations précédentes. De plus, mon travail a révélé que la détection d'oscillations périodiques inhabituellement soutenues indique que le quasar pourrait héberger un trou noir binaire supermassif avec une séparation de l'ordre du milli-parsec. L'improbabilité d'observer ce type de système juste avant leur fusion peut indiquer que leur temps de coalescence prédit est sous-estimé.

Dans le cadre des futures observations synoptiques qui observeront des milliers de quasars lentillés, j'ai dirigé le développement d'un réseau neuronal qui peut rapidement et efficacement identifier les paires d'images de quasars subissant des événements de microlentille. En mettant en évidence la fenêtre temporelle pertinente pour des observations complémentaires, cet algorithme de prévision maximisera le rendement scientifique de tels événements, avec la possibilité de révéler des caractéristiques de la structure des quasars jusqu'à présent invisibles.

L'objectif de la collaboration TDCOSMO est de mesurer H_0 avec une précision de 1% pour certifier la tension de H_0. En tant que contribution à cet effort, j'ai mené l'analyse complète de HE 1104−1805, le deuxième quasar à double image de l'échantillon. Cela impliquait de mesurer le délai temporel, de mesurer la dispersion de vitesse de la lentille en 2D, d'analyser la ligne de visée et de modéliser la masse de la lentille. Chaque étape nécessitait de manipuler un ensemble de données différent et une enquête approfondie de la robustesse de la mesure. Malgré le faible nombre d'images, la faible luminsité de l'arc lentillé et le grand nombre de perturbateurs, j'ai pu déterminer H_0 avec une précision de 12 %. Cette mesure contribuera à améliorer la précision de la mesure de H_0 grâce à l'échantillon combiné TDCOSMO et fera partie de la prochaine mesure majeure de H_0 de la collaboration. La création d'un échantillon de quasars à double lentille pour la mesure de H_0 est cruciale pour identifier d'éventuels biais de sélection dans l'échantillon TDCOSMO actuel, qui est principalement composé de quasars quadruplement lentillés. De plus, la population de quasars à double image dépasse celle des quadruples d'un facteur de 4. Les utiliser pour mesurer H_0 est donc crucial pour atteindre l'objectif de TDCOSMO.

Mots clefs : Quasars, Disque d'accrétion, Lentille gravitationnelle forte, Microlentilles, Constante de Hubble-Lemaitre, Cosmographie par délai temporel.

Contents

Acknowledgements **i**

Abstract (English/Français/Deutsch) **iii**

List of figures **ix**

List of tables **xiii**

1 Introduction **1**
- 1.1 Evolution of the cosmological paradigm . . . 1
  - 1.1.1 First conceptions . . . 1
  - 1.1.2 From Einstein's happiest thought to the current paradigm . . . 2
- 1.2 Active Galactic Nuclei (AGN) . . . 10
  - 1.2.1 A bit of history . . . 10
  - 1.2.2 Unified Models . . . 11
  - 1.2.3 Quasar optical variability. . . . 17
  - 1.2.4 Interplays with the host galaxy . . . 18
- 1.3 Gravitational lensing . . . 18
  - 1.3.1 Formalism . . . 18
  - 1.3.2 Gravitational lensing regimes and their applications . . . 21
- 1.4 H_0 measurement methods . . . 29
  - 1.4.1 History of the H_0 measurement . . . 29
  - 1.4.2 Late Universe measurements . . . 29
  - 1.4.3 Early Universe measurements . . . 34
  - 1.4.4 The H_0-tension: status and possible resolutions . . . 36
- 1.5 Outline of this work . . . 40

2 Quasar structure study **41**
- 2.1 Main probes of quasar structure . . . 41
  - 2.1.1 Reverberation Mapping . . . 41
  - 2.1.2 Quasar microlensing . . . 47
  - 2.1.3 The accretion disk size problem . . . 54
- 2.2 A new method to measure Broad Line Region with microlensing light curves . . . 55
  - 2.2.1 Computing the power spectrum of a microlensing light curve . . . 55
- 2.3 Binary black hole detection using microlensing light curves . . . 71
- 2.4 Forecast of microlensing events in the incoming wide field monitoring surveys. . . . 90
  - 2.4.1 Training set . . . 90
  - 2.4.2 Machine learning algorithm . . . 95

2.5 Summary 98

3 Time Delay Cosmography 101
3.1 Overview of the technique 101
3.1.1 A long list of ingredients 101
3.1.2 Current status 114
3.2 COSMOGRAIL lightcurves 117
3.2.1 Target selection 119
3.2.2 Photometric measurement 119
3.3 Measurement of H_0 with the doubly lensed quasar HE 1104−1805 124
3.3.1 Lens redshift 124
3.3.2 Time Delay measurement 124
3.3.3 Resolved kinematics measurement 130
3.3.4 Line-Of-Sight analysis 137
3.3.5 Lens modelling 142
3.3.6 Combining lensing, kinematics and external convergence for cosmographic inference 152
3.3.7 Discussion and conclusion 155
3.4 Summary 157

Bibliography 161

List of Figures

1.1 First representations of planets trajectories according to the geocentric and heliocentric models. . . . 1
1.2 Illustration of the curvature of spacetime caused by a massive object such as the Sun. . . 3
1.3 Hubble diagrams through the ages. . . . 5
1.4 Luminous and dark matter distribution in the Bullet cluster. . . . 6
1.5 Cosmic Microwave background map and Universe's chronology. . . . 8
1.6 Spectra of different types of AGNs compared to a standard galaxy. . . . 10
1.7 Imaging of the first discovered quasar 3C273. . . . 11
1.8 Scheme showing the structure of AGNs following the unified model. . . . 13
1.9 Decomposition of a typical AGN Spectral Energy Distribution. . . . 14
1.10 Event Horizon Telescope first resolved observation of the Super Massive Black Hole M87. 16
1.11 Scheme of gravitational lens system. . . . 19
1.12 Simulated microlensing images position and size according to the relative alignment of the point source and the point mass with the observer. . . . 23
1.13 OGLE observation of a microlensing event caused by a point mass passing in front of a star. 24
1.14 Different possible image configurations in galaxy-scale strong gravitational lensing. . . . 28
1.15 Distance Ladder used for the H_0 measurement by Riess et al. (2022). . . . 33
1.16 Power spectrum of the Cosmic Microwave background used by Planck Collaboration et al. (2020b) to measure H_0. . . . 35
1.17 Current status of the various H_0 measurements. . . . 37
1.18 H_0-tension predicted by different cosmological models implying changes in the late or early Universe physics or the existence of dark radiations. . . . 39

2.1 Example of a reverberation mapping measurement of the apparent size of an accretion disk as a function of the observation wavelength. . . . 43
2.2 Example of a reverberation mapping measurement of the Broad Line Region size using spectroscopic monitoring. . . . 44
2.3 First 3D modelization of a quasar's Broad Line Region using spectroscopic monitoring. . 46
2.4 Scheme of a standard strongly lensed quasar system affected by microlensing stars in the lensing galaxy. . . . 49
2.5 Examples of magnification maps assuming different Initial Mass Functions. . . . 50
2.6 Examples of simulated microlensing light curves with different source light profiles. . . . 53
2.7 Examples of microlensing light curves observed by the COSMOGRAIL program. . . . 54
2.8 Illustration of the spectral leakage phenomenon and use of the windowing to mitigate the problem. . . . 56
2.9 Choice of the correct window function to limit spectral leakage in the power spectrum. . 57
2.10 Example of a microlensing light curve simulated for image A of Q2237. . . . 91

2.11 Extraction of the correlated noise from the observed RXJ 1131−1231 microlensing light curve. 92
2.12 Computation of the red noise power spectrum added to the simulated microlensing light curves. 94
2.13 Improvement of the RNN during the training. 96
2.14 Examples of microlensing peak forecasts on realistic microlensing light curves. 97

3.1 Scheme depicting the image reconstruction of a strong gravitational lens. 105
3.2 Examples of the most used mass and light parametrizations. 108
3.3 Effect of a mass-sheet on a power-law mass model. 109
3.4 Simulated $\sigma_{\rm LOS}$ measurements with slit and IFU spectrographs. To constrain the MST. . . 111
3.5 Sample of lenses with a complete TDC analysis. 115
3.6 Current status of the TDCOSMO H_0 measurement depending on the MSD treatment. . . 117
3.7 Cover page of Millon et al. (2020b), the largest COSMOGRAIL public data release. . . 118
3.8 Example of the MCS deconvolution applied to a Nordical Optical Telescope observation of SDSSJ0921+2854. 120
3.9 Deconvolved images of the NOT targets. 121
3.10 NOT light curves of J1817+2729 and J2145+6345. 121
3.11 NOT light curves of SDSSJ0921+2854. 122
3.12 NOT light curves of PSJ1721+8842. 123
3.13 HE 1104−1805 R-band light curve obtained by joining three datasets: SMARTS, ECAM and WFI. 125
3.14 Example of a time delay point estimate with `PyCS` 126
3.15 $\Delta t_{\rm AB}$ measurements for different configurations of $(\eta_{\rm intr}, \eta_{\rm ml})$ with the merged ECAM+SMART+WFI dataset. 128
3.16 Final measurement of $\Delta t_{\rm AB}$ for using the three data sets. 129
3.17 MUSE IFU observation of HE 1104−1805 and PSF subtraction process. 131
3.18 Spectra of HE 1104−1805 quasar images, lens and perturbers 132
3.19 Velocity dispersion point-estimate in the 3 radial bins of HE 1104−1805's lens galaxy. . 134
3.20 Final measurement of the velocity dispersion in the 3 radial bins of HE 1104−1805's lens galaxy. 135
3.21 Measurement of the P5 stellar kinematics. 136
3.22 Wide-Field Imaging of HE 1104−1805. 138
3.23 Detection of a 9th perturber near image B. 139
3.24 Weights of galaxies in the HE 1104−1805 field. 140
3.25 $\kappa_{\rm ext}$ measurement for HE 1104−1805. 141
3.26 HE 1104−1805 imaging in the filter F160W band using HST WFC3. 142
3.27 Prior on the four flexion coefficients. 144
3.28 PSF reconstruction for the 3 HST bands. 145
3.29 Power-law reconstruction of the HST imaging data of HE 1104−1805. 146
3.30 HE 1104−1805 separate light components. 147
3.31 HE 1104−1805 modelled potential with power-law and different satellite inclusion strategies. 147
3.32 Composite reconstruction of the HST imaging data of HE 1104−1805. 148
3.33 HE 1104−1805 modelled composite potential with different satellite inclusion strategies. 149
3.34 Posterior of the power-law models of HE 1104−1805. 150
3.35 Posterior of the composite models of HE 1104−1805. 151
3.36 BIC weighted comparison of the power-law and composite models. 153
3.37 Determination of the MST core size. 154

3.38 Posterior of $\lambda_{\rm int}$, $D_{\Delta t}$ and D_{ℓ} using kinematics. 155
3.39 H_0 measurement with HE 1104−1805. 156

List of Tables

1.1 Observational characteristics of the different types of AGNs. 12

2.1 Physical parameters used to generate the training set microlensing light curves. 91
2.2 Architecture of the forecasting RNN. 96

3.1 Estimations of the perturbers' Einstein radii and flexion shifts based on their luminosity and the M/L ratio computed with P5. 137
3.2 Every modelling scenario considered and their weight in the final posterior. 152
3.3 Summary of all the relevant measurements on HE 1104−1805. 156

1 Introduction

1.1 Evolution of the cosmological paradigm

1.1.1 First conceptions

Throughout history, beliefs about the shape and position of the Earth have been heavily influenced by cosmogony. In ancient Mesopotamia, the Babylonians thought the Earth was flat and floating on an ocean. At the same time, the Egyptians integrated cosmology into their religious practices without explicitly describing the planet's shape or location. Greek philosophers like Pythagoras and Plato, however, proposed a spherical Earth. Aristotle's "On the Heavens", written in 350 BC, suggested that the Earth was at the center of the Universe and that celestial bodies moved in perfect circles around it. This view prevailed in Western civilisations until the 16th century when Copernicus revived Aristarchus' proposition of a heliocentric system with the Sun at the center (see Fig. 1.1). Galileo's discovery of Jupiter's satellites and Kepler's laws of planetary motion further supported this revolutionary idea.

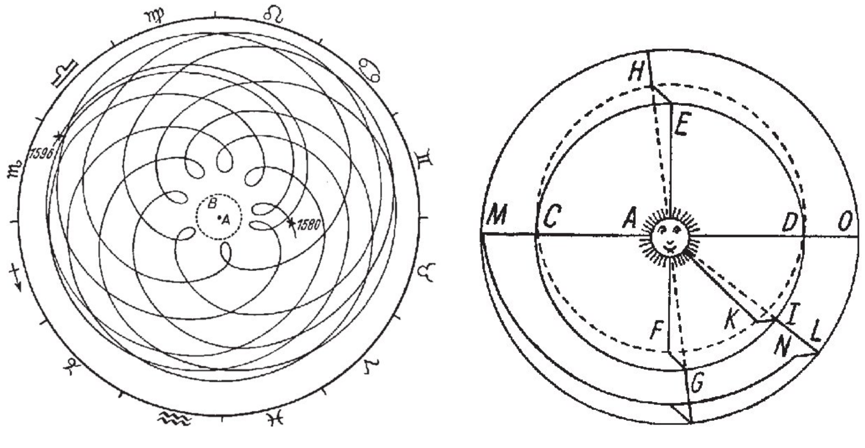

Figure 1.1: ***Left panel:*** Trajectory of Mars recorded by Tycho Brahe and Johannes Kepler in the case of a geocentric system with the Sun in a circular orbit around the Earth displayed in *Astronomia Nova*. ***Right panel:*** : The orbit of a planet in the heliocentric model displayed in *Epitome of Copernican Astronomy*

In the 17th century, Isaac Newton published *Philosophiae naturalis principia mathematical* in which he postulates the existence of a universal force applied to all matter: gravity. He also presents a mathematical framework that demonstrates Kepler's laws and enables accurate prediction of the motion of celestial bodies. In continuation with Kepler's work, astronomers of the 19th century, such as Alexis Bouvard, realised that Uranus' trajectory was not following Newton's law of motion and hinted towards the presence of a nearby planet affecting its orbit. The existence of this planet, Neptune, was demonstrated by its first observation in 1846. Similarly, the orbit of Mercury displayed peculiar precession of its perihelion that astronomers also attributed to the presence of another undetected planet, in vain. This discrepancy was only solved when the cosmological paradigm took another major turn with Albert Einstein's general theory of relativity (Einstein 1915). In the 18th century, Thomas Wright made the first serious proposition about the size of the Universe by stating that the Milky Way was a flattened disk of stars filling the whole Universe, with our solar system within it. This idea laid the groundwork for future investigations into the structure of the Milky Way. Later, Immanuel Kant published *Universal Natural History and Theory of the Heavens* in 1755, where he postulated that the Milky Way was only one of many self-contained "island Universes", which was verified when significant improvements to telescope technology allowed Edwin Hubble to distinguish various types of distant galaxies.

1.1.2 From Einstein's happiest thought to the current paradigm

General Relativity

In 1905, Albert Einstein introduced the theory of special relativity (Einstein 1905). Based on the constancy of the speed of light in all inertial frames of reference, Einstein postulated that the laws of physics are the same for all observers in uniform motion, regardless of their relative velocities. This revolutionary theory abolished the notion of absolute space and time and introduced the idea of **spacetime** as a unified framework. The metric tensor $g_{\mu\nu}$ was introduced to characterise its geometry and encode the relationships between distances, time intervals, and curvature. The interval between two neighbouring events is then given by:

$$ds^2 = g_{\mu\nu} dx^{\mu} dx^{\nu}, \tag{1.1}$$

with **dx** being the spacetime position vector. Following his special relativity theory, Einstein's happiest thought was realising that a free-falling person does not feel their own weight. He concluded that a body's inertial and gravitational mass are equal, which he called the "equivalence principle". This led him to believe that gravity is a force that only appears in a non-inertial reference frame caused by the curvature of spacetime around a mass. Consequently, nearby bodies or particles move along the shortest path determined by the curvature of spacetime known as the geodesic line, as shown in Figure 1.2.

This deformation was formulated by the Einstein tensor $G^{\mu\nu}$ and expressed as:

$$G^{\mu\nu} = \frac{8\pi G}{c^4} T^{\mu\nu} + \Lambda g_{\mu\nu}, \tag{1.2}$$

where $T^{\mu\nu}$ is the energy-momentum tensor, c is the speed of light and G is the gravitational constant. To make this equation consistent with the then-common belief that the Universe is static, Einstein introduced the cosmological constant Λ, which would prevent the Universe from contracting onto itself under the influence of gravitation.

This new formulation of the gravitation principles completed the understanding of the solar system dynamics since it successfully predicts the precession of Mercury's orbit. During a historic expedition to observe the solar total eclipse of 1919, Dyson et al. (1920) brought an additional confirmation of this theory when he measured the deflection angle α induced by the Sun on the light rays of a background star. It was twice as large as predicted by Henry Cavendish in the 19th century based on Newtonian mechanics but followed Einstein's prediction:

$$\alpha = \frac{4GM}{c^2\xi} = 1.75'' \left(\frac{M}{M_\odot}\right)\left(\frac{\xi}{R_\odot}\right)^{-1}, \tag{1.3}$$

with ξ the impact parameter.

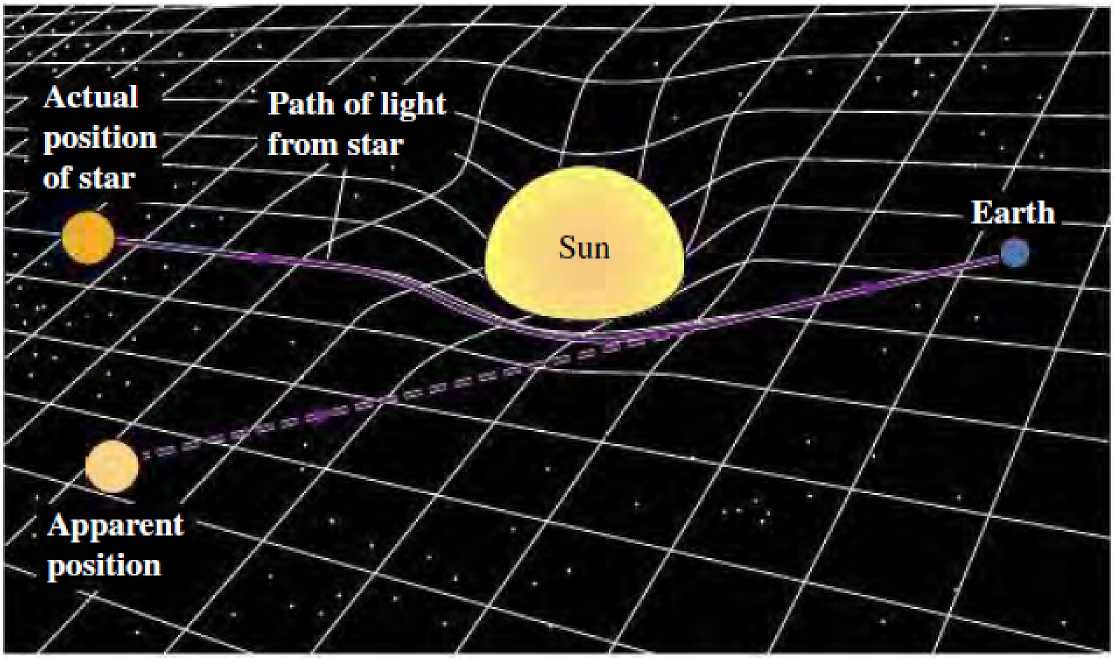

Figure 1.2: Illustration of the curvature of spacetime caused by the Sun. As the light ray moves across a geodesic line, its trajectory is bent, and the apparent position of the source is shifted. (Adapted from physics.stackexchange.com)

Towards an expanding Universe

In contradiction with Einstein's intuition, various cosmologists proposed a solution to Einstein's equation while assuming a homogeneous, isotropic, and inflating Universe that originates from an initial state of high density and temperature. The Friedmann-Lemaître-Robertson-Walker (FLRW) metric was created to characterize such conditions and is formulated as:

$$g_{00} = 1,\; g_{11} = -\frac{a(t)^2}{1-kr^2},\; g_{22} = -a(t)^2r^2,\; g_{33} = -a^2r^2sin^2\theta, \tag{1.4}$$

$$\mathbf{dx} = (t, r, d\theta, d\phi^2), \tag{1.5}$$

where $a(t)$ is the scale factor accounting for the expansion of the metric, t is the cosmic time, r, θ, and ϕ are the spatial coordinates, and k is the curvature parameter (-1 for open, 0 for flat, and +1 for closed universes). Transforming Eq. 1.1 into:

$$ds^2 = -dt^2 + a(t)^2 \left[\frac{dr^2}{1-kr^2} + r^2(d\theta^2 + \sin^2\theta d\phi^2) \right]. \tag{1.6}$$

The stretching of space between a distant object and the observer induces an apparent recessional velocity (along the line of sight) of the source, increasing the wavelength of the light of the source, which appears redder. This phenomenon, known as the cosmological Doppler redshift is given by $z \equiv \frac{\lambda_{\text{obs}}}{\lambda_{\text{emitted}}} - 1$ and is related to the recessional velocity v through:

$$z = \sqrt{\frac{1+v/c}{1-v/c}} - 1, \tag{1.7}$$

$$z \approx \frac{v}{c} \text{ if v << c.} \tag{1.8}$$

It scales from 0 for an object at the observer's position and increases with the distance of the source. Because the speed of light is finite, we only see an image emitted in an older epoch than the present time t_0. The cosmological redshift z and the time t can be used conversely. The scale factor of an object at the time its light was emitted t is then given by:

$$a(t) \equiv a(z) \equiv \frac{1}{1+z}. \tag{1.9}$$

With the same assumptions, the energy-momentum tensor takes the form:

$$T_{\mu\nu} = (\rho + P)u_\mu u_\nu - Pg_{\mu\nu}, \tag{1.10}$$

where ρ, P, and u_μ are the energy density, pressure, and four-velocity of the matter treated as a fluid.

By plugging this metric in Eq. 1.2, we can model our Universe with the so-called Friedmann equations:

$$\left(\frac{\dot{a}}{a}\right)^2 = \frac{8\pi G}{3}\rho - \frac{kc^2}{a^2} + \frac{\Lambda}{3}, \tag{1.11}$$

$$\frac{\ddot{a}}{a} = -\frac{4\pi G}{3}(\rho + 3P) + \frac{\Lambda}{3}. \tag{1.12}$$

We can hence define the expansion rate of the Universe at a time t, a.k.a the Hubble-Lemaitre parameter, and by extension H_0, the present space expansion rate as:

$$H(t) \equiv \frac{\dot{a}(t)}{a(t)} \tag{1.13}$$

$$H_0 \equiv H(t_0) \equiv \frac{\dot{a}(t_0)}{a(t_0)} \equiv \frac{\dot{a}(z=0)}{a(z=0)}. \tag{1.14}$$

As shown by the left panel of Fig. 1.3, Edwin Hubble's measurement of distant galaxies velocity measurement (Hubble 1929) confirmed the linear relation between recession velocity v of a distant object and its distance from us d predicted by Georges Lemaitre (Lemaître 1927), the Hubble-Lemaitre law. It

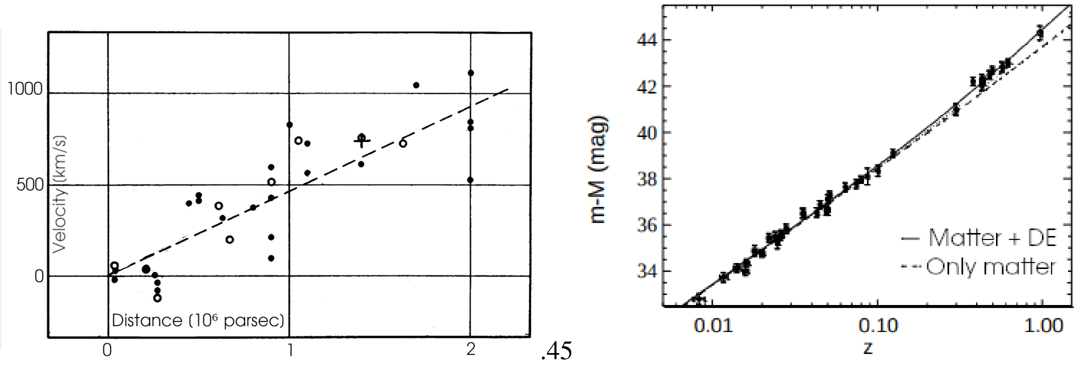

Figure 1.3: ***Left panel:*** Hubble diagram assessing the linear relation between the recessional velocity and the distance to galaxies (Adapted from Hubble 1929)). Following Eq. 1.15, the slope gave a first estimate of $H_0 = 500 \text{km s}^{-1}\text{Mpc}^{-1}$. ***Right panel:*** Hubble diagram obtained by the High-Z Supernova Search (adapted from Riess et al. (1998)). The best-fitting model includes a non-zero cosmological constant materialized as *Dark Energy*.

can also be expressed in terms of redshift z:

$$v = H_0 \cdot d \leftrightarrow z = H_0 \frac{d}{c}. \tag{1.15}$$

In 1948, George Gamow and his PhD student Ralph Alpher developed the theory of nucleosynthesis, which explained the formation of light elements in the hot, dense early state of the Universe (Alpher et al. 1948). They coined the term "Big Bang" as a metaphorical description of the Universe's origin to officially give birth to the Big Bang Theory. This theory successfully predicted the existence of background radiation emitted at the time of the recombination when the Universe matter transitioned from a hot plasma to neutral gas. This radiation, known as the **Cosmic Microwave Background** (CMB), was serendipitously discovered by Penzias & Wilson (1965) with a reported excess antenna temperature corresponding to a microwave emitting body of 4.2 Kelvin. Later, the satellite COBE obtained the first complete map of the CMB (Smoot et al. 1992) by measuring the microwave radiation in all possible directions.

At that time, the Universe was modelled without the cosmological constant (Λ=0). With the mechanism behind the primordial explosion unknown, cosmologists assumed that the expansion of the Universe should be decreasing under the influence of the dominant interaction of gravity. However, they debated the fate of the Universe: is it going to expand infinitely, or will it collapse back to its initial condition in a "Big Crunch"? To settle this question, the Supernova Cosmology Project and the High-Z Supernova Search collaborations measured the distance to remote Supernovae. They both independently realized that the recession velocities of the supernovae were higher than predicted by the Hubble-Lemaitre law (Riess et al. 1998; Perlmutter et al. 1998). As shown by the right panel of Fig. 1.3, at high redshifts, observation deviates from a scenario where the Universe is filled with matter (with a Ω_m=1). This could be only explained by the fact that the Universe's expansion is accelerated. Therefore, a non-zero cosmological constant was reinstated to represent the influence of a so-called **dark energy** (DE) that fuels the acceleration of the Universe expansion.

In the meantime, the study of galaxy clusters by Fritz Zwicky revealed that luminous matter does not account for the total mass of the galaxy cluster (Zwicky 1933). Later, by analyzing the rotation curve of spiral galaxies, Vera Rubin showed that galaxies are rotating faster than expected from their luminous mass (e.g., Rubin et al. 1978). To resolve these discrepancies, the existence of non-baryonic matter, which

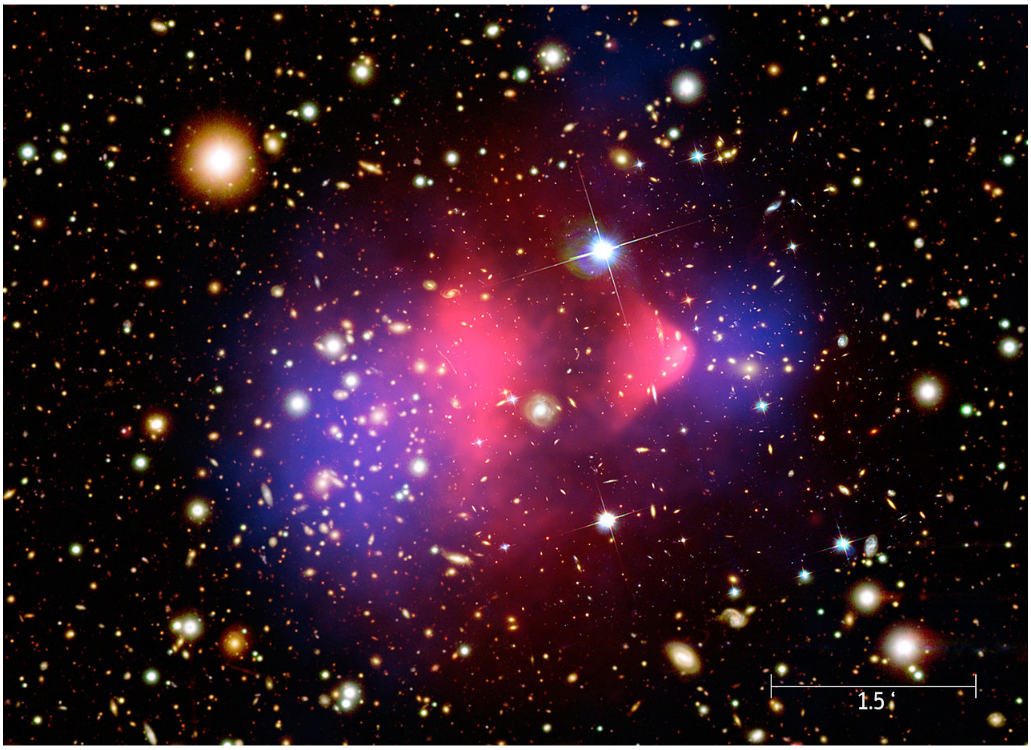

Figure 1.4: Chandra telescope X-ray observation on top of optical imaging of the Bullet cluster (Adapted from Clowe et al. 2006). The pink regions depict two galaxies' interacting baryonic mass components (mostly gas) right after their collision. The blue halos show the reconstitution of the dark matter halo obtained via gravitational lensing.

does not interact with baryonic matter other than through gravitation and does not emit any detectable radiation, was postulated. The "Bullet cluster" shown in Fig. 1.4 depicts two galaxy clusters right after their collision (Clowe et al. 2004). By comparing their mass distribution obtained with gravitational lensing to the luminous matter observed with X-ray observations, it becomes evident that part of the matter is baryonic and interacts with its environment, while the other part is in the form of a cold and smoothly distributed halo. This observation is one of the most compelling proof of the existence of the so-called **dark matter** (DM).

The flat-ΛCDM model

Our cosmological model, therefore, consists of an expanding Universe filled with baryonic matter (BM), cold dark matter (CDM) and dark energy, materialized by the cosmological constant Λ, leading to its denomination: the Λ Cold Dark Matter (ΛCDM) model. We can hence decompose the energy density ρ accordingly:

$$\rho = \rho_{\mathrm{BM}} + \rho_{\mathrm{CDM}} + \rho_{\Lambda} + \rho_{\mathrm{r}} + \rho_{\mathrm{k}}, \tag{1.16}$$

where ρ_{r} refers to the density of radiation, i.e., components such as photons and neutrinos that move at relativistic speed and ρ_{k} is the curvature's energy density.

To investigate the large-scale curvature of the Universe, the average density of matter required for the Universe to have a flat geometry, called **critical density**, was introduced and formulated as $\rho_{\mathrm{crit}} = \frac{3H^2}{8\pi G}$. We can now express the dimensionless density as a function of time (or redshift) as:

$$\Omega_{\mathrm{BM,z}} = \left.\frac{\rho_{\mathrm{BM}}}{\rho_{\mathrm{crit}}}\right|_{\mathrm{z=z}}, \Omega_{\mathrm{CDM,z}} = \left.\frac{\rho_{\mathrm{CDM}}}{\rho_{\mathrm{crit}}}\right|_{\mathrm{z=z}}, \Omega_{\Lambda,\mathrm{z}} = \left.\frac{\rho_{\Lambda}}{\rho_{\mathrm{crit}}}\right|_{\mathrm{z=z}}, \Omega_{\mathrm{r,z}} = \left.\frac{\rho_{\mathrm{r}}}{\rho_{\mathrm{crit}}}\right|_{\mathrm{z=z}}, \Omega_{\mathrm{k,z}} = \left.\frac{\rho_{\mathrm{k}}}{\rho_{\mathrm{crit}}}\right|_{\mathrm{z=z}}. \tag{1.17}$$

We can hence reformulate the Friedman equations (Eq. 1.12) into a single equation that allows us to model the Universe at all stages using only eight parameters:

$$H(z)^2 = H_0^2\left[\Omega_{\mathrm{r},0}(1+z)^4 + \left(1+\Omega_{\mathrm{CDM},0}\right)(1+z)^3 + \Omega_{\mathrm{k},0}(1+z)^2 + \Omega_{\Lambda,0}(1+z)^{3(1+w)}\right], \tag{1.18}$$

where the Dark Energy is parametrized as the equation of state of a perfect fluid:

$$w = P_{\Lambda}/\rho_{\Lambda}, \tag{1.19}$$

fixed to $w = -1$ in the ΛCDM model.

One of the most remarkable predictions of the ΛCDM model is the presence of small fluctuations in the temperature of the CMB, shown in Fig. 1.5, caused by mild inhomogeneities in the primordial plasma. However, creating precise CMB maps requires careful consideration of various biases, including the effects of the Milky Way and foreground emission sources (e.g., Kogut et al. 1993; Copi et al. 2006). The first mapping of these anisotropies by the space-based Wilkinson Microwave Anisotropy Probe (WMAP) confirmed the predicted statistical properties of the CMB fluctuations (Spergel et al. 2003) and allowed an estimation for most of the quantities of the ΛCDM model. The latest observation of the CMB with the similar and improved Planck satellite released in Planck Collaboration et al. (2020a) locates it at $z = 1090$ and gives a precise measurement of the ΛCDM quantities:

$$\Omega_{\mathrm{r},0} \approx 9 \cdot 10^{-5}, \tag{1.20}$$

$$\Omega_{\mathrm{BM},0} = 0.0493 \pm 0.0002, \tag{1.21}$$

$$\Omega_{\mathrm{CDM},0} = 0.264 \pm 0.002, \tag{1.22}$$

$$\Omega_{\mathrm{k},0} = 0.0007 \pm 0.0019, \tag{1.23}$$

$$\Omega_{\Lambda,0} = 0.685 \pm 0.007. \tag{1.24}$$

These measurements corroborate the diagnosis of previous ones regarding the composition of the Universe, and since $\Omega_{\mathrm{k},0}$ is highly compatible with 0, it confirmed that the Universe is flat.

Using these values and the formalism introduced in Eq. 1.18, we are now able to retrace the main stages of the Universe's evolution according to the flat-ΛCDM illustrated in the bottom panel of Fig. 1.5. It starts with all the matter and energy of the Universe concentrated in a single point. At this extremely high energy density, the fundamental forces of nature are believed to be unified, and the laws of physics, as we understand them, break down. During its first instants, up to 10^{-34}s later, the Universe undergoes a phase of "Inflation"[1] during which its volume is multiplied by 10^{26}. As it expands, the Universe cools down, the interactions differentiate, and elementary particles of the standard model (quarks, hadrons and leptons) are created within the first second after the Big Bang. The nucleosynthesis began producing protons and neutrons, which combined into hydrogen, helium and lithium atoms within the first 20 minutes. Because of the different exponents assigned to each energy density term in Eq. 1.18, the expansion of the Universe is alternatively dominated by its components. Radiation are predominant until about 40 000 years after the Big Bang, after which matter prevails. The recombination happened around 375 000 years after the Big

---

[1] This scenario was proposed by Alan Guth (Guth 1981) to resolve the 'Flatness problem' which is out of the scope of this work

Bang when the photons decoupled from atoms; the baryonic matter of the Universe was then mainly in the form of neutral gas. This period is referred to as the "Dark Ages" as a consequence of the complete opaqueness of this neutral gas to radiation. The first stars and galaxies formed a few hundred million years later and emitted energetic radiation. This progressively re-ionized the intergalactic medium and made the Universe transparent to radiation. Since 9.8 billion years after the Big Bang, the expansion of the Universe became dominated by Dark Energy and is now exponential.

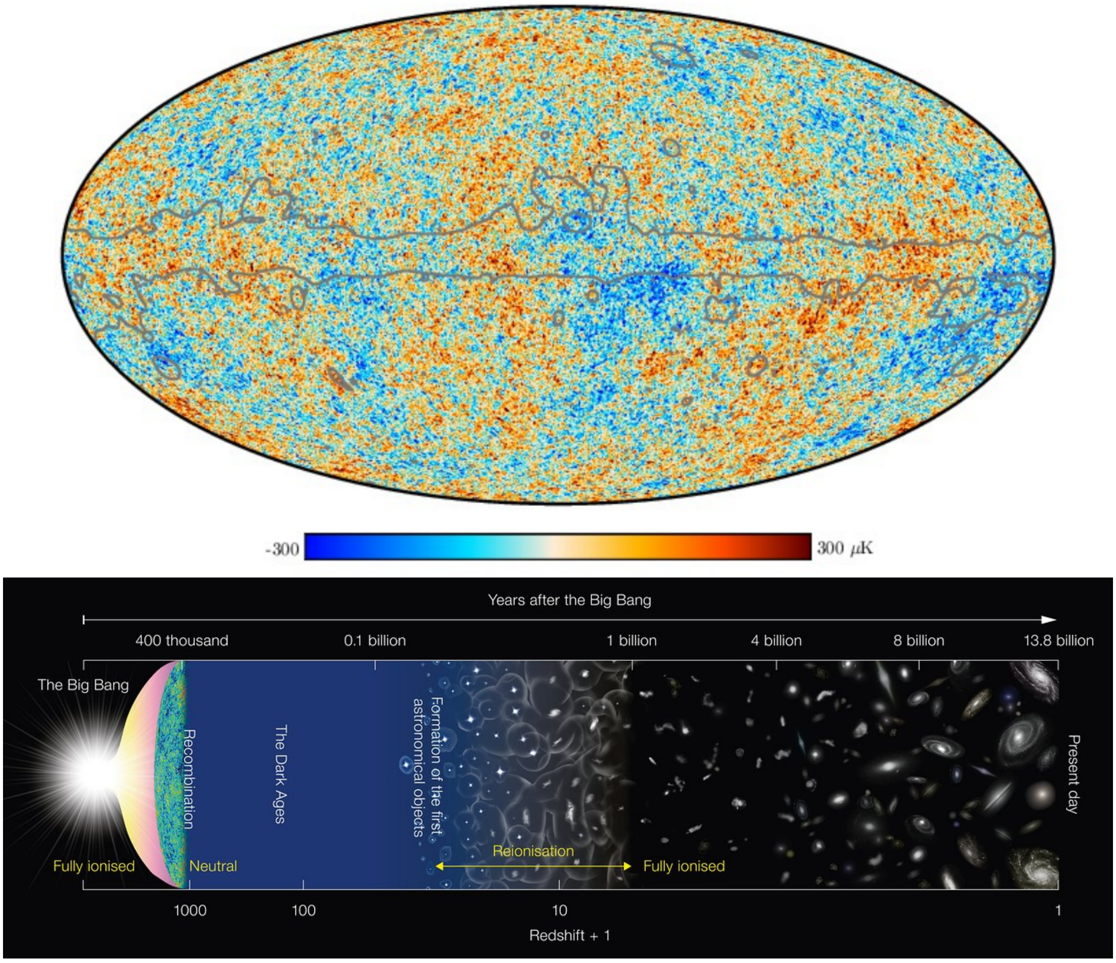
-300
300 μK
Years after the Big Bang
400 thousand
0.1 billion
1 billion
4 billion
8 billion
13.8 billion
The Big Bang
Recombination
The Dark Ages
Formation of the first astronomical objects
Present day
Fully ionised
Neutral
Reionisation
Fully ionised
1000
100
10
1
Redshift + 1

Figure 1.5: ***Top panel:*** Mapping of the background temperature across all directions in the sky (adapted from Planck Collaboration et al. (2020a)). Anisotropies of the order of 10^4 K provide insights into the distribution of matter and energy in the early Universe, helping to unravel the mysteries of cosmic evolution and the origins of structures we observe today. ***Bottom panel:*** Chronology of the evolution of the Universe as modelled by the flat-ΛCDM. Credits: ESO

Questions unanswered by the flat-ΛCDM model

In the present-day paradigm, the ΛCDM model is the most successful and accepted cosmological framework as it explains a wide range of observed phenomena. However, the improvement of observational tools and numeric simulation resolution revealed flaws in the model's predictions.

Some of the notable limitations include:

- Nature of the Dark Matter: Various kinds of particles with different hypothetical masses, generation mechanisms and potential interaction with baryonic matter were imagined to compose Dark Matter. Among the most popular candidates, we can find Weakly Massive Particles (WIMP, introduce by Ellis et al. 1984), sterile neutrinos (e.g., Dodelson & Widrow 1994) or axions (e.g., Peccei & Quinn 1977). These particles have yet to be directly observed, and multiple experiments are trying to narrow down their properties to increase the probability of detecting them.

  Another interesting dark matter component candidate is the Primordial Black Holes (PBH). First hypothesized by Zel'dovich & Novikov (1966), they may have been formed during the inflation period or shortly after when quantum fluctuations may have created sufficiently high-density fluctuations that gravitationally collapsed. The mass of PBHs is hence determined by the scale at which the density fluctuations occur and can range from fractions of a solar mass to several hundreds of solar masses $M_{\odot}$. The non-detection of such objects through microlensing nor gravitational waves indicates that PBH make up at most 10% of the total Dark matter (see e.g. Green & Kavanagh 2020, for a full review).

- Nature of Dark Energy: It is represented by the cosmological constant (Λ) in the model, but its physical origin and properties remain elusive. The most straightforward and longstanding interpretation of Λ postulates that it arises from the inherent energy density of empty space, often called "vacuum energy". An alternative theory suggests that it may arise from the potential energy of a dynamic field, leading to a temporary form of vacuum energy (Peebles & Ratra 1988). Referred to as "quintessence", this dynamic dark energy would exhibit variations in space and time, which could be discriminated from a cosmological constant (see, e.g., Tsujikawa 2013, for a full review). More recently, Farrah et al. (2023) studied black holes spanning ten orders of magnitude in mass across cosmic history and suggested that the mass of a black hole can increase with the expansion of the universe. They supported the notion that black holes contribute to dark energy and explained the onset of accelerating expansion at a redshift of around 0.7. Therefore, more observational and experimental data are needed to confirm any of these theories and better understand dark energy.

- The H_0-tension: Last but not least, the discrepancy between early-Universe and late-Universe probes of the current expansion rate hints towards unknown physics beyond the ΛCDM model. The nature of this tension and its potential resolution are discussed extensively in section 1.4

1.2 Active Galactic Nuclei (AGN)

1.2.1 A bit of history

At the beginning of the 20th century, the spectra of multiple galaxies presented dominant narrow emission lines (e.g., Fath 1909; Slipher 1917; Humason 1932). Carl Seyfert then found up to 8,000$km \cdot s^{-1}$ wide broad emission lines in several other galaxies (Seyfert 1943). These observations were unusual because, as shown in the bottom left panel of Fig. 1.6, the spectrum of standard galaxies is dominated by a continuum of stellar emission with some absorption and faint emission lines, which give insights into their chemical composition. The peculiar lines corresponding to hydrogen Balmer emission are induced by another phenomenon Seyfert identified as taking place in the galaxy's nucleus. Their brightness (equivalent to the luminosity of the rest of the galaxy $10^{10} L_{\odot}$) and compactness lead to the denomination "quasi-stellar nuclei", and these galaxies were classified as Seyfert Type I (broad emission lines) and II (narrow emission lines). With the development of radio astronomy, it quickly appeared that many surrounding galaxy centers (even the center of our Milky Way) emitted radio waves (e.g., Bolton et al. 1949; Baade & Minkowski 1954). The 3C radio survey conducted with the Cambridge Interferometer expanded the catalogue of radio-emitting objects and had a sufficient resolution to identify their optical counterpart (Hewish & Ryle 1955). As shown by the left panel of Fig1.7, the optical imaging of some of the 3C systems (here 3C273) displays a point-like source that can be easily confused with a Milky Way star. Still, because of their abnormal spectra, such systems were named "quasi-stellar object" (QSO) or **quasar**. The redshift measurement of the quasar 3C273 $z = 0.158$ by Schmidt (1963) established that the source was not a star

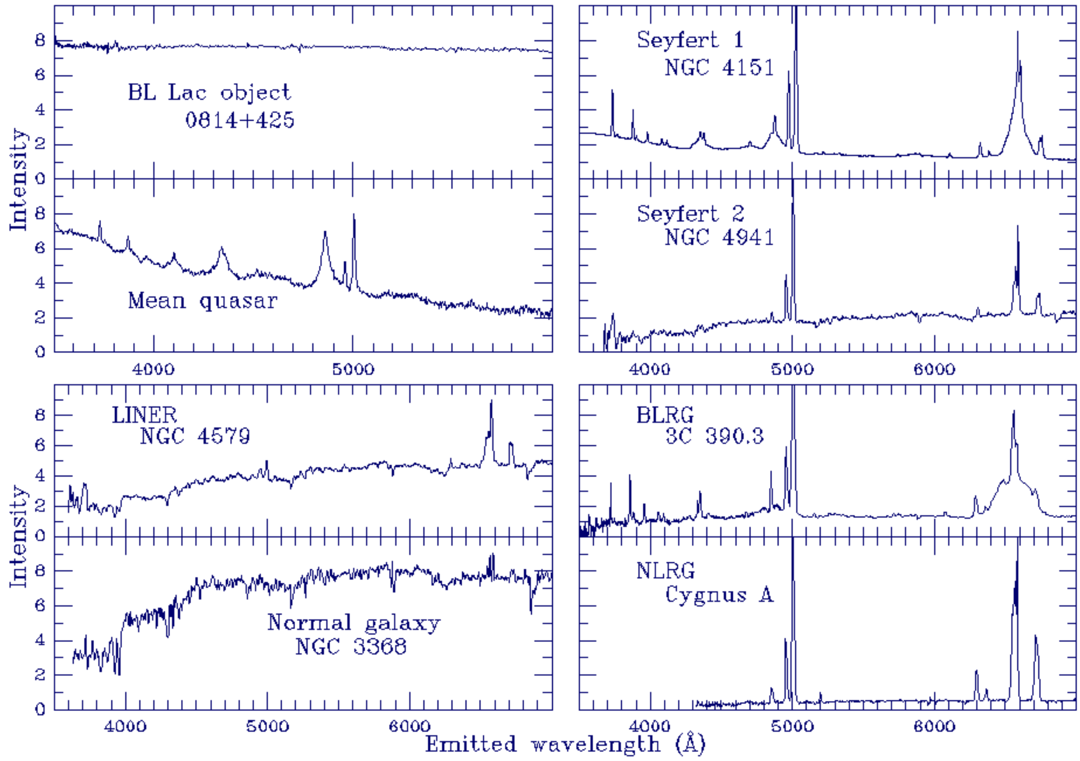

Figure 1.6: Spectra of different types of AGNs and the spectrum of a "standard" galaxy. Seyfert Type I (broad emission lines), II (narrow emission lines)(Adapted from Combes (2021))

but a galaxy with a nucleus so bright that it outshines the rest of the galaxy. As shown by the right panel of Fig. 1.7, the host galaxy is revealed when the central point source is correctly subtracted. Following this breakthrough, it appeared that many mistakenly assumed stars with various types of unexplained spectra were located at the center of distant galaxies. These were hence called Active Galactic Nuclei (AGN), referring to the processes unrelated to stellar nuclear fusion dominant in standard galaxies. As shown in Fig. 1.6, the diversity of spectra observed led to the classification of AGNs into five prominent families: Seyfert galaxies, Radio-quiet quasars, Radio-loud, Blazars, and Radio galaxies. Table 1.1 gives a summary of each family's observational specificities. These families can be regrouped into Radio-quiet AGNs (Seyfert galaxies and Radio-quiet Quasars making up to 80% of known AGNs (Kellermann et al. 2016; Mengistue et al. 2023)) and Radio-loud AGNs (Blazars, Radio-Loud Quasars, making up 20% of known AGNs).

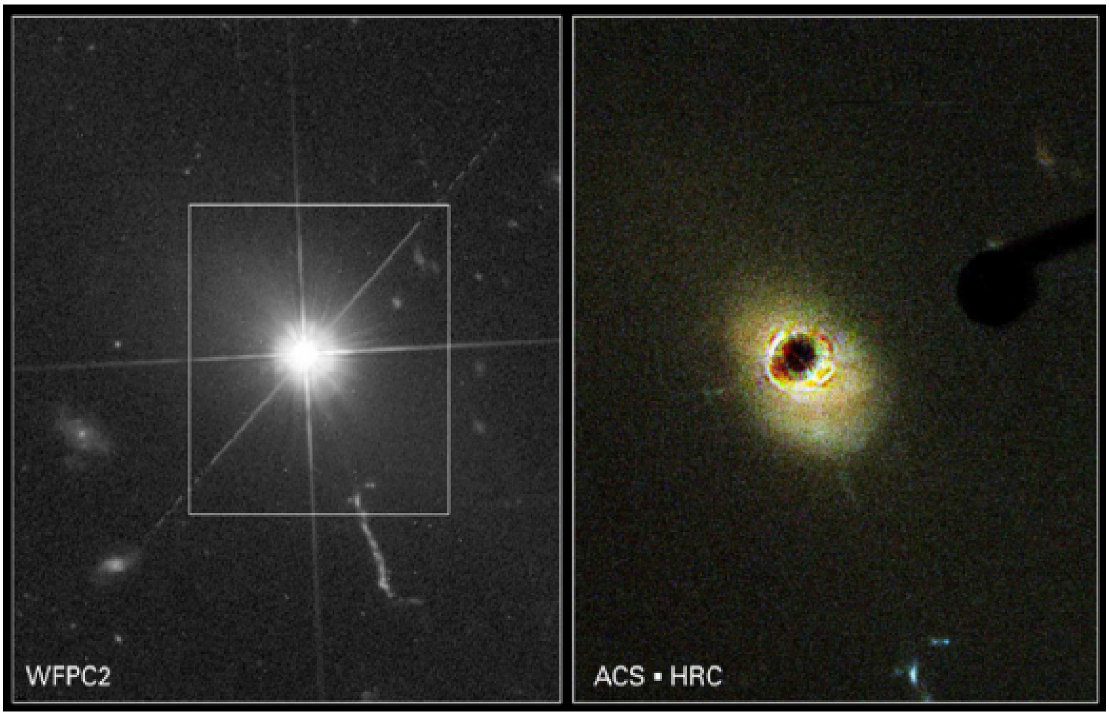

Figure 1.7: ***Left panel:*** HST imaging of the quasar 3C273, the visible diffraction spikes emphasize the point-like nature of quasars. ***Right panel:*** PSF subtracted imaging revealing the host galaxy of the quasar.(Adapted from Martel et al. (2003))

1.2.2 Unified Models

To explain the high luminosity and time variability of AGNs, Salpeter (1964) and Zeldovich (1964) independently suggested that AGN are powered by accretion, the process of matter falling onto a central supermassive black hole (SMBH). However, these early models did not provide a detailed explanation of how the energy release occurs during the accretion process.

Later, Lynden-Bell (1969) expanded on these earlier ideas and introduced the concept of an accretion disk surrounding a black hole. He proposed that the infalling matter forms a rotating disk as it spirals inward toward the black hole. This accretion disk acts as a reservoir of gravitational potential energy and as the

Table 1.1: Observational characteristics of the different types of AGNs. The indicative luminosity ranges are compiled from Schechter (1976); Weedman (1976); Terebizh (1980); Xie et al. (2004). FSRQ stands for Flat Spectrum Radio Quasar and LINER for Low-ionization nuclear emission-line region.

Type	Narrow-line	Broad-line	X-rays	Excess of UV	Excess of far-IR	Radio	Luminosity range [$L_\odot$]
				Seyfert Galaxies			
I	yes	yes	some	some	yes	no	$[10^9 - 10^{11}]$
II	yes	no	some	some	yes	no	$[10^7 - 10^9]$
				Radio-quiet Quasars			
I	yes	yes	some	yes	yes	no	$[10^{11} - 10^{14}]$
II	yes	no	some	yes	yes	no	$[10^9 - 10^{11}]$
				Radio-loud Quasars			
I	yes	yes	some	yes	yes	yes	$[10^{11} - 10^{14}]$
II	yes	no	some	yes	yes	yes	$[10^9 - 10^{11}]$
				Blazars			
BL lac	no	no	yes	yes	no	yes	$[10^6 - 10^{11}]$
FSRQ	no	yes	yes	yes	no	yes	$[10^8 - 10^{13}]$
				Radio Galaxies			
Broad Line	yes	yes	some	some	yes	yes	$[10^9 - 10^{11}]$
Narrow Line	yes	no	some	some	yes	yes	$[10^7 - 10^9]$
				Standard Galaxies			
Std galaxy	weak	no	no	no	no	no	$[10^5 - 10^{11}]$
LINER	weak	weak	no	no	no	no	$[10^5 - 10^{11}]$

matter falls deeper into the gravitational well, it releases a tremendous amount of energy in various forms, including radiation. Furthermore, he paved the way toward a unified model of all AGN by proposing that Seyfert galaxies were collapsed quasars.

Currently, the most widely accepted model of the structure of AGN was proposed by Antonucci (1993) and Urry & Padovani (1995) is displayed in Fig. 1.8. When accounting for the line of sight angle, this model allows the unification of AGNs under a single structure. Radio-loud quasars and Radio galaxies only differ by their luminosity. Seyfert galaxies can similarly be unified with the same structure as radio-loud ones without a jet. As shown in Fig. 1.9, the spectral energy density of the different regions covers the whole electromagnetic spectrum.

Super Massive Black Hole and the accretion disk When solving the Einstein equation 1.2 for a spherical mass, Karl Schwartzschild proved that if a body is smaller than its Schwartzschild radius computed as $R_\mathrm{S} = 2GM/c^2$, it will create a singularity in spacetime out of which even light can not escape (Schwarzschild 1916) called a black hole. Later, Kerr (1963) resolved Einstein's equation for a rotating black hole, referred to as "Kerr black hole", as an extension to the non-rotating Schwartzschild black hole. According to their mass, black holes are classified as:

- Micro black holes (μBH): $M_\mathrm{BH} \leq 10^{-1} M_\odot$, $R_\mathrm{S} \leq 10^2 m$. They are still hypothetical, and their formation is supposed to rely on quantum fluctuations in the early Universe (Hawking 1971)

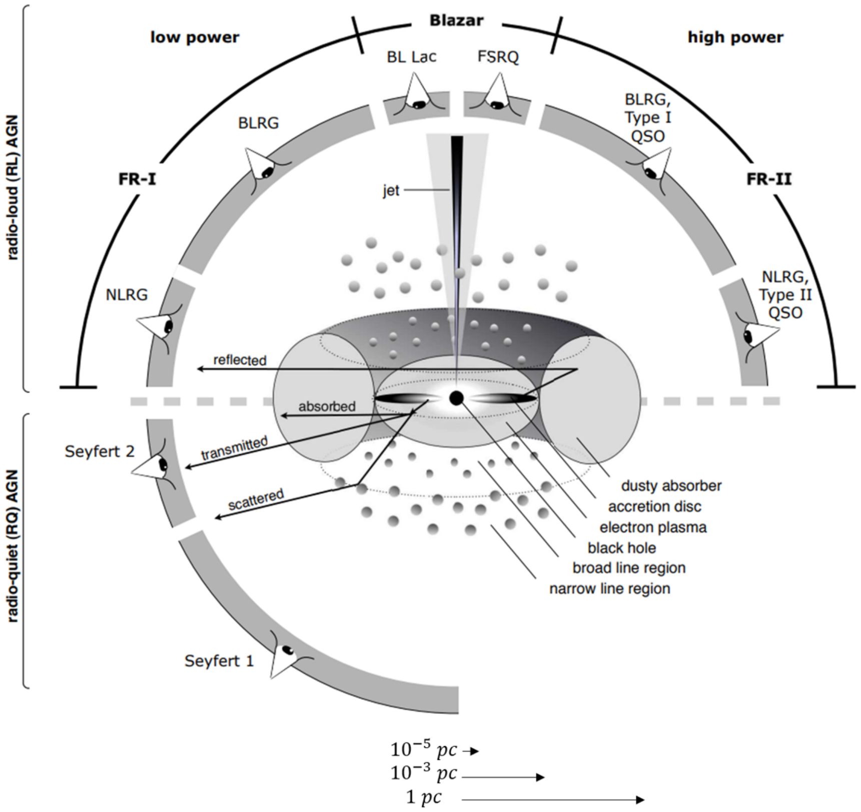
radio-loud (RL) AGN
radio-quiet (RQ) AGN
low power
Blazar
high power
BL Lac
FSRQ
BLRG
BLRG,
Type I
QSO
FR-I
FR-II
jet
NLRG
NLRG,
Type II
QSO
reflected
absorbed
transmitted
scattered
Seyfert 2
Seyfert 1
dusty absorber
accretion disc
electron plasma
black hole
broad line region
narrow line region
10^{-5} pc
10^{-3} pc
1 pc

Figure 1.8: Unified model of AGN. The central SMBH is surrounded by a swirling disk of gas and dust falling towards it, which, in the radio loud case, produces a twin jet launched in opposite directions from the center. The accretion disk is embedded in a proton and electron plasma called the corona. Further away, ionized gas clouds populate the broad and narrow line regions (BLR and NLR). An optically thick torus of dust encircles the whole in the same plane as the disk. The BLR is hidden by the torus when viewed edge-on, while the NLR, further away from the disk, is not. This explains the difference in the spectra of type I and II quasars, Seyfert galaxies, and BLRG and NLRG. When viewed face-on, the emission of the AGN is dominated by the jet, which emits uniformly across the electromagnetic spectrum. Indicative sizes of the ISCO, accretion disk and dust torus are displayed. (Adapted from Britto et al. 2017)

- Stellar black holes (SBH): $1M_{\odot} \leq M_{\rm BH} \leq 10^2 M_{\odot}$, $R_{\rm S} \leq 10^5 m$. They are formed by the collapse of massive stars, which causes energetic supernovae explosions of which numerous examples were observed (e.g., Chandrasekhar 1935; Oppenheimer & Volkoff 1939).
- Intermediate-mass black holes (IMBH): $10^2 M_{\odot} \leq M_{\rm BH} \leq 10^5 M_{\odot}$, $R_{\rm S} \leq 10^8 m$. They are believed to be formed by the accretion of matter towards a seed SBH.
- Supermassive black holes (SMBH): $M_{\rm BH} \geq 10^5 M_{\odot}$, $R_{\rm S} \geq 10^8 m$. They could result from the accretion of matter by an initial SBH seed and the merger with other black holes (e.g., Kulier et al. 2015; Pacucci & Loeb 2020). However, the discovery of such objects less than a billion years after the Big Bang (e.g., Bañados et al. 2018) could indicate that they can form by the direct collapse of large metal-free gas clouds (e.g., Bromm & Loeb 2003).

For the purpose of this work, we will focus on SMBH, which is most likely the centrepiece of the AGN

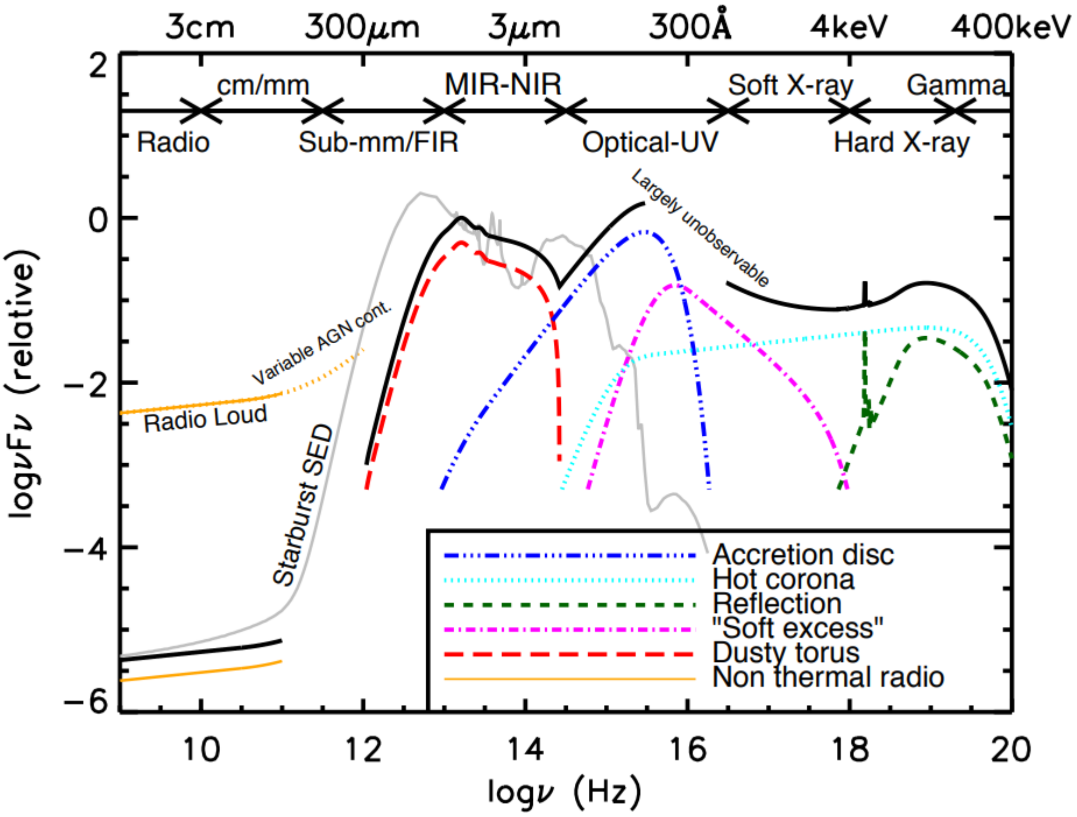

Figure 1.9: Schematic representation of a typical AGN (black curve), separated into the main physical components with arbitrary amplitude (coloured curves). The SED of a star-forming galaxy (light grey curve) is also shown for comparison. (Adapted from Harrison 2016)

structure around which an accretion disk can form. The accretion mechanism affects matter within $\sim 100 R_S$ of the SMBH center, subject to extreme gravitational pull. As this matter spirals into the black hole, tidal stretch and viscous frictions convert gravitational energy into heat and light.

The Innermost Stable Circular Orbit (ISCO) represents the closest orbit at which a photon (or any relativistic particle) can stably orbit the black hole object without falling into it or being expelled. Its radius depends both on the magnitude and direction of black hole spin a and is given by:

$$\begin{aligned} R_{\mathrm{ISCO}} &= 3R_S && \text{if } a = 0, \\ R_S \leq R_{\mathrm{ISCO}} &\leq 3R_S && \text{if } a > 0, \\ 3R_S \leq R_{\mathrm{ISCO}} &\leq 4.5R_S && \text{if } a < 0, \end{aligned} \tag{1.25}$$

The corresponding rotation regimes are non-rotating, prograde (same direction as the accretion disk), and retrograde (opposite direction).

Outside this radius, the light emitted by the accretion process travels outwards through radiative transfer and gives the quasar the luminosity:

$$L_{\mathrm{acc}} = \eta \dot{M} c^2, \tag{1.26}$$

with η the radiative efficiency, which depends on the spin of the black hole (0.06 for non-rotating up to 0.32) but is commonly estimated to be around 0.1 (e.g., Bardeen 1970; Fabian & Lasenby 2019; Pacucci & Loeb 2020; Pacucci & Loeb 2021), and $\dot{M}$ the mass accretion rate.

The Eddington luminosity defines the maximum luminosity achievable by accretion before the outward radiation pressure exceeds the inward gravitational force. It is given by:

$$L_{\mathrm{E}} = \frac{4\pi G M_{\mathrm{BH}} m_{\mathrm{p}}}{\sigma_{\mathrm{T}}}, \tag{1.27}$$

where G is the gravitational constant, M_{BH} is the mass of the black hole, m_{p} is the mass of a proton, and σ_{T} is the Thomson scattering cross-section.

The Eddington ratio defined as $\lambda_{\mathrm{E}} = L/L_{\mathrm{E}}$ is helpful to compare the accretion rate in a population of AGNs.

The dynamic of the accreted material is governed by the combined influences of the gravity pull, the rotational forces and the pressure exerted by outgoing radiation. Different regimes of rotation speed and radiation pressure induce different shapes of the accretion disk. In the case of quasars, the SMBH imposes a high-speed rotation of the accretion disk, but its thickness grows with the radiative pressure (Abramowicz & Fragile 2013). Quasar accretion disks could, therefore be modelled as thin disks with a low accretion rate or slim disks with a high accretion rate.

The thin disk model introduced by Shakura & Sunyaev (1973) stems from the resolution of the equations describing the mass, energy, angular and radial momentum conservations and continuity conditions [II]. It describes the structure and properties of thin accretion disks, assuming it is axisymmetric and in a steady state, i.e. with a constant mass accretion rate. The disk's viscosity ν transporting angular momentum outward to allow the matter to move inward is modelled by $\nu \propto \alpha H$, where α represents the angular momentum transport's efficiency and H the thickness of the disk.

The radial temperature profile of the disk for a given accretion rate $\dot{M}$, and mass of the black hole M_{BH} is:

$$T(r) = \left[\frac{G\dot{M}M_{\mathrm{BH}}}{8\pi\sigma r^3}\left(1 - \frac{R_{\mathrm{ISCO}}}{r}\right)\right]^{-1/4} K, \tag{1.28}$$

with σ the Boltzmann constant. Since the accreted matter emits black body radiation, the Spectral Energy Distribution (SED) of the whole accretion disk combines black body spectra with a peak at different temperatures following this radial profile. As shown in Fig. 1.9, the total SED of the accretion disk peaks in the optical range.

The light profile can therefore be expressed as:

$$I_0(r) \propto [\exp(\xi) - 1]^{-1}, \quad \text{where} \tag{1.29}$$
$$\xi = \left(\frac{r}{R_{\mathrm{S}}}\right)^{3/4}\left(1 - \sqrt{\frac{R_{\mathrm{in}}}{r}}\right)^{-1/4},$$

where R_{S} is the scale radius, defined as the radius at which the temperature of the disk matches the

---

[II] we refer the curious reader to Eqs. 1-9 of Sądowski (2009)

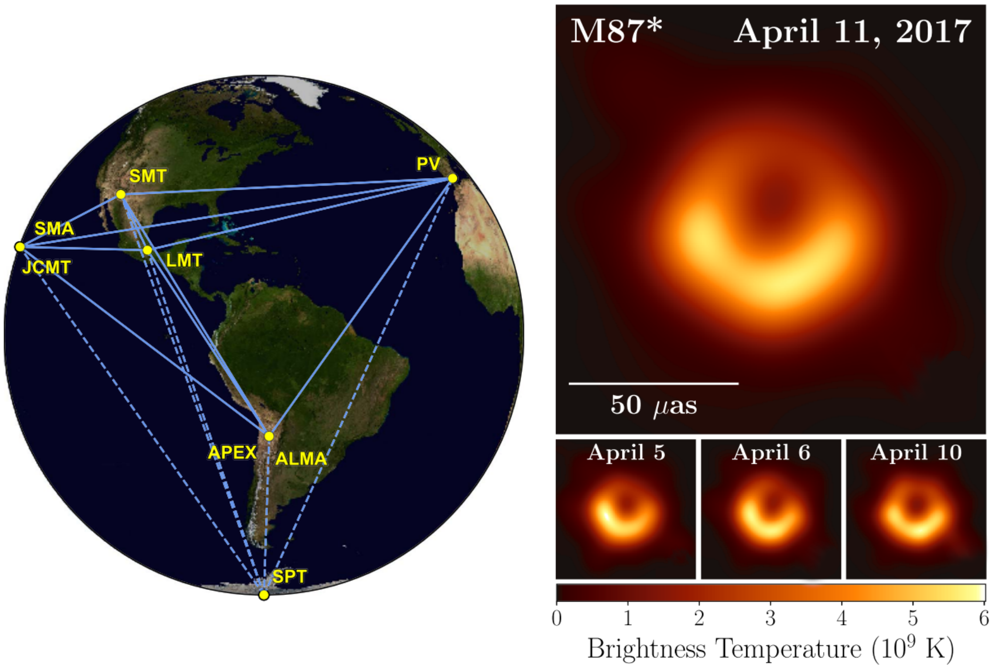

Figure 1.10: ***Left panel:*** Location of the six radiotelescopes used for the EHT setup. ***Right panel:*** First resolved observation of the SMBH at the center of the M87 galaxy and its accretion disk captured by the radio telescope EHT. The brightness temperature fluctuations between consecutive observations highlight the variability of the accretion. (Adapted from Event Horizon Telescope Collaboration et al. 2019)

observation rest wavelength $_{\text{rest}}$ ($kT = hc/\lambda_{\text{rest}}$) expressed as:

$$R_\lambda \propto D_s \lambda^{3/2} 10^{-m}, \tag{1.30}$$

with D_s the angular diameter distance to the source and m its magnitude. We can also express this radius as a function of the black hole mass:

$$R \propto (\lambda_{\text{rest}})^{4/3} (M_{\text{BH}})^{2/3} (L)^{1/3} . \tag{1.31}$$

The assumption that quasars follow the Shakura-Sunyaev solution is grounded in the understanding that the accretion process in quasars is dominated by gravitational energy release and radiative cooling. It has been successful in explaining the observed luminosities and spectra of many quasars (e.g., Caditz 1993). It is important to note that there can be variations and deviations from this model under certain conditions. For instance, at very high accretion rates, near or above the Eddington limit, radiation pressure becomes significant and can affect the disk structure (Abramowicz et al. 1988). In these cases, the accretion disk becomes geometrically thick, as in slim disks or advection-dominated accretion flows (see Abramowicz & Fragile 2013, for a full review). The assumptions of the thin disk model may no longer hold, and the temperature radial profile follows a different power-law $T(r) \propto r^{-1}$ (Spruit 2010).

Studying the temperature gradient of quasar accretion disk is, hence, a powerful probe of the accretion mechanics but also of the central SMBH, which gravitational influence can change the axisymmetry of the apparent shape of the accretion disk because of relativistic effects induced (e.g., Best et al. 2022).

In 2019, the Event Horizon Telescope (EHT, Event Horizon Telescope Collaboration et al. 2019) used simultaneously six radio telescopes around the globe to create a Very Long Baseline Interferometer which is roughly the size of the Earth (see left panel of Fig. 1.10. This unprecedented setup reached the resolution needed to image the shadow of the SMBH M87* (see right panel of Fig. 1.10) and in 2022: Sagittarius A, the SMBH at the center of our galaxy (Event Horizon Telescope Collaboration et al. 2022a). By allowing precise measurement of $R_{\rm ISCO}$ and $M_{\rm BH}$, these observations offered a new laboratory to study the metric of the black holes as well as the mechanisms running the accretion process (e.g., Akiyama et al. 2021; Event Horizon Telescope Collaboration et al. 2022b). Unfortunately, this technique only applies to nearby SMBH, which are less active than distant quasars. To extend these studies to different accretion regimes, different methods to probe the structure of distant quasars are presented in Chapter 2. As discussed in Section 2.1.3, these different method do not all agree with the thin-disk model.

Broad and Narrow line regions The high energy radiation of the accretion disk excite clouds of gas gravitationally bound to the system, producing line emission. In the Broad Line Region, which is typically 10^{-1} pc wide, these lines are broadened by the high velocity of the gas. The emission lines from the Broad Line Region exhibit distinctive profiles with broad wings and narrow cores. The broad wings result from gas moving at high velocities, ranging from thousands to tens of thousands of kilometres per second. The narrow cores arise from gas clouds with lower velocities that may be more distant from the central black hole. As further described in Section 2.1.1, the width of the broad lines can give a virial estimation of the black hole mass, which, in turn constrains the accretion disk model. The exact geometry and structure of these are still under investigation, but it is generally thought to be a thin shell (e.g., Zu et al. 2011; Pancoast et al. 2011; Zu et al. 2013; Williams et al. 2020).

Further away, the speed of the gas decreases, and the lines are narrower. The NLR can be as big as 100 pc and is therefore visible regardless of the angle of the line of sight.

1.2.3 Quasar optical variability.

As presented in Fig. 1.9, the optical luminosity of quasars is dominated by the accretion disk. Because of the stochastic nature of the accretion process and the different time scales of the mechanisms at play, the brightness across various timescales exhibits complex and erratic changes. Characterizing the quasar variability offers another way to probe the accretion dynamics as the amplitude of the variation is linked, among other parameters, to the Eddington ratio and the black hole mass (e.g., Giveon et al. 1999; MacLeod et al. 2010; Rumbaugh et al. 2018). Furthermore, by unveiling a universal variability structure function for quasars, Tang et al. (2023) opens a way to determine outlier objects whose internal processes deviate from standard models.

The damped random walk (DRW) process is a simple yet powerful framework for describing the stochastic nature of quasar variability (Kelly & Siemiginowska 2009). It is a Gaussian Process in which the kernel is parametrized by the amplitude of short-time scale stochastic variations σ and the relaxation time τ, which sets the time scale of long-term finite variations. The DRW parametrization allowed us to characterize the variability of large quasar samples in the Sloan Digital Sky Survey (SDSS) and Pan-STARRS survey (e.g., MacLeod et al. 2010; Ivezić & MacLeod 2014; Suberlak et al. 2021).

Alternatively, the Continuous-time AutoRegressive Moving Average (CARMA) process offers a more complex representation of variability (Kelly et al. 2014). The CARMA process involves autoregressive and moving average components and is described by a characteristic polynomial that governs the system's behaviour. CARMA models can capture a broader range of behaviours, including quasi-periodic oscillations, which are often present in observed quasar light curves (e.g., Gupta et al. 2008; Zhang et al. 2017; Zhang 2022a,c).

Machine learning methods such as latent stochastic differential equations or auto encoder networks have also emerged as a potent tool for modelling quasar variability (e.g., Tachibana et al. 2020; Lin et al. 2020; Fagin et al. 2023; Kovačević et al. 2023). These non-parametric modelizations of quasar variability algorithms are more flexible than the DRW process. They are thus able to capture short patterns more efficiently and extract the physical properties, such as the mass of the black hole, but are yet to be applied to real data.

1.2.4 Interplays with the host galaxy

The energy released during the black hole's accretion process affects the surrounding gas and dust. The feedback mechanisms between quasars and their host galaxies, such as powerful winds and jets emanating from the quasar's central region, can impact star formation rates, galaxy morphology, and even the distribution of stellar populations (e.g., Hopkins et al. 2007; Kormendy & Ho 2013). Furthermore, these feedback mechanisms can regulate the black hole's accretion, as shown by Poitevineau et al. (2023), who found that radio-loud AGN displays distinct black hole mass to galaxy mass (M_{BH}/M) ratios. Therefore, radio feedback may control the growth of supermassive black holes and the formation of stellar masses in these sources. In contrast, simulations by Soliman et al. (2023) suggest that different accretion disk models can result in varying SMBH and host galaxy coevolution.

These findings emphasize the need to investigate the inner structure of AGN for a complete understanding of galaxy and quasar co-evolution.

1.3 Gravitational lensing

1.3.1 Formalism

In Section 1.1, we reviewed how Einstein's theory of general relativity describes the deformation of spacetime caused by massive objects, resulting in the bending of surrounding light rays. It was therefore imagined that, much like an optical lens, the gravitational influence of an object (known as the deflector or lens) could focus light rays from a distant background source coming from different directions, creating the illusion of multiple sources for the observer. Indeed, Einstein (1936) showed that an observer positioned more than 542 AUs from the Sun could see multiple images of a background star, and Zwicky (1937) showed that this phenomenon is very likely to be observed from Earth if we consider a galaxy acting as a lens. A few years later, the serendipitous discovery of a twin quasar at redshift $z = 1.29$ by Walsh et al. (1979) turned out to be the first observed gravitationally lensed object when very similar jets were observed in both quasars (Gorenstein et al. 1984). The galaxy acting as the main deflector was identified at $z = 0.355$. In this section, we will introduce the basics of gravitational lensing formalism, which allows us to connect the observables of a gravitational lens system to the physical properties of the source and the deflector.

As illustrated by the first predictions of Einstein and the first discovery of a gravitational lens system, the distance between the observer, the lens and the source are orders of magnitude larger than the size of the deflector. We can, therefore, safely treat the lens as a two-dimensional surface with negligible thickness.

This shortcut, referred to as the **thin-lens approximation**, allows us to ignore any effects arising from the finite thickness of the lens and focus solely on the refraction of light at the lens surfaces.

Fig. 1.11 shows a typical gravitational lensing system scheme. A light ray emitted by the source reaching the lens plane at a distance ξ or angle θ from the deflector is deflected by an angle $\hat{\alpha}$ and the unobservable separation of the source relative to the optical axis is noted β. The geometry displayed instinctively shows us that, in the limit of small angles induced by the astronomical distances, we have:

$$\beta D_{\mathrm{s}} = \theta D_{\mathrm{s}} - \hat{\alpha} D_{\mathrm{ds}}, \tag{1.32}$$

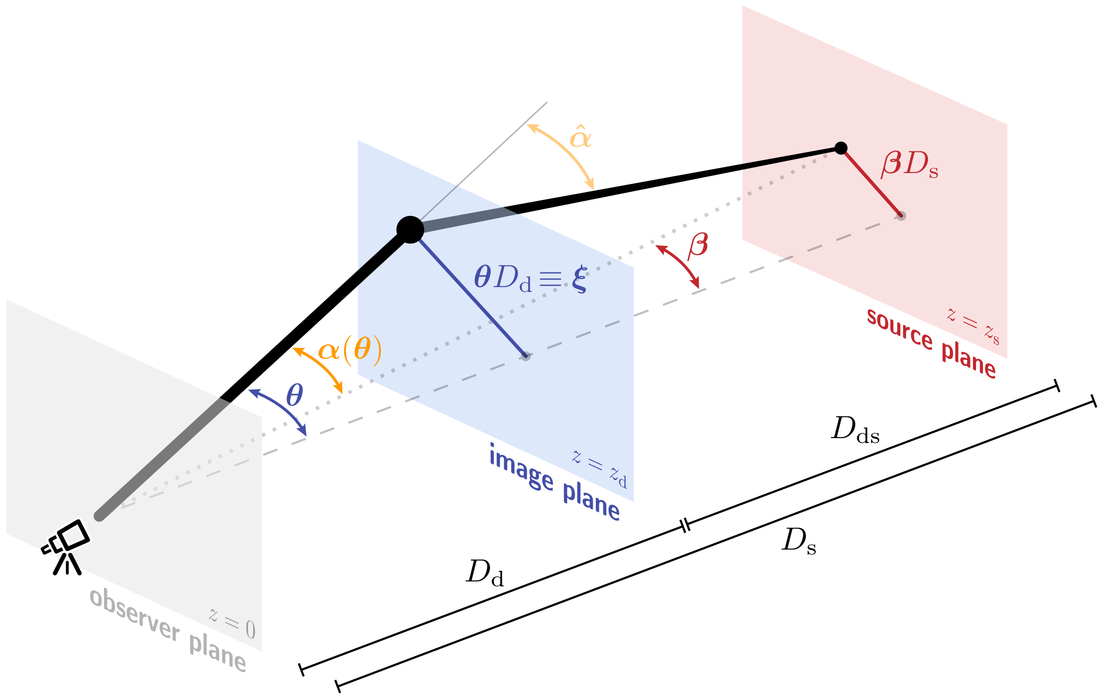

Figure 1.11: Scheme of gravitational lens system. Following the thin-lens approximation, the observer, image and source are characterized by planes. D_{d}, D_{s} and D_{ds} refer to the angular diameter distance between the planes. The optical axis (dashed grey line) connects the origin of each plane, defined as the position of the observer, the position of the deflector and its projection in the source plane. The angle θ is subtended by the impact parameter ξ given by the position of the image in the image plane. The deflection angle $\hat{\alpha}$ is subtended by the observed light ray trajectory with the actual trajectory. The position of the source relative to the optical axis induces the angle β. Figure credits: Aymeric Galan

by defining the scaled deflection angle $\alpha(\theta) = D_{\mathrm{ds}}/D_{\mathrm{d}}\hat{\alpha}$ (hereafter referred to as deflection angle), we obtain the fundamental **lens equation:**

$$\beta = \theta - \alpha(\theta). \tag{1.33}$$

In the thin-lens approximation, $\hat{\alpha(\xi)}$ is given by:

$$\alpha(\xi) = \frac{4G}{c^2} \int d^2\xi' \Sigma(\xi') \frac{\xi - \xi'}{|\xi - \xi'|^2} \text{ with } \Sigma(\xi') = \int \mathrm{d}\xi'_3 \rho(\xi', \xi'_3), \tag{1.34}$$

where $\Sigma(\xi')$ is the surface mass density obtained by projecting the volumic density $\rho(\xi', \xi'_3)$ onto the image plane, and $d^2\xi'$ is the 2-dimensional distance element connecting the center of the lens mass distribution to the orthogonal projection on the lens plane of each mass element.

The minimal surface density required to produce multiple images is defined as the **critical surface density** and is computed by:

$$\Sigma_{\mathrm{crit}} = \frac{c^2 D_{\mathrm{s}}}{4\pi G D_{\mathrm{ds}} D_{\mathrm{d}}}, \tag{1.35}$$

it is used to define the **convergence** i.e the dimensionless surface density:

$$\kappa(\theta) = \frac{\Sigma(\theta)}{\Sigma_{\mathrm{crit}}}. \tag{1.36}$$

We can, therefore express the deflection angle as:

$$\alpha(\theta) = \frac{1}{\pi} \int \frac{(\theta - \theta')\kappa(\theta')}{|\theta - \theta'|^2} d\theta', \tag{1.37}$$

The **deflection potential** defined as:

$$\psi(\theta) = \frac{1}{\pi} \int \kappa(\theta') ln|\theta - \theta'| d\theta', \tag{1.38}$$

allows us to express the convergence and deflection angle as:

$$\kappa(\theta) = \frac{1}{2}\nabla^2\psi(\theta), \tag{1.39}$$

$$\alpha(\theta) = \nabla\psi(\theta). \tag{1.40}$$

The arrival time of a hypothetical photon passing through the image plane at the coordinate θ, also referred to as the **Fermat potential** $\phi(\theta)$, can be expressed as:

$$\phi(\theta,\beta) = \frac{(\theta - \beta)^2}{2} - \psi(\theta). \tag{1.41}$$

Following Fermat's principle, according to which a light ray always takes the quickest path, we find an alternative expression of the lens equation by looking for the stationary points of $\phi\,(\theta)$:

$$\nabla\phi(\theta) = 0. \tag{1.42}$$

Resolving this equation hence gives the location of the observed images.

We can now compute the transformation of an unlensed coordinate system β into a lensed one θ through the Jacobian matrix of the lensing operator given by the lens equation 1.33 or the Hessian matrix of the Fermat potential of Eq. 1.41:

with δ_{ij} being the Kronecker delta. The matrix can then be decomposed into the convergence term κ, which magnifies the image, and the **shear** term with $||\gamma|| = \sqrt{\gamma_1^2 + \gamma_2^2}$ characterizing the stretching of the image.

$$A = \begin{pmatrix} 1-\kappa & 0 \\ 0 & 1-\kappa \end{pmatrix} + \begin{pmatrix} -\gamma_1 & \gamma_2 \\ \gamma_2 & \gamma_1 \end{pmatrix}, \tag{1.43}$$

In the case where the deflector potential is complex, this transformation is better represented with an additional higher-order referred to as the flexion term, $\mathcal{F}$ (e.g., Goldberg & Natarajan 2002):

$$\beta_{\mathrm{i}} = A_{\mathrm{ij}}\theta_{\mathrm{j}} + \frac{1}{2}\mathcal{F}_{\mathrm{ijk}}\theta_{\mathrm{j}}\theta_{\mathrm{k}}, \tag{1.44}$$

$$\mathcal{F}_{\mathrm{ijk}} = \partial_{\mathrm{k}} A_{\mathrm{ij}}, \tag{1.45}$$

where the flexion operator $\mathcal{F}$ can be expressed through the cartesian third derivative of the potential f_{xxx}, f_{xxy}, f_{xyy} and f_{yyy} :

$$\mathcal{F}_{\mathrm{ij1}} = \begin{pmatrix} -2f_{\mathrm{xxx}} - f_{\mathrm{yyy}} & f_{\mathrm{xxy}} \\ f_{\mathrm{xxy}} & -f_{\mathrm{yyy}} \end{pmatrix} \qquad \mathcal{F}_{\mathrm{ij2}} = \begin{pmatrix} -f_{\mathrm{xxy}} & -f_{\mathrm{yyy}} \\ -f_{\mathrm{yyy}} & -2f_{\mathrm{xyy}} - f_{\mathrm{xxy}} \end{pmatrix}. \tag{1.46}$$

The magnification of the image, μ, multiplies the flux of the source because lensing increases the size of the image while conserving its surface brightness; it is given by:

$$\mu = \frac{1}{det(A)} = \frac{1}{(1-\kappa)^2 - \gamma^2}, \tag{1.47}$$

Positions of the image plane where the Jacobian matrix has null eigenvalues and magnification diverges are called **critical lines**. These lines separate areas of the image plane within which the Fermat potential reaches an extremum or a saddle point, mapping them toward the source plane with the lens equation 1.33, we obtain the **caustic curve**. It is important to note that even if a source is located on a caustic, it will not be infinitely magnified. The assumptions of geometrical optics used to derive the equations are no longer applicable, and wave optics predicts magnification values that are finite but very high.

1.3.2 Gravitational lensing regimes and their applications

The lens's mass and alignment along the optical axis set the number of solutions to the lens equation Eq. 1.33. Because of the diversity of massive bodies in the Universe and their (at first order) homogeneous spatial repartition, several regimes of gravitational lensing may be observed:

- **Microlensing** creates multiple images, but they are not resolvable because at most, a few milli-arcseconds (mas) separate them. Still, the magnification of the source across time is detectable. This regime is generally seen when a star or a planet ($0.001 M_\odot$ <M<$10 M_\odot$) acts as the main deflector.

- **Strong-lensing** is observed when multiple magnified images of a background source are separately resolvable. This regime is generally seen when a galaxy or cluster ($M > 10^{10} M_\odot$) acts as the main deflector.

- **Weak lensing** does not create multiple images but deforms and magnifies the background source. This regime is generally seen when a galaxy or cluster acts as the main deflector, but the alignment of the source with the lens is too poor to allow multiple images to form.

Microlensing

By considering a compact spherical mass in front of a star, we can model a typical microlensing system as a point mass M in front of a point source. This configuration provides a simple mathematical framework to apprehend lensing properties.

By assuming that the mass M is enclosed in a surface smaller than the impact parameter ξ, we can use the deflection angle given in Eq. 1.3 and express the lens equation Eq. 1.33 as:

$$\beta = \theta - \frac{D_{\rm ds}}{D_{\rm d} D_{\rm s}} \frac{4GM}{c^2} \frac{1}{\theta}, \tag{1.48}$$

$$\theta^2 - \beta\theta - \theta_{\rm E}^2 = 0, \tag{1.49}$$

yielding the solution:

$$\theta_\pm = \frac{1}{2}\left(\beta \pm \sqrt{\beta^2 + 4\theta_{\rm E}^2}\right), \tag{1.50}$$

$$\theta_{\rm E} = \sqrt{\frac{D_{\rm ds}}{D_{\rm d} D_{\rm s}} \frac{4GM}{c^2}}, \tag{1.51}$$

where we defined the **Einstein radius** $\theta_{\rm E}$. As illustrated by Fig. 1.12, when the source is perfectly aligned with the lens ($\beta = 0$), $|\theta| = \theta_{\rm E}$ solves the lensing equation and the source is deformed to the point where it forms a so-called **Einstein ring**. In other cases, however, only two images are formed, with a constant separation of $2\theta_{\rm E}$. Even though these images were historically unresolved because $\theta_{\rm E} \sim 1$ (mas) in these kinds of systems, the technological progress made with the GRAVITY instrument on the Very Large Telescope allowed Dong et al. (2019) to separately resolve the two images of a microlens system to get unprecedented 2% precision on the mass measurement of the microlens.

In other cases, the main observable of such a system is the total magnification measured, obtained by summing the magnification of individual images:

$$\mu_\pm = \left[1 - \left(\frac{\theta_{\rm E}}{\theta_\pm}\right)^4\right]^{-1}, \tag{1.52}$$

$$\mu = \mu_+ + \mu_- = \frac{\bar{\beta}^2 + 2}{\bar{\beta}\sqrt{\bar{\beta}^2 + 4}}, \tag{1.53}$$

$$\tag{1.54}$$

where we introduced $\bar{\beta} \equiv \beta/\theta_{\rm E}$. We note that μ diverges when $\theta = \theta_{\rm E}$ inducing a critical curve that tangentially magnifies images as they approach it, giving its name: the **tangential critical line**.

Due to the proper motion of the observer, lens and source, with a resulting transverse velocity $v_{\rm trans}$,

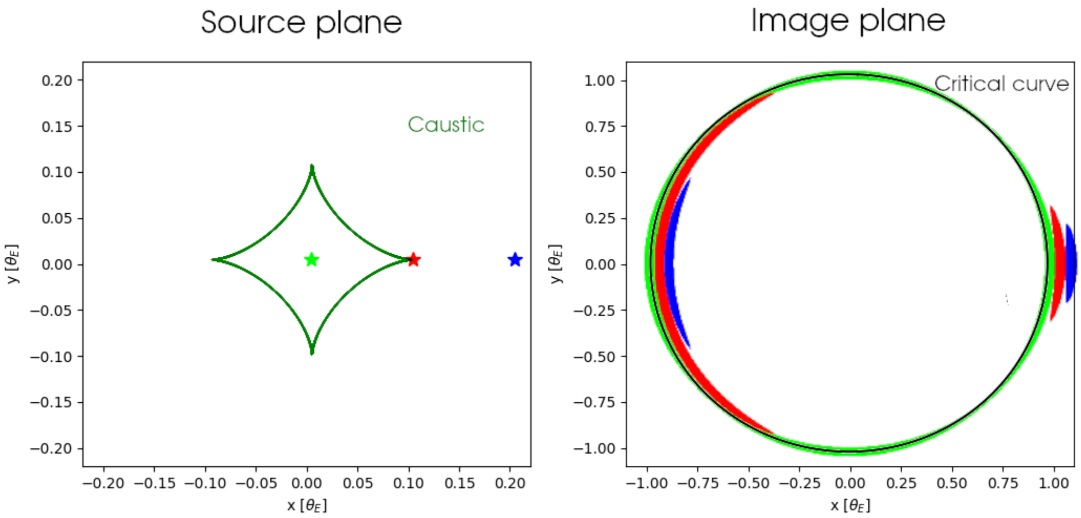

Figure 1.12: A microlensing system simulated by a point mass and a source. Shear was added to emulate the effect of surrounding bodies that do not affect the magnification but still distort the images. ***Left panel:*** Source plane displaying the caustic along with different positions of the source. ***Right panel:*** Image plane displaying the critical curve and image configuration induced by the matching colour source position.

changes in the magnification are expected on a timescale defined as the **Einstein time**:

$$t_\mathrm{E} = \frac{D_\mathrm{d}\theta_\mathrm{E}}{v_\mathrm{trans}}, \tag{1.55}$$

which is of the order of a month for stars in our Milky Way. Assuming a rectilinear and uniform transverse motion, we can express the evolution of $\bar{\beta}$ with time:

$$\bar{\beta}(t) = \sqrt{\bar{\beta}_0 + \left(\frac{t - t_0}{t_\mathrm{E}}\right)^2}, \tag{1.56}$$

where t_0 is the time where the distance $\bar{\beta}_0$ is minimal. Therefore, the observed photometry of a microlensed source evolves with time as a function of its mass M and its shortest distance to the optical axis $\bar{\beta}_0$.

Several programs such as Microlensing Observations in Astrophysics (MOA) (Bond et al. 2001) and Optical Gravitational Lensing Experiment (OGLE) (Udalski et al. 1994) are currently monitoring the luminosity of stars in the Milky Way and the Magellanic Clouds. The sudden magnification of a star proves that a compact body passed in front of it; the magnification's amplitude and length then give the microlens' mass. An example of a magnification event reported by Lam et al. (2022) is shown in Fig. 1.13. The characteristic microlensing light curve fit to the OGLE and HST observations shows that the microlens has a 1.6–4.4 $M_\odot$ mass. The high mass of this body allowed for the detection of a $\sim$ 1 mas shift of the position of the image throughout the event, making it the first astrometric detection of microlensing. Furthermore, such a mass could correspond to a solitary black hole, uncovering the population of such objects in our galaxy.

Microlensing can, in theory, be induced by a wide range of mass (between $10^{-6} < M/M_\odot < 10^6$, Schneider et al. 2006) and can therefore be used to study the population of various objects with a direct measurement of their mass. Most commonly, if multiple superposed magnification events are observed, it means that the

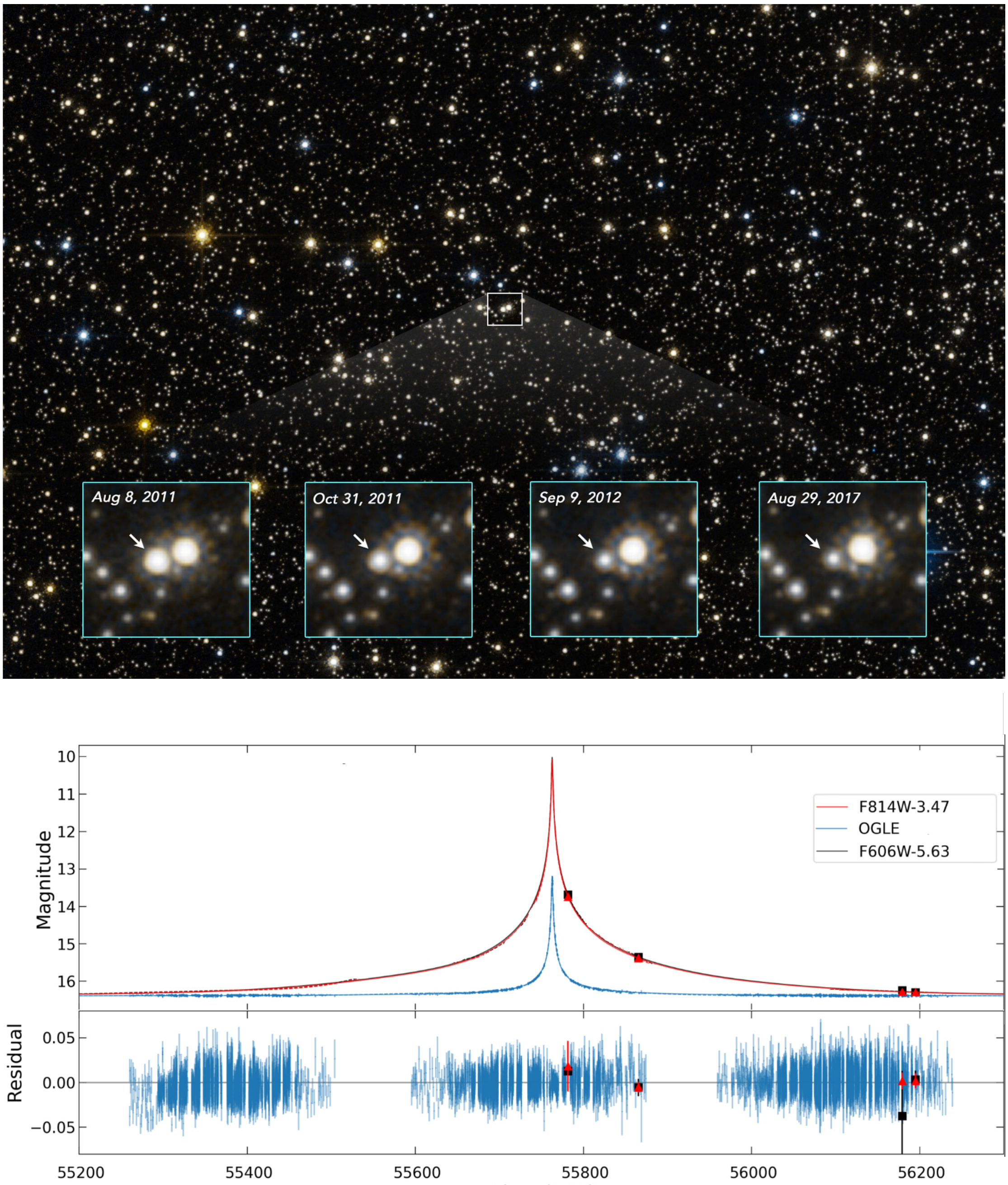

Figure 1.13: ***Top panel:*** Four epoch, two band HST imaging of a microlensing demagnification event, the luminosity of a faint star decreases as the microlensing body moves out of the alignment. ***Bottom panel:*** By combining Eqs. 1.54 and 1.56, light curves are fit simultaneously to the four HST epochs and the OGLE higher cadence observation to determine the mass of the microlens. (Adapted from Lam et al. 2022)

star is microlensed by a many-body system such as a binary star (e.g. Skowron et al. 2007; Maccarone et al. 2019; Soszyński et al. 2021) or a planetary system (e.g. Gould et al. 2014; Yee et al. 2021; Shin et al. 2022).

Among multiple other science uses, we will describe in Section 2.1.2 how microlensing can also be observed in other galaxies and study extragalactic objects.

Strong lensing

To identify the main observables of a typical strong lens system, we will consider the simple case where the lens is an elliptical galaxy, and the source is a quasar hosted in a galaxy.

Image position By assuming a constant volumic density throughout the elliptical galaxy, we can approximate its surface mass distribution with a finite maximum surface density at the center and a power-law decline with the radius, i.e. a Non-Singular Isothermal Ellipsoid (NIE) function. Contrarily to the case where the lens is spherical, the lensing equation cannot be solved analytically, but numerical methods such as ray tracing are used to find the position of the images to show that the tangential critical line is now enclosed in a **radial critical line**.

As shown by Fig. 1.14, when the source is within the radial caustic, it will create five images, while only three are created when the source is between the two caustics. In fact, Burke (1981) demonstrated that elliptical mass profiles always induce an odd number of images. In the image plane, the Fermat potential's maximum, saddle, and minimal points induce an image within the tangential critical curve, between the two critical curves, and outside both curves. This means that the eigenvalues of the transformation matrix A defined in eq. 1.43 are either negative, one negative, one positive, or both positive. Consequently, the magnification of saddle and minima images have opposite signs. Even though the observed flux of the image is multiplied by the absolute value of the magnification, the magnification sign determines the parity of an image. Negative-parity (or odd) images will appear as mirror images or mirrored compared to the background source. In practice, if a lens creates a central image, it would be highly demagnified and hidden by the lens.

Flux ratio Since the Einstein radius of strong lens system is typically ~ 1 arcsec, their Einstein time is much longer than for microlensing systems. Therefore, the magnification of an image is assumed to be constant, and the ratio between the flux of an image pair provides a measurement of the corresponding magnification ratio. The measurement of this ratio is very sensitive to absorption by the interstellar medium (e.g. Falco et al. 1999), magnification by satellite, substructures (e.g. Dalal & Kochanek 2002), or stars (i.e. microlensing Chang & Refsdal 1979). Comparing the observation to flux ratios predicted by a lens mass model can, hence, provide valuable insights on the lens galaxy morphology and composition.

Lensed arc As shown by the left column of Fig. 1.14, in some systems, the galaxy hosting the background quasar is extended enough to form a lensed arc superposed to the images of the quasar point source. The shape of this arc gives additional constraints on the enclosed projected mass and allows us to measure precisely the Einstein radius of the lens.

Time delay As the photon does not travel across a straight line from the source to the observer as it would in a non-lensed case, we can express the additional time induced as a function of the Fermat potential given by:

$$\tau(\theta,\beta) = \frac{1+z_\mathrm{d}}{c}\frac{D_\mathrm{s}D_\mathrm{d}}{D_\mathrm{ds}}\phi(\theta,\beta). \tag{1.57}$$

$$\tau(\theta,\beta) = \frac{1+z_\mathrm{d}}{c}\frac{D_\mathrm{s}D_\mathrm{d}}{D_\mathrm{ds}}\left(\frac{(\theta-\beta)^2}{2} - \psi(\theta)\right). \tag{1.58}$$

where $\frac{(\theta-\beta)^2}{2}$ characterizes the geometrical delay while $\psi(\theta)$ is the so-called **Shapiro delay** due to the time dilation caused by the gravitational field of the lens (Shapiro 1964). From which we can deduce the difference in time taken by a light ray from an image A relative to an image B, Δt_AB:

$$\Delta t_\mathrm{AB} = \frac{D_{\Delta\mathrm{t}}}{c}\Delta\phi_\mathrm{AB}, \tag{1.59}$$

$$\Delta t_\mathrm{AB} = \frac{D_{\Delta\mathrm{t}}}{c}\left(\frac{(\theta_\mathrm{A}-\beta)^2}{2} - \frac{(\theta_\mathrm{B}-\beta)^2}{2} - \psi(\theta_\mathrm{A}) + \psi(\theta_\mathrm{B})\right), \tag{1.60}$$

where we defined the **Time delay distance**, $D_{\Delta\mathrm{t}} = (1+z_\mathrm{d})\frac{D_\mathrm{s}D_\mathrm{d}}{D_\mathrm{ds}}$. Hence, given a proper modelization of the Fermat potential, the measurement of Δt_AB gives the ratio of angular diameter distances involved in a strong lensing system.

We can generalize Eqs 1.60 and 1.41 in the case where multiple lenses lie at different redshifts, creating with P different lens planes. The time-delay then becomes (e.g., Schneider et al. 1992):

$$\Delta t_\mathrm{AB} = \sum^{\mathrm{P_{i=1}}} \frac{D_{\Delta\mathrm{t,i,i+1}}}{c}\left[\frac{(\theta_\mathrm{A,i}-\theta_\mathrm{A,i+1})^2}{2} - \frac{(\theta_\mathrm{B,i}-\theta_\mathrm{B,i+1})^2}{2} - \zeta_\mathrm{i,i+1}\left(\psi_\mathrm{i}(\theta_\mathrm{A,i}) + \psi_\mathrm{i}(\theta_\mathrm{B,i})\right)\right], \tag{1.61}$$

$$D_{\Delta\mathrm{t,i,i+1}} \equiv \frac{1+z_\mathrm{i}}{c}\frac{D_\mathrm{i}D_\mathrm{j}}{D_\mathrm{ij}}, \qquad \mathrm{i<j}, \tag{1.62}$$

$$\zeta_\mathrm{i,j} \equiv \frac{DD_\mathrm{s}}{D_\mathrm{j}D_\mathrm{s}}, \tag{1.63}$$

$i = 1$ refers to the nearest plane to the observer and $i = P + 1$ is the source plane. $D_{\Delta\mathrm{t,i,i+1}}$ is the time delay distance between two planes and $\zeta_\mathrm{i,j}$ is a rescaling factor.

By defining $D^\mathrm{eff}_{\Delta\mathrm{t}} \equiv D_{\Delta\mathrm{t l,s}}$ as the time-delay distance between the main lens plane and the source plane, the time delay can be rewritten:

$$\Delta t_\mathrm{AB} = \frac{D^\mathrm{eff}_{\Delta\mathrm{t}}}{c}\Delta\phi^\mathrm{eff}_\mathrm{AB} \tag{1.64}$$

With the effective Fermat potential:

$$\phi^\mathrm{eff}(\theta) = \sum^{\mathrm{P_{i=1}}} \frac{1+z_\mathrm{i}}{1+z_\mathrm{d}}\frac{D_\mathrm{i}D_\mathrm{i+1}D_\mathrm{ds}}{D_\mathrm{d}D_\mathrm{s}D_\mathrm{i,i+1}}\left[\frac{(\theta_\mathrm{i}-\theta_\mathrm{i+1})^2}{2} - \zeta_\mathrm{i,i+1}\psi_\mathrm{i}(\theta_\mathrm{i})\right]. \tag{1.65}$$

As we will discuss in section 3.1, Refsdal (1964) first stated that since these distances depend on cosmology, one can measure H_0 through a technique called "Time-delay Cosmography".

The most straightforward application of strong lensing is to measure the mass of the lensing body. In gravitational lens systems created by galaxy clusters, it is possible to model the mass distribution of the associated dark matter halo. It is, therefore possible to test the structure formation models within the framework of the Cold Dark Matter paradigm (e.g., Dahle et al. 2003; Newman et al. 2013; Grillo et al. 2015; Lagattuta et al. 2023). On single galaxy scale lensing, gravitational lensing allows us to detect faint dark substructures that are otherwise challenging to observe directly. For example, the detection of substructures with masses around 10^8 solar masses within massive elliptical galaxies (e.g. Vegetti et al. 2012) will give additional constraints to the CDM model, as the number of subhalos vary significantly in alternative Warm Dark Matter models (e.g. Ritondale et al. 2019). Another application involves studying a uniformly selected sample of lenses, such as the Sloan Lens ACS Survey sample (SLACS Bolton et al. 2006), to infer population properties like the mass profile slope and its evolution with redshift (e.g., Bolton et al. 2008), the characteristic scale of their dark matter halo (e.g., Gavazzi et al. 2007), or the mass-to-light ratio (M/L) in the lens galaxy (e.g., Shajib et al. 2021). Similar population studies can be expected for galaxies hosting quasar to probe the quasar-host co-evolution at high redshifts, Millon et al. (2023) benefitted from the rare occurrence of strong lensing by a quasar to measure the mass of both the quasar and its host galaxy with an unprecedented 0.5% precision, significantly better than with conventional photometric or spectroscopic techniques ($\sim$ 10% precision). In addition, this co-evolution can be further studied when the quasar is the lensed object thanks to the high magnification, which enables the mass measurement of the host galaxy, otherwise too small and faint to be observable with a standard telescope (e.g., Ding et al. 2020, 2021). The magnification of the source can also be used to probe the profile and characterize star formation regions of distant galaxies and bring valuable insights on the galaxy evolution model (e.g. Nagy et al. 2022; Dessauges-Zavadsky et al. 2023).

As discussed in Section 3.1, the cosmological distances between lens planes in a strong lens system allow us to measure H_0 in a cosmological-independent way. Additionally, the rare event where a single galaxy lenses sources at different redshifts provides constraints on $\Omega_{\mathrm{m},0}$ and on the dark energy equation of state (Eq. 1.19) (e.g. Collett & Auger 2014; Sharma et al. 2023).

Weak lensing

No additional images are formed if the source is far enough from the optical axis to be outside the tangential and radial caustic. However, its position in the image plane is still deflected, and its shape is stretched tangentially. Since it is in a region where $\kappa < 1$, it is only mildly magnified.

The primary impact of weak lensing is on the ellipticity and alignment of the sources relative to the lens. However, distinguishing whether the distorted shape of a single object is due to its geometric configuration or weak lensing is challenging. A statistical analysis of the spatial distribution of many objects' ellipticities and alignments over a large field is required to detect weak lensing.

The first detection of weak lensing occurred more than a decade after the initial observation of a lensed quasar. Tyson et al. (1990) demonstrated that galaxies within a large cluster tended to align perpendicular to the cluster center. Subsequently, Bacon et al. (2000), Kaiser (2000) and Van Waerbeke et al. (2000) independently observed a similar alignment caused by large-scale structures across cosmological distances, named **cosmic shear**.

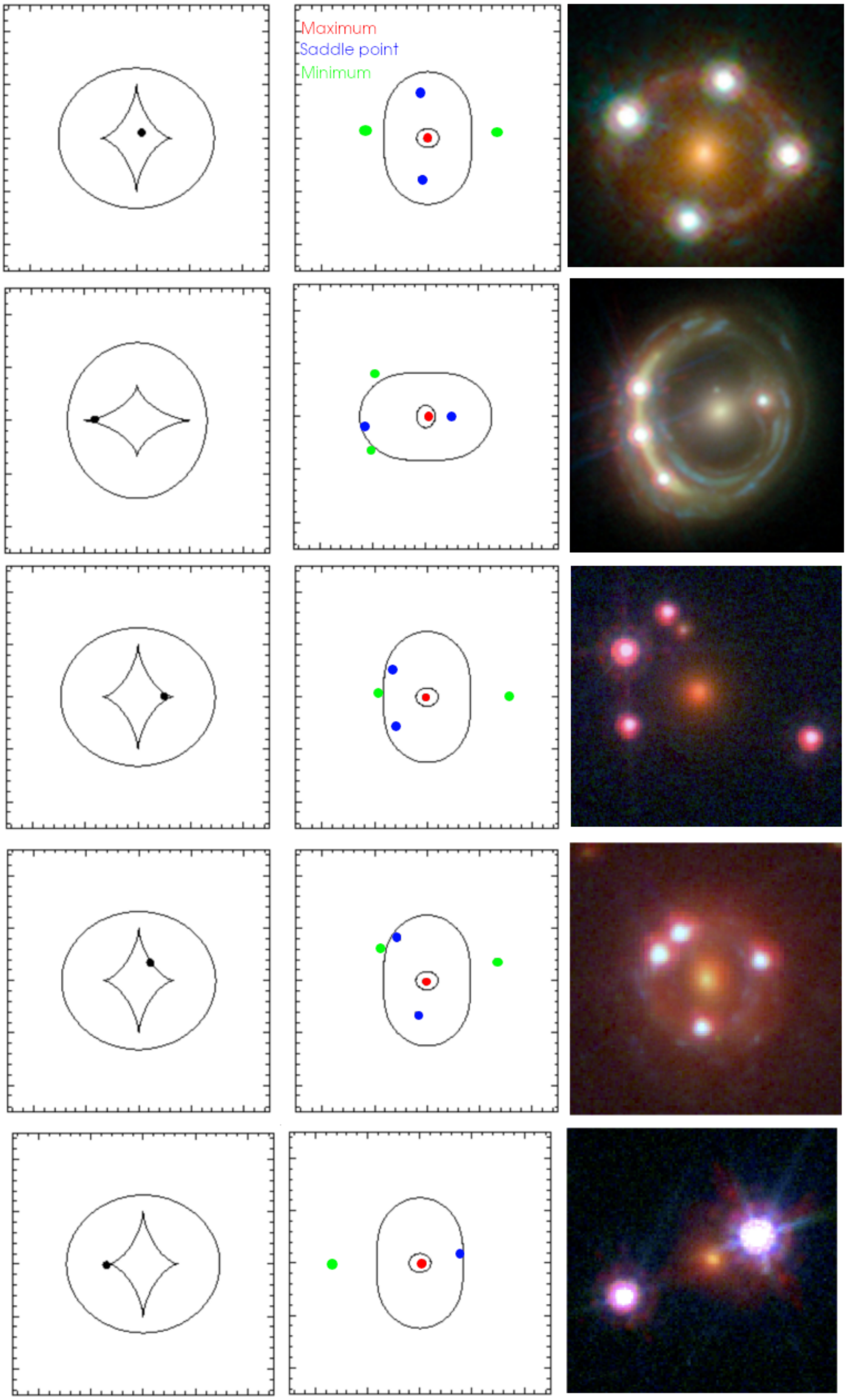

Figure 1.14: **Left column:** Source plane illustration of the strong lens with a fiducial source position. **Middle column:** Image position along with their denomination according to the nature of the corresponding stationary point in the Fermat potential of Eq. 1.41. **Right column:** HST imaging of a similar configuration real galaxy-quasar lenses. From top to bottom, the configuration names are: cross (HE 04351223), a long-axis cusp (RX J11311231), a short-axis cusp (J0659+1629), a fold (GRAL 11314419) and a double (HE 11041805) are shown. (Adapted from Martin Millon's PhD thesis. Image credit: HST/NASA

1.4 H_0 measurement methods

1.4.1 History of the H_0 measurement

The Hubble-Lemaître constant, H_0, has garnered significant interest and debate in astrophysics for over a century, with over 1000 estimations published since 1980 and more than 200 since 2020. As it is directly observable, it can be easily used to validate predictions of any cosmological model, rendering it vital for comprehending the Universe's evolution. H_0 can be inferred from the ΛCDM parameters, providing a comprehensive model test and assisting in clarifying dark energy's nature by untangling the parameter degeneracies (e.g., Weinberg et al. 2013; Motta et al. 2021; Kamionkowski & Riess 2022). Throughout history, astronomers have encountered numerous challenges in estimating the Hubble constant. The first estimation, credited to Lemaître (1927), yielded approximately 625 km $\mathrm{s}^{-1}\mathrm{Mpc}^{-1}$based on galaxies' radial velocities measurements. Subsequent revisions by Hubble (1929) and Hubble & Humason (1931) reduced the value to around 500 km $\mathrm{s}^{-1}\mathrm{Mpc}^{-1}$. However, these early estimates proved to be significantly overestimated. They presented a cosmic age problem, as they implied an age of only 2 billion years for the Universe, contradicting radioactive dating of rocks that suggested Earth's age to be at least 3 billion years.

The following decades saw the measurement of H_0 being performed with various astrophysical phenomena such as Cepheid stars (more details in Section 1.4.2 on the technicalities), which allowed the identification of numerous sources of biases (e.g., Mineur 1944; Baade & Minkowski 1954; Humason et al. 1956; Sandage 1958). A consensus range of 50-100 km $\mathrm{s}^{-1}\mathrm{Mpc}^{-1}$was then established, although debates persisted between groups advocating for lower or higher values (e.g., Sandage & Tammann 1976; de Vaucouleurs & Bollinger 1979).

The launch of the Hubble Space Telescope in 1990 seemed to settle the debate momentarily. Through the recalibration of the Cepheids Period-Luminosity relation, the Hubble Key Project provided an estimate of $H_0 = 72 \pm 8$ km $\mathrm{s}^{-1}\mathrm{Mpc}^{-1}$ (Freedman et al. 2001), in agreement with the measurement based on the observation of the CMB with the WMAP satellite: ($H_0 = 72 \pm 5$ km $\mathrm{s}^{-1}\mathrm{Mpc}^{-1}$ Spergel et al. 2003). Nevertheless, with the increasing precision of the CMB observation mission, the so-called "early-Universe" measurements have been in growing tension with "local-Universe" or "late-Universe" measurements, relying on nearby astrophysical objects or observations of the CMB. In this section, we will present both families of H_0 measurement methods and the relevance of this **H_0-tension** for our understanding of the Universe.

1.4.2 Late Universe measurements

Distance definitions

The Hubble-Lemaitre law introduced in Eq. 1.15 shows that the distance to astrophysical objects is directly related to H_0. It is, therefore, helpful to introduce several definitions of distances in the Universe.

The most straightforward way to compute a distance given its cosmological redshift in a Universe with a constant expansion rate is the **Hubble distance**, given by:

$$d_{\mathrm{H}}(z) = \frac{cz}{H_0}. \tag{1.66}$$

However, since the expansion rate of the Universe is time-dependent (e.g. 1.18), it is only valid for very low redshifts ($z \lesssim 0.1$). We can hence express the distance to points further away using the **co-moving distance** between two points, constant over time:

$$d_{\mathrm{C}}(z) = \frac{c}{H_0} \int_0^z \frac{dz'}{E(z')}, \tag{1.67}$$

with $E(z) = \frac{H(z)}{H_0}$, the dimensionless Hubble parameter.

The **angular diameter distance** defined as the ratio between the size of an object x and its apparent angular size θ:

$$d_{\mathrm{A}} = \frac{x}{tan(\theta)} \approx \frac{x}{\theta}, \tag{1.68}$$

is related to the comoving distance (ergo the cosmological model) through $d_{\mathrm{A}}(z) = d_{\mathrm{C}}(z)/(1+z)$.

Alternatively, in a static Universe, the **luminosity distance** of an object with a luminosity L and an observed flux F is given by $d_{\mathrm{L}} = \sqrt{L/4\pi F}$. To account for the Universe's expansion, this translates to:

$$d_{\mathrm{L}}(z) = (1+z)\frac{c}{H_0} \int_0^z \frac{dz'}{E(z')}, \tag{1.69}$$

$$d_{\mathrm{L}}(z) = (1+z) d_{\mathrm{C}}(z). \tag{1.70}$$

The luminosity distance is also therefore determined by the difference between the apparent magnitude of an object m and its absolute magnitude M, the **distance modulus**:

$$m - M = -2.5log\left(\frac{L}{4\pi d_{\mathrm{L}}^2}\right) + 2.5log\left(\frac{L}{4\pi 10[pc]^2}\right) = 5log(d_{\mathrm{L}}) - 5 \tag{1.71}$$

Therefore, astrophysical objects with a known size or luminosity allow us to measure the angular diameter or luminosity distance to this object without any dependence on the cosmological model. These **standard rulers** and **standard candles** can be used to constrain cosmological parameters such as H_0.

Distance Ladder

One of the first standard candles used to measure H_0 are the type Ia supernovae (SNIa). These have a predictable peak luminosity because they are triggered when a white dwarf star accretes to the Chandrasekhar mass limit of $1.44 M_{\odot}$ (Chandrasekhar 1935). As they are one of the most luminous phenomena in the Universe, they are observable at distances large enough so that their recessional velocity is dominated by the Universe expansion rather than their peculiar velocity, i.e. in the Hubble flow.

However, Phillips (1993) showed that the peak magnitude could noticeably change from one SNIa to the other, hindering their standard candle status. To recover their standardizable quality, we need to calibrate the SNIa distance modulus with independent measurements of distances.

Therefore, The distance ladder is created by a two-step calibration of secondary distance indicators in the Hubble flow (such as SNIa) on primary distance indicators to inter-galactic objects, which are calibrated on geometrical distance indicators within the Milky Way. The distance overlap between the indicators ensures the continuity of the distance ladder from short intra-galactic distance to the Hubble flow.

Geometric distance indicators

1. **Parallax** measurements rely on the apparent shift in the position of a star relative to background stars when observed six months apart from two diametrically opposed points on Earth's orbit. By measuring the parallax angle, we can calculate the distance to the star using basic trigonometric principles. Parallax measurements are widely regarded as one of the most commonly used and robust geometric methods for estimating distances to stars in the Milky Way. The recent data release of the Gaia mission (EDR3 Gaia Collaboration et al. 2021) reached a very high precision measurement of the parallaxes to 1.8 billion stars within the Milky Way. However, it is important to note that the parallax technique has inherent limitations and generally applies only to stars within a distance of approximately 5 kiloparsecs (kpc).

2. **Detached Eclipsing Binaries (DEBs)** are binary star systems in which the two stars orbit each other at a sufficient distance that their shapes and sizes remain unaffected by mutual interaction.

   The DEB distance measurement technique relies on observing the eclipses occurring when one star passes in front of the other as seen from Earth. By monitoring the light curve during these eclipses, we can determine the orbital properties, including the orbital period and the depth and duration of the eclipse. This information allows us to determine the relative sizes and masses of the stars, as well as the size of their orbit, using Kepler's law. By dividing the latter by the apparent angular size of the orbit (determined astrometrically or spectroscopically), the angular diameter distance to the DEB is determined.

   DEBs play a crucial role as a distance indicator not only for globular clusters (Rozyczka et al. 2022) but also for nearby galaxies, such as the Small Magellanic Cloud (SMC, Graczyk et al. 2018), the Large Magellanic Cloud (LMC, Graczyk et al. 2020), and the Andromeda galaxy (Bonanos et al. 2006; Vilardell et al. 2010). The DEB technique provides a valuable means of distance estimation, extending our reach to galaxies located up to approximately 1000 kiloparsecs (kpc). By studying the properties of DEBs in nearby galaxies, we gain insights into stellar evolution, the cosmic distance ladder, and the structure of these neighbouring systems.

Primary indicators

1. **Cepheids** are pulsating stars that exhibit a strong correlation between their period and their luminosity, first discovered by Leavitt (1908). Their absolute luminosities and distance can be established by measuring the pulsation period of Cepheids and calibrating their period-luminosity relation using geometric distance indicators in the Milky Way. This technique proves effective for distances up to 40 Mpc, given the availability of highly precise photometry from instruments like the Hubble Space Telescope (Riess et al. 2019). Although Cepheids cannot be directly resolved in distant galaxies within the Hubble flow due to their faintness, they still play a crucial role in astrophysics. Their primary application lies in calibrating the absolute magnitude of Type Ia supernovae (SNIa) in galaxies where both Cepheids and SNIa have been observed.

2. **The Tip of the Red Giant Branch (TRGB)** marks the inflexion point of the red giant branch within a colour-magnitude diagram corresponding to the triggering of helium fusion, consistently arising at the same luminosity in red giants (e.g., Mould & Kristian 1986; Freedman 1988).

Secondary indicators to H_0 measurements

1. **Type Ia Supernovae**: As shown by Fig. 1.15, the SH0ES collaboration (Supernovae and H_0 for the Equation of State of dark energy) built a distance ladder using parallax and DEBs as geometrical indicators, Cepheids and SNIa, resulting in the measurement $H_0 = 73.30 \pm 1.04$ km s^{-1}Mpc^{-1} (Riess et al. 2022).

2. **Baryonic Tully-Fisher relation (bTF)**: First introduced by Tully & Fisher (1977), this linear correlation between the rotational velocity of spiral galaxies is indicative of their luminous mass, and their absolute luminosity. It hence provides a mechanism to standardize the luminosity of spiral galaxies within the Hubble flow, facilitating luminosity distance measurement. Recently, Kourkchi et al. (2022) refined the calibration of the Tully-Fisher method through a dataset comprising 94 galaxies with well-determined distances derived from Cepheids or TRGB stars. Their analysis yielded a H_0 value of 75.5 ± 2.5 km s^{-1}Mpc^{-1}.

3. **Surface Brightness Fluctuation technique (SBF, Tonry & Schneider 1988)**: This method leverages the observation that nearby galaxies exhibit a more "granular" appearance than galaxies located farther away. The reason behind this is the decreasing resolution of individual stars as the distance to the galaxy increases. A distance indicator can be derived and calibrated using Cepheids or TRGB distances by quantifying the amplitude of these surface brightness fluctuations. Blakeslee et al. (2021) utilized the SBF technique, in combination with Cepheids and the TRGB as calibrators, to obtain a value of H_0 equal to 70 ± 2.5 km s^{-1}Mpc^{-1}. Alternatively, SBF has also been used as a primary distance indicator to calibrate SNIa to get $H_0 = 70.50 \pm 5.0$ km s^{-1}Mpc^{-1} (Khetan et al. 2021).

The comparison of distance ladder measurements using different astrophysical objects allows for studying eventual sources of systematic errors in the measurements. By anchoring SNIa on TRGB calibrated on DEBs in the LMC and SMC, Freedman et al. (2020) measured $H_0 = 69.6 \pm 2.5$ km s^{-1}Mpc^{-1} which is in slight tension with the Cepheid-based measurement of Riess et al. (2022). However, Anderson et al. (2023) emphasized that the Red Giant Branch hosts several families of Red Giant stars, and varying stars mostly populate its tip. By determining the tip while solely using the Small Amplitude Red Giants (OSARGs), they recovered $H_0 = 71.8 \pm 1.5$ km s^{-1}Mpc^{-1}, which is in better agreement with Riess et al. (2022).

Water Mega Masers

Water molecules in Keplerian motion around a Supermassive Black Hole may create radio emission lines due to the Microwave Amplification by Stimulated Emission of Radiation (MASER), creating Water Megamasers. By measuring the radial velocity of these water masers, it becomes possible to calculate the physical size of their orbits using Keplerian dynamics, which can then serve as a standard ruler for distance determination (Humphreys et al. 2013; Reid et al. 2019). Utilizing this technique, the Megamaser Cosmology Project (MCP) measured distances to six galaxies, reaching distances of approximately 130 Mpc allowing for direct measurement of H_0 (73.9 ± 3.0 km s^{-1}Mpc^{-1} Pesce et al. 2020). This measurement is, however, limited to nearby resolvable megamasers for which the peculiar velocity is not negligible compared to the Hubble flow, creating the primary source of systematic bias of this technique. Alternatively, it can be used in the distance ladder to extend the calibration of Cepheid measurement to higher distances (Reid et al. 2019; Riess et al. 2022).

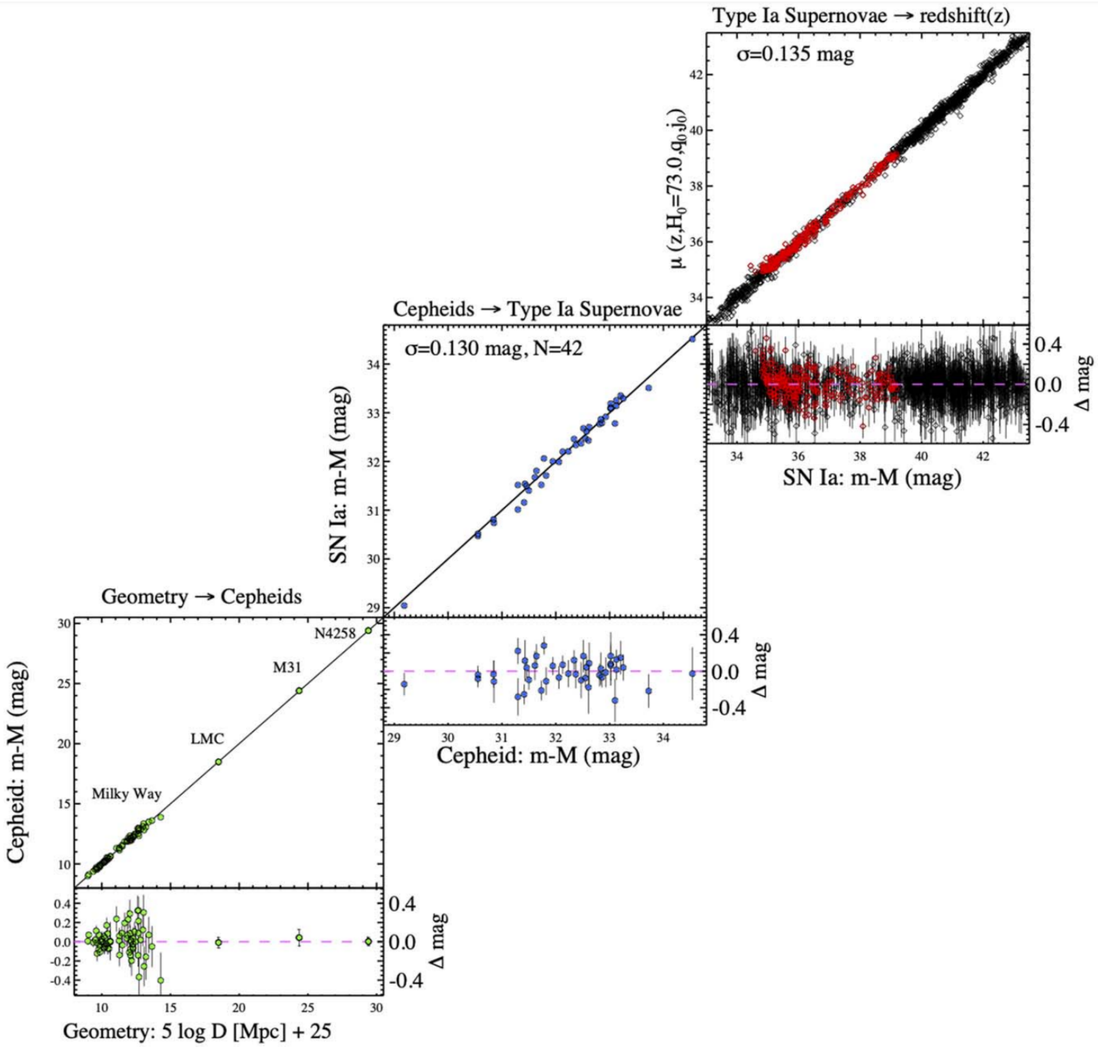

Figure 1.15: Complete distance ladder built by the SH0ES collaboration. The distance moduli of 42 SNIa are calibrated on the ones of Cepheids within the same host galaxies, which are calibrated on geometrical indicators. Including 277 SNIa in the Hubble flow extends the ladder as far as z=2.26. (Adapted from Riess et al. 2022)

Gravitationnal waves

In addition to verifying yet another prediction of Einstein's general relativity, the first direct observation of gravitational waves by the Laser Interferometer Gravitational-Wave Observatory (LIGO Abbott et al. 2016) opened a new era of astronomy and created a novel opportunity to measure H_0. Gravitational waves are ripples in the fabric of spacetime that are generated by the acceleration of massive objects. The first detection came from the merger of two black holes, but since then, scientists have also observed mergers involving binary neutron star systems.

During a binary neutron star merger, the in-spiralling motion of the two neutron stars emits a distinct gravitational wave signal, allowing us to determine the chirp mass of the system, i.e., a combination of the masses of the merging neutron stars.

Using General Relativity, the chirp mass can be used to predict the total energy released in the form of gravitational waves during the merger. By comparing this predicted energy to the amplitude of the gravitational wave signal detected on Earth, scientists can infer the luminosity distance to the system dubbing it as **standard siren**.

However, the measurement of H_0 using standard sirens also relies on the observation of electromagnetic counterpart (possible only for neutron star mergers), needed for the redshift determination of the system. Only one such event, known as GW170817, has been discovered so far and the precision of its associated H_0 value ($H_0 = 70^{12}_{-8}$ km s^{-1}Mpc^{-1} Abbott et al. 2017) is altered by the degeneracy between the inclination angle of the system and the Hubble constant. Using constraints on the orientation from radio observations yielded an improved: $H_0 = 70.3 \pm 5.0$ km s^{-1}Mpc^{-1} (Hotokezaka et al. 2019).

As the sensitivity of gravitational wave detectors continues to improve, it is expected that more binary neutron star mergers will be detected, leading to a rapid advancement in the precision of Hubble constant measurements using standard sirens (see e.g., Bailes et al. 2021, for a full review of upcoming GW detectors.)

Time delay cosmography

Based on the gravitational lensing formalism detailed in Section 1.3, Refsdal (1964) proposed that measuring the time-delay between different images combined with the mass modelling of a strong lens system provided a measurement of H_0 without relying on multiple calibration steps. For a comprehensive description of this technique, we refer to Chapter 3 of this manuscript. Here, we present some key results for comparison with other observational probes.

The first measurement with the first gravitationally lensed quasar Q0957+561 yielded $H_0 = 50 \pm 17$ km s^{-1}Mpc^{-1} (Rhee 1991). It was, however, subject to many sources of biases as the time delay of this system was subject to controversies for a long time (only solved by Kundić et al. 1997) and the mass modelling techniques were too simplistic then. In the most recent studies, Wong et al. (2020) derived a Hubble constant measurement of $H_0 = 73.3^{+1.7}_{-1.8}$ km s^{-1}Mpc^{-1} using six strongly lensed quasars, while Shajib et al. (2020) obtained $H_0 = 74.2^{+2.7}_{-3.0}$ km s^{-1}Mpc^{-1} from a single system. Birrer et al. (2020) re-evaluated the constraints using these seven lenses, adopting minimal assumptions regarding the mass profile of the lensing galaxies. They reported a Hubble constant of $H_0 = 74.5^{+5.6}_{-6.1}$ km s^{-1}Mpc^{-1}. To further improve precision, the inclusion of 33 SLACS lenses without time delays resulted in tighter constraints and a lower value for the Hubble constant: $H_0 = 67.4^{+4.1}_{-3.2}$ km s^{-1}Mpc^{-1}. Alternatively, Shajib et al. (2023) used resolved kinematics of the lens to constrain the mass profile of a single lens and obtained $H_0 = 77.1^{+7.3}_{-7.1}$ km s^{-1}Mpc^{-1}.

Further discussion about the assumptions susceptible to bias in this measurement is made in Chapter 3. Still, Time-delay cosmography stands out as one of the most precise techniques to measure H_0.

1.4.3 Early Universe measurements

CMB observations

As discussed in Section 1.1, the temperature fluctuations of the CMB observed by the WMAP and Planck satellites (see Fig. 1.5) are a central prediction of the ΛCDM. They can, therefore be used to measure cosmological parameters such as H_0. Indeed, these observed structures are due to the complex interactions between baryons, photons, and neutrinos during the pre-recombination epoch (e.g., Peebles 1968; Bond & Efstathiou 1984). By decomposing the observed temperature map of Fig. 1.5 onto spherical harmonics characterized by a multipole order l, related to the inverse of the angular size of anisotropy features, the Planck collaboration achieved remarkable constraints on the angular power spectrum of the CMB anisotropies shown in Fig. 1.16. Assuming ΛCDM cosmology, this power spectrum may be fit to constrain the cosmological parameters (eq. 1.24 which allows the extrapolation of $H_0 = 67.27 \pm 0.60$ km s^{-1}Mpc^{-1}.

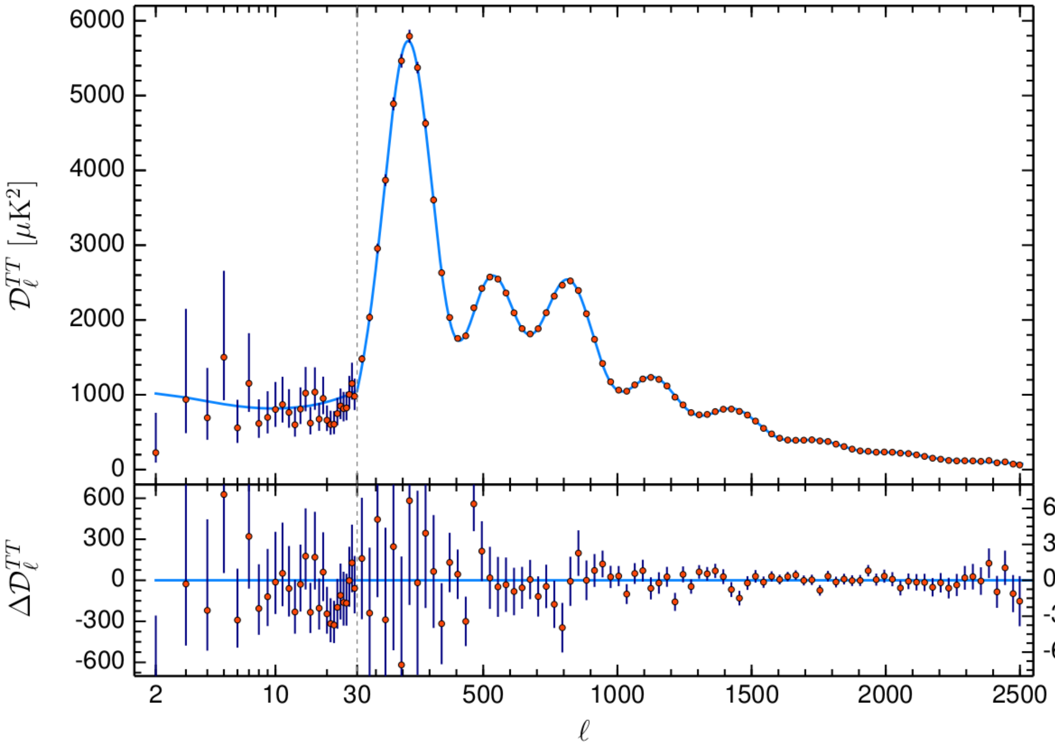

Figure 1.16: Angular TT power spectrum of the CMB (Planck Collaboration et al. 2020c). The ΛCDM fit of this spectrum shows good agreement with the data and constrains the cosmological parameters.

Ground-based experiments, like the Atacama Cosmology Telescope (ACT Kosowsky 2003), have also contributed to CMB measurements. This experiment trades off the atmospheric thickness for larger collector sizes (6-meter primary mirror compared to 1.5 meter for Planck). ACT focuses on smaller, well-selected regions of the sky, enabling it to probe small-scale fluctuations in the CMB that are inaccessible to space instruments (Fowler et al. 2010). Their H_0 measurement is in good agreement with Planck's ($H_0 = 67.9 \pm 1.5$ km s^{-1}Mpc^{-1} Aiola et al. 2020).

CMB experiments are able to constrain multiple cosmological parameters simultaneously with unprecedented precision, considering a broad range of physical scales. However, since these parameters are interconnected, changing one value affects the others. Consequently, CMB experiments do not provide independent determinations of cosmological parameters but rather joint constraints. Determining the Hubble constant from CMB measurements requires additional steps and assumptions, as H_0 is a local parameter related to the present-day acceleration of the universe. It is deduced from combining other cosmological parameters, necessitating a comparison with more direct measurements.

Baryonic Acoustic Oscillations

Like the temperature variations in the CMB, the distribution of galaxies in space is not uniform. Before the recombination, the Universe was a hot plasma crossed by baryonic acoustic oscillation created by cosmological perturbations. The transition of this plasma to neutral gas during the recombination suddenly dropped the speed of sound and effectively froze the acoustic waves. During the period between the formation of perturbations and the epoch of recombination, modes with varying wavelengths undergo different oscillation periods. This phenomenon converts the characteristic time into a characteristic length scale, resulting in a harmonic series of peaks and troughs in the power spectrum of anisotropies, as shown in Fig. 1.16. This characteristic is known as the sound horizon at the end of the baryon drag epoch, $r_{\rm s}^{\rm drag} \equiv r_{\rm d}$.

As the Universe expanded, the colder regions of the CMB map formed denser regions of the Universe hosting more stars and galaxies. As a result, the signature of BAOs can still be observed today in the spatial distribution of galaxies.

The Sloan Digital Sky Survey (SDSS York et al. 2000), the Baryon Oscillation Spectroscopic Survey (BOSS Dawson et al. 2013) and extended BOSS (eBOSS Alam et al. 2021) have measured the redshift of millions of galaxies, enabling the creation of a three-dimensional map of the Universe. By measuring the distance between galaxies at different redshifts, it is possible to track the overdensities of galaxies throughout the Universe and the size of BAOs throughout cosmic history. This makes BAOs a powerful tool for bridging the gap between local and high-redshift measurements of H_0.

BAOs do not directly measure H_0 but rather the product $r_{\rm d} \cdot H_0$ and require external information to calibrate $r_{\rm d}$. For example, Raichoor et al. (2021) used data from SDSS, BOSS and eBOSS to measure the characteristic scale of the BAO, dependent on H_0 and Alam et al. (2021) used constraints on $\Omega_{\rm m}$ from Big Bang Nucleosynthesis (BBN) to constrain $r_{\rm d}$ within the framework of ΛCDM. Their analysis independently confirmed the CMB H_0 measurement, $H_0 = 67.35 \pm 0.97$ km s^{-1}Mpc^{-1}. When adding the constraints from the CMB power spectrum, they got an even more precise value of $H_0 = 68.20 \pm 0.81$ km s^{-1}Mpc^{-1}.

1.4.4 The H_0-tension: status and possible resolutions

By summing up the different aforementioned H_0 measurements, Fig. 1.17 highlights a discrepancy between early-Universe measurements that depend on the ΛCDM model ($\approx$ 67.5km s^{-1}Mpc^{-1}) and late-Universe measurements which are independent of cosmological assumptions ($H_0 \approx$ 73km s^{-1}Mpc^{-1}). As the different techniques gain in precision and accuracy, the H_0-tension is closing in on the symbolic 5-σ significance level (e.g., Verde et al. 2019) meaning that a simple statistical fluke is highly unlikely.

The hypothesis suggesting that we reside in an under-dense region of the Universe has been proposed to account for the higher expansion rate observed in "local" measurements. According to this scenario, denser regions surrounding the Milky Way would pull galaxies away from us. As a result, the Universe's expansion rate, as perceived by an observer within the void, would appear faster than the average expansion rate on a large scale. However, several studies (e.g., Wu & Huterer 2017; Kenworthy et al. 2019) demonstrated that this scenario can only account for a negligible portion of the observed tension.

The reason behind this tension is either an unidentified source of systematic error in one of the families of measurement, or we found a limit to what the ΛCDM model can explain, and a new cosmological model is needed. As discussed, each probe has been tested with various datasets and assumptions. Even though

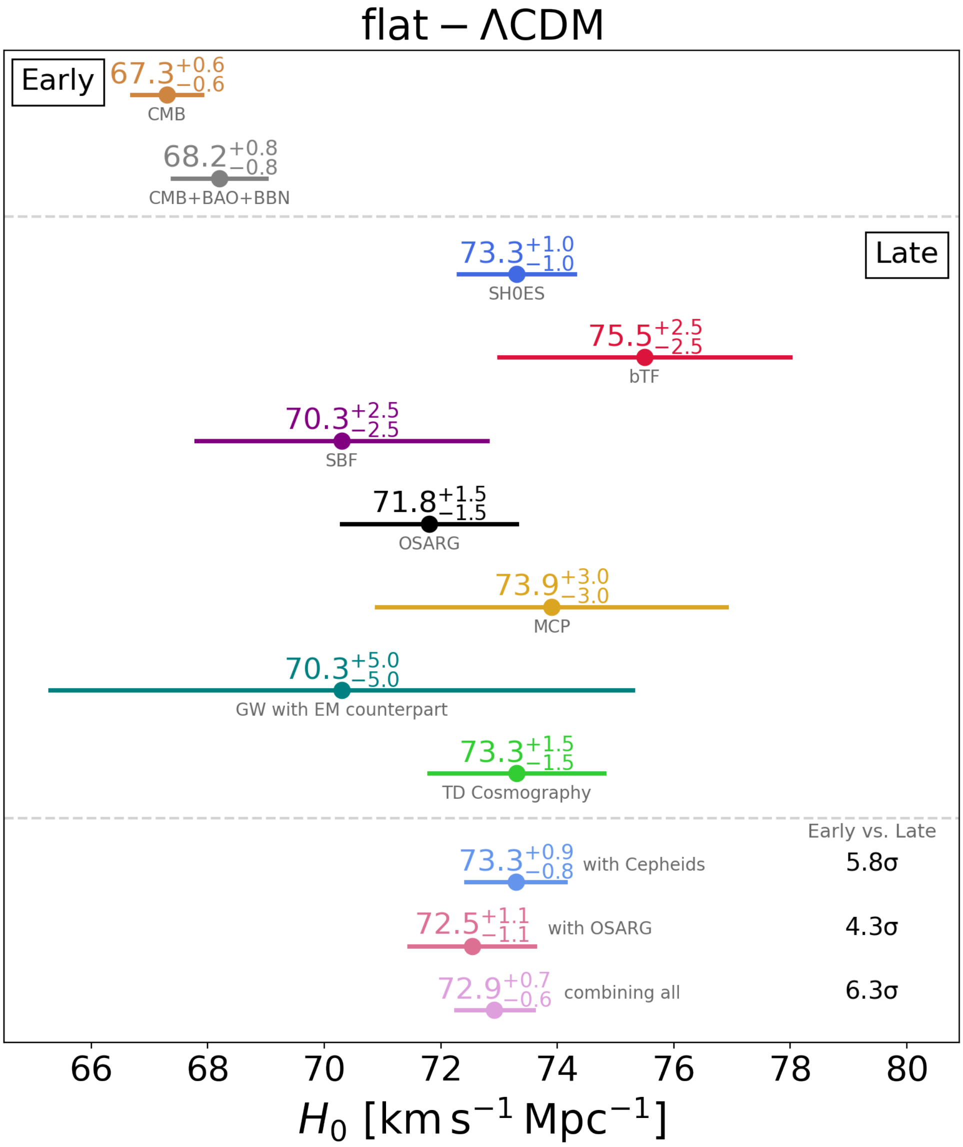

Figure 1.17: Recent measurements of H_0. Early Universe measurements are given by CMB power-spectrum fitting (Planck Collaboration et al. 2020a) and BAO with constraints from BBN and the CMB (Alam et al. 2021). Late Universe measurements are given by distance ladders of SH0ES (Riess et al. 2022), bTF (Kourkchi et al. 2022), SBF (Blakeslee et al. 2021), and OSARGs (Anderson et al. 2023); MCP (Pesce et al. 2020); Gravitational-wave with an electromagnetic counterpart (Hotokezaka et al. 2019); and Time Delay Cosmography (Wong et al. 2020). By ignoring eventual covariances within late Universe probes, we compute an indicative joint constraint of H_0 of TDC with the distance ladder measurements. The combined constraint of every late Universe probe is also shown with the associated tension with the early Universe measurement. (Adapted from Bonvin & Millon 2020)

sources of systematic error are still being investigated, there is no sign of a source of systematic bias that would influence every early or late Universe probe in the same direction.

Jumping on the exciting opportunity to discover new physics, a multitude of new cosmological models have been proposed to resolve the tension (see Di Valentino et al. 2021, for a full review). To "shift" one group of measurements towards the other, these models focus on modifying either early-Universe or late-Universe physics.

Early-Universe solutions: By reconsidering the composition and interactions of the early Universe, the cosmological parameters can be modified and predict higher observed values of H_0 in the Late-Universe. For example, the addition of massless dark relics, modelled as an increased effective number of neutrinos, can enhance the radiation density Ω_r at early times and introduce a degeneracy with the Hubble parameter when observing CMB anisotropies. As their nature is totally unknown, these **dark radiations** were successively modelled as Free-streaming (FSDR, e.g. Bashinsky & Seljak 2004), self-interacting (SIDR, e.g. Ghosh et al. 2021), a mix of both (mixed DR e.g. Brust et al. 2017), SIDR scattering on Dark matter (DR-DM, e.g. Buen-Abad et al. 2015), exotic massive self-interacting neutrinos plus FSDR (SIν+DR, e.g. Kreisch et al. 2020), or even the Majoron, a Goldstone boson resulting from the spontaneous break of the lepton number conservation (Escudero & Witte 2020, e.g.,). The main differences between these models are the number of parameters added to the ΛCDM and their links to other physical observations such as the neutrino oscillation and the cosmic neutrino background (see, e.g. Archidiacono & Gariazzo 2022, for a detailed review).

Alternatively, the size of the sound horizon r_d may have been overestimated by ΛCDM because various unaccounted mechanisms could reduce the speed of sound in the primordial plasma. The length of the sound horizon may have been affected by Primordial magnetic fields (e.g., Jedamzik & Abel 2013), varying electron effective mass m_e (e.g., Franchino-Viñas & Mosquera 2021) combined or not with the curvature of the Universe Ω_k (e.g., Sekiguchi & Takahashi 2021), early dark energy models from Karwal & Kamionkowski (2016) (EDE) or Niedermann & Sloth (2020) (NEDE) or early modified gravity (EMG, e.g. Braglia et al. 2021).

Late Universe solutions: Introducing additional degrees of freedom in the equation of state of dark energy (fixed to $w = -1$ in the standard ΛCDM model), provides a means to alter the value of H_0 today while preserving the early Universe physics. These modifications have a limited impact on the CMB observations because dark energy had negligible influence in the pre-recombination era (as demonstrated by 1.18). Models such as the wCDM add a parameter w to include the dark energy state equation (Eq. 1.19) and replace the cosmological constant Λ. Values of $w < -1$ increase the acceleration of the expansion of the Universe and tend to decrease the H_0-tension (Planck Collaboration et al. 2020a), but w is only weakly constrained by the CMB or any other observable and hence remain a hypothetical solution. Alternatively, the Chevallier–Polarski–Linder (CPL, a.k.a. $w_0 w_\mathrm{a} CDM$ Chevallier & Polarski 2001) allows a time-varying Dark matter $w(z) = w_0 + w_\mathrm{a}\frac{z}{1+z}$. We can also mention the Generalized Phenomenologically Emergent Dark Energy (GPEDE, e.g. Li & Shafieloo 2020) which suggests that DE would only emerge at low redshifts as well as models where Dark Matter decays into Dark Radiations (DM → DR, e.g. Poulin et al. 2016).

So which one is the best ? In an attempt to rank all these possible new cosmological models, Schöneberg et al. (2022) used the CMB power spectra measured by Planck as well as the BAO data from the BOSS collaboration (Philcox & Ivanov 2022) to constrain the respective cosmological parameters and H_0. As shown by Fig. 1.18, none of the proposed models completely agree with both early and late Universe measurements and therefore, no clear "winner" can be designated. Still, some are able to lower the tension between the two significantly. For example, the varying m_e models and the Majoron and GPEDE models put the tension below $3 - \sigma$.

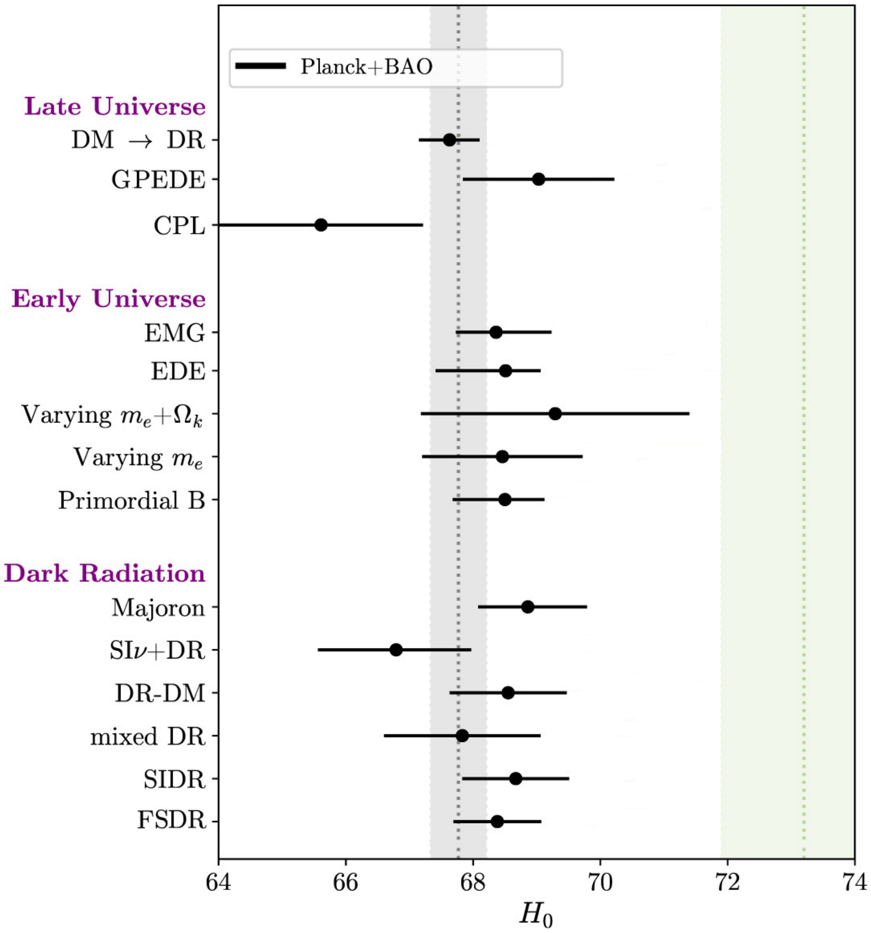

Figure 1.18: H_0-tension predicted by different cosmological models implying changes in the late or early Universe physics or the existence of dark radiations. For each model, the value of H_0 was computed using the latest Planck data (Planck Collaboration et al. 2020c) and BAO data from Philcox & Ivanov (2022). The most precise H_0 measurements of each family are highlighted by the grey column (CMB measurement by Planck Collaboration et al. (2020a)) and the green column (Distance ladder measurement by Riess et al. (2019)). (Adapted from Schöneberg et al. 2022)

These results highlight the complexity of finding a new cosmological model. It is important to note that, given the addition of parameters with each of these models, the precision of these H_0 measurements is hindered, which motivates the need for additional observational constraints.

1.5 Outline of this work

As introduced in this first Chapter, our understanding of the Universe's evolution took giant steps in the last century to reach the flat-ΛCDM model. This model explains a wide range of observations but opens new questions regarding the nature of Dark Matter and Dark Energy. Moreover, it is challenged in its prediction of the value of H_0 by measurements using late Universe probes. As they are the brightest objects in the Universe, quasars can be observed at a high distance and probe the cosmology. Furthermore, studying their structure gives us insight into gravity in extreme conditions and the evolution of their hosting galaxy.

In this thesis, I aim to use gravitational lensing of quasars to learn more about their inner structure and use them as a cosmological probe to measure H_0.

In Chapter 2, I highlight my contribution to the study of quasar structure using their microlensing light curves and in Chapter 3, I present my contribution to the Time Delay Cosmography method.

2 Quasar structure study

2.1 Main probes of quasar structure

As described in Section 1.2, quasars are powered by accreting supermassive black holes and play a crucial role in galaxy evolution. However, their central processes occur on scales too small to be directly resolved in most cases. In this section, we will review the state-of-the-art techniques used to study the geometry of the accretion disk and the BLR: reverberation mapping and microlensing of strongly lensed quasars.

2.1.1 Reverberation Mapping

The optical luminosity of a quasar is dominated by the central accretion disk. The scheme of the quasar structure shown in Fig. 1.8 illustrates how photons from this "driving engine" can be scattered or reverberated by the other regions of the quasar. A photon that undergoes such effects experiences a time lag proportional to the size of the reverberating region $\tau = R/c$ compared to a pristine photon coming directly from the accretion disk. Reverberation mapping is the method that measures this time delay in the variability of surrounding gas and dust to probe the inner regions indirectly and measure black hole masses.

Reverberation mapping relies on several fundamental simplifying assumptions. Firstly, it assumes that the irradiating flux stems from a sole central source. Secondly, it considers the light travel time as the primary timescale of significance. Lastly, it assumes a linear association between the observed reprocessed and ionizing fluxes. If we express the ionizing and reprocessed light curves as the sum of a constant component and a variable component:

$$F_{\mathrm{i}}(t) = \bar{F}_{\mathrm{i}} + \Delta F_{\mathrm{i}}(t), \tag{2.1}$$

$$F_{\mathrm{r}}(t) = \bar{F}_{\mathrm{r}} + \Delta F_{\mathrm{r}}(t), \tag{2.2}$$

the relationship between the variable components of each light curve can be elucidated as follows:

$$\Delta F_{\mathrm{r}}(t) = \int_{0}^{\tau_{\mathrm{max}}} \Psi(\tau) \Delta F_{\mathrm{i}}(t-\tau) d\tau, \tag{2.3}$$

with $\Psi(\tau)$ the transfer function, which encodes the geometry of the reverberating region. The reprocessed light curve can be viewed as a blurred and delayed rendition of the ionizing light curve, with $\Psi(\tau)$ as the blurring kernel. This framework has the potential for expansion to incorporate velocity (or energy) dependencies within the light curves and transfer function. Such extensions enable a comprehensive investigation of the kinematics of the reprocessing region.

As illustrated by Fig. 1.9, the different regions of a quasar emit in different wavelengths. To perform reverberation mapping, it is necessary to measure the changes in the flux of the quasar at different wavelengths. The lag between the light curves provides valuable information about the responsivity-weighted radius of the reprocessing region. However, the ultimate goal is to recover the transfer function, which enables a comprehensive mapping of the geometry and dynamics of the region. Reverberation mapping was initially used to measure the sizes of the BLR by studying lags between the UV/optical continuum and broad emission lines like C IV and Hβ (typically 10 to 1000 days). It has since been expanded to investigate the dusty torus (typically >1000 days), the accretion disk (UV/optical continuum, 1 to 100 days), and the X-ray corona (1 to 10 hours).

Optical light curves obtained from ground-based observations are often non-continuous due to observability issues. Consequently, a time domain approach is typically employed to measure the lag. One standard method is the cross-correlation function, where the light curves are shifted in time relative to each other, and the correlation degree is quantified for each lag. Linear interpolation is frequently used to fill the gaps, or the discrete correlation function can be employed to avoid interpolation (e.g. Gaskell & Sparke 1986; White & Peterson 1994; Peterson 2006). The advantage of cross-correlation methods is their simplicity and reliance solely on the data without making assumptions. However, these methods may not perform well when the data is poorly sampled. Over the years, Markov Chain Monte Carlo (MCMC) methods have been developed for lag determination. These methods assume that the underlying variability of the AGN follows a damped random walk (DRW) or Gaussian processes to estimate the lag (e.g. Zu et al. 2011; Starkey et al. 2016; Yu et al. 2020). The advantage of MCMC methods is their ability to provide lag estimates even with sparsely sampled data, compared to traditional cross-correlation methods. However, they rely on assumptions regarding the characteristics of variability and the shape of the transfer function, which introduces a dependence on the validity of these assumptions.

In the case of X-rays, the short timescales involved allow for the acquisition of uniformly sampled light curves, enabling the use of Fourier analysis techniques. In this case, the cross-spectrum of the light curves in two different X-ray bands is computed. Its phase provides the phase lag, which can be converted to a time lag (e.g. Wilkins 2019).

Accretion disk reverberation In luminous quasars, material moves inward through the disk until it reaches the innermost stable circular orbit (ISCO). In contrast, lower accretion rate quasars exhibit truncated accretion disks due to low flow density and minimal energy radiation (e.g. Narayan 1996). X-rays offer the best way to study quasars' ISCO. UV photons are generated within a few Schwartzchild radii from the SMBH and boosted to X-rays through inverse Compton scattering. Therefore, X-ray reverberation measurements can determine the location of the inner disk edge and, in radiatively efficient quasars, infer the black hole's spin. Doppler broadened features in the X-ray spectrum, such as the iron Kα emission line, are the most prominent reverberation features (e.g. Risaliti et al. 2013; Walton et al. 2014). The extent of these features' wings gives supplementary information on the ISCO's size by allowing the gravitational redshift measurement experienced by the reverberated rays. This method has been used to measure the spins of more than 50 nearby AGNs (see Reynolds 2019, for a review). Alternatively, UV/optical continuum reverberation mapping involves measuring lags in the hot inner region of the accretion disk and the cooler outer region using the correlated light curve where the UV leads the optical (e.g. Cackett et al.

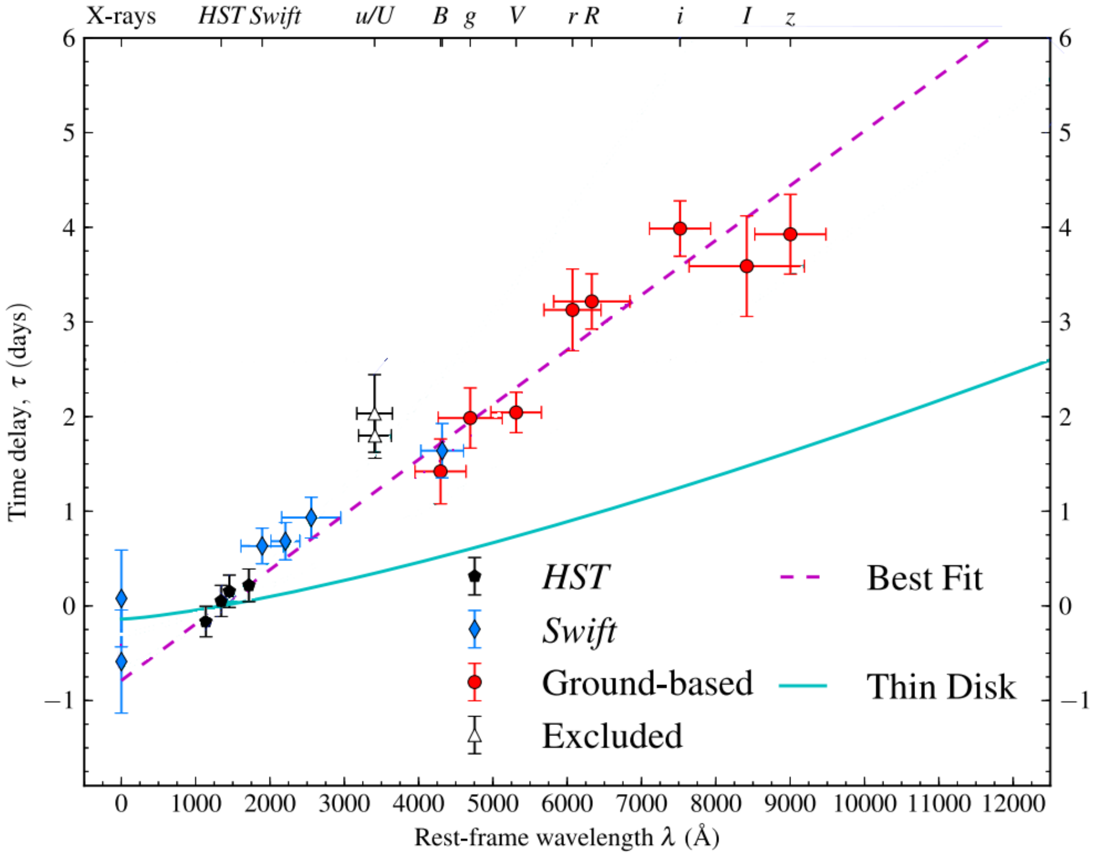

Figure 2.1: Time lag as a function of the wavelength of the filters measured for the quasar NGC5548. The dashed line shows the best fit of equation 2.4 with τ_0 and β left as free parameters. The expected $\tau(\lambda)$ relation computed with independently measured $M = (5.2 \pm 1.3) \cdot 10^7) M_\odot$. Adapted from Fausnaugh et al. (2016)

2007). The lag depends on the disk's temperature profile (see eq. 1.28) and is modelled by a power-law:

$$\tau(\lambda) = \tau_0 \left[\left(\frac{\lambda}{\lambda_0} \right)^{\beta} - 1 \right], \tag{2.4}$$

where the index, β, is 4/3 in the thin disk model of Shakura & Sunyaev (1973), λ_0 is the reference wavelength and τ_0 is the reference lag (assumed to be the lag of the X-rays) which can be expressed as a function of the mass of the black hole M and the Eddington ratio λ_E, $\tau_0 \propto (M\lambda_E)^{1/3}$ by the thin-disk model (see eq. 12 of Fausnaugh et al. 2016, for the full derivation of τ_0).

Recent monitoring campaigns of the Swift spatial telescope (Burrows et al. 2005) demonstrated high precision in lag measurements and revealed longer lags than expected based on the standard thin disk model (e.g., Shappee et al. 2014; McHardy et al. 2014). Groundbreaking constraints on quasar structure were obtained when the Space Telescope and Optical Reverberation Mapping Program (AGN STORM, De Rosa 2015) utilized Swift along with the HST and ground-based observations to monitor NGC 5548, resulting in a significant increase in sampling rate (Fausnaugh et al. 2016). As shown by Fig. 2.1, this campaign found wavelength-dependent lags mildly shallower than thin disk predictions ($\beta \approx 1 < 4/3$). It also showed that the standard assumption for the accretion rate yielded lags on average three times smaller than measured ones (i.e. for a given temperature, disk sizes are three times larger than expected). Subsequent campaigns on other quasars found similar results (e.g. Edelson et al. 2019; Cackett et al. 2020; Hernández Santisteban et al. 2020) with U band lags being consistent outliers in the $\tau(\lambda)$ power-law fit.

A complementary approach to intensive high-cadence monitoring of a few objects is to study a larger sample of objects with lower cadence, utilizing large surveys. By examining the population of objects as a whole, valuable insights can be gained despite individual objects not yielding precise lag-wavelength relations. For instance, Jiang et al. (2017) analyzed 240 quasars observed by the Panoramic Survey Telescope and Rapid Response System (PanSTARRS) and found that the average lags were 2-3 times larger than expected. Similarly, Mudd et al. (2018) reported disk sizes consistent with being three times larger than anticipated with DES data. In contrast, Homayouni et al. (2019) and Yu et al. (2020) observed disk sizes in agreement with the expectations from a standard disk model using SDSS observations.

Future large surveys like the Large Synoptic Survey and Telescope at the Vera C. Rubin Observatory (Rubin-LSST) will significantly expand the number of AGNs with multi-waveband photometric light curves, providing ample opportunities to explore continuum reverberation in greater detail. For example, Chan et al. (2020) showed that the shape of the transfer function can be investigated through the distortion induced on different waveband LSST light curves.

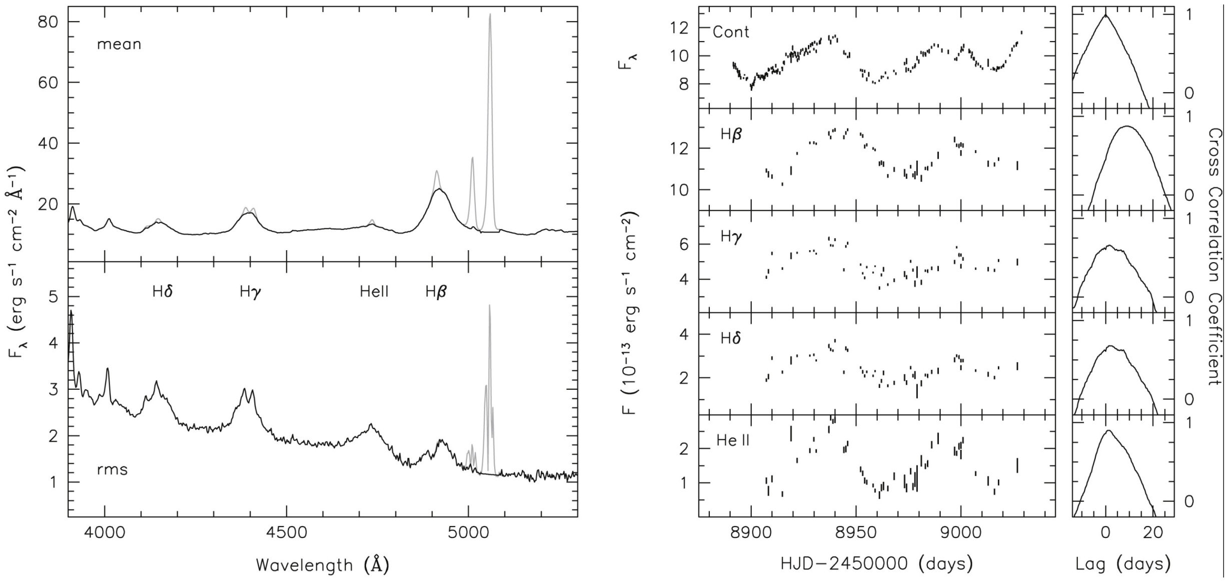

Figure 2.2: Example of a reverberation mapping measurement of the BLR size. ***Left panel:*** Mean and spectrum root-mean-square optical spectrum of the quasar NGC 3783. ***Right panel:*** Lightcurve of the continuum and several emission lines with the corresponding cross-correlation found lag is displayed. (Adapted from Bentz et al. 2021)

Broad Line region reverberation The first accurate measurement of broad-line reverberation in quasars came in the early 1990s with the collaborative efforts of the International AGN Watch consortium [I], which conducted coordinated UV and optical photometric and spectroscopic monitoring from both ground-based and space-based observatories. The initial findings ofPeterson et al. (1993) showed that high ionization lines, such as C IV and *HeII*, were observed to respond first, followed by lower ionization lines like Hβ,

---

[I] https://www.asc.ohio-state.edu/astronomy/agnwatch/

indicating the presence of ionization stratification within the BLR. This motivated a new representation of the BLR as a "locally optimally emitting cloud (LOC)" (Baldwin et al. 1995), which successfully reproduced early reverberation results by considering a broader range of gas conditions within the BLR in opposition to the previous belief in a single representative cloud. As our understanding of the necessary observational constraints for successful reverberation mapping programs improved (length, sampling, SN ratio, and flux calibration of the monitoring observations), there was a rapid increase in the number of accurate measurements of broad-line reverberation (Peterson et al. 2004). Fig. 2.2 shows an example of a recent BLR reverberation mapping measurement by (Bentz et al. 2021).

The achieved accuracy measurements of broad-line time delays in quasars allowed reverberation mapping to give an estimate of the central black hole mass. Indeed, Peterson & Wandel (1999) showed that by measuring the time lag, τ and line width V of a broad emission line, the mass of the black hole, M_{BH} could be determined by:

$$M_{\mathrm{BH}} = \frac{f c \tau V^2}{G}, \tag{2.5}$$

with f, a scaling factor that accounts for the unknown geometry and kinematics of the broad line region gas. Notably, observations have shown that high ionization lines exhibit shorter time delays and broader widths compared to low ionization lines, consistent with the expected virial motion and leading to consistent determinations of M_{BH} (e.g. Kollatschny et al. 2001). The scaling factor f has been constrained by comparing the correlation between the mass of the central SMBH and the velocity dispersion of the stars, σ_* (e.g. Gültekin et al. 2009; McConnell & Ma 2013) for quasars and quiescent galaxies. Assuming that all galaxies are drawn from the same parent sample, the scaling factor required to align the intercept of the quasar relationship with that of quiescent galaxies provides an estimate of f. Values range from 2.8 to 5.5, with most values falling around 4-5 (e.g. Onken et al. 2004; Grier et al. 2013; Batiste et al. 2017). In a few nearby AGNs, dynamical modelling of surrounding stars allows us to measure the mass of the central SMBH(e.g. Davies et al. 2006; Onken et al. 2014). The reverberation masses based on f are generally consistent with those obtained from the dynamical models (e.g., Denney et al. 2010).

Assuming that the inclination angle contributes significantly to the value of f, values of 4-5 imply that the average quasar is observed at an inclination angle of approximately 25-30 degrees, which aligns with the current understanding of AGN unification models (described in Section 1.2). However, individual AGNs may deviate from the average inclination angle, introducing an additional uncertainty of approximately 2-3 in reverberation masses when using f.

Recent advancements in the quality of reverberation datasets allowed researchers to map the geometry and kinematics of the BLR gas for a select number of objects (e.g. Pancoast et al. 2014; Grier et al. 2017; Williams et al. 2020).

Although the specifics vary among objects, there are notable similarities. The BLR gas tends to adopt a thick disk-like configuration with a moderate inclination relative to our line of sight (around 10 to 40+ degrees). The dominant motion observed is typically rotational, with varying contributions from the inward flow. In these cases, it is often possible to directly determine the black hole mass (M_{BH}) without needing a scaling factor, and the values obtained generally agree well with the constraints based on the scaling factor for the same objects.

Most recent analyses have primarily focused on the Hβ emission line, Williams et al. (2020) used modelling of the reverberation response across high- and low-ionization emission lines to demonstrate that Hβ also arises from a thick disk-like structure in NGC 5548. As shown in Fig. 2.3, the kinematics indicate a prominent outflowing component, although the orbits may still be bound. On the other hand,Ly α and

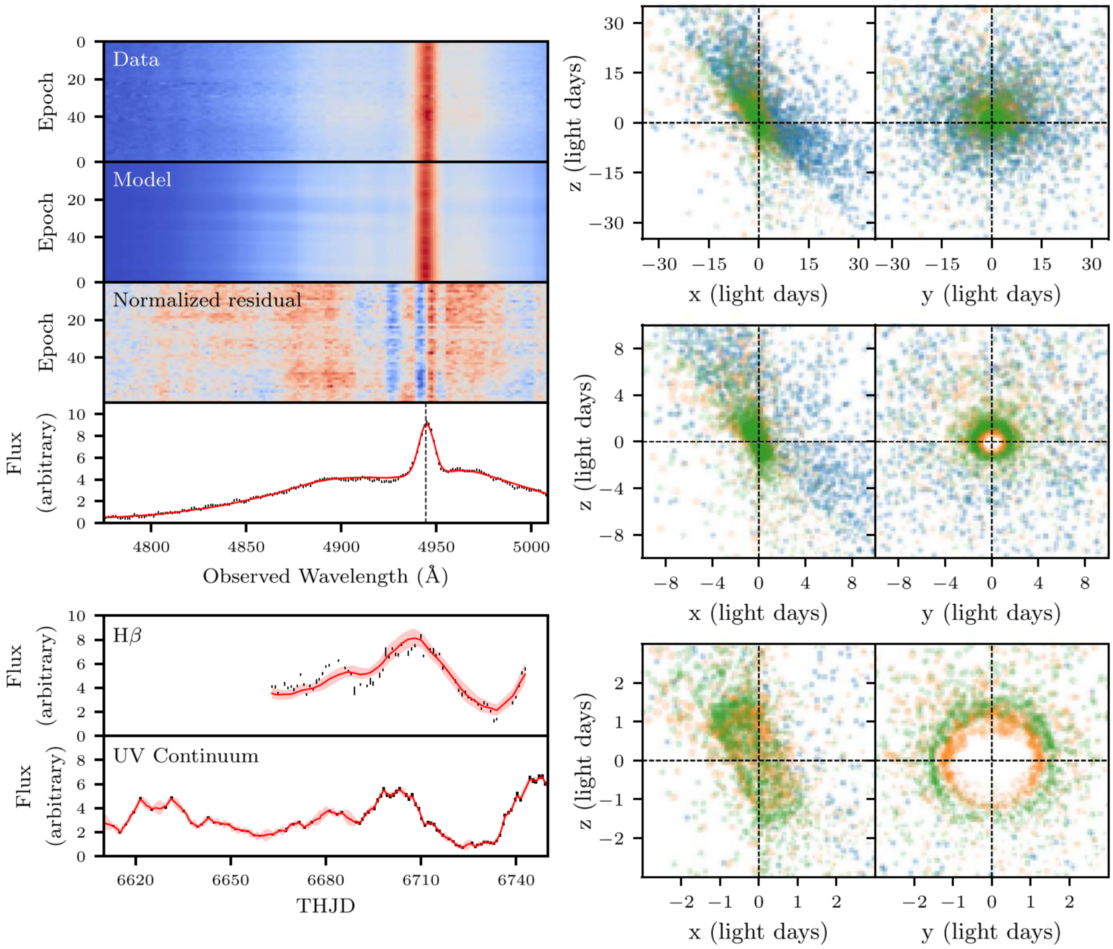

Figure 2.3: ***Left panel:*** The top three panels display the observed Hβ emission line profile for each observation epoch, the profiles generated by a specific broad-line region model, and the normalized residual. The fourth panel exhibits the observed Hβ profile of the 10th epoch in black, and the emission-line profile produced by the model is depicted in the second panel in red. The vertical dashed line represents the emission line center in the observed frame. The time series of the integrated Hβ line and the continuum data in black are shown in panels 5 and 6; the light red band shows the 1σ scatter of all models in the posterior sample. ***Right panel:*** Best fitting geometry of the BLR composed by the three line-emitting regions, represented by Hβ, C IV, and Ly α in blue, orange, and green, respectively. Each panel presents the same three geometries, viewed from different angles and at different distance scales.

C IV appear to originate from a shell-like structure, and surprisingly, C IV exhibits a weaker outflowing contribution compared to Hβ.

The multiplication of accurate reverberation mapping measurements unveiled a relationship between the BLR's size and the central AGN's luminosity (e.g., Kaspi et al. 2000, 2005). Once the contamination from host-galaxy starlight is correctly subtracted, the relationship takes the form $R_{\rm BLR} \propto L_{\rm AGN}^{1/2}$ (e.g., Bentz et al. 2009, 2013) for local broad line AGNs. The size of the BLR in the quasar 3C 273, resolved in the near-infrared using the GRAVITY instrument on VLT, agrees well with that derived from reverberation mapping (e.g., Gravity Collaboration et al. 2018).

The established relationship between the BLR size and the AGN luminosity has been employed to estimate the size for large samples of broad-lined AGNs with only a single spectrum per target. These predictions can then be combined with the broad-line width to estimate the black hole mass (e.g. Shen et al. 2011; Mosquera & Kochanek 2011).

Most measured BLR sizes correspond to the Hβ emitting region, making the Hβ relationship the most well-constrained. Efforts have been made to extend these results to Mg II and C IV emission lines in the rest-frame UV (e.g. Woo et al. 2018) to estimate black hole masses for high-redshift quasars. Therefore, current estimates for quasars depend on the Hβ relationship established for local broad-lined AGNs. Ongoing multiplexed reverberation mapping programs at high redshift are expected to enhance these estimates in the future as calibrated relationships for C IV and other emission lines become available (e.g., Grier et al. 2019; Kaspi et al. 2021).

However, efforts to broaden the range of AGNs studied through reverberation mapping have included objects with higher mass accretion rates. Several studies have shown that many AGNs, including those with the highest accretion rates, deviate from the standard relationship (e.g. Du et al. 2015; Fonseca Alvarez et al. 2020). The reasons for this deviation are not yet fully understood, with some attributing it to physical changes arising from high accretion rates (e.g. Dalla Bontà et al. 2020), while others propose a link to differences in the shape of the ionizing continuum (e.g. Fonseca Alvarez et al. 2020). Nonetheless, local Seyferts are unsuitable models for high-redshift quasars; therefore, new methods are needed to measure the size of BLR in distant quasars to properly investigate this relation in higher accretion rate systems.

2.1.2 Quasar microlensing

Right after the discovery of the first strongly lensed quasar, **?** stated that stars in a shear field (caused by smooth dark matter in the lensing galaxy) could split each image separately into multiple images separated by $\sim 10^{-5}$ arcsec and impact the flux of each image independently.

Microcaustic maps to model the micromagnification

To model these effects accurately, a common approach involves using two components to describe the convergence $\kappa = \kappa_* + \kappa_{\mathrm{DM}}$ in the galaxy at the position of the images. As defined in Wambsganss (1999), the number of microlenses is therefore determined by:

$$N_* = \frac{\kappa_* A}{\pi \langle M \rangle}, \tag{2.6}$$

with A the area of the galaxy considered and $\langle M \rangle$ the mean mass of stars in the lens galaxy.

The interaction between two or more point lenses with projected separations similar to their Einstein radii exhibits nonlinear behaviour that can not be modelled analytically.

Therefore, magnification maps are used to model the effect of a population of microlenses in the lens galaxy on one of the strong lens images. Several techniques are employed to create microlensing magnification maps. One commonly used approach is inverse ray shooting (e.g., Kayser et al. 1986; Wambsganss 1999). After drawing N_* stars from an Initial Mass Function (IMF, the distribution of stellar masses at their formation within a population of stars) with a given mean mass, $\langle M \rangle$, multiple rays are shot from the observer plane through the lens plane using the adapted lens equation. In the presence of both smoothly distributed and compact matter and shear γ at the position of the image, the lens equation Eq.1.33 becomes:

$$\beta = \begin{pmatrix} 1-\gamma & 0 \\ 0 & 1-\gamma \end{pmatrix} \theta - \kappa_{\mathrm{DM}}\theta - \sum_{\mathrm{i}=1}^{N_*} m_{\mathrm{i}} \frac{\theta - \theta_{\mathrm{i}}}{|\theta - \theta_{\mathrm{i}}|^2}. \tag{2.7}$$

The position of each lightray in the source plane allows the construction of a magnification map. As shown in Fig. 2.4, this method offers flexibility in capturing intricate magnification patterns, including regions of high magnification and complex caustics, but is computationally expensive. Recent speed-up of the process through the use of GPU (Thompson et al. 2010; Vernardos & Fluke 2014) and improvement of algorithms (Jiménez-Vicente & Mediavilla 2022) made the generation maps large enough to be statistically representative of the microlensing properties of a given system. Another technique, inverse polygon mapping (Mediavilla et al. 2006), involves dividing the lens plane into polygons and mapping each polygon to the source plane using the lens equation. This method is computationally efficient and approximates the lensing effects well. However, it may not capture fine-scale structures and sharp caustics as accurately as inverse ray shooting. While κ, κ_* and γ are well constrained by macro models (e.g. Birrer & Amara 2018; Chen et al. 2019; Rusu et al. 2020), various IMFs have been proposed based on observational data and theoretical models. As the evolution of stars depends mainly on their initial mass, the IMF are a key tracer of chemical history and evolution of galaxies (see Hopkins 2018, for a complete review). One commonly used IMF is the Salpeter IMF (Salpeter 1955), which follows a power-law distribution with a slope of -2.35. This IMF implies that low-mass stars are more abundant than high-mass stars, resulting in a significant contribution from low-mass stars to the total stellar mass.

Another widely used is the Chabrier IMF Chabrier (2003), which incorporates a log-normal distribution for low-mass stars. This IMF predicts a higher fraction of low-mass stars than the Galactic disk's Salpeter IMF. Alternatively, the Kroupa IMF (Kroupa 2001) consists of multiple power-law segments. It is characterized by a shallower slope for low-mass stars and a steeper slope for high-mass stars. This IMF is motivated by the need to reproduce the observed mass distribution in stellar clusters and the field population.

Fig. 2.5 shows a selection of magnification maps obtained with the same κ and γ but different IMFs. It is important to note that the number and position of stars are identical in each case. To add compact dark matter in the last case, a population of compact objects was drawn from the same IMF as the stars (i.e. Salpeter with -2.35 slope) which is equivalent to considering that all matter is in the form of stars ($\kappa_* = \kappa$). The mean mass of the compact objects (here $\langle M \rangle = 0.3\ M_\odot$) sets the physical scale of the map, which is expressed in the corresponding Einstein radii R_{E}.

By comparing the magnification maps obtained, we notice changes in the size and shapes of the caustic network, but the magnification histograms give a better idea of the impact of the microlensing properties of these maps. These reveal that Chabrier and standard Salpeter maps are qualitatively equivalent. Nevertheless, changing the slope of the Salpeter IMF or adding compact dark matter mildly impacts the magnification distribution of a given map.

In most cases, quasars are strongly lensed by early-type galaxies (e.g. Lemon et al. 2018; Shajib et al. 2019; Lemon et al. 2023) in which the stellar population is well described by a Salpeter IMF (e.g. Treu et al. 2010). Therefore, the Salpeter IMF with $0.2 \leq \langle M \rangle \leq 0.5 M_\odot$ is a standard choice for microlensing studies intending to study the source properties by fixing the lens properties (e.g. Kochanek 2004; Mortonson et al. 2005; Morgan et al. 2008; Morgan et al. 2012; Cornachione et al. 2020b). It is important to note

---

[II] https://gerlumph.swin.edu.au/tools/map_database

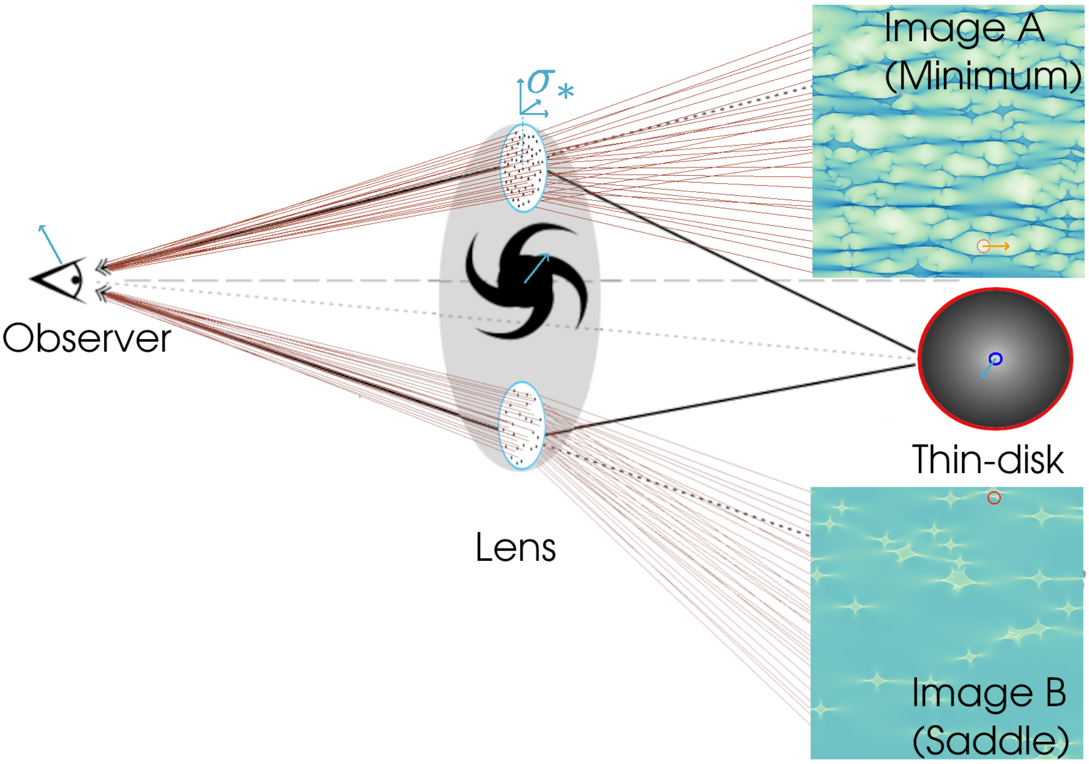

Figure 2.4: Scheme of a standard strongly lensed quasar system, the solid black lines depict the path of the light rays forming images A and B. Shooting rays through the lens plane to the source one generates the magnification maps corresponding to the microlensing effect of a star population. As the micro magnification is combined with the macro magnification, saddle and minimum images have opposite sign magnification maps. A thin-disk light profile with R_S displayed as a blue circle materializes the quasar source; the red circles on the magnification maps indicate the relative size of the disk to the caustics. The light blue arrows show the peculiar motions of individual components of the system, and the orange arrows show the resulting effective velocity of the source in the magnification map. The maps were taken from the GERLUMPH database[II]with physical properties similar HE 1104−1805: $\kappa_A = 0.65, \kappa_B = 0.33, \gamma_A = 0.605, \gamma_B = 0.290$, $R_E = 2.36 \cdot 10^{16}$.

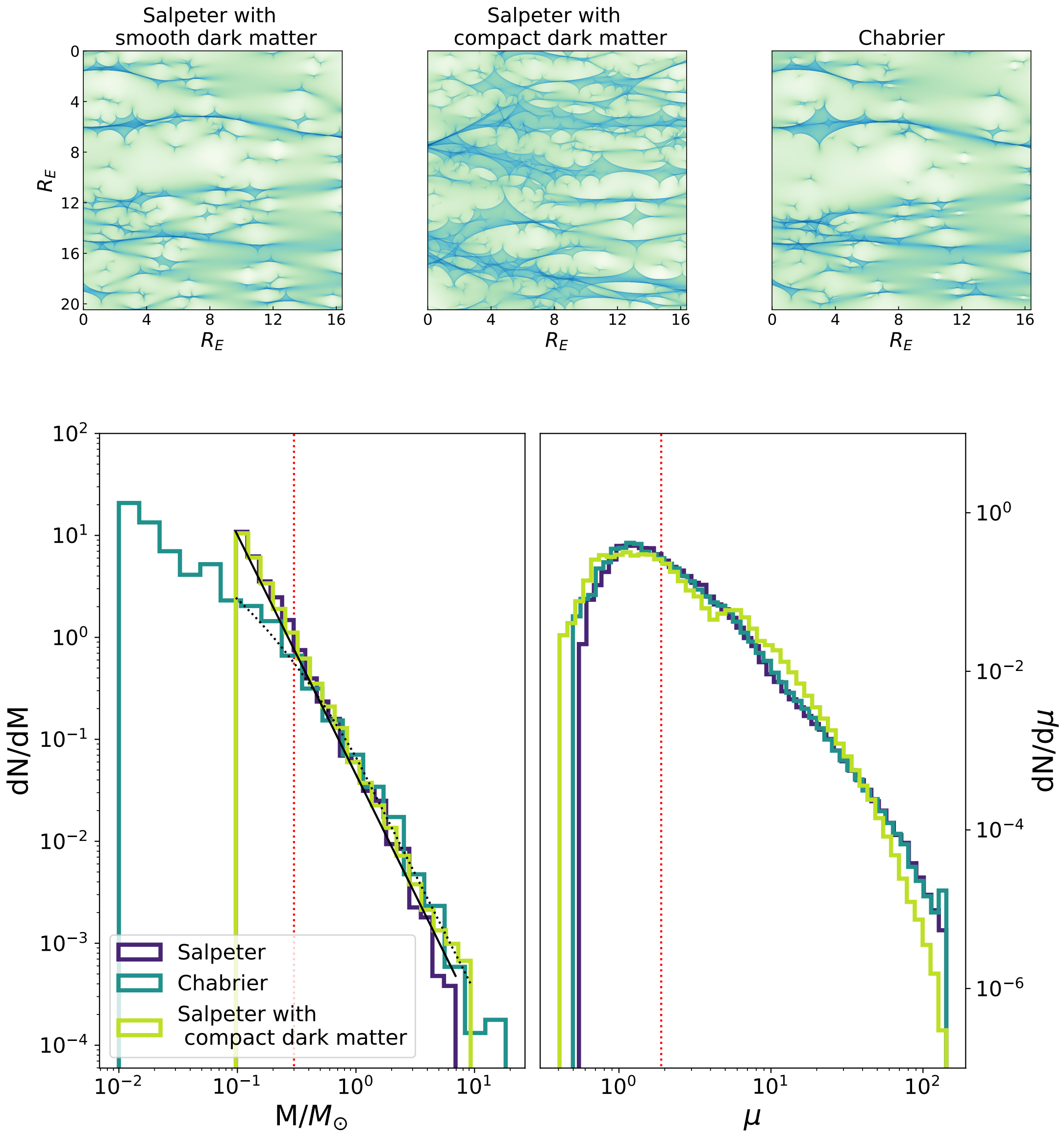

Figure 2.5: ***Top panel:*** Different magnification maps generated with different IMFs. For the case without smooth dark matter, we assumed that dark matter is under the form of a compact object following the same IMF as the stars[III]. ***Bottom panel:*** *Left:* Histogram of the mass of microlenses which induce the magnification maps shown above along with analytical Salpeter (solid) and Chabrier (dotted) distributions. the red dotted line highlights $\langle M \rangle = 0.3 M_\odot$. *Right:* Magnification distribution of the corresponding magnification maps, the red dotted line shows the macro-magnification of the image, which corresponds to the mean magnification of the map.

that microlensing of quasars can also be used as a tool to probe the IMF's slope (e.g. Jiménez-Vicente & Mediavilla 2019, found a slightly different slope of -2.9 ± 0.9) or the existence of compact dark matter component such as PBHs (e.g. Awad et al. 2023, showed that quasar microlensing could discriminate between the existence or absence of close dark matter using the large sample of observations soon available with Rubin-LSST).

The relative motion of the source $\mathbf{v}_\mathrm{s}$, lens $\mathbf{v}_\mathrm{l}$, stars in the lens σ_* and observer $\mathbf{v_o}$ can be modeled as a resulting effective velocity $\mathbf{v}_\mathrm{e}$ of the source in the source plane with:

$$\mathbf{v}_\mathrm{e} = \frac{\mathbf{v}_\mathrm{o}}{1+z_\mathrm{l}}\frac{D_\mathrm{ls}}{D_\mathrm{o}} - \frac{\sigma_*}{1+z_\mathrm{l}}\frac{D_\mathrm{s}}{D_\mathrm{l}} + \mathbf{v}_\mathrm{g}, \tag{2.8}$$

with $\mathbf{v}_\mathrm{g}$ and gaussian random variable with a standard deviation σ_g:

$$\sigma_\mathrm{g} = \left[\left(\frac{\sigma_\mathrm{l}}{1+z_\mathrm{l}}\frac{D_\mathrm{s}}{D_\mathrm{l}}\right)^2 + \left(\frac{\sigma_\mathrm{s}}{1+z_\mathrm{s}}\right)\right]^{1/2}, \tag{2.9}$$

where σ_l and $\sigma_\mathrm{s}00$ are the standard deviations of the peculiar velocity distributions of the lens and the source. Following Eq. 1.55, the time for a thin disk to cross a micro caustic, t_E, for most strongly lensed quasar is of the order of years (e.g., Irwin et al. 1989; Schmidt & Wambsganss 2010; Mosquera & Kochanek 2011). During this time, the luminosity of separate images of a strongly lensed quasar describes an independent microlensing lightcurve.

Such light curves can be simulated by computing the total magnification of the accretion disk at each epoch. As shown by the top panel of Fig. 2.6, since the total radius of a thin disk is generally comparable to the Einstein radius R_E of the microlenses (even though the scale radius is generally smaller, e.g., Mosquera & Kochanek 2011) the accretion disk will not be magnified uniformly as it moves across the magnification map. By convolving the magnification map with the assumed light profile of the source results, we obtain the total magnification applied to the disk as a function of its position in the source plane. By drawing trajectories in this convolved map, we can then generate microlensing light curves which, as displayed by the lower panel of Fig. 2.6, depend both on the size and shape of the light profile.

As displayed, a wider accretion disk will induce smoother and longer microlensing events. Features in the profile reflect on the shape of the peaks of the lightcurve corresponding to the moment when the accretion disk enters or leaves a caustic (i.e. a **caustic crossing**). Converting the scale of the simulated curve to observed time is possible through Eq. 1.55 with assumptions on the velocity dispersion and $\langle M \rangle$.

Observation of microlensed quasars

As first stated by Irwin et al. (1989) with the photometric monitoring of the first strongly lensed quasar Q0957, the microlensing light curve can, therefore, give significant constraints on the size of the source and its shape. In practice, each image's photometric light curve $S_\alpha(t)$ is the sum of the intrinsic variability of the quasar $I(t)$ from the microlensing variability $m_\alpha(t)$ and the strong lensing macro magnification M_α. After shifting the curves by the appropriate time delay (see Chapter 3 for a detailed explanation of the time delay measurement), the difference between the two curves gives us the differential microlensing light curve (hereafter referred to as microlensing light curve) which can be expressed as:

$$S_\mathrm{A}(t) - S_\mathrm{B}(t - \Delta t_\mathrm{AB}) = m_\mathrm{A}(t) - m_\mathrm{B}(t) + \mathcal{M}_\mathrm{A} - \mathcal{M}_\mathrm{B}. \tag{2.10}$$

Long-term monitoring programs were able to release multiple years-long microlensing light curves of diverse systems both in the optical (OGLE (e.g., Udalski et al. 2006), SMARTS (e.g., Kochanek et al. 2006; Morgan et al. 2010) and COSMOGRAIL (e.g. Millon et al. 2020b,a, Fig. 2.7 shows examples of lightcurves obtained)) and in the X-ray (e.g., Dai et al. 2010; Morgan et al. 2012). To constrain the size of accretion disks, Kochanek (2004) proposed a Monte Carlo right curve fitting method to fit the size of accretion disks. Numerous realizations of light curves are generated by sampling random tracks in the magnification patterns, as illustrated in Fig. 2.6. These simulated light curves are then compared to the observed microlensing light curves using a goodness-of-fit estimator. Using Bayesian statistics, it is possible to derive probability distributions for the quantities of interest, such as source size or microlens mass. This approach was used to measure the accretion disk size of a broad sample of quasars (e.g. Morgan et al. 2008; Dai et al. 2010; Poindexter & Kochanek 2010; Morgan et al. 2018; Cornachione et al. 2020a). Using the 15 accretion disks measured with this technique, Cornachione & Morgan (2020) highlighted that the estimate obtained based on the luminosity and the thin disk profile was, on average, four times lower than the measurements. Hence echoing the statement of multiple reverberation mapping studies discussed previously.

Alternatively, the size of the accretion disk can be determined with single epoch multi-waveband observation by measuring the temperature gradient of the accretion disk. Indeed, the apparent size of the disk varies with wavelength due to its temperature distribution $T(R) \propto r^{-1/\beta}$, with $\beta = 4/3$ in the thin disk model (see Eq. 1.28 for the full expression). The inner region is hot and appears in the bluest bands, whereas the outskirts are detected in the redder bands. Influenced by the source size, micro-magnification also becomes wavelength-dependent despite the achromatic nature of microlensing. This results in chromatic flux ratios between the observed images of strongly lensed quasars, as observed in spectrophotometric monitoring data (e.g., Anguita et al. 2008; Eigenbrod et al. 2008b). A single epoch chromatic flux ratio can be simulated using magnification maps for a given size and temperature gradient. Similarly to the light curve fitting method, the goodness of fit of an observed chromatic flux ratio can be used to derive the size of a quasar accretion disk sizes and profile (e.g., Bate et al. 2008). Although this method may be affected by the strength of wavelength-dependent microlensing, it remains a reliable approach for determining accretion disk sizes (e.g., Bate et al. 2018a). While this technique generally agrees with the thin-disk theory in many strongly lensed quasars (e.g., Bate et al. 2008; Floyd et al. 2009; Mediavilla et al. 2011; Rojas et al. 2014), some systems exhibit accretion disk sizes underestimated by the thin-disk model by up to an order of magnitude and (e.g., Blackburne et al. 2011; Motta et al. 2017; Bate et al. 2018b; Rojas et al. 2020).

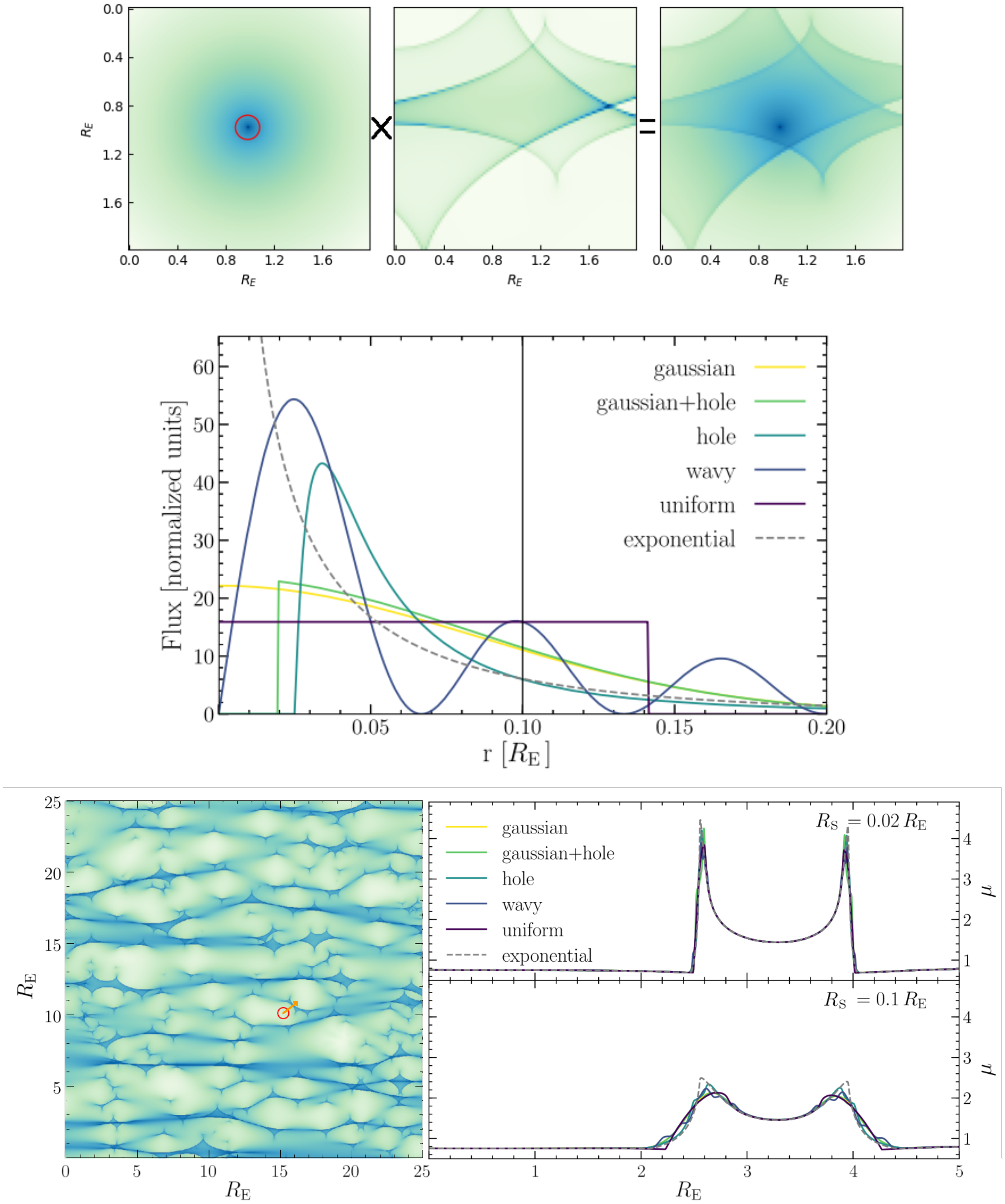

Figure 2.6: ***Top panel:*** Illustration of the magnification of a thin disk (with a $R_\mathrm{S} = 0.1 R_\mathrm{E}$ highlighted by the red circle) by a region of the magnification map corresponding to image A of HE 1104−1805 (see caption of Fig. 2.4). **Middle panel:** Different radial light profile corresponding to standard or exotic models of the accretion disk. Adding a hole in the light profile materializes the size of the black hole shadow, while the wavy light profile models relativistic knots in the accretion disk. ***Bottom panel:*** Light curves obtained for a given trajectory in the magnification map when changing the shape and size of the source light profile. (Reproduced from Vernardos & Tsagkatakis 2019)

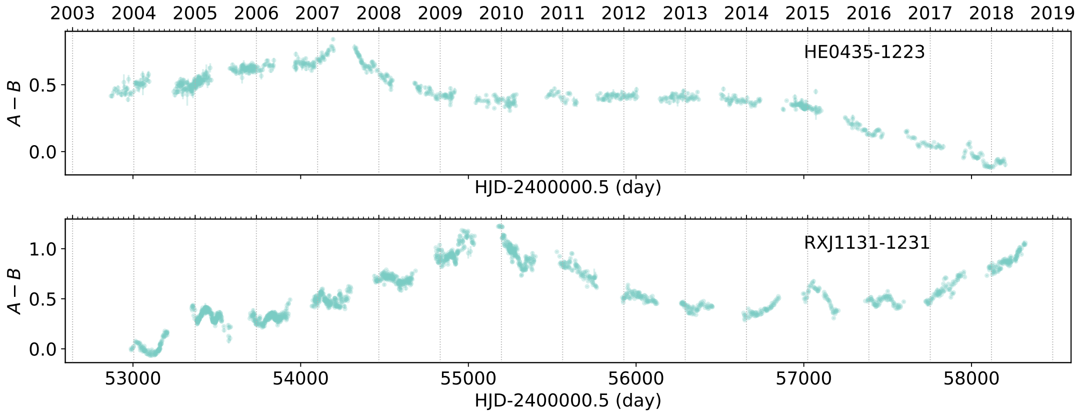

Figure 2.7: Microlensing light curve obtained by the COSMOGRAIL program (Millon et al. 2020b) for the strongly lensed quasar HE0435 and RXJ1131. The corresponding caustic crossing time are $t_{\mathrm{E},0435} = 18.3$ years and $t_{\mathrm{E},0435} = 11.13$ years. Sharp and long features in both light curves likely correspond to a caustic crossing event. In contrast, as shown in Section 2.2, shorter features are manifestations of reverberated intrinsic variability.

With a lensing galaxy unusually close to us ($z_l = 0.039$), the strongly lensed quasar Q2237+030, also named the "Einstein Cross", is an exceptional laboratory for microlensing studies. Its typical Einstein time is of the order of month compared to years for other systems (e.g., Mosquera & Kochanek 2011) which makes lightcurves with a similar level of details as the ones simulated in Fig. 2.6 quickly accessible. By using multi-wavelength microlensing light curves of the system, Eigenbrod et al. (2008a) was able to merge the constraints offered by both light curve fitting and chromatic flux ratio to precisely measure the slope of the temperature profile and the accretion disk size in agreement with the thin disk model. As forecasted by Oguri & Marshall (2010), the advent of the Rubin-LSST survey will give a multi-waveband light curve of hundreds of strongly lensed quasars, which will allow such measurements to be applied to a much larger sample and provide more constraints to the temperature profile of accretion disks.

This new profusion of data will also increase the chance of observing the exact moment when an accretion disk crosses a caustic. As shown by Best et al. (2022), this will allow us to measure the size of the ISCO and directly probe the properties of the central SMBH.

2.1.3 The accretion disk size problem

As described previously, both reverberation mapping and microlensing methods observe contradictions to the thin disk model of Shakura & Sunyaev (1973). Both reveal discrepancies in the profile of the disk materialized by the lag slope or the temperature slope, which are steeper than expected in multiple instances, and the disk size is up to an order of magnitude larger than expected. These observations gave rise to the so-called **accretion disk size problem**, which could hint toward modifications of the thin-disk model (e.g. Cackett et al. 2021). One possibility is that disks are more complex than initially assumed. As suggested by Dexter & Agol (2011), local fluctuations within the disk structure, creating an inhomogeneous and time-dependent configuration, can account for the observed larger sizes. Another consideration is the assumption of the disk emitting as a blackbody, which may not hold. Hall et al. (2018) propose that disks with a low-density scattering atmosphere can explain the larger observed sizes in continuum reverberation. Such an atmosphere leads to different temperature profiles, longer lags, and a flatter wavelength dependence of the apparent size, consistent with observations of NGC 5548.

Additionally, more sophisticated disk reprocessing models utilizing general relativistic ray-tracing, as investigated by Kammoun et al. (2021), yield longer lags and can reproduce the observed sizes with reasonable mass and mass accretion rate estimates. Papadakis et al. (2022) propose that X-ray illumination of the accretion disk can significantly increase its half-light radius. Geometrical considerations have also been explored. Gardner & Done (2017) propose that the inner disk may puff up to prevent direct UV/optical disk irradiation by hard X-rays, and they associate the lags with variations in the outer disk's vertical structure. Another class of models, the corona-heated accretion-disk reprocessing models (e.g. Sun et al. 2020), attribute quasar UV/optical variability and disk lags to the coupling between the X-ray-emitting corona and the accretion disk through magnetic fields. The magnetohydrodynamic waves in the corona induce X-ray variability and temperature fluctuations in the disk, resulting in longer lags compared to the simple disk reverberation model. Furthermore, factors beyond the disk itself can contribute to the observed lags.

As for every discrepancy between measurements and theory, the development of new measurement methods as a means to investigate potential bias of current practices is primordial.

2.2 A new method to measure Broad Line Region with microlensing light curves

Reverberation mapping for unlensed quasars requires multiple waveband light curves to disentangle the stochastic variability of the quasar from the reverberated emission. For strongly lensed quasar, however, the multiplicity of images allows us to isolate the microlensing and reverberated signal from the intrinsic one. As highlighted by Sluse & Tewes (2014), the flux of one image F_α, is the macrolensed sum of the microlensed intrinsic flux $\mu_\alpha(t)F_i(t)$ and the reverberated flux coming from the BLR $F_{BLR}(t)$. As the latter originates from a region much broader than the accretion disk, we neglect the effect of microlensing on this component:

$$F_\alpha(t) = M_\alpha \mu_\alpha(t) F_i(t) + M_\alpha F_{BLR}(t), \tag{2.11}$$

with M_α the macro magnification at image α. When including the reverberation in each image light curve, the differential microlensing light curve expressed in Eq. 2.10 presents imprints of the reverberated signal. As shown in Fig. 2.7, in contrast to the long and large amplitude variations of microlensing, these imprints have a small amplitude and are short as they follow the same time variability as the accretion disk.

In the following paper, we dissect the different frequency ranges of each component by studying the microlensing light curve in the Fourier space with its power spectrum. We apply this novel technique to the microlensing light curve of QJ 0158−4325 as it showcases distinct high-frequency features that could be apparent to BLR reverberation.

2.2.1 Computing the power spectrum of a microlensing light curve

The spectral density of a given time series $x(t)$ at a given frequency f is defined by:

$$S_{xx}(f) = |\hat{x}(f)|^2 , \tag{2.12}$$

Where $\hat{x}(f)$ is the Fourier transform of $x(t)$ computed using the definition:

$$\hat{x}(f) = \int_{-\infty}^{+\infty} e^{-2\pi i f t} x(t) dt, \tag{2.13}$$

For a discrete evenly sampled signal of N points, the Discrete Fourier Transform is used:

$$\hat{x}_k = \sum_{n=0}^{N-1} e^{-\frac{2\pi i}{N} kn} x_n, \tag{2.14}$$

While performing a discrete Fourier transform, a window function must be applied to the light curve to avoid the so-called spectral leakage.

As illustrated by Fig. 2.8, when the signal is not composed by an integer number of periods because of its finiteness, the waveform of a given frequency can be truncated, hence inducing discontinuities between the periods. This introduces sharp transitions in the signal that are not supposed to exist, which in turn show up by transferring the power of a frequency to other frequencies. The role of the window function $w(t)$ is to convolve the signal to smooth the transitions between the periods so that the spectral leakage is avoided.

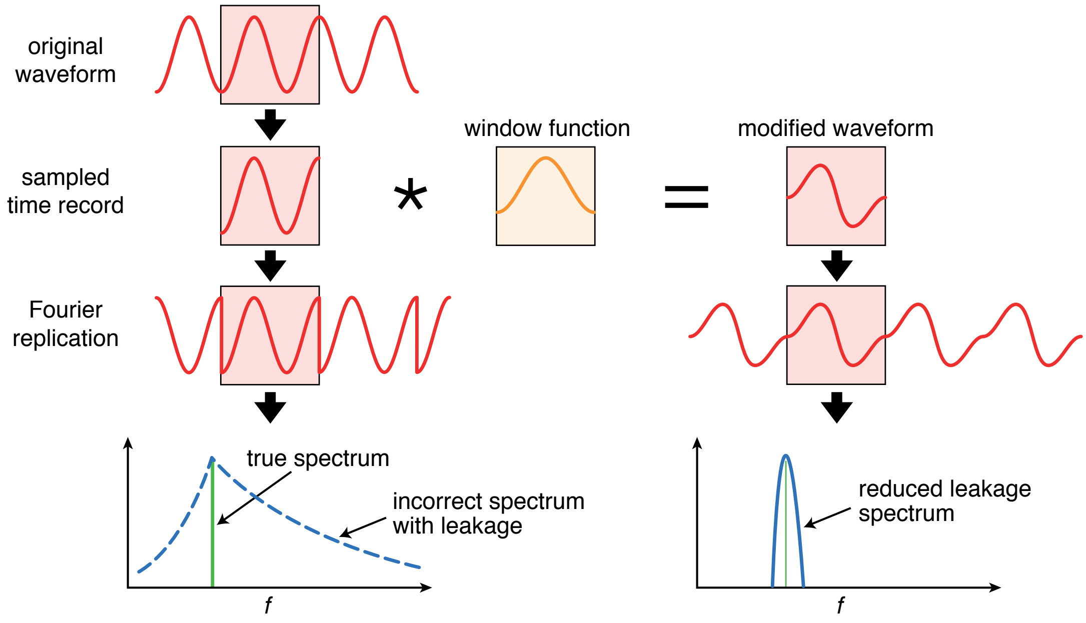
original waveform
sampled time record
Fourier replication
window function
modified waveform
*
=
true spectrum
incorrect spectrum with leakage
f
reduced leakage spectrum
f

Figure 2.8: Illustration of the spectral leakage phenomenon and use of the windowing to mitigate the problem.

The Fourier transform then becomes:

$$\hat{x}(f) = \int_{-\infty}^{+\infty} w(t) e^{-2\pi i f t} x(t) dt, \tag{2.15}$$

Different window functions have been developed, each with its unique characteristics. To assess the reliability of a specific window function, we separate the long and short-term scale variations in the data

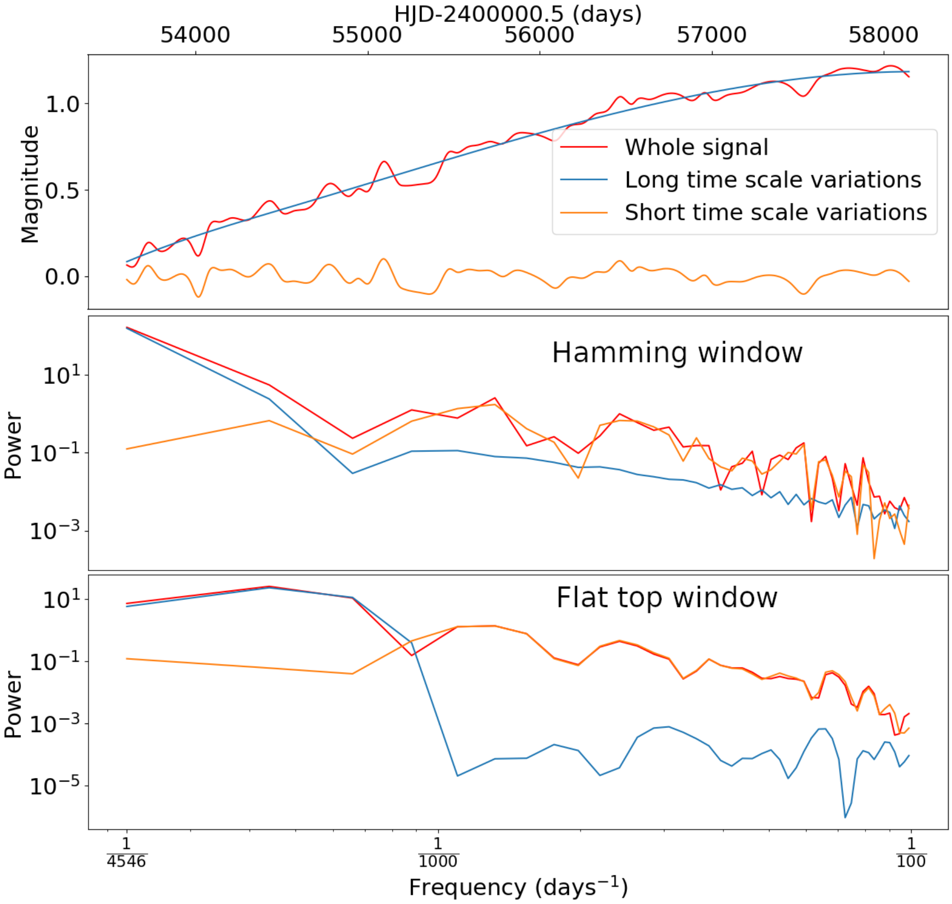

Figure 2.9: ***Top panel:*** In red, a spline fits the microlensing light curve of QJ 0158−4325, capturing both long and short features. Another spline with few knots reproduces the longest variations in blue; subtracting it from the first spline gives the short time scale variations. ***Middle panel:*** Power spectrum of the corresponding curves with Hamming window, displaying significant spectral leakage ***Bottom panel:*** Power spectrum of the corresponding curves done with flat top window exhibiting no spectral leakage.

and compare their power spectra to the original spectrum in the relevant frequency range. The middle panel of Fig. 2.9 displays the power spectra obtained using the Hamming window function, while the bottom panel shows the spectra obtained using the flat top window function.

The power spectrum of the long-timescale variation closely resembles that of the entire dataset for frequencies below $\frac{1}{1000}$ days^{-1} when the flat top window function is used. Similarly, the power spectrum of the short time scale variation is nearly identical to that of the entire dataset for frequencies higher than $\frac{1}{1000}$ days^{-1}, indicating minimal spectral leakage. On the other hand, the Hamming window function does not exhibit such desirable characteristics, as it introduces significant spectral leakage.

Using various window functions, it was found that the flat-top window function minimizes the difference between low, and high frequencies and the data in the corresponding frequency ranges.

A&A 659, A21 (2022)
https://doi.org/10.1051/0004-6361/202141808
© ESO 2022

Astronomy & Astrophysics

Constraining quasar structure using high-frequency microlensing variations and continuum reverberation

E. Paic[1], G. Vernardos[1], D. Sluse[2], M. Millon[1], F. Courbin[1], J. H. Chan[1], and V. Bonvin[1]

[1] Institute of Physics, Laboratory of Astrophysics, Ecole Polytechnique Fédérale de Lausanne (EPFL), Observatoire de Sauverny, 1290 Versoix, Switzerland
e-mail: `eric.paic@epfl.ch`
[2] STAR Institute, Quartier Agora, Allée du six Août, 19c, 4000 Liège, Belgium

Received 16 July 2021 / Accepted 6 October 2021

ABSTRACT

Gravitational microlensing is a powerful tool for probing the inner structure of strongly lensed quasars and for constraining parameters of the stellar mass function of lens galaxies. This is achieved by analysing microlensing light curves between the multiple images of strongly lensed quasars and accounting for the effects of three main variable components: (1) the continuum flux of the source, (2) microlensing by stars in the lens galaxy, and (3) reverberation of the continuum by the broad line region (BLR). The latter, ignored by state-of-the-art microlensing techniques, can introduce high-frequency variations which we show carry information on the BLR size. We present a new method that includes all these components simultaneously and fits the power spectrum of the data in the Fourier space rather than the observed light curve itself. In this new framework, we analyse COSMOGRAIL light curves of the two-image system QJ 0158-4325 known to display high-frequency variations. Using exclusively the low-frequency part of the power spectrum, our constraint on the accretion disk radius agrees with the thin-disk model estimate and the results of previous work where the microlensing light curves were fit in real space. However, if we also take into account the high-frequency variations, the data favour significantly smaller disk sizes than previous microlensing measurements. In this case, our results are only in agreement with the thin-disk model prediction only if we assume very low mean masses for the microlens population, i.e. $\langle M \rangle = 0.01\ M_\odot$. At the same time, including the differentially microlensed continuum reverberation by the BLR successfully explains the high frequencies without requiring such low-mass microlenses. This allows us to measure, for the first time, the size of the BLR using single-band photometric monitoring; we obtain $R_{\rm BLR} = 1.6^{+1.5}_{-0.8} \times 10^{17}$ cm, in good agreement with estimates using the BLR size–luminosity relation.

Key words. gravitational lensing: micro – gravitational lensing: strong – quasars: individual: QJ 0158-4325 – quasars: emission lines

1. Introduction

There is a plethora of astrophysical and cosmological applications of strongly lensed quasars. The photometric variability of the multiple lensed images allows us to measure the time delays between arrival times of photons in the frame of the observer and to measure cosmological parameters such as H_0 (e.g., Refsdal 1964; Wong et al. 2020). The lensing magnification offers an augmented view of quasar host galaxies by stretching the image of the regions in the immediate vicinity of the central supermassive black hole (SMBH), and therefore allows us to extend the study of co-evolution of galaxies and active galactic nuclei (AGN) to otherwise inaccessible redshifts (Gebhardt et al. 2000; Peng et al. 2006; Ding et al. 2017a,b, 2021). In the microlensing regime, photometric variations induced by stellar-mass objects passing in front of the quasar images allow us to both study the fraction of mass under compact form in lensing galaxies and to dissect the structure of the central AGN on scales as small as parsecs or even light days, even at high redshifts (see Schmidt & Wambsganss 2010, for a general overview).

The bulk of quasar luminosity originates from the innermost regions containing the SMBH, and these are surrounded by an accretion disk. Further out, clouds of ionised gas revolve around this central power engine and form the broad and narrow line regions (hereafter BLRs and NLRs), as illustrated in Fig. 1 (e.g., Urry & Padovani 1995; Elvis 2000). The main difference between these two regions lies in their sizes, which imply different rotation velocities and therefore different widths of the observed spectral lines. As most of the energy in a quasar is generated from accretion processes in the central disk, it is essential to measure its size and energy profile. The latter is commonly assumed to follow the thin-disk model of Shakura & Sunyaev (1973) but research testing this model is ongoing (e.g., Edelson et al. 2015; Lobban et al. 2020; Li et al. 2021). Beyond the central accretion disk, the nature and dimensions of the BLR as well as its interaction with the host galaxy are still not fully understood (e.g., Peterson et al. 2006; Czerny & Hryniewicz 2011; Tremblay et al. 2016). Measuring the size of the BLR is therefore also of interest because this is related to the mass of the central SMBH (e.g., Williams et al. 2021), and can be used to constrain models of the inner structure of AGNs and of galaxy formation and evolution in general.

As the BLRs and accretion disks of quasars are generally smaller than 10^{-1} pc (Mosquera & Kochanek 2011), these regions are not spatially resolved by any existing instrument[1], and several techniques have been developed to infer the structure of the BLR and the accretion disk indirectly. The first measurements of the sizes of accretion disks were derived from the flux–size estimate, which relies on the relation between the luminosity

---

[1] The Event Horizon Telescope (`https://eventhorizontelescope.org`) can resolve the accretion disk while the BLR can be resolved using the VLT, although these are both limited to a handful of nearby AGNs.

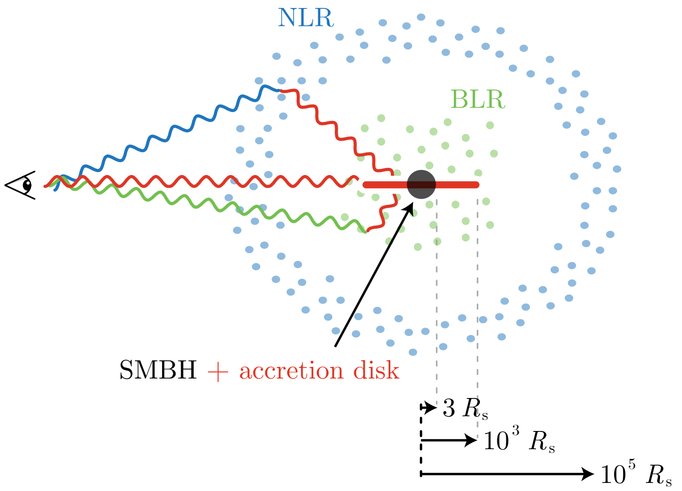

Fig. 1. Schematic view of the relative location and size of the different regions of a quasar and illustration of the reverberation effect. R_S is the Schwarzschild radius of the central SMBH. The continuum light from the central accretion disk (red) is reverberated both in the BLR (green) and in the NLR (blue), which are much larger than the accretion disk and are therefore much less affected by microlensing (see Sect. 3.3).

and radius of the accretion disk, R_0, given by the thin-disk model and following $R_0 \propto L^{1/3}$ (Collin et al. 2002; Morgan et al. 2010). Using this approach, Mosquera & Kochanek (2011) predicted the radii of accretion disks in 87 strongly lensed quasars. Alternatively, continuum reverberation mapping, that is, the measurement of the time-lag between different parts of the continuum, has been used to estimate the size of the accretion disk under the assumption of the lamp-post model (e.g., Krolik et al. 1991; Chan et al. 2020). Examples of such measurements of quasar accretion disks in non-lensed quasars can be found in Mudd et al. (2018), Homayouni et al. (2019), and Yu et al. (2020). As for the BLR size measurement, the reverberation mapping technique (Blandford & McKee 1982) relies on the time-lag between the light rays coming straight from the accretion disk and those scattered (reverberated) by the BLR, as shown in Fig. 1. This method has been used to measure the size of the BLR and infer the mass of the SMBH through spectrophotometric monitoring (e.g., Bentz et al. 2009; Du et al. 2016; Williams et al. 2021; Kaspi et al. 2021).

A complementary and independent approach to studying quasar structure is to use microlensing by stars in the lensing galaxy of strongly lensed quasars (Chang & Refsdal 1979). In any given strongly lensed quasar, stars passing in front of the lensed images split the wavefronts of the incoming light, creating additional micro-images of the source separated by a few micro-arcseconds. The image splitting is not observable with existing instrumentation, but the resulting microlensing magnification is. In practise, the relative motion between observer, lens, microlenses, and source induces a flickering of the macro-lensed observable images. This flickering acts over timescales of weeks to years (e.g., Mosquera & Kochanek 2011) and is a nuisance when measuring time delays (e.g., Tewes et al. 2013; Millon et al. 2020b) or macro-magnification ratios between the quasar images (Blackburne et al. 2006). However, because the variable micro-magnification depends on the dimensions of the source, it also presents an opportunity to measure the size and energy profile of accretion disks (Eigenbrod et al. 2008b) and to study quasar structure in general. Microlensing techniques are mainly sensitive to the half-light radius of the source and are less sensitive to the shape of its light profile (Mortonson et al. 2005; Vernardos & Tsagkatakis 2019).

The apparent radius of an accretion disk is wavelength dependent because its inner region is hotter than its outskirts and therefore emits more energy (Shakura & Sunyaev 1973). As a consequence, the micro-magnification, which depends on the size of the source, depends on the wavelength of observation as well, even though microlensing is by nature achromatic. This leads to chromatic flux ratios between the observed images of a strongly lensed quasar, which have been identified in spectrophotometric monitoring data (e.g., Eigenbrod et al. 2008a). Such chromaticity also enables the measurement of quasar accretion disks through single-epoch multi-wavelength observations (Bate et al. 2008), and although this method may be biased by the strength of the wavelength-dependent microlensing, it is a reliable way to measure the sizes of accretion disks (Bate et al. 2018). While in many strongly lensed quasars this method yields results in agreement with the thin-disk theory (e.g., Bate et al. 2008; Floyd et al. 2009; Mediavilla et al. 2011; Rojas et al. 2014), in other systems it was found that the thin-disk model underestimates the size of the accretion disk by up to an order or magnitude (e.g., Blackburne et al. 2011; Motta et al. 2017; Bate et al. 2018; Rojas et al. 2020), which according to Cornachione & Morgan (2020) would favour shallower accretion disk temperature profiles than predicted by the thin-disk model.

A second approach to measuring quasar structure with microlensing is to use the pair-wise difference light curves between quasar images corrected for the time-delay and macro-magnification – often called ‘microlensing light curves’ – as they are assumed to be corrected for intrinsic quasar variations by construction. Currently, most methods currently in use interpret such pair-wise differences in light curves by following the fitting technique introduced by Kochanek (2004). This latter consists of a Monte Carlo analysis comparing huge amounts of simulated microlensing light curves ($\sim 10^{11}$) generated by varying a number of physical parameters on quasar structure, microlensing, and velocities until a fit to the data is obtained. The main limitation of this approach is that, as the microlensing light curves get longer, their complexity grows because of the inclusion of more microlensing events, and consequently the number of simulations required to fit the data rises drastically. In addition, this method assumes that microlensing occurs over long timescales, of the order of years, and focuses on the long-term effects while overlooking short-term variability. As a consequence, features shorter than ~1 year have much less weight in the final inference than the longer features, resulting in a frequency filtering of the microlensing signal that may lead to overestimation of the disk size[2]. Measuring the disk size with this technique has been achieved by a number of authors (Morgan et al. 2008, 2012, 2018; Cornachione et al. 2020b). By comparing their microlensing measurements with luminosity-based ones, Morgan et al. (2010) and Cornachione et al. (2020b) pointed out a systematic discrepancy, which they explain by a possible shallower temperature profile of the disk than predicted by the thin-disk model. Finally, a novel approach to microlensing light curve analysis was introduced by Vernardos & Tsagkatakis (2019), who employ machine learning to measure the accretion disk size. Such an

---

[2] Dai et al. (2010) show that accounting for a magnification offset due to contamination from the BLR of up to 40% translates into shrinkage of the measured accretion disk by up to 50%. However, these authors do not consider the impact of reverberation on the frequency content of the light curves.

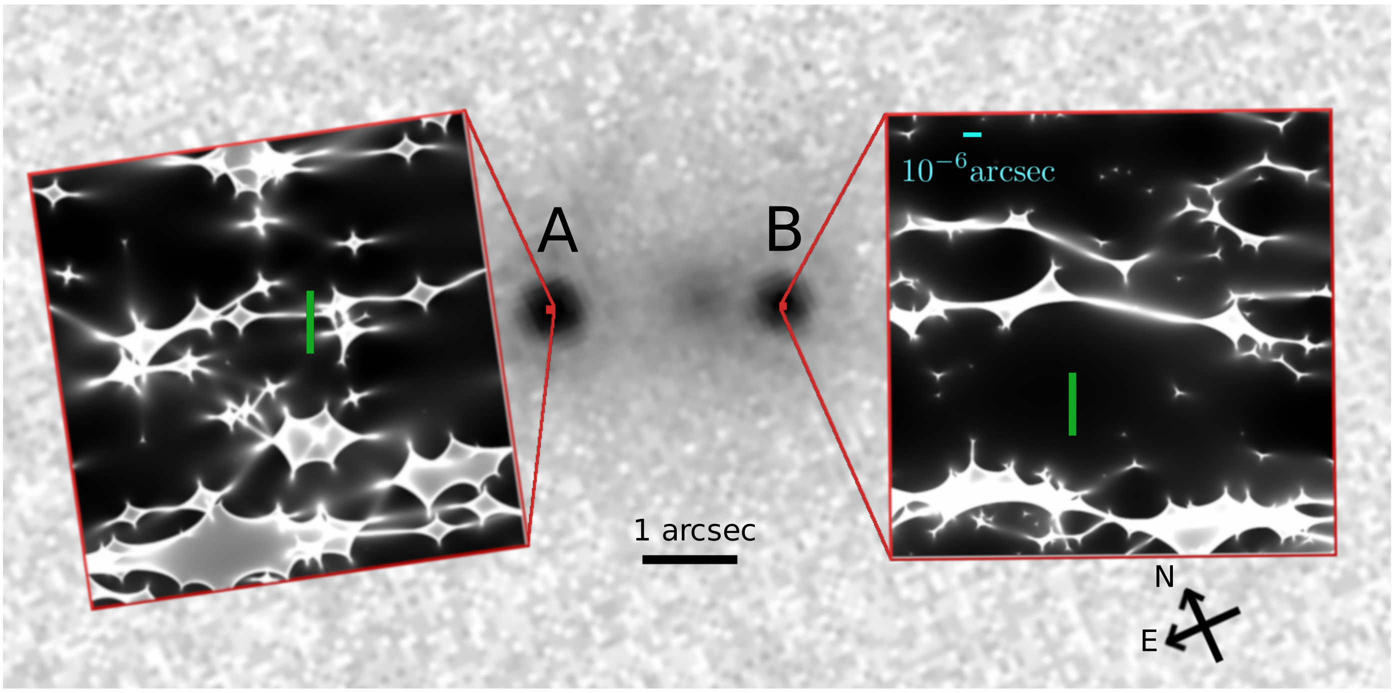

Fig. 2. QJ 0158-4325 observed with the *Hubble* Space Telescope in the F814W filter (program ID 9267; PI: Beckwith). The microlensing magnification maps (corresponding to $\langle M \rangle = 0.3\, M_{\odot}$) are shown for each quasar image using the same colour scale, and are rotated with respect to the shear angle. The green line indicates a realisation of a trajectory of the source, the same in orientation and length for both maps drawn from the probability density function of v_e shown on Fig. 5.

approach has the potential to capture both long- and short-term (low- and high-frequency) variability in the signal, but has not yet been applied to data.

High-frequency variations are visible in high-cadence monitoring campaigns of strongly lensed quasars (e.g., Millon et al. 2020a), potentially carrying valuable information on quasar structure, but their analysis is not possible with the light-curve-fitting method because of the previously mentioned flaws. In addition, high-frequency signals can be introduced either by microlensing or can be partly due to reverberation processes occurring between the inner accretion region and the BLR (e.g., see Fig. 1). The characteristics of the high-frequency variations depend on the relative sizes of the accretion disk and the BLR and lead to the so-called 'microlensing-aided reverberation' first suggested by Sluse & Tewes (2014). In the present work we consider this effect for the first time in the analysis of real data.

In order to study high-frequency variations, we introduce a new method that relies on the Fourier power spectrum of the microlensing light curve, which allows us to characterise the overall properties of the observed signal rather than any specific realisation of the light curve. Fitting the power spectrum enables us to investigate every timescale of variation, both in the high and low frequencies in a computationally tractable way. The method is applied to the light curve of QJ 0158-4325, previously studied by Morgan et al. (2012) using the light-curve-fitting method, who estimated a significantly larger disk size than that obtained by Mosquera & Kochanek (2011) using a flux-based source size. As we show in our study, the power spectrum method demonstrates that part of the high-frequency variation in the microlensing light curve can be explained by continuum light being reverberated in the BLR. For the first time, we estimate the size of the BLR via microlensing-aided reverberation.

The paper is organised as follows: Sect. 2 explains how the microlensing light curve of QJ 0158-4325 is obtained, together with its power spectrum. Section 3 describes our new power-spectrum analysis approach. Section 4 explains the validation process of the method as well as the constraints obtained on the structure of the quasar with and without taking into account the reverberation process. We conclude with a discussion of our results in Sect. 5. Throughout this work we assume $\Omega_m = 0.3$, $\Omega_\Lambda = 0.7$, and $H_0 = 72\,\mathrm{km\,s^{-1}\,Mpc^{-1}}$.

2. Data

QJ 0158-4325 is a doubly imaged quasar (see Fig. 2) discovered by Morgan et al. (1999) that has been monitored for 13 years by the *Leonhard Euler* 1.2m Swiss Telescope in the context of the COSmological MOnitoring of GRAvItational Lenses (COSMOGRAIL) program (Courbin et al. 2005; Eigenbrod et al. 2005). In Millon et al. (2020b), the light curves of this object were extracted following three main steps: first, the instrumental noise and the sky level were subtracted; then a point spread function (PSF) estimated from nearby stars was fitted to each quasar image; before the flux was extracted at the image position with the MCS deconvolution algorithm (Magain et al. 1998; Cantale et al. 2016). This procedure allows one to extract the individual fluxes of the quasar images decontaminated from the light of the lensing galaxy (see Millon et al. 2020b, for more details). The resulting light curves of QJ 0158-4325 are shown in Fig. 3.

2.1. Microlensing light curve

The observed light curve of a quasar image, $S_\alpha(t)$, in magnitudes is the sum of the macro-magnification, $\mathcal{M}_\alpha$, the intrinsic variation in each image, $V_\alpha(t)$, and the microlensing magnification $m_\alpha(t)$:

$$S_\alpha(t) = \mathcal{M}_\alpha + V_\alpha(t) + m_\alpha(t). \quad (1)$$

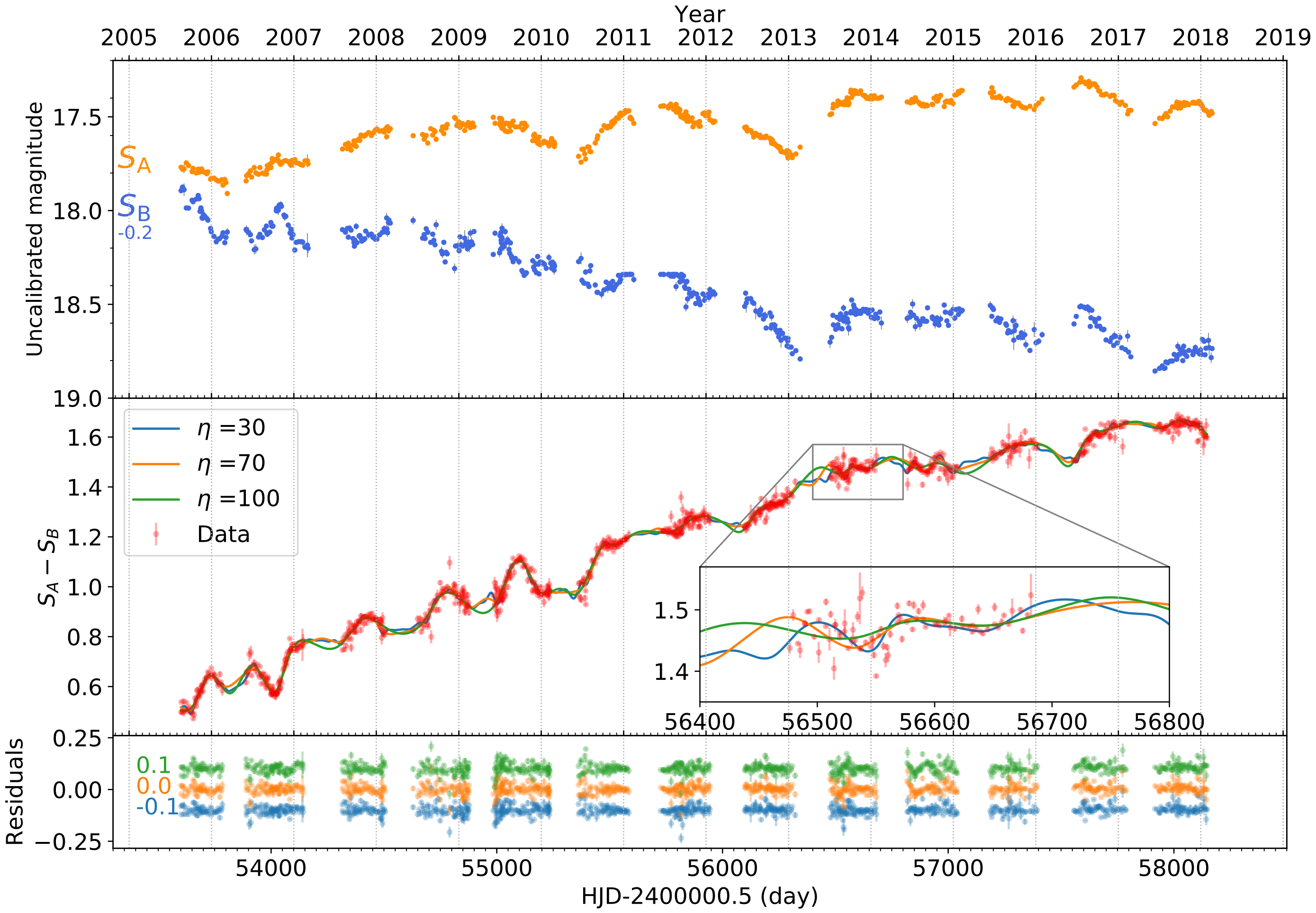

Fig. 3. *Top*: COSMOGRAIL R-band light curves of images A and B of QJ 0158-4325 over a period of 13 years. For clarity, the B curve has been artificially shifted upwards by 0.2 mag (adapted from Millon et al. 2020b). *Middle*: microlensing light curve (red) obtained from the observations using Eq. (2) with $\Delta t_{\mathrm{AB}} = 22.7$ days (Millon et al. 2020b), along with examples of spline fitting with different values of the η parameter (defined in Sect. 2.2). *Bottom*: residuals of the three illustrative spline fits to the microlensing light curve. The number on the left indicates the artificial shifts applied for the purpose of clarity.

Without loss of generality, we can assume that the signal of image B of QJ 0158-4325 is simply a time-shifted version of image A, that is, $V_B(t) = V_A(t - \Delta t_{\mathrm{AB}})$, where Δt_{AB} is the time-delay between the two images. Hence, the microlensing signal can be found by subtracting the observed light curves after correcting for the time-delay and macro-magnification:

$$S_A(t) - S_B(t - \Delta t_{\mathrm{AB}}) = m_A(t) - m_B(t) + \mathcal{M}_A - \mathcal{M}_B. \tag{2}$$

We note that we refer to this signal as ‘microlensing’ but it can well include a fraction of non-microlensed continuum light from the BLR, as shown below. This microlensing curve should therefore be seen as containing any ‘extrinsic’ variations, that is, variations unrelated to the quasar instrinsic variability. We keep the macro-magnification constant across the length of the light curve as we assume that it only changes on much longer timescales (see Table 1 for the values used in this work).

As detailed in Millon et al. (2020b), the determination of Δt_{AB} is done by fitting the observed light curves with free-knot splines implemented in the PyCS package (Millon et al. 2020c). Such splines are piece-wise polynomials with the mean distance between two knots assigned by a parameter η which controls the smoothness of the resulting fit. Free-knot splines allow the positions of the knots to be adjusted so that they capture both long and short features in the data being fitted. A single free-knot spline is fitted simultaneously to all light curves to model the intrinsic variation of the quasar while additional splines model the extrinsic (microlensing) variations in each light curve separately. A simultaneous fit of all instrinsic and extrinsic splines then allows us to adjust the time delays.

For QJ 0158-4325, the time-delay was found to be $\Delta t_{\mathrm{AB}} = 22.7 \pm 3.6$ days (Millon et al. 2020b) and the resulting microlensing light curve (Eq. (2)) is shown in the middle panel of Fig. 3. We do not expect the uncertainty on the time-delay to alter our constraints on the quasar structure because it is much smaller than the shortest timescale of interest, as discussed below. In the present study, we focus on features in the differential light curve that are longer than 100 days. The microlensing signal shows a steady rise throughout the period of observations, resulting in an overall increase of ≈1.2 mag, on top of which short modulations are observed within a single season; small-scale variations are seen in the first seven seasons (from 2005 to 2011) with a typical peak-to-peak amplitude of 0.1 magnitudes. Among the many lensed quasars monitored by the COSMOGRAIL project, very few exhibit such rich and diverse microlensing and/or extrinsic behaviour. QJ 0158-4325 is therefore a promising test bench for investigating both high- and low-frequency variability.

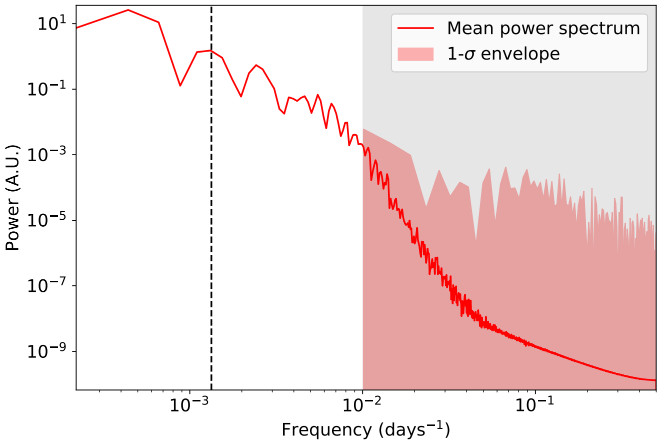

Fig. 4. Power spectrum of the observed microlensing light curve computed as the mean of the power spectra obtained for 1000 different realisations of photometric noise for every value of η sampling the range [30:100] days with steps of 5 days used for the spline fitting parameter (see text). The 1−σ envelope is given by the standard deviation of the same set of power spectra. The dashed black line marks the boundary between low and high frequency and the grey area indicates our adopted frequency limit of 10^{-2} days^{-1}, below which photometric uncertainties dominate the data.

2.2. Power spectrum of the microlensing light curve

We represent the data in Fourier space in order to capture the high-frequency features that are missed by the light-curve-fitting method applied to QJ 0158-4325 in Morgan et al. (2012). The resulting power spectrum therefore holds information across all the frequencies and allows us to treat high- and low-frequency signals simultaneously. In the following, we compute power spectra of both observed and simulated light curves using a standard Fourier transform. To tackle the so-called spectral leakage problem (Harris 1978), that is, the spurious broadening of spectral lines in frequencies for which the length of the signal is not a multiple of the corresponding period, we use a standard flat-top window function.

As shown in the upper panel of Fig. 3, the light curves are not evenly sampled: within a season, two measurements may be separated by three or four days, and season gaps prevent the signal from being evenly sampled throughout the entire curve. The latter would in fact introduce a pattern in the Fourier transform that can be mistakenly interpreted as a periodic signal. To mitigate this, we interpolate the data through the season gaps using the continuous spline that resulted from the fitting technique to measure the time-delays, as outlined above. This offers a flexible and model-independent way to fit time-series. We set the sampling rate to one day and then compute the power spectrum.

The resulting power spectra have two main sources of uncertainty: on one hand, the photometric uncertainties of the raw data induce uncertainty in the very high frequencies corresponding to the sampling rate of the light curve (of the order of 1-10 days). On the other hand, the choice of the parameter η can have a significant impact on the fitting of short-timescale variations because, as illustrated in the middle panel of Fig. 3, features shorter than η are filtered out. The difference between underfitting and overfitting the data depends on the origin we attribute to a given short-timescale variation and whether we want to discard it or not. As we aim to use as few hypotheses as possible on the nature of these short variations, we do not make any assumption on the actual value of η but rather consider a plausible range in order to estimate the uncertainty induced by this parameter. We define this range as [30:100] days in order that it be superior to the time sampling of the data while still capturing most of the high-frequency features. The scatter of the residuals in the bottom panel of Fig. 3 shows that the selected range smoothly fits the data and most of the high-frequency variability is accounted for.

In order to quantify the uncertainty on the power spectrum induced by these effects, 1000 different realisations of photometric noise are produced for every value of η sampling the range [30:100] days with steps of 5 days used for the spline fitting, yielding a set of 14000 data-like light curves. The power spectrum of the data that will be used further in this study is given by the mean and standard deviation of this set of light curves, shown in Fig. 4. As the extreme values of η either overfit or underfit the light curve, the resulting uncertainty is conservative. We note that the relative uncertainties are negligible up to frequencies of 10^{-2} days^{-1} . For higher frequencies, the power drops below 10^{-3} and the relative uncertainties diverge because of the two aforementioned sources of uncertainty. As the Einstein crossing time is around 18 years in the QJ 0158-4325 system (Mosquera & Kochanek 2011), we do not expect the light curve to contain features with timescales shorter than 100 days. As a result, there should not be a significant amount of signal above the 10^{-2} days^{-1} threshold and the power present in these frequencies is induced by photometric noise. Therefore, we exclude the frequencies above 10^{-2} days^{-1} (i.e. features shorter than 100 days) from the following analysis.

3. Methods

In this section, the procedure of generating simulated light curves is described, as well as the way the simulated and observed power spectra are compared. The simulated variable flux of a quasar image, $F_\alpha(t)$, is assumed to be the combination of three components (Sluse & Tewes 2014): the intrinsic flux variability, $I(t)$, due to the stochastic emissions of the accretion disk; the microlensing magnification, $\mu(t)$, due to stars in the lens galaxy; and the flux arising from the BLR, $F_{\rm BLR}(t)$, which echoes the intrinsic variability of the continuum light of the accretion disk. As the BLR is much larger than the accretion disk (typically ten times larger, Mosquera & Kochanek 2011), microlensing of the resulting reverberated light is expected to be small[3]. Hence we have:

$$F_\alpha(t) = M_\alpha \mu_\alpha(t) I(t) + M_\alpha F_{\rm BLR}(t), \tag{3}$$

where μ_α is the time-dependent microlensing magnification and M_α is the constant macro-magnification. Each component in this equation is separately described below.

3.1. Intrinsic variability

The variability of the accretion disk is commonly described by a damped random walk model (Kelly & Siemiginowska 2009; MacLeod et al. 2010; Ivezić & MacLeod 2013). As the variability of QJ 0158-4325 shows no major deviation from the standard quasar optical variability, we model it using a damped random walk model parametrized by a characteristic timescale, $\tau_{\rm DRW}$, and amplitude, $\sigma_{\rm DRW}$, of the variations. We use the JAVELIN code presented by Zu et al. (2013) to create simulations of intrinsic light curves, which are designed for studying the variability of quasars (Zu et al. 2011). A damped random walk consists of a Gaussian Process, $\mathcal{GP}$, with mean intensity $\overline{I}$ and covariance $Cov(\Delta t)$ between two moments in time separated by Δt such that:

---

[3] Although Sluse et al. (2012) showed that 10%-20% of the flux is typically microlensed, Sluse & Tewes (2014) found that this effect marginally impacts the variations in the microlensing light curve.

$$I(t) = \mathcal{GP}\left[\overline{I}, Cov(\Delta t)\right], \tag{4}$$

with the covariance given by :

$$Cov(\Delta t) = \sigma^2_{\rm DRW} \times \exp(-|\Delta t|/\tau_{\rm DRW}). \tag{5}$$

Knowing $\tau_{\rm DRW}$ and $\sigma_{\rm DRW}$ completely defines the $\mathcal{GP}$, from which different but equivalent realisations of the intrinsic light curve can be drawn.

3.2. Microlensing variability

Magnification maps are used to simulate microlensing events produced by a given population of stars in the lens galaxy. In order to simulate a stellar population, we need to compute the values of the convergence, κ, the stellar surface density, κ_*, and the shear, γ, at each image location from the smooth model of the lens galaxy mass distribution (i.e. macro-model; see Sect. 4 and Table 1). We then use a Salpeter initial mass function (IMF) to describe the stellar mass distribution around a given mean stellar mass $\langle M\rangle$. The maps are generated with the GPU-D software, which implements the direct inverse ray-shooting method as described in Vernardos et al. (2015), used in other microlensing studies as well (e.g., Chan et al. 2021).

The characteristic scale of the magnification patterns created by such compact objects in the lens galaxy is their Einstein radius, R_E, defined in the source plane as:

$$R_E = \sqrt{\frac{4G\langle M\rangle}{c^2}\frac{D_{\rm ls}}{D_s D_l}}, \tag{6}$$

where G is the gravitational constant, c the speed of light, and D_l, D_s, and $D_{\rm ls}$ correspond to the angular diameter distances from the observer to the lens, from the observer to the source, and from the lens to the source, respectively. The map dimensions are 8192 × 8192 pixels, corresponding to a physical size of $20R_E \times 20\,R_E$ and a pixel size of $0.0024\,R_E$. Figure 2 shows the configuration of the QJ 0158-4325 lens system along with a realisation of magnification maps corresponding to the κ, κ_*, and γ given by the smooth mass model at the given quasar image positions.

In order to study the magnification of a finite-sized source by a given caustic, we need to assume a light distribution projected on the plane of the sky. The accretion disk of the source is assumed to be described by the thin-disk model (Shakura & Sunyaev 1973), in which a monochromatic light profile as a function of radius is given by:

$$I_0(R) \propto [\exp(\xi) - 1]^{-1}, \quad \text{where} \tag{7}$$
$$\xi = \left(\frac{R}{R_0}\right)^{3/4}\left(1 - \sqrt{\frac{R_{\rm in}}{R}}\right)^{-1/4},$$

with R_0 being the scale radius, that is, the radius at which the temperature matches the rest-frame wavelength of the observation assuming black body radiation, and $R_{\rm in} < R$ is the inner edge of the disk. Here we assume $R_{\rm in} = 0$[4] and we explore a range of R_0 values that contains the value estimated by Mosquera & Kochanek (2011), i.e. $R_0 \approx 0.067 \times R_E$ (in the case of $\langle M\rangle = 0.3\,M_\odot$), which is ≈15 pixels on the maps that we use. To compute the magnification induced on the source, we need to convolve the magnification map with the light profile.

Table 1. Fixed parameter values and free parameter ranges for the models of QJ 0158-4325 used in this study (see Sect. 3).

	Name	Value	Unit
Intrinsic			
	$\tau_{\rm DRW}$ $^{(a)}$	810	days
	$\sigma_{\rm DRW}$	[9–95]	Flux units
Microlensing			
	Lens mass model $^{(b)}$		
	$f_{\rm M/L}$	0.9	–
	$\langle M\rangle$	[0.3, 0.1, 0.01]	$M_\odot$
	Corresponding R_E	[3.41, 1.97,0.623]	10^{16} cm
	Image A		
	κ	0.23	–
	γ	0.39	–
	κ_*/κ	0.81	–
	$\mathcal{M}_A$	2.24	–
	Image B		
	κ	0.72	–
	γ	1.03	–
	κ_*/κ	0.92	–
	$\mathcal{M}_B$	0.84	–
	Effective velocity		
	$\sigma_{\rm pec}(z_l)$ $^{(c)}$	277	$\rm km\,s^{-1}$
	$\sigma_{\rm pec}(z_s)$ $^{(c)}$	248	$\rm km\,s^{-1}$
	$v_{\rm CMB}$ $^{(d)}$	328	$\rm km\,s^{-1}$
	v_* $^{(d)}$	203	$\rm km\,s^{-1}$
	$\langle v_e\rangle \pm \sigma_e$	786^{+450}_{-304}	$\rm km\,s^{-1}$
	Accretion disk light profile		
	R_0	[0.1–6.1]	$R_{\rm MK11}$
	$R_{\rm MK11}$ $^{(e)}$	1.62×10^{15}	cm
Reverberation			
	$f_{\rm BLR}$ $^{(a)}$	0.43 ± 0.034	–
	$R_{\rm BLR}$	[0.1–2.5]	$R_{\rm BLR_{MK11}}$
	$R_{\rm BLR_{MK11}}$ $^{(d)}$	1.71×10^{17}	cm

Notes. [a]See Sect. 4, [b]taken from Morgan et al. (2008), [c]Morgan et al. (2012), [d]Kogut et al. (1993), [e] Mosquera & Kochanek (2011).

The timescale of a microlensing event is set by the effective velocity in the source plane, v_e, which is the vectorial sum of the transverse velocities of the microlenses, v_*, of the lens galaxy v_l, of the source, v_s, and of the observer, v_o. As described in Neira et al. (2020), the direction of the microlense velocity is random and is uniformly sampled in the $[0;2\pi]$ interval. The magnitude of this velocity vector is given by:

$$v_* = \sqrt{2}\,\epsilon\,\sigma_*, \tag{8}$$

where ϵ is a factor depending on κ and γ, and is assumed to be 1 (Kochanek 2004), and σ_* is the velocity dispersion at the lens galaxy centre. The directions of v_l and v_s are random and their magnitude is drawn from a Gaussian distribution with a given standard deviation, $\sigma_{\rm pec}(z)$, as a function of redshift. Therefore, these can be combined into a single normal variable $\mathbf{v}_g$ with a random direction and a magnitude given by a Gaussian with a standard deviation given by:

$$\sigma^2_g = \left(\frac{\sigma_{\rm pec}(z_l)}{1+z_l}\frac{D_s}{D_l}\right)^2 + \left(\frac{\sigma_{\rm pec}(z_s)}{1+z_s}\right)^2. \tag{9}$$

---

[4] $R_{\rm in}$ is very small compared to R_0 and should not have an impact on the result because the half light radius $R_{1/2}$ remains mostly unchanged.

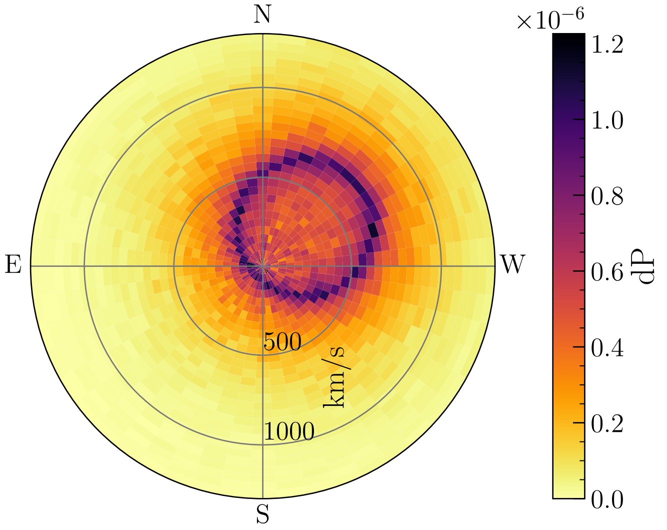

Fig. 5. Probability density of the effective velocity, $\mathbf{v}_e$, in the source plane for QJ 0158-4325 from Eq. (11).

The velocity of the observer is measured with respect to the cosmic microwave background velocity dipole:

$$\mathbf{v}_o = \mathbf{v}_{\mathbf{CMB}} - (\mathbf{v}_{\mathbf{CMB}} \cdot \hat{z})\hat{z}, \tag{10}$$

where $\mathbf{v}_{\mathbf{CMB}}$ is the measured velocity vector with respect to the cosmic microwave background, and $\hat{z}$ the line of sight of the observer. The magnitude and direction of this component are computed using the position of the object on the plane of the sky. Combining these terms, the effective velocity is:

$$\mathbf{v}_e = \frac{\mathbf{v}_o}{1+z_l}\frac{D_{ls}}{D_l} - \frac{\mathbf{v}_*}{1+z_l}\frac{D_s}{D_l} + \mathbf{v}_g. \tag{11}$$

In the case of QJ 0158-4325, $z_l = 0.317$ and $z_s = 1.29$ (Chen et al. 2012). All other relevant parameters for QJ 0158-4325 are given in Table 1 and the resulting probability distribution of $\mathbf{v}_e$ from which the effective velocity in the source plane is drawn is shown in Fig. 5. The probability density function in Fig. 5 is approximated by a Gaussian kernel density estimator and then sampled through the inverse transform sampling method.

3.3. Reverberated variability

As shown in Sluse & Tewes (2014), delayed reverberation of the continuum light from the BLR can significantly alter the observed microlensing signal with modulations on short timescales. In the case of QJ 0158-4325, Faure et al. (2009) showed that the Mg II as well as the Fe II spectral lines, both arising from the BLR, fall into the R-band used in this work. It therefore makes sense to consider continuum reverberation as a mechanism contributing to the observed light curves.

We can describe the reverberation component in Eq. (3) as $F_{\rm BLR}(t) = f_{\rm BLR} r(t)$, where $f_{\rm BLR}$ is the flux ratio between the line and the continuum and $r(t)$ is the reverberated flux. The latter can be computed as a convolution, $r(t) = \Psi(t,\tau) * I(t)$, between the intrinsic signal, $I(t)$, and $\Psi(t,\tau)$, a time-lagging transfer function that depends on the radius of the BLR through a corresponding time lag $\tau = R_{\rm BLR}/c$. Equation (3) then becomes:

$$F_\alpha(t) = M_\alpha \mu_\alpha(t) I(t) + M_\alpha f_{\rm BLR} \left[\Psi(t,\tau) * I(t)\right]. \tag{12}$$

In this work we model the reverberation region as a diffuse ionised gas cloud with the geometry of a thin shell (Peterson et al. 1993), so that $\Psi(t,\tau)$ is a top hat kernel with an amplitude A and a width equal to twice the assumed time-lag τ:

$$\Psi(t,\tau) = \begin{cases} A/\tau & \text{if} 0 \le t < 2\tau, \\ 0 & \text{otherwise.} \end{cases} \tag{13}$$

The values of the $f_{\rm BLR}$ and $R_{\rm BLR}$ parameters examined here are given in Table 1.

3.4. Light-curve simulation and fitting

Combining all the above model components, we are now able to simulate light curves for each quasar image using Eq. (12). The free parameters are $\langle M\rangle$, $\mathbf{v}_e$, R_0, $\sigma_{\rm DRW}$, and $R_{\rm BLR}$, which we refer to as vector $\boldsymbol{\zeta}$. The final light curve to be compared to the data is obtained by dividing (subtracting) the flux (magnitudes) of pairs of simulated light curves for images A and B. Examples of simulated light curves with and without reverberation along with their corresponding power spectra are shown in Fig. 6.

For any given $\boldsymbol{\zeta}$, a batch of 10^5 curves is created from the magnification maps and their power spectrum is computed. The mean $P_{\rm sim}(\omega)$ and standard deviation $\sigma_{\rm sim}(\omega)$ of the power spectrum in each frequency bin are then compared to the data using a chi-square statistic:

$$\chi^2(\zeta) = \frac{1}{N_\omega}\sum_f \frac{(P_{\rm data}(\omega) - P_{\rm sim}(\omega))^2}{\sigma_{\rm sim}(\omega)^2 + \sigma_{\rm data}(\omega)^2}, \tag{14}$$

where $P_{\rm data}(\omega)$ is the mean power spectrum of the data at the frequency ω and $\sigma_{\rm data}(\omega)$ its standard deviation shown in Fig. 4. This can be turned into a likelihood through:

$$\mathcal{L}(d|\boldsymbol{\zeta}) = \exp(-\chi^2(\boldsymbol{\zeta})/2). \tag{15}$$

Eventually, the posterior probability is obtained using Bayes theorem:

$$P(\zeta|d) = \mathcal{L}(d|\zeta)\cdot\mathcal{P}(\zeta)/E(d), \tag{16}$$

where $\mathcal{P}(\boldsymbol{\zeta})$ is the prior probability of the parameters $\boldsymbol{\zeta}$ and $E(d)$ is the probability of the data, that is, the Bayesian evidence. Calculating $E(d)$ requires integration of the posterior across the whole parameter space, which is beyond the computational limits of this study. This means that we cannot compare different models, but we can still use relative probabilities within any given model. All parameters are assumed to have a uniform prior except v_e, whose prior is given in Eq. (11). Finally, we obtain the posterior probability marginalised over a given parameter or subset of parameters ζ_i through:

$$P(\zeta_i|d) = \int_{j\neq i} P(\zeta_j|d)\cdot\mathcal{P}(\zeta_j)d\zeta_j. \tag{17}$$

4. Results

We studied the effect of high-frequency variability, such as that introduced by a reverberated BLR component, when measuring the size of the accretion disk. In doing so, we found a new way to measure the size of the BLR using the microlensing light curves from Eq. (2) in the full frequency range. Before describing our results, we present our prior assumptions for the various model parameters listed in Table 1.

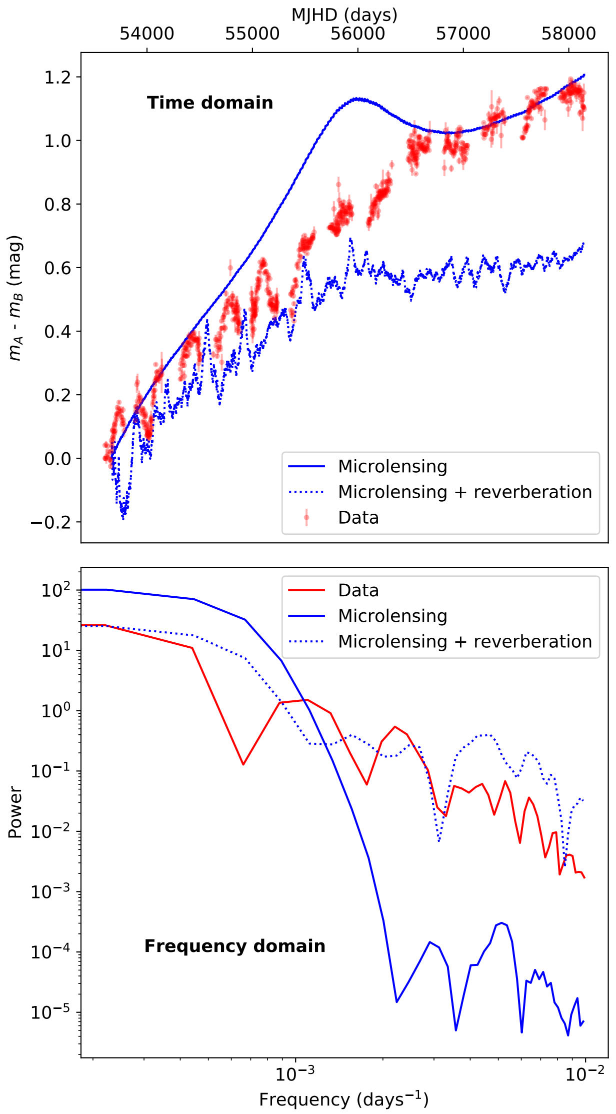

Fig. 6. *Top panel*: example of a simulated light curve with and without reverberation (dotted and solid lines respectively). *Bottom panel*: corresponding power spectra. The curves and power spectra have been produced using $\langle M \rangle = 0.3\,M_\odot$, $v_e = 1236\,\mathrm{km\,s^{-1}}$, $R_0 = 0.5R_{\mathrm{MK11}}$, $\sigma_{\mathrm{DRW}} = 30$ and $R_{\mathrm{BLR}} = R_{\mathrm{BLR_{MK11}}}$. Adding reverberation clearly adds power to the high-frequency part of the spectrum.

Intrinsic variability. The long-term brightness decrease of image B (see Fig. 3) compared to the behaviour of the light curve A, which consists of oscillations around a mean, suggests two possible scenarios: the intrinsic luminosity of the quasar is decreasing and image A is microlensed or the intrinsic luminosity of the quasar is rather constant and a microlensing event which started in image B before the beginning of the observations is now ending, leading to a decrease in the micro-magnification. According to MacLeod et al. (2016), photometric changes of $|\Delta m| \geq 1$ mag over ≈10 years, such as those observed in light curve B, are very rare (around 1% of quasars display this kind of variability). Furthermore, spectra of QJ 0158-4325 shown in Faure et al. (2009) (i.e. taken during the first quarter of the light curve of Fig. 3), show a typical Type 1 QSO spectrum for image A whereas the B spectrum shows faint and deformed emission lines. Altogether, these observations lead us to favour the second scenario. We therefore consider image A to be microlensing-free, and use its light curve as a proxy for the quasar intrinsic variability. Using the JAVELIN software (Zu et al. 2013), which employs a maximum likelihood approach in a Markov chain Monte Carlo (MCMC) framework, we find $\tau_{\mathrm{DRW}} = 810$ days for the assumed damped random walk intrinsic variability model. However, the observed light curve is the result of a convolution between the driving source and the light profile of the quasar. Therefore, the amplitude of the variations, σ_{DRW}, cannot be constrained, because it is degenerate with the radius of the source R_0 which is also unknown in this study. A large interval is therefore considered for exploring this parameter, which includes the values of σ_{DRW} for all the known quasars (Suberlak et al. 2021).

Lens-mass model and magnification maps. Morgan et al. (2012) explore a list of lens-mass models with a stellar mass fraction, $f_{\mathrm{M/L}}$, of between 0.1 and 1, and give a relation between $f_{\mathrm{M/L}}$ and the time-delay between the two images Δt. Using this relation and the time-delay measured by Millon et al. (2020b), we obtain $f_{\mathrm{M/L}} = 0.9$, which we use throughout the following. We adopt the κ, γ, and κ_* values at image locations from Morgan et al. (2008), also listed in Table 1, to compute the magnification maps that we use below. As model uncertainties are not given, we assume $\delta\kappa, \delta\gamma \leq 0.01$, as quoted in most modelling works (e.g., see Table B1 of Wong et al. 2017). According to Vernardos & Fluke (2014), magnification maps within these uncertainties have a statistically equivalent magnification probability distribution. As a sanity check, the same experiment was performed with a different mass model with $\Delta\kappa, \Delta\gamma \geq 0.03$ leading to the same general conclusions. We therefore do not expect the uncertainty on the macro-model to influence our study.

In most microlensing light-curve-fitting studies (Kochanek 2004; Morgan et al. 2008; Cornachione et al. 2020b), $\langle M \rangle = 0.3\,M_\odot$ is taken as a reference mass around which a range of mean mass is explored. Because we are interested in high-frequency variability, we also explore the effect of smaller values of the mean mass, that is, $\langle M \rangle = 0.1\,M_\odot$ and $\langle M \rangle = 0.01\,M_\odot$, which can introduce shorter microlensing events for any given effective velocity due to the corresponding small physical size of the caustics. Choosing a shallower Chabrier IMF instead of the steeper Salpeter one used here leads to fewer low-mass microlenses and therefore reduces any effect of high-frequency variability. Although this has been shown to affect magnification map properties (see Chan et al. 2021), our goal here is to understand such short-timescale variability and therefore we use the Salpeter IMF for all values of $\langle M \rangle$.

Accretion disk size. In order to limit the number of free parameters of our study, we assume a face-on thin-disk model. The expected maximal inclination angle of a type-I AGN is ~60 degrees with respect to the line of sight (e.g., Borguet et al. 2008; Poindexter & Kochanek 2010) and can induce, at most, a factor two systematic effect on the determination of R_0. Nevertheless, R_0, v_e, and the inclination angle are degenerate. We therefore repeated our measurement of R_{BLR} each time varying R_0 and v_e by factors of several and found no significant differences from our results in the face-on disk assumption. We use $\log(R_0/\mathrm{cm}) = 15.07 \equiv R_{\mathrm{MK11}}$ from Mosquera & Kochanek (2011) as a reference value for the scale radius. We explore R_0 in the range $0.1{-}6 \times R_{\mathrm{MK11}}$, which is bound at the low end by the magnification map resolution and extends high enough to include the measurement of Morgan et al. (2012).

Reverberated variability. As mentioned previously, microlensing is dominant in image B compared to image A. Therefore we use the spectrum from image A to derive

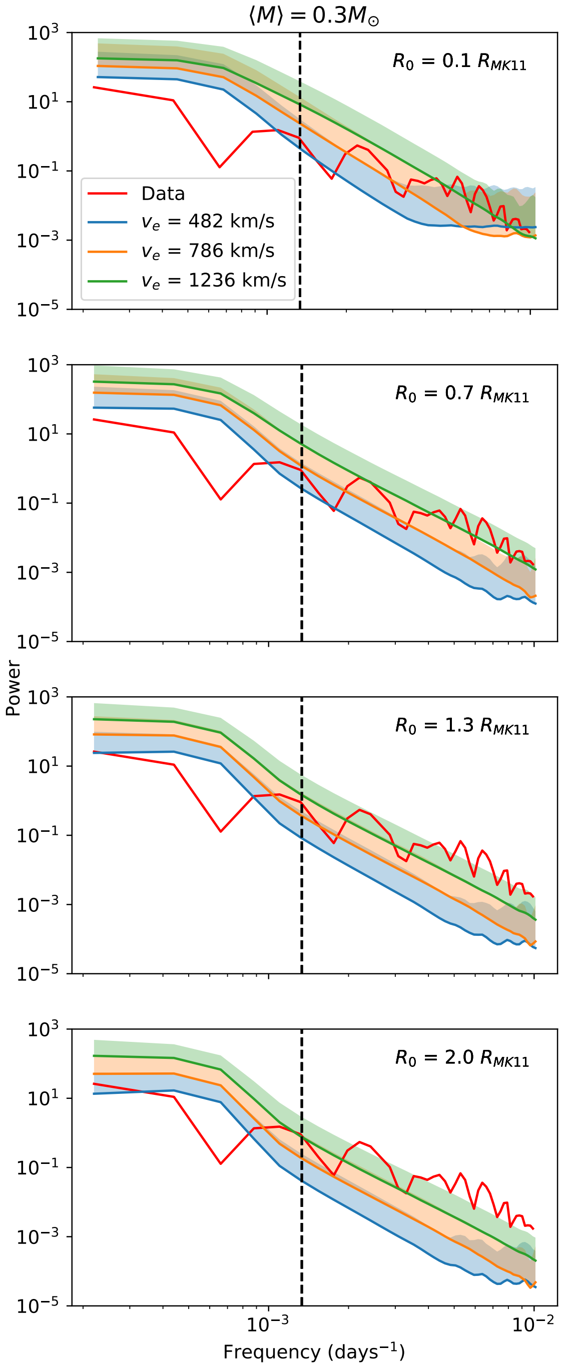

Fig. 7. Mean (lines) and upper 1−σ envelope (shaded area) of power spectra from 100 000 simulated curves for different (v_e, R_0) configurations, in the absence of reverberation ($F_{\rm BLR}$ = 0 in Eq. (3)), compared to the data (same as Fig. 4). Due to the logarithmic scale, the lower envelopes extend almost to the x-axis and are not displayed for clarity. The vertical dashed line marks the boundary between low and high frequency.

$f_{\rm BLR}$ in order to avoid any contamination from a possibly microlensed continuum. To do so, the spectrum presented in Faure et al. (2009) was analysed using a multi-component decomposition as in Sluse et al. (2012). However, contrary to Sluse et al. (2012), a MCMC approach was used to estimate the median $f_{\rm BLR}$ and a 68% credible interval (see Table 1). We emphasise the fact that $f_{\rm BLR}$ is computed as the fraction of flux coming from the BLR compared to the continuum in the R-band, irrespective of the atomic species, and therefore both the Mg II and Fe II emissions are included. As for the radius of the BLR, Mosquera & Kochanek (2011) used the Hβ-BLR size–luminosity relationship (Bentz et al. 2009) to estimate $R_{\rm BLR} = 1.71 \times 10^{17}$ cm $\approx$ 39 light days, which we adopt here as our reference value, $R_{\rm BLR_{MK11}}$. The lower bound of the $R_{\rm BLR}$ range that we explore is $0.1 \times R_{\rm BLR_{MK11}} \approx 5$ light days, which is the smallest reverberation delay observable with the sampling of the light curve set to one point every 2–3 days. The upper bound is set to $2.5 \times R_{\rm BLR_{MK11}}$ to include the confidence interval of the Mosquera & Kochanek (2011) estimate.

To understand the effect of key parameters in the frequency of the signal in the simulated light curves we provide an illustrative example in Fig. 7, where we show power spectra calculated for different values of the transverse velocity, v_e with corresponding directions drawn from the probability density function shown in Fig. 5, and the scale radius, R_0, two of the main free parameters in subsequent models. Firstly, we note that for a given value of R_0 the power has a tendency to increase with v_e, which is justified because, the higher the velocity, the faster the source crosses caustics, inducing more high-magnification events in both the high and low frequencies. Secondly, for a given value of v_e, the power in the high frequencies is inversely proportional to R_0. This is explained by the microlenses magnifying an ever decreasing portion of larger accretion disks, with the resulting magnification effect being diluted within the overall flux, leading to smoother and weaker high-frequency variations.

Furthermore, Fig. 7 shows that in the low frequency regime the models match reasonably well the data, while most of the model differences occur in the high frequencies. It is almost impossible to simultaneously match both the low and high frequencies, whatever the model parameters may be. This suggests that other physical mechanisms might be at play, in addition to microlensing, which we explore with the following three experiments:

- Low frequency (LF): we apply the power spectrum method in the same setup as that used by Morgan et al. (2012), that is, we use only the low-frequency part of the power spectrum, imposing a cutoff at 1/750 days^{-1} that corresponds to the typical timescale considered in Fig. 2 of Morgan et al. (2012). At this stage, we do not include any reverberation signal and set $F_{\rm BLR}$ = 0 in Eq. (3). As a result, even though intrinsic variability is included in this model, it is cancelled out because we are studying the differential microlensing light curves. This model is therefore not sensitive to the intrinsic variability parameters $\sigma_{\rm DRW}$ and $\tau_{\rm DRW}$.
- Full frequency (FF): we perform the same analysis as above, this time including the high frequencies up to 1/100 days^{-1}.
- Reverberation full frequency (RFF): we use the full frequency range of the data, as in the FF model, but this time we include the reverberation of the continuum.

The details and outcomes of each experimental setup are detailed below.

4.1. LF: Low frequencies without reverberation

In Morgan et al. (2012), the shortest features in the light curves last approximately two consecutive seasons, or ≈750 days (see their Fig. 2). This translates into frequencies of up to 1/750 days^{-1}, which is lower than the 1/100 days^{-1} limit that we set in Sect. 2. We therefore adopt 1/750 days^{-1} as being our boundary between what we define as low and high frequency. Here, we model only the low-frequency power spectrum of the data, which contains by design the same signal frequencies as the data used in Morgan et al. (2012).

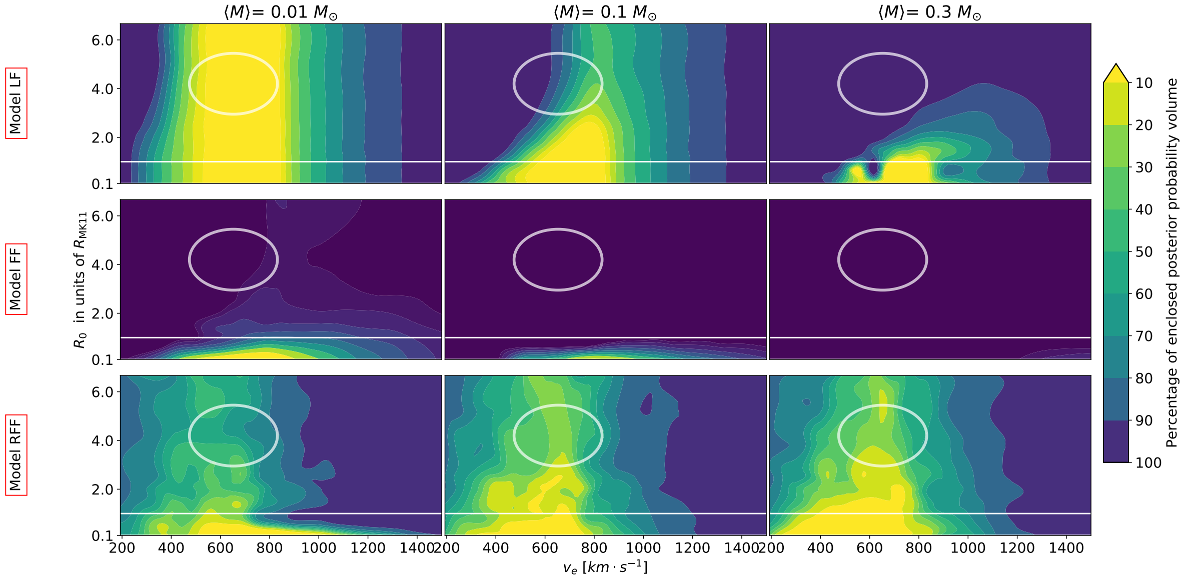

Fig. 8. Slices of the marginalised posterior probability of the (v_e, R_0, $\langle M\rangle$) parameter space (three-dimensional after the marginalisation over the angle of v_e using Eq. (17)) for each of the three models described in Sect. 4. *Model LF*: light curves simulated without reverberation and fitted only to the low-frequency data, i.e. up to 1/750 days^{-1}, which corresponds to the same frequency cut as in Morgan et al. (2012). *Model FF*: same simulations are fitted to the full frequency range, i.e. up to 1/100 days^{-1}. *Model RFF*: light curves are now simulated with reverberation ($f_{\rm BLR}$ = 0.432 ± 0.036, $\sigma_{\rm DRW}$ = 55 and $R_{\rm BLR} = R_{\rm BLR_{MK11}}$) and the full observed frequency range up to 1/100 days^{-1} is considered. The solid line corresponds to $R_{\rm MK11}$, the estimate of Mosquera & Kochanek (2011), the ellipse represents the (v_e, R_0) measurement interval from Morgan et al. (2012). The coloured contours encapsulate [10–100]% of the probability volume and are projected in each of the displayed slices. We note that our probability densities are not scaled by the evidence and therefore cannot be compared across different models.

The top row of Fig. 8 shows the posterior probability from Eq. (16) as a function of v_e, R_0, and $\langle M\rangle$. The distribution of R_0 broadens with decreasing $\langle M\rangle$, becoming almost uniform for the smallest mean mass of $\langle M\rangle = 0.01\,M_\odot$, and therefore not providing any useful constraint. This can be understood in terms of the physical size of the magnification maps, which depends on $\langle M\rangle$ through the Einstein radius of the microlenses, R_E (see Eq. (6) and Table 1), with respect to the velocity: decreasing $\langle M\rangle$ is equivalent to rescaling the magnification map to a smaller physical size that allows the source to cross the map more rapidly for the same effective velocity (which is equivalent to increasing the effective velocity while keeping the mass fixed). Thus, small masses and larger radii can induce enough high-frequency power to fit the data as well as the smaller radii and larger masses.

Overall, our power spectrum measurement is in good agreement with the estimate of Mosquera & Kochanek (2011), while it is consistent within 1 to 2σ with the result of Morgan et al. (2012) in the $\langle M\rangle = 0.01{-}0.1\,M_\odot$ cases. In the $\langle M\rangle = 0.3\,M_\odot$ case, we note a slight discrepancy with the results of Morgan et al. (2012). This can be explained by our use of longer light curves (6 more seasons) and the use of a model-driven prior on the angle of v_e, as illustrated in Fig. 5, instead of the uniform prior used in previous studies[5]. Model LF is a sanity check demonstrating that, when restricted to low frequencies, the power spectrum and light-curve-fitting methods give compatible results and the data can be explained by microlensing alone.

4.2. FF: Full frequency range without reverberation

We now include the high-frequency signal in the data and attempt to explain it assuming that the observed variations come solely from microlensing of the accretion disk, that is, exactly the same model as in the LF setup. Our results, shown in the second row of Fig. 8, favour much smaller accretion disks with $R_0 < 0.5R_{\rm MK11}$, excluding both the result of Morgan et al. (2012) and the estimation of Mosquera & Kochanek (2011). This is less prominent for the case with $\langle M\rangle = 0.01\,M_\odot$, where we observe the same behaviour for larger R_0 as in the LF case, extending the compatible sizes to somewhat larger values. Clearly, microlensing alone has problems in explaining the high-frequency signal and we need to invoke additional sources of variability to explain the data, as we do in the following case.

4.3. RFF: Full frequency range with reverberation

Adding the reverberation process to the simulated light curves is expected to increase the power of the high frequencies in the signal. In the bottom row of Fig. 8 we show the posterior probability as a function of v_e, R_0, and $\langle M\rangle$ for a fiducial reverberation model with $R_{\rm BLR} = R_{\rm BLR_{MK11}}$ and $\sigma_{\rm DRW}$ = 55 (see also Fig. 10 and Sect. 4.4).

As we can see in the third row of Fig. 8, when including the reverberation effect, the constraint obtained for the radius of the accretion disk R_0 is now dominated by the prior on v_e and R_0 for every $\langle M\rangle$ explored. Still, we note that the areas corresponding to any given percentage of enclosed posterior probability shrink with the value of $\langle M\rangle$. Indeed, if a simulated power spectrum is compatible with the data for $\langle M\rangle = 0.3\,M_\odot$, the addition of power induced by the decrease in $\langle M\rangle$ (as discussed in Sect. 4.1) pulls the simulated power spectrum away from the data, thereby reducing their compatibility. Therefore, this model tends to favour the standard value of $\langle M\rangle = 0.3\,M_\odot$.

4.4. $R_{\rm BLR}$ measurement

In order to measure the size of the reverberating region, $R_{\rm BLR}$, we first explore the effect of the amplitude of the intrinsic variability,

---

[5] The experiment ran with a uniform prior on the angle actually yields a 1−σ to 2−σ compatible measurement.

$\sigma_{\rm DRW}$, and of $R_{\rm BLR}$ on the simulated power spectra, while keeping the microlensing parameters fixed at $\langle M\rangle = 0.3\,M_\odot$, $R_0 = R_{\rm MK11}$, and $v_e = 700\,{\rm km\,s^{-1}}$. The use of $\langle M\rangle = 0.3\,M_\odot$ is motivated by the fact that galaxies are unlikely to host a population of objects with $\langle M\rangle = 0.1 {\rm or} 0.01\,M_\odot$ (see Sect. 4.3). Including reverberation in the analysis allows us to explain the high frequency using a realistic value of $\langle M\rangle$, or at least a consensus one. As for v_e, we use a value close to the mean value from Eq. (11) (see also Table 1 and Fig. 5). We stress the fact that, if the microlensing is identical in both images (i.e. $\mu_A(t) = \mu_B(t)$ in Eq. (3), which is more likely to happen if both images are not microlensed), the effect of reverberation is absent from the differential light curve we analyse. Therefore, reverberation is not a stand-alone part of this study and the reverberation-induced variability ends up being weighted as a function of time because of microlensing in the differential light curve. Figure 9 shows that increasing $\sigma_{\rm DRW}$ leads to more power at the high frequencies, mostly because the now stronger intrinsic variations are reverberated after a time-lag ($\tau = R_{\rm BLR}/c$, see Eq. (13)) of the order of tens to hundreds of days, i.e. with a frequency $>1/750\,{\rm days}^{-1}$. Analysing the effect of the BLR size, $R_{\rm BLR}$, is more complex. For a given transfer function, $\Psi(t, R_{\rm BLR}/c)$, a short variation of typically ≈100 days in the intrinsic signal $I(t)$ appears twice in light curves simulated using Eq. (3): once at time t and a second time at $t + R_{\rm BLR}/c$. As $R_{\rm BLR}$ is increased, the echoed signal moves further, eventually becoming fully separated spatially from the one originating at the disk, and is seen as a whole new feature of the light curve. This adds power to the high-frequency domain, justifying the difference between the $R_{\rm BLR} = 0.2 R_{{\rm BLR}_{\rm MK11}}$ and $R_{\rm BLR} = R_{{\rm BLR}_{\rm MK11}}$ cases in Fig. 9. As we keep increasing $R_{\rm BLR}$, $\Psi(t, R_{\rm BLR}/c)$ gets wider and starts to smooth out the short intrinsic variations, reducing their power. This explains the drop in power in the highest of the frequencies when considering the highest values of $R_{\rm BLR}$ in Fig. 9.

Comparing Figs. 7 and 9, we see that a reverberated variability component has a stronger effect on the high-frequency power than increasing v_e or decreasing R_0. This is to be expected because intrinsic quasar variations generally have shorter timescales than microlensing. As a consequence the choice of microlensing model (i.e the v_e and R_0 values) has little impact on the measurement of $R_{\rm BLR}$.

Using Eq. (16), we derive the probability density in the parameter space ($\sigma_{\rm DRW}, R_{\rm BLR}$) for a given set of parameters $\langle M\rangle$, $f_{\rm BLR}$, v_e, and R_0. By marginalising on v_e and R_0 we obtain the measurement of $R_{\rm BLR}$ shown in Fig. 10. One could argue that we obtain a bi-modal distribution in the posterior probability for $R_{\rm BLR}$. This observation can be explained by the fact that, as shown in Sect. 4, the R-band encapsulates the Mg II and Fe II emission lines which can arise from two distinct regions of the BLR. Indeed, the Hβ (used in Mosquera & Kochanek 2011) and Mg II lines seem to arise from the same part of the BLR in various quasars (e.g., Karouzos et al. 2015; Khadka et al. 2021) and should both yield similar sizes; whereas the Fe II line is thought to arise from a larger part of the BLR (e.g., Sluse et al. 2007; Hu et al. 2015; Zhang et al. 2019; Li et al. 2021). Therefore, the combination of the two signals modelled as a single BLR emission could broaden our measurement and induce its slight bi-modality. Still, the core of the probability lies in the [0.1–1.5] $R_{{\rm BLR}_{\rm MK11}}$ range and the second mode observed for higher values of $R_{\rm BLR}$ rises only for the highest values of $\sigma_{\rm DRW}$. The marginalisation of this posterior over $\sigma_{\rm DRW}$ yields a probability distribution for $R_{\rm BLR}$ and by taking its 16th, 50th, and 84th percentiles we measure $R_{\rm BLR} = 1.6^{+1.5}_{-0.8} \times 10^{17}$ cm. With a relative precision of ≈80% our method is less precise than recent spectroscopical reverberation mapping measurements (e.g., Grier et al. 2019; Penton et al. 2022 have around 30% relative precision for quasars with $z > 1.3$) but is more precise than photometric reverberation mapping (e.g., Kaspi et al. 2021 have above 100% relative precision when using a cross-correlation function with R and B filter light curves). The value of $R_{{\rm BLR}_{\rm MK11}}$ predicted by the luminosity–size relation is in agreement with our measurement at the 1−σ level.

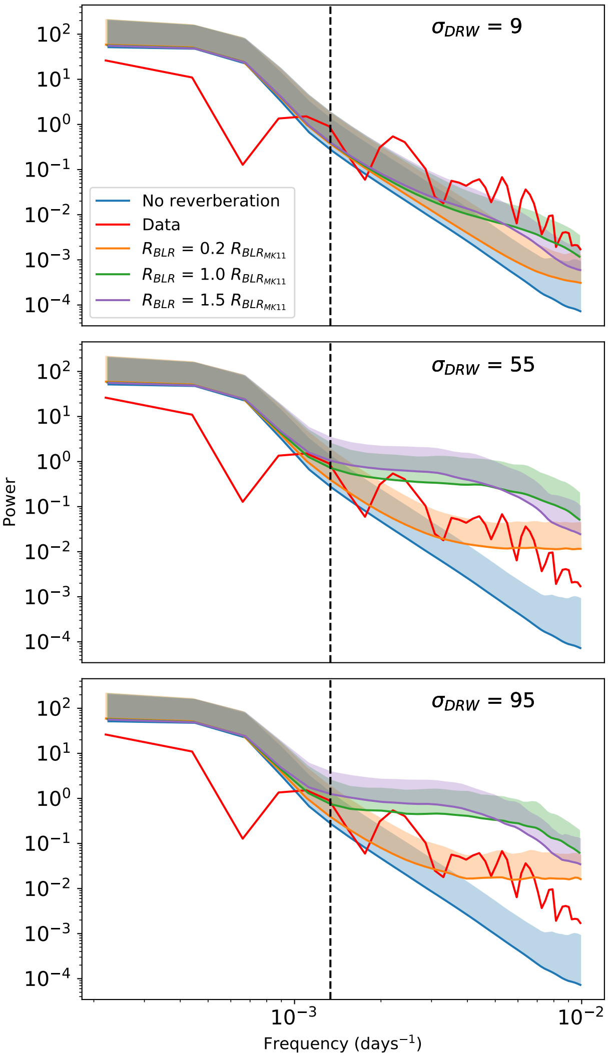

Fig. 9. Effect of the reverberation process on the power spectrum. The data are shown as a solid red line. The coloured envelopes display the power spectra from 100 000 simulated curves for different values of $R_{\rm BLR}$. Each panel considers different values for $\sigma_{\rm DRW}$. In this plot we use $R_0 = R_{\rm MK11}$, $\langle M\rangle = 0.3\,M_\odot$, $v_e = 700\,{\rm km\,s^{-1}}$, and $f_{\rm BLR} = 0.432 \pm 0.036$. The black dashed line marks the boundary between low and high frequency. While the high-frequency range is never well represented with pure microlensing (blue), it is very sensitive to a change in the reverberation parameters.

5. Discussion

We now review the implications of the constraints on the accretion disk scale radius, R_0, found using the three different models. The first model shows that the low-frequency variations of the microlensing light curve do not have a strong constraining power on R_0 when using the power spectrum method.

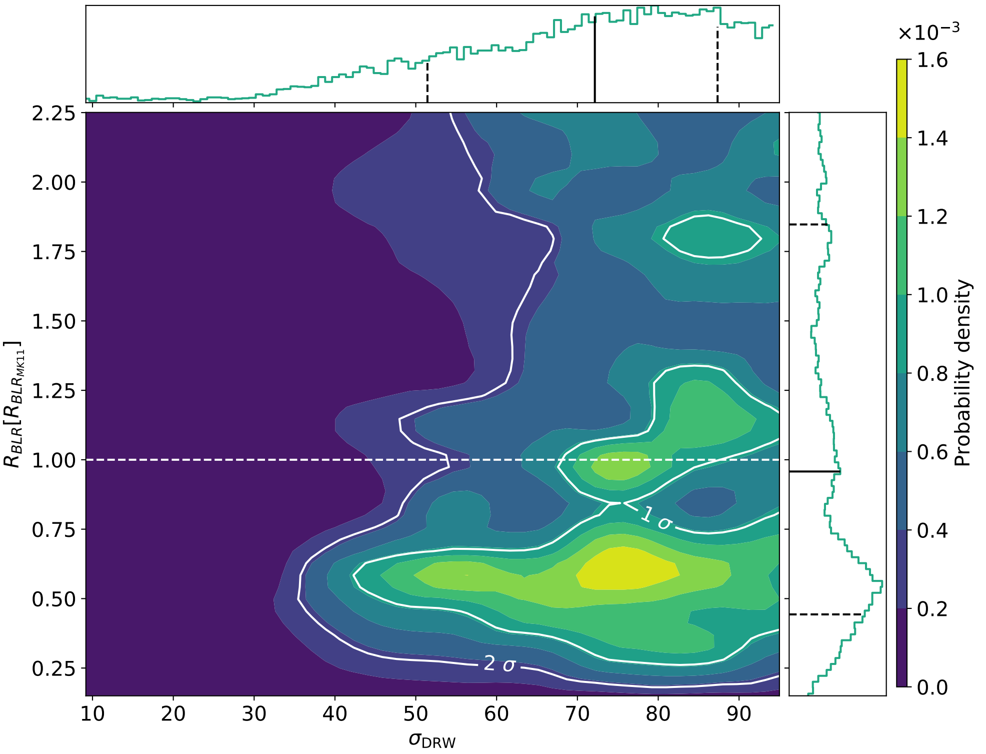

Fig. 10. Posterior probability density in the ($\sigma_{\rm DRW}$, $R_{\rm BLR}$) parameter space marginalised over the microlensing parameters given $\langle M \rangle = 0.3\,M_{\odot}$. $R_{\rm BLR}$ is given in units of $R_{\rm BLR_{MK11}} = 1.71 \times 10^{17}$ cm, indicated by the white dashed line. The contours correspond to the 1 and 2−σ confidence intervals. Marginalised probability distributions of $\sigma_{\rm DRW}$ and $R_{\rm BLR}$ are given in the top and right histograms respectively. In each histogram, the black line shows the 50th percentile (median value) of the distribution and the dashed lines highlight the 16th and 84th percentiles. Hence, we obtain $\sigma_{\rm DRW} = 72^{+16}_{-21}$ and $R_{\rm BLR} = 1.6^{+1.5}_{-0.8} \times 10^{17}$ cm.

The second model indicates that the high-frequency part of the power spectrum adds significant constraints to the accretion disk measurement because the range of R_0 compatible with the data is shrunk and leans towards the smallest values. Therefore, ignoring the high-frequency variations may lead to overestimation of R_0.

The first two models, which rely only on microlensing variability, both require lower values of the mean stellar mass $\langle M \rangle$. However, a galaxy populated by stars with $\langle M \rangle = 0.01\,M_{\odot}$ is barely conceivable because the least massive star known to this day has a mass of $0.07\,M_{\odot}$ (Kasper et al. 2007). This means that, according to these two models, the population of compact objects that is most likely to produce the observed variability is not made of stars. Hypothetical populations of primordial black holes (Hawkins 2020b,a) and galaxies with a significant number of brown dwarfs and/or free-floating Jupiter-like planets (Dai & Guerras 2018; Cornachione et al. 2020a) have been invoked to explain unexpected microlensing features. Unfortunately, primordial black holes have, to date, never been observed in nearby galaxies despite huge efforts of multiple collaborations (Alcock et al. 2001; Niikura et al. 2019a,b). In addition, the theoretical mass of a primordial black hole is poorly constrained and spans the very broad range of $\left[10^{-16}, 10^{2}\right]\,M_{\odot}$ (Green & Kavanagh 2020). Similarly, a low-mass stellar population is not observed in the Milky Way (Mróz et al. 2017). In both cases, the explanation behind the observed variability relies on an exotic population of microlenses in the lens galaxy for which we do not have any observational proof so far.

Continuum reverberation in the BLR is an acknowledged and observed effect (Blandford & McKee 1982; Bentz et al. 2009; Du et al. 2016; Williams et al. 2021) and supports the validity of our third model. The latter encapsulates our best understanding of microlensing light curve variability. It is also the only model that favours a more standard value of the mean stellar mass, $\langle M \rangle = 0.3\,M_{\odot}$, which does not require any exotic population of microlenses. This suggests that reverberation of the continuum by the BLR, which was observed multiple times with spectroscopic monitoring, is also observable in single-band photometric light curves through their high-frequency variations on the differential light curve.

Last but not least, this offers a new way of measuring the size of the BLR illustrated by Fig. 10. The relative insensitivity of this measurement to the microlensing parameters (v_e, R_0) is due to the fact that, as stated in Sect. 4.1, the main challenge of a given set of parameters ζ is to fit the high-frequency power and these are mainly set by the reverberated variability. The downside of this is that we are not able to discriminate between the values of R_0. Nevertheless, in the case of QJ 0158-4325, the measurement of $R_{\rm BLR}$ is in agreement with the Hβ-BLR size–luminosity relation (Mosquera & Kochanek 2011).

6. Conclusions and perspectives

In this work, we present a new method whereby we use the power spectrum of microlensing light curves to study the strongly lensed quasar QJ 0158-4325 system. This method allows us to take into account the high-frequency variations of the data and simultaneously include the reverberated variability in the microlensing paradigm. Our main results are summed up in the following points:

1. Ignoring the high-frequency variations, as is the case with the light-curve-fitting method, may lead to an overestimation of the scale radius of the accretion disk R_0. Indeed, we show that the use of short-timescale variations excludes the values of R_0 found with the light-curve-fitting method in Morgan et al. (2012).
2. In the context of standard paradigm microlensing light-curve simulations, the data favour an exotic microlens population drawn from an IMF with an unprecedentedly low mean mass $\langle M \rangle$ whereas with the model we propose, including the BLR

reverberation, the data favour stellar populations drawn from a standard Salpeter IMF with $\langle M \rangle = 0.3\,M_\odot$.

3. For the first time, continuum reverberation by the BLR is observed in a single waveband photometric light curve. We use this opportunity to measure the size of the BLR in QJ 0158-4325, obtaining $R_{\mathrm{BLR}} = 1.6^{+1.5}_{-0.8} \times 10^{17}$ cm, which is compatible with the expectation of the luminosity–size relation with a better precision than standard photometric reverberation mapping techniques.
4. The power-spectrum-fitting method is insensitive to the scale radius of the accretion disk R_0 in the presence of reverberated variability in the single-waveband light curve.

In light of the encouraging results this method gave for QJ 0158-4325, we are looking forward to applying it to other systems for which a microlensing light curve is available. In the upcoming *Vera C. Rubin* Observatory era, this method offers a new way to probe the luminosity–BLR size relation of quasars for a large range of redshifts and luminosities.

Acknowledgements. This work is supported by the Swiss National Science Foundation (SNSF) and by the European Research Council (ERC) under the European Union's Horizon 2020 research and innovation program (COSMICLENS: grant agreement No 787886). G.V. has received funding from the European Union's Horizon 2020 research and innovation program under the Marie Sklodovska-Curie grant agreement No 897124. The authors wish to thank Aymeric Galan for useful comments and graphical contribution. Finally, we thank the anonymous referee for the useful comments that improved the clarity of the paper.

References

Alcock, C., Allsman, R. A., Alves, D. R., et al. 2001, ApJ, 550, L169
Bate, N. F., Floyd, D. J. E., Webster, R. L., & Wyithe, J. S. B. 2008, MNRAS, 391, 1955
Bate, N. F., Vernardos, G., O'Dowd, M. J., et al. 2018, MNRAS, 479, 4796
Bentz, M. C., Walsh, J. L., Barth, A. J., et al. 2009, ApJ, 705, 199
Blackburne, J. A., Pooley, D., & Rappaport, S. 2006, ApJ, 640, 569
Blackburne, J. A., Pooley, D., Rappaport, S., & Schechter, P. L. 2011, ApJ, 729, 34
Blandford, R. D., & McKee, C. F. 1982, ApJ, 255, 419
Borguet, B., Hutsemékers, D., Letawe, G., Letawe, Y., & Magain, P. 2008, A&A, 478, 321
Cantale, N., Courbin, F., Tewes, M., Jablonka, P., & Meylan, G. 2016, A&A, 589, A81
Chan, J. H. H., Millon, M., Bonvin, V., & Courbin, F. 2020, A&A, 636, A52
Chan, J. H. H., Rojas, K., Millon, M., et al. 2021, A&A, 647, A115
Chang, K., & Refsdal, S. 1979, Nature, 282, 561
Chen, B., Dai, X., Kochanek, C. S., et al. 2012, ApJ, 755, 24
Collin, S., Boisson, C., Mouchet, M., et al. 2002, A&A, 388, 771
Cornachione, M. A., & Morgan, C. W. 2020, ApJ, 895, 93
Cornachione, M. A., Morgan, C. W., Burger, H. R., et al. 2020a, ApJ, 905, 7
Cornachione, M. A., Morgan, C. W., Millon, M., et al. 2020b, ApJ, 895, 125
Courbin, F., Eigenbrod, A., Vuissoz, C., Meylan, G., & Magain, P. 2005, in Gravitational Lensing Impact on Cosmology, ed. Y. Mellier, & G. Meylan, 225, 297
Czerny, B., & Hryniewicz, K. 2011, A&A, 525, L8
Dai, X., & Guerras, E. 2018, ApJ, 853, L27
Dai, X., Kochanek, C. S., Chartas, G., et al. 2010, ApJ, 709, 278
Ding, X., Liao, K., Treu, T., et al. 2017a, MNRAS, 465, 4634
Ding, X., Treu, T., Suyu, S. H., et al. 2017b, MNRAS, 472, 90
Ding, X., Treu, T., Birrer, S., et al. 2021, MNRAS, 501, 269
Du, P., Lu, K.-X., Hu, C., et al. 2016, ApJ, 820, 27
Edelson, R., Gelbord, J. M., Horne, K., et al. 2015, ApJ, 806, 129
Eigenbrod, A., Courbin, F., Vuissoz, C., et al. 2005, A&A, 436, 25
Eigenbrod, A., Courbin, F., Meylan, G., et al. 2008a, A&A, 490, 933
Eigenbrod, A., Courbin, F., Sluse, D., Meylan, G., & Agol, E. 2008b, A&A, 480, 647
Elvis, M. 2000, ApJ, 545, 63
Faure, C., Anguita, T., Eigenbrod, A., et al. 2009, A&A, 496, 361
Floyd, D. J. E., Bate, N. F., & Webster, R. L. 2009, MNRAS, 398, 233
Gebhardt, K., Bender, R., Bower, G., et al. 2000, ApJ, 539, L13
Green, A. M., & Kavanagh, B. J. 2020, Primordial Black Holes as a dark matter candidate
Grier, C. J., Shen, Y., Horne, K., et al. 2019, ApJ, 887, 38
Harris, F. J. 1978, Proc. IEEE, 66, 51
Hawkins, M. R. S. 2020a, A&A, 643, A10
Hawkins, M. R. S. 2020b, A&A, 633, A107
Homayouni, Y., Trump, J. R., Grier, C. J., et al. 2019, ApJ, 880, 126
Hu, C., Du, P., Lu, K.-X., et al. 2015, ApJ, 804, 138
Ivezić, V., & MacLeod, C. 2013, Proc. Int. Astron. Union, 9, 395
Karouzos, M., Woo, J.-H., Matsuoka, K., et al. 2015, ApJ, 815, 128
Kasper, M., Biller, B. A., Burrows, A., et al. 2007, A&A, 471, 655
Kaspi, S., Brandt, W. N., Maoz, D., et al. 2021, ApJ, submitted [arXiv:`2106.00691`]
Kelly, B. C., & Siemiginowska, A. 2009, ApJ, 698, 895
Khadka, N., Yu, Z., Zajaček, M., et al. 2021, MNRAS, 508, 4722
Kochanek, C. S. 2004, ApJ, 605, 58
Kogut, A., Lineweaver, C., Smoot, G. F., et al. 1993, ApJ, 419, 1
Krolik, J. H., Horne, K., Kallman, T. R., et al. 1991, ApJ, 371, 541
Li, S.-S., Yang, S., Yang, Z.-X. 2021, ApJ, 920, 9
Lobban, A. P., Zola, S., Pajdosz-Śmierciak, U., et al. 2020, MNRAS, 494, 1165
MacLeod, C. L., Ivezić, Ž., Kochanek, C. S., et al. 2010, ApJ, 721, 1014
MacLeod, C. L., Ross, N. P., Lawrence, A., et al. 2016, MNRAS, 457, 389
Magain, P., Courbin, F., & Sohy, S. 1998, ApJ, 494, 472
Mediavilla, E., Muñoz, J., Kochanek, C., et al. 2011, ApJ, 730, 16
Millon, M., Courbin, F., Bonvin, V., et al. 2020a, A&A, 642, A193
Millon, M., Courbin, F., Bonvin, V., et al. 2020b, A&A, 640, A105
Millon, M., Tewes, M., Bonvin, V., Lengen, B., & Courbin, F. 2020c, J. Open Source Softw., 5, 2654
Morgan, N. D., Dressler, A., Maza, J., Schechter, P. L., & Winn, J. N. 1999, AJ, 118, 1444
Morgan, C. W., Eyler, M. E., Kochanek, C., et al. 2008, ApJ, 676, 80
Morgan, C. W., Kochanek, C., Morgan, N. D., & Falco, E. E. 2010, ApJ, 712, 1129
Morgan, C. W., Hainline, L. J., Chen, B., et al. 2012, ApJ, 756, 52
Morgan, C. W., Hyer, G. E., Bonvin, V., et al. 2018, ApJ, 869, 106
Mortonson, M. J., Schechter, P. L., & Wambsganss, J. 2005, ApJ, 628, 594
Mosquera, A. M., & Kochanek, C. S. 2011, ApJ, 738, 96
Motta, V., Mediavilla, E., Rojas, K., et al. 2017, ApJ, 835, 132
Mróz, P., Udalski, A., Skowron, J., et al. 2017, Nature, 548, 183
Mudd, D., Martini, P., Zu, Y., et al. 2018, ApJ, 862, 123
Neira, F., Anguita, T., & Vernardos, G. 2020, MNRAS, 495, 544
Niikura, H., Takada, M., Yasuda, N., et al. 2019a, Nat. Astron., 3, 524
Niikura, H., Takada, M., Yokoyama, S., Sumi, T., & Masaki, S. 2019b, Phys. Rev. D, 99
Peng, C. Y., Impey, C. D., Rix, H.-W., et al. 2006, ApJ, 649, 616
Penton, A., Malik, U., Davis, T., et al. 2022, MNRAS, 509, 4008
Peterson, B. 2006, in The Broad-Line Region in Active Galactic Nuclei, eds. D. Alloin, R. Johnson, & P. Lira (Berlin, Heidelberg: Springer, Berlin Heidelberg), 77
Peterson, B. M., Ali, B., Horne, K., et al. 1993, ApJ, 402, 469
Poindexter, S., & Kochanek, C. S. 2010, ApJ, 712, 668
Refsdal, S. 1964, MNRAS, 128, 307
Rojas, K., Motta, V., Mediavilla, E., et al. 2014, ApJ, 797, 61
Rojas, K., Motta, V., Mediavilla, E., et al. 2020, ApJ, 890, 3
Schmidt, R. W., & Wambsganss, J. 2010, Gen. Relativ. Gravit., 42, 2127
Shakura, N. I., & Sunyaev, R. A. 1973, A&A, 24, 337
Sluse, D., & Tewes, M. 2014, A&A, 571, A60
Sluse, D., Claeskens, J. F., Hutsemékers, D., & Surdej, J. 2007, A&A, 468, 885
Sluse, D., Hutsemékers, D., Courbin, F., Meylan, G., & Wambsganss, J. 2012, A&A, 544, A62
Suberlak, K. L., Ivezić, Ž., & MacLeod, C. 2021, ApJ, 907, 96
Tewes, M., Courbin, F., & Meylan, G. 2013, A&A, 553, A120
Tremblay, G. R., Oonk, J. B. R., Combes, F., et al. 2016, Nature, 534, 218
Urry, C. M., & Padovani, P. 1995, PASP, 107, 803
Vernardos, G., & Fluke, C. J. 2014, MNRAS, 445, 1223
Vernardos, G., & Tsagkatakis, G. 2019, MNRAS, 486, 1944
Vernardos, G., Fluke, C. J., Bate, N. F., Croton, D., & Vohl, D. 2015, ApJS, 217, 23
Williams, P. R., Treu, T., Dahle, H., et al. 2021, ApJ, 911, 64
Wong, K. C., Suyu, S. H., Auger, M. W., et al. 2017, MNRAS, 465, 4895
Wong, K. C., Suyu, S. H., Chen, G. C. F., et al. 2020, MNRAS, 498, 1420
Yu, Z., Martini, P., Davis, T. M., et al. 2020, ApJS, 246, 16
Zhang, Z.-X., Du, P., Smith, P. S., et al. 2019, ApJ, 876, 49
Zu, Y., Kochanek, C. S., & Peterson, B. M. 2011, ApJ, 735, 80
Zu, Y., Kochanek, C. S., Kozłowski, S., & Udalski, A. 2013, ApJ, 765, 106

2.3 Binary black hole detection using microlensing light curves

Super Massive Binary Black Holes (SMBBH) are expected to arise from the merger of massive galaxies harbouring an SMBH in their center. The life cycle of these can be divided into three main parts (Begelman et al. 1980; Khan et al. 2013): 1) As each SMBH orbits around the new barycenter of the galaxy potential, they lose kinematic energy because of kinematic friction induced by stars in the interstellar medium. This phenomenon shrinks the orbit of the SMBHs until they bind into a binary system with a stabilized orbit of the order of 1 pc. 2) Interaction with incoming third bodies, such as incoming stars, continues to reduce the SMBBH kinematic energy through the gravitational slingshot mechanism, which transfers kinetic energy from the most massive to the least massive interacting body. 3) Once the orbit radius is below $\sim 0.01pc$, general relativity predicts the generation of gravitational waves that quickly dissipate the remaining energy of the system and precipitate the merge of the two SMBHs.

The first and third steps are predicted to be relatively rapid (respectively $\sim 10^7$ years and 10^5 years). However, the middle stage could reach up to $\sim 10^{11}$ years (i.e. more than the Universe age) because of the low probability of interaction of the SMBBH with stars after the first step "cleaned" the surrounding region. This stalling of the merger is referred to as the "Final parsec problem".

This is indeed a problem since the discovery of a gravitational wave background by the NanoGrav Pulsar Timing Array strongly suggests that the merger of SMBBH is standard in the Universe Agazie et al. (2023b,a). Several scenarios were imagined to break the stalling mechanism, such as the implication of a third SMBH (Iwasawa et al. 2006) or deviations from spherical symmetry of the stellar distribution in the inner parts of the galaxy (e.g., Khan et al. 2013; Vasiliev et al. 2015). While observed quasi-periodic oscillations in quasars and blazars light curves are often reported (e.g., Gupta 2014; Zhang 2022b) and could be associated with SMBBH (O'Neill et al. 2022), their period is often badly constrained due to the overlaying stochastic variability of the quasar (Dong et al. 2022). Therefore, we lack observational evidence to study the merger mechanisms on particular systems with only one serious candidate close separation SMBBH (Valtonen et al. 2008).

The following paper focuses on a shorter part of the QJ 0158−4325 microlensing light curve. Indeed, we detect seven consecutive oscillations with a period of 172.6 ± 0.9 days and a maximal amplitude of 0.26 ± 0.02 mag between 2006 and 2012. Fig. 4 of Paic et al. (2022) suggests that when considering the light curve between 2005 and 2018, these features blend with the BLR reverberation. Still, we show in Fig. 4 and A.3 of Millon et al. (2023) that if we focus on the part 2006-2012 part of the light curve, this specific feature is not likely due to this phenomenon. We are left with four main possible explanations related to the nature of the microlens or complex structures in the source, which are thoroughly investigated in the paper. The most likely hypothesis is that the source quasar is a Super Massive Binary Black Hole (SMBBH) with only a few milli-pc separation. While additional observations, such as spectroscopic monitoring, are necessary to confirm the binary nature of the object, the sustained periodic oscillations provide more substantial evidence than in any previous SMBBH candidate.

A&A 668, A77 (2022)
https://doi.org/10.1051/0004-6361/202244440
© M. Millon et al. 2022

Astronomy & Astrophysics

Evidence for a milliparsec-separation supermassive binary black hole with quasar microlensing[★,★★]

M. Millon[1,2], C. Dalang[3], C. Lemon[1], D. Sluse[4], E. Paic[1], J. H. H. Chan[1], and F. Courbin[1]

[1] Institute of Physics, Laboratory of Astrophysics, Ecole Polytechnique Fédérale de Lausanne (EPFL), Observatoire de Sauverny, 1290 Versoix, Switzerland
e-mail: `martin.millon@epfl.ch`
[2] Kavli Institute for Particle Astrophysics and Cosmology and Department of Physics, Stanford University, Stanford, CA 94305, USA
[3] Université de Genève, Département de Physique Théorique and Center for Astroparticle Physics, 24 quai Ernest-Ansermet, 1211 Genève 4, Switzerland
[4] STAR Institute, Quartier Agora–Allée du Six-Août, 19c, 4000 Liège, Belgium

Received 7 July 2022 / Accepted 22 September 2022

ABSTRACT

We report periodic oscillations in the 15-year-long optical light curve of the gravitationally lensed quasar Q J0158−4325 at $z_s = 1.29$. The signal is enhanced during a high magnification microlensing event of the quasar that the fainter lensed image, B, underwent between 2003 and 2010. We measure a period of $P_o = 172.6 \pm 0.9$ days, which translates to 75.4 ± 0.4 days in the quasar frame. The oscillations have a maximum amplitude of 0.26 ± 0.02 mag and decrease concurrently with the smooth microlensing amplitude. We explore four scenarios to explain the origin of the periodicity: (1) the high magnification microlensing event is due to a binary star in the lensing galaxy, (2) Q J0158−4325 contains a supermassive binary black hole system in its final dynamical stage before merging, (3) the quasar accretion disk contains a bright inhomogeneity in Keplerian motion around the black hole, and (4) the accretion disk is in precession. Of these four scenarios, only a supermassive binary black hole can account for both the short observed period and the amplitude of the signal, through the oscillation of the accretion disk towards and away from high-magnification regions of a microlensing caustic. The short measured period implies that the semi-major axis of the orbit is $\sim 10^{-3}$ pc and that and the coalescence timescale is $t_{\rm coal} \sim 1000$ yr, assuming that the decay of the orbit is solely powered by the emission of gravitational waves. The probability of observing a system so close to coalescence, in a sample of only 30 monitored lensed quasars, suggests either a much larger population of supermassive binary black holes than predicted or, more likely, that some other mechanism significantly increases the coalescence timescale. Three tests of the binary black hole hypothesis include: (i) the recurrence of oscillations in photometric monitoring during any future microlensing events in either image, (ii) spectroscopic detection of Doppler shifts (up to $\sim 0.01c$) associated with optical emission in the vicinity of the black holes, and (iii) the detection of gravitational waves through pulsar timing array experiments, such as the Square Kilometre Array, which will have the sensitivity to detect the ~100 nano-hertz emission.

Key words. gravitational lensing: micro – quasars: supermassive black holes – methods: data analysis

1. Introduction

The formation of supermassive binary black holes (SMBBHs) is an expected end product that naturally emerges from the hierarchical assembly of multiple galaxy mergers (Haehnelt & Kauffmann 2002; Volonteri et al. 2003). The binding of the two black holes in the central parsec of the merging galaxies is first driven by dynamical friction until other mechanisms, such as stellar hardening and disk-driven torques, shrink the orbits further (see e.g. Amaro-Seoane et al. 2022, for a review). Once the SMBBH reaches a separation of the order of 0.01 parsec, the emission of gravitational waves (GWs) efficiently dissipates the angular momentum and the merger of the two black holes becomes inevitable (Begelman et al. 1980).

The process that leads to the merger of two supermassive black holes (SMBHs) is described in numerical simulations over a wide range of dynamical scales (e.g. Merritt 2006; Dotti et al. 2007; Cuadra et al. 2009) but remains largely unobserved[1]. Measuring the number density of SMBBHs across redshift would improve our understanding of the mechanisms that lead to the formation of black hole pairs, and help refine the expected number of mergers that current and future GW interferometers will detect. The main observational difficulty comes from the insufficient resolution of the imaging surveys, which limits the minimum separation between the detected pairs of active galactic nuclei to a few kiloparsecs (see e.g. Tang et al. 2021; Chen et al. 2022a; Lemon et al. 2022, for recent discoveries). The higher resolution of radio observations offers the possibility to detect closer pairs (Rodriguez et al. 2006), but this technique remains limited to the nearest galaxies and to a minimal separation of ~10 pc, leaving the sub-parsec-separation SMBBHs undetected. These systems are, however, the most interesting ones as they

---

[★] Light curves presented in this paper are only available at the CDS via anonymous ftp to `cdsarc.cds.unistra.fr` (`130.79.128.5`) or via `https://cdsarc.cds.unistra.fr/viz-bin/cat/J/A+A/668/A77`

[★★] Animated Figs. 5 and 9 are available at `https://www.aanda.org`

[1] To date, OJ 287 is the only confirmed close SMBBH, which was detected from the repeated pairs of outbursts every 12.2 yr, interpreted as a secondary black hole crossing the accretion disk of the primary black hole (Valtonen et al. 2008).

Open Access article, published by EDP Sciences, under the terms of the Creative Commons Attribution License (https://creativecommons.org/licenses/by/4.0), which permits unrestricted use, distribution, and reproduction in any medium, provided the original work is properly cited.
This article is published in open access under the Subscribe-to-Open model. Subscribe to A&A to support open access publication.

are potential sources of GWs in the nano-hertz frequency range. These frequencies fall within the highest sensitivity band of pulsar timing array (PTA) experiments, which means this signal may be observable in the future. Unfortunately, they are also notoriously difficult to detect since their separation is far below the resolution limit of even the largest radio telescopes.

Consequently, candidates have been searched for through indirect techniques, although the observable signature of such close SMBBHs remains an open question (Bogdanović et al. 2008; Shen & Loeb 2010; Montuori et al. 2011; Gültekin & Miller 2012). Spectroscopic observations can potentially reveal the presence of small-separation SMBBHs through the presence of double-peaked emission lines (e.g. Dotti et al. 2009; Bogdanović et al. 2009; Boroson & Lauer 2009) or through a change in the broad line velocities over time (Eracleous et al. 2012), although the displacement of the lines could also be attributed to unusual structures in the broad line region (BLR). With the advent of recent time-domain surveys, candidates have also been proposed from the observed periodicity in some quasar light curves (Graham et al. 2015; Liu et al. 2016; Charisi et al. 2016; Chen et al. 2020, 2022b; O'Neill et al. 2022). With this technique, Jiang et al. (2022) reported a rapidly decaying signal in optical and X-ray light curves, interpreted as the imminent merger of a secondary black hole on a highly eccentric orbit. However, this interpretation is called into question by the recent spectroscopic observations of Dotti et al. (2022), which rather favour the possibility of a precessing accretion disk to explain the periodicity seen in the optical light curves. This debate illustrates the difficulty of unambiguously identifying the signature of a SMBBH through spectroscopy or spatially unresolved light curves.

In this work we exploit gravitational microlensing to zoom in onto the inner structure of the $z_s = 1.29$ strongly lensed quasar Q J0158−4325 (Morgan et al. 1999). This allows us to reveal the presence of a sub-structure in the accretion disk far beyond the resolving power of any other imaging techniques. We interpret this sub-structure as a new candidate SMBBH, with a separation of the order of a milliparsec.

Microlensing is a phenomenon that can occur in strongly lensed quasars when a star from the lens galaxy approaches one of the multiple images of the quasar. In addition to the gravitational lensing effect produced by the entire galaxy, the star itself acts as a gravitational lens, also producing a splitting of the quasar's image. The typical image separation produced by a microlens is of the order of a micro-arcsecond and is thus far too small to be resolved. However, the lensing micro-(de)magnification produced by the star can be detected. As the star passes in front of one of the quasar images, it modulates its magnification, hence producing 'extrinsic' variations on top of the 'intrinsic' stochastic variations of the quasar. The first detection of extrinsic variability attributed to microlensing is reported in Irwin et al. (1989) in the Einstein Cross (Q 2237+0305). This signal is now commonly seen in the light curves of strongly lensed quasars and is a nuisance for time-delay measurements (e.g. Poindexter et al. 2007; Tewes et al. 2013; Millon et al. 2020a).

It is a remarkable coincidence that the Einstein radii of the stars acting as microlenses are typically slightly smaller than or are similar to the characteristic angular size of accretion disks (Mosquera & Kochanek 2011). This has an extremely important consequence: as the alignment between the quasar, the star, and the observer slowly changes over time, different regions of the disk are magnified, hence offering the possibility to scan the structure of the accretion disk on nano-arcsecond scales. Microlensing is therefore a unique tool for probing the inner parsec near the central black hole. This method is also highly sensitive to additional structures in the accretion disk, for example mini-disks around a binary companion (Yan et al. 2014).

The COSmological MOnitoring of GRAvItational Lenses (COSMOGRAIL) programme (Courbin et al. 2005; Millon et al. 2020a) provides the largest dataset to date in which to search for such microlensing events. It consists of a sample of ~30 strongly lensed quasar light curves with measured time delays. Once the time delays are measured, the microlensing signal can easily be isolated by shifting the curves by their time delays and subtracting them pair-wise. The resulting difference light curves are therefore free of the intrinsic variability of the quasar and contain only the extrinsic microlensing variations. Most of the COSMOGRAIL systems have been observed for more than 10 yr, thus offering a long enough baseline to detect microlensing signatures. Slow microlensing variations (i.e. on a timescale of years) are observed in most of the lensed systems and are often used to set constraints on the accretion disk size (see e.g. Morgan et al. 2018; Cornachione et al. 2020, for recent measurements) or on the temperature profile of the disk (Eigenbrod et al. 2008; Goicoechea et al. 2020).

However, several studies have reported that the microlensing signal is in fact much more complex than just a slow modulation of the image magnification (Schild 1996; Hjorth et al. 2002; Burud et al. 2002; Schechter et al. 2003; Millon et al. 2020b). It also contains high-frequency variations (on a timescale of weeks to months) that are too fast to be attributed to stars passing in front of one of the quasar images, unless the stars in the lens galaxy move at relativistic speeds. The fast variations have been tentatively attributed to microlensing by a population of planet-mass microlenses (Schild 1996), variations in the accretion disk size over time (Blackburne & Kochanek 2010), inhomogeneities in the accretion disk (Gould & Miralda-Escudé 1997; Schechter et al. 2003; Dexter & Agol 2011), or broad absorption clouds shadowing the quasar (Wyithe & Loeb 2002). Works by Sluse & Tewes (2014) and Paic et al. (2022) also propose that a differential magnification of the reverberated flux by the BLR could produce extrinsic variations on the same timescale as the intrinsic variations of the quasar.

In the case of Q J0158−4325, the fast microlensing variations appear to be periodic, which is not observed in any other lensed system monitored by COSMOGRAIL. This periodic signal is visible over the period 2003–2010, which coincides with the period where the microlensing magnification of image B is maximal. In this work we aim to qualitatively explain the origin of this periodicity. This paper is organised as follows: In Sect. 2 we describe the observational data used in this analysis and how the microlensing signal is extracted. Section 3 presents the measurement of the period and amplitude of the periodic signal detected in the difference curve of Q J0158−4325 with a simple analytical model. Section 4 tests different hypotheses regarding the origin of this periodicity. Finally, we conclude with a discussion of our results in Sect. 5. Throughout this paper we convert the angular size into physical size, assuming flat Λ cold dark matter (CDM) cosmology with $\Omega_m = 0.3$, $\Omega_\Lambda = 0.7$, and $H_0 = 70\,\mathrm{km\,s^{-1}Mpc^{-1}}$.

2. Observational data

2.1. Data reduction

We use the *R*-band light curves of the doubly lensed quasar Q J0158−4325 obtained from 13 years of monitoring at

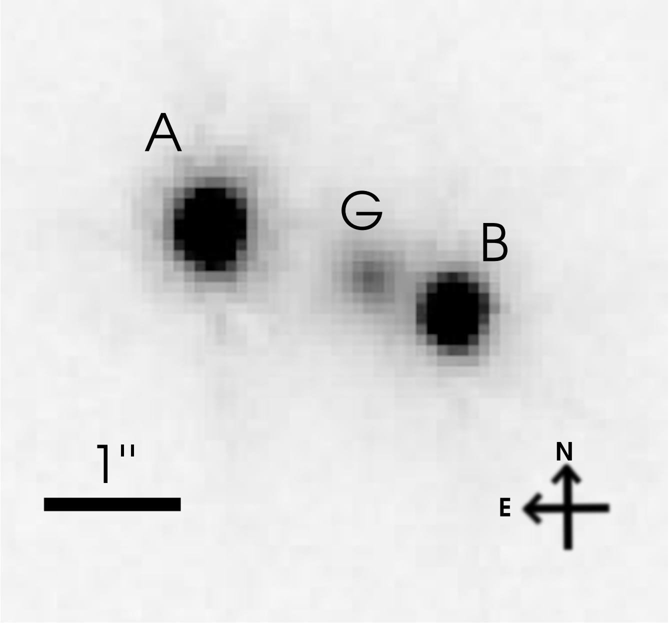

Fig. 1. HST image of doubly imaged quasar Q J0158−4325 in the $F814W$ filter (programme ID 9267; PI: Beckwith).

the Leonhard Euler 1.2 m Swiss Telescope (hereafter Euler) in La Silla, Chile, in the context of the COSMOGRAIL programme. Figure 1 shows the lensing configuration of Q J0158−4325, as observed by the *Hubble* Space Telescope (HST). The reduction and deconvolution of the Euler images are described in detail in Millon et al. (2020a) and are based on the MCS deconvolution algorithm (Magain et al. 1998). This procedure allows us to precisely extract the flux at the position of the multiple images while removing the contamination from the lens galaxy. The Euler data cover the period August 2005–February 2018, with 527 epochs. Compared to the data presented in previous publications, the light curves are now calibrated using the star located ~2″ to the east-south-east of the lens, labelled N1 in Fig. A.1 of Millon et al. (2020a). We used the Dark Energy Survey (DES) Data Release 2 photometry (Abbott et al. 2021) of this star in the R band to compute the zero point of the instrument and calibrate the light curves. We note that this absolute calibration is only approximate due to a possible mismatch between the DES r filter and the RG ('Rouge Genève') filter used for these observations. This does not affect the present work.

In addition, we complement our dataset with 252 epochs taken between August 2003 and December 2010 at the SMARTS 1.3 m telescope with the ANDICAM optical and infrared camera, published in Morgan et al. (2012). Since these data overlap with the Euler monitoring campaign, we merge all datasets into a single light curve after fitting a flux and magnitude correction to compensate for the slight photometric offsets mainly due to the differences in the filters and detector responses. This is performed with the curve-shifting package `PyCS3`[2] (Tewes et al. 2013; Millon et al. 2020c), which we use to fit a spline model on each image's SMARTS light curve. We then minimise the difference between the spline-interpolated light curves and the Euler data by applying a magnitude shift, followed by a shift in flux. Including both the Euler and SMARTS data, we obtain an interrupted light curve between August 2003 and February 2018 totalling 779 epochs[3].

2.2. Microlensing curve

The time delay between image A and image B of Q J0158−4325 has been measured to be $\Delta t_{AB} = 22.7 \pm 3.6$ days from the Euler and SMARTS monitoring data, with image A leading image B (Millon et al. 2020a). The microlensing signal can be extracted by shifting the curves by the estimated time delay and subtracting them. In doing this, we use a Gaussian process regression to interpolate between the data points before performing the subtraction. The resulting difference curve is shown in the second panel of Fig. 2. We refer to this curve as the 'microlensing curve' in the rest of this paper, but we note that it contains all extrinsic variations from both images not related to the quasar intrinsic variations. We do not interpolate over season gaps since the Gaussian process regression is poorly constrained in these parts of the light curves. Thus, the seasons of the microlensing curve are 22.7 days shorter than the visibility season. The photometric uncertainties of the microlensing curve are computed by adding in quadrature the photometric uncertainties of image B and the uncertainties of the Gaussian process model fitted onto image A. The uncertainty in the time delay does not significantly impact our microlensing curve as a shift of the time delay by 3.6 days in either direction only introduces an additional error of the order of 3 mmag, that is, ~7 times smaller than the average photometric uncertainty of the Euler difference light curve. We therefore neglect this additional source of uncertainty.

The dotted horizontal line on the second panel of Fig. 2 indicates the expected magnitude difference from the macro-models of Morgan et al. (2008), $\Delta_0 = 0.87$ mag. The microlensing curve shows a slow decrease between 2005 and 2018, with image B initially ~0.55 mag brighter than predicted by the macro-models published by Morgan et al. (2008). The brightness of image A increases slightly while that of image B decreases more consistently over the same period. In this particular case, it seems that the microlensing variation is dominant in image B, especially in the first half of the monitoring campaign. This scenario is supported by the spectra of Q J0158−4325 obtained in 2006 (Faure et al. 2009), which reveal an unusually low contrast between the continuum and the broad lines in image B, which is best interpreted as strong microlensing in that image. For these reasons, we assume in the rest of the paper that the microlensing activity was dominant in image B, whereas image A mostly contains the intrinsic signal of the quasar. By removing the intrinsic variations visible in image A, we assume that we obtain clean observations of the extrinsic microlensing activity happening in image B.

It is remarkable to observe periodic variations in the first part of the microlensing curve, between 2003 and 2011, also corresponding to a period when image B is highly magnified by microlensing. Over this period, the microlensing magnification varies by about 0.7 mag with modulations of ~0.2 mag (peak-to-peak) with a period of ~170 days in the observer frame. The period is significantly smaller than 6 months, which rules out the possibility of a seasonal effect. Moreover, the amplitude of the periodic signal is maximal when the microlensing magnification is also maximal, reaching, for example, 0.26 ± 0.02 mag during the season 2005–2006. This corresponds to a modulation

---

[2] https://gitlab.com/cosmograil/PyCS3

[3] Our data are publicly available from the COSMOGRAIL database: https://obswww.unige.ch/~millon/d3cs/COSMOGRAIL_public/

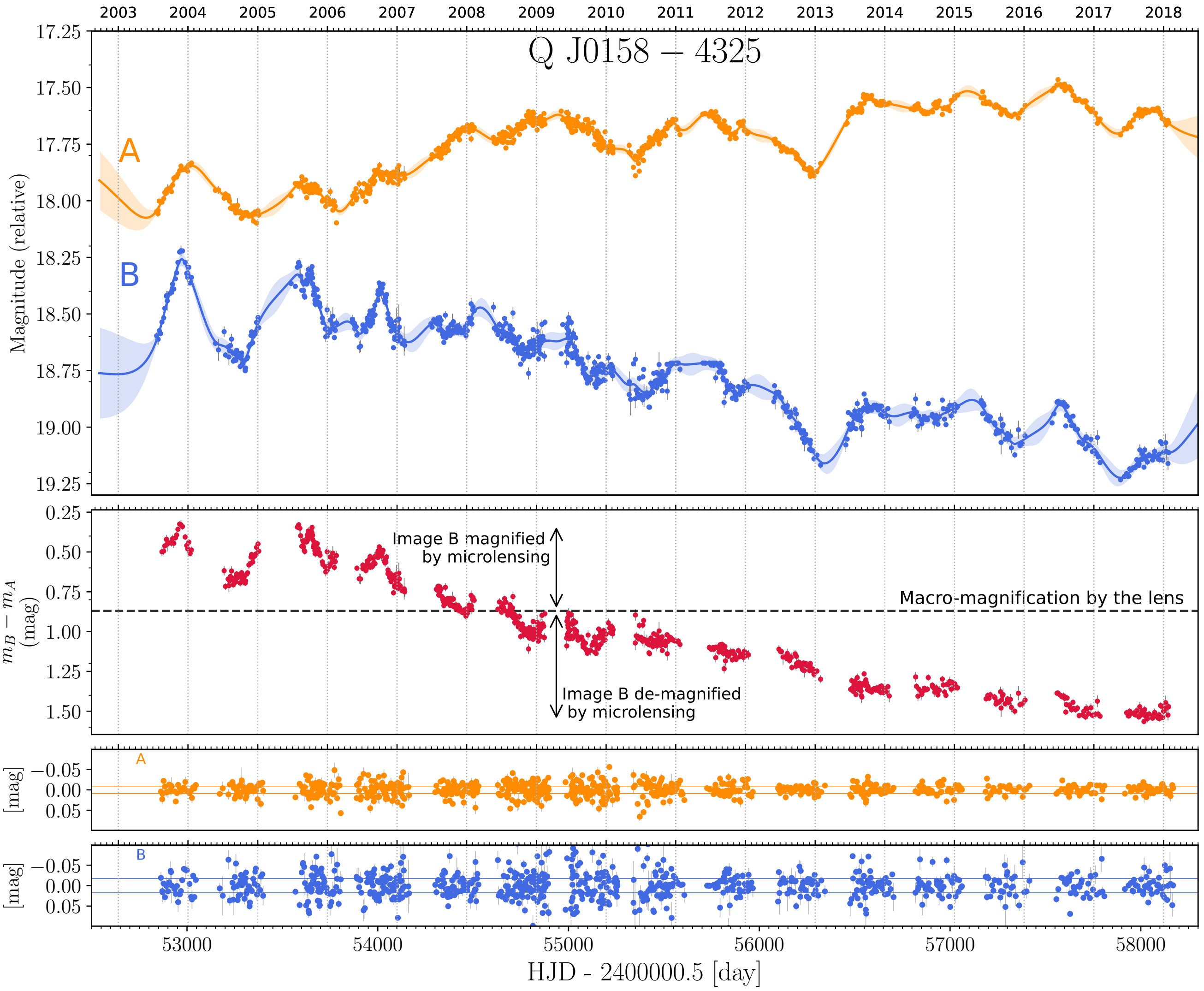

Fig. 2. *R*-band light curve of the lensed quasar Q J0158−4325. The light curves combine the data obtained at Euler (2005–2018; Millon et al. 2020a) and SMARTS (2003–2010, Morgan et al. 2012). *Top panel*: the solid blue and orange lines correspond to the Gaussian process regression used to interpolate the data, along with their uncertainties (shaded envelope). *Second panel*: difference light curve between image B and image A, shifted by the time delay. We interpolate between the data points using the Gaussian process regression shown in the *top panel*. The horizontal dashed line shows the expected flux ratio, in the absence of microlensing, computed from the macro lens model. *Third and fourth panels*: residuals of the Gaussian process regression.

of the flux of image B by 26%. The periodicity then disappears after 2011, when image B likely becomes de-magnified. Over the 15 yr of our monitoring, the microlensing magnification has changed by 1.22 mag, making Q J0158−4325 one of the most microlensing-affected systems of the COSMOGRAIL sample.

3. Period measurement

3.1. Empirical model definition

We considered a simple model to represent the periodic variations seen in the microlensing curve over the period 2005–2010, which become largely attenuated over the period 2010–2012. Here, we fit the observed flux ratio between the two images of the quasar, $F_{\mu,\mathrm{o}}(t)$, rather than the magnitude difference:

$$F_{\mu,\mathrm{o}}(t) \equiv \frac{F_{\mathrm{B}}(t)}{F_{\mathrm{A}}(t)}. \tag{1}$$

We include a smooth model $S(t)$ for the long-term variation in the microlensing as well as the zero-point flux ratio, described as a third-order polynomial:

$$S(t) = a_3 t^3 + a_2 t^2 + a_1 t + a_0, \tag{2}$$

which is sufficient to represent the long-term change of the flux ratio over the period 2005–2012. Our model considers that the amplitude of the periodic signal is linearly related to the microlensing amplitude:

$$F_{\mu,\mathrm{m}} = (A \cdot S(t) + C) \cdot \sin\left(\frac{2\pi}{P_{\mathrm{o}}} t + \phi\right) + S(t), \tag{3}$$

where $F_{\mu,\mathrm{m}}$ is the modelled flux ratio, A and C are free scaling parameters, P_{o} is the period in the observed frame and ϕ is the phase.

We perform a Bayesian fit with the likelihood defined as

$$\ln \mathcal{L} = -\frac{1}{2} \sum_{i=1}^{N} \left(\frac{(F_{\mu,\mathrm{o}}(t_i) - F_{\mu,\mathrm{m}}(t_i))^2}{s_i^2} + \ln(s_i^2) \right), \tag{4}$$

Table 1. Best-fit reduced χ^2 and median values of the main model parameters for the Euler, SMARTS, and joined Euler+SMARTS datasets.

Dataset	$\chi^2_{\rm red}$	A	T [days]	ϕ	C	δ	Time span
SMARTS	4.55	$0.07^{+0.02}_{-0.02}$	$175.83^{+1.52}_{-1.54}$	$2.41^{+0.25}_{-0.23}$	$-0.018^{+0.011}_{-0.012}$	$0.018^{+0.001}_{-0.001}$	2005–2012
Euler	6.46	$0.11^{+0.02}_{-0.02}$	$172.57^{+0.85}_{-0.86}$	$2.32^{+0.15}_{-0.16}$	$-0.030^{+0.009}_{-0.009}$	$0.019^{+0.001}_{-0.001}$	2005–2012
Euler+SMARTS	6.26	$0.07^{+0.02}_{-0.02}$	$173.85^{+0.90}_{-0.86}$	$2.49^{+0.16}_{-0.15}$	$-0.018^{+0.007}_{-0.008}$	$0.020^{+0.001}_{-0.001}$	2005–2012

Notes. Reported uncertainties correspond to the 16th and 84th percentiles of the posterior distributions.

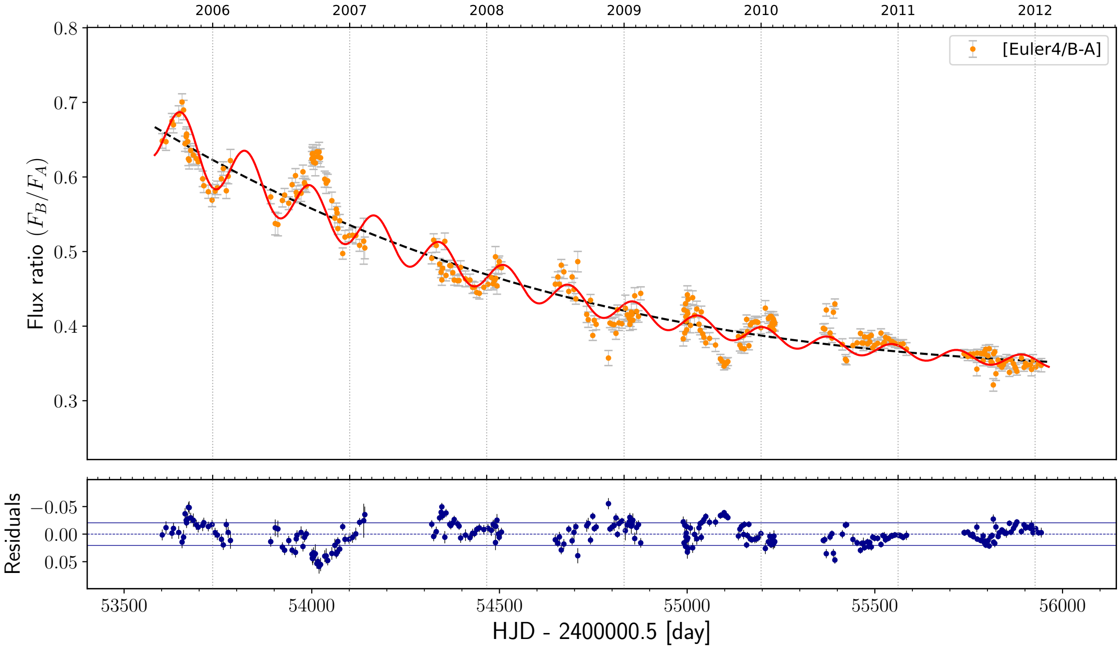

Fig. 3. Flux ratio $F_{\rm B}/F_{\rm A}$ as observed by the Euler telescope over the period 2005–2012. The solid red line shows our best-fit model. The dashed black line shows the smooth polynomial model representing the slow microlensing variations.

where $s_i^2 = \sigma_i^2 + \delta^2$, σ_i is the individual epoch photometric uncertainty, and δ is the global intrinsic scatter. We add the intrinsic scatter δ as a free parameter to account for possibly underestimated photometric uncertainties, or additional complexity in the data not captured by this simple model.

Following Bayes' theorem, we used the posterior distribution of the free parameters, $\boldsymbol{\omega}$,

$$\mathcal{P}(\boldsymbol{\omega}|\boldsymbol{d}_{\rm Euler}, \boldsymbol{d}_{\rm SMARTS}) \propto \mathcal{L}(\boldsymbol{d}_{\rm Euler}, \boldsymbol{d}_{\rm SMARTS}|\boldsymbol{\omega}) P(\boldsymbol{\omega}). \qquad (5)$$

We chose uninformative flat priors; $A \in [0, 5]$, $P_{\rm o} \in [0, 300]$ days, $\phi \in [0, 2\pi)$, $C \in [-1, 1]$, $\delta \in [0, 1]$ and $a_0, a_1, a_2, a_3 \in [-1, 1]$. We restrict our analysis to the period 2005–2012 where the periodic variations are the most prominent and clearly seen above the noise level. We leave the interpretation of the complex microlensing signal over the period 2003–2005 for the discussion in Sect. 5.

3.2. Results

The posterior distributions are sampled using the nested sampling python package `DYNESTY` (Speagle 2020). The median as well as the 16th and 84th percentiles of the marginalised posterior distributions are quoted in Table 1 for the SMARTS, the Euler and the joined SMARTS-Euler dataset. Here, the reported $\chi^2_{\rm red}$ only include the photometric uncertainties. The derived periods from the three datasets are compatible within 2σ. Our most precise estimation is from the Euler dataset with $P_{\rm o} = 172.6^{+0.9}_{-0.9}$ days. The best-fit to the SMARTS data has a significantly smaller $\chi^2_{\rm red}$ but mostly because of larger photometric uncertainties. This results in a degraded precision on the derived period when adding this dataset. For this reason, we restrict our analysis to the Euler data only for the rest of this paper. The best-fit on the Euler dataset is shown in Fig. 3.

The $\chi^2_{\rm red}$ of the fit is significantly above 1 for all three datasets, indicating that our single sinusoid, whose amplitude is linearly related to the microlensing magnification, is not sufficient to capture the full complexity of the signal. This is also reflected in the intrinsic scatter, which is significantly larger than 0. We experimented with higher-order corrections of the amplitude of the sinusoid without obtaining a significantly better fit. We thus decided to keep our model as simple as possible but this might be an indication that more complex phenomena, such as the differential reverberation proposed by Paic et al. (2022), are happening.

3.3. Lomb-Scargle periodogram

A standard technique for the spectral analysis of unevenly spaced time series is the Lomb-Scargle periodogram (Lomb 1976; Scargle 1982). Here, we used the `PyAstronomy`[4] (Czesla et al. 2019) implementation of the generalised Lomb-Scargle (GLS) periodogram (see Zechmeister & Kürster 2009),

---

[4] `https://github.com/sczesla/PyAstronomy`

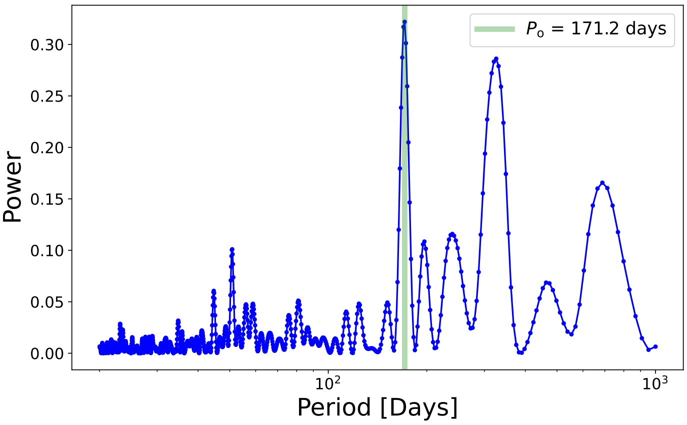

Fig. 4. Generalised Lomb-Scargle periodogram of the flux ratio observed by the Euler telescope over the period 2005–2011. The data were corrected from the long-term microlensing trend before computing the periodogram. The vertical green line indicates the peak frequency.

which accounts for offsets and variable uncertainties across the data points. We first corrected our data from the best-fit polynomial found in the previous section in order to remove the long-term microlensing trend. We then applied the GLS algorithm to the corrected data, with frequencies ranging from 20^{-1} to 1000^{-1} days^{-1}. The resulting periodogram on the Euler dataset is displayed in Fig. 4, which shows a clear peak at a period of about 171 days as well as smaller harmonic peaks at about 342 and 684 days. The same three peaks are also clearly detected on the SMARTS and the joined Euler-SMARTS datasets.

Red-noise like variability observed in active galactic nuclei has been shown to potentially produce spurious periodic signals, if only a few cycles are observed (Vaughan et al. 2016). In the present case, we stress that we observe more than ten cycles between 2005 and 2011. Moreover, the periodic signal is not obvious in the direct emission but is unveiled only in the microlensing light curve, where the intrinsic variations of the quasars are expected to be cancelled. We therefore do not expect the microlensing light curve to be affected by the red noise variability of the quasar. However, Sluse & Tewes (2014) have proposed a mechanism where the stochastic variability of the quasar could be echoed in the microlensing curve if a significant fraction of the R-band flux is emitted from a region unaffected by microlensing. We show in Appendix A that this mechanism is not sufficient to reproduce the large amplitude of the extrinsic variations seen in the microlensing light curve. We still used this physically motivated model to generate 5000 simulated light curves from a damped random walk (DRW) and compute the microlensing curve for each of them, using the same differential microlensing model as presented in Paic et al. (2022). The simulated light curves have the same sampling and photometric noise as the real data (see Appendix A for the details of this test).

Only 0.6% of the curves produces a peak in the GLS periodogram with more power than observed in the Euler data over the period 2005–2011. We conclude that this differential reverberation model is unable to reproduce the periodicity observed in the first part of our observations at 3.7σ significance level. Although it might still explain the small amplitude flickering seen in the second part of our observations and in other systems of the COSMOGRAIL sample, we conclude that it is improbable that the observed periodicity arises by chance from the differential reverberation model proposed by Sluse & Tewes (2014) and Paic et al. (2022).

4. Origin of the periodic signal

We propose four hypotheses to explain the periodicity observed in the extrinsic variability of image B.

Hypothesis 1: The microlensing magnification is modulated by a secondary star (or a planet) in the lens plane. The microlensing event seen in image B is in fact produced by a pair of microlenses.

Hypothesis 2: Q J0158−4325 is a binary black hole, with two SMBHs in their final stage before merging. The motion of the accretion disk around the centre of mass of the system in the source plane is at the origin of the observed signal.

Hypothesis 3: The accretion disk contains an inhomogeneity in Keplerian motion around the central SMBH, which is approaching the micro-caustic periodically.

Hypothesis 4: The inner part of the accretion disk is in precession. This precession could be due to the Bardeen-Peterson effect (Bardeen & Petterson 1975) or because the disk is eccentric, which implies that the pericentre of elliptical orbits advances at each revolution in a Schwarzschild potential.

Each of these scenarios is detailed in the following subsections, where we propose simple toy models to evaluate if these hypotheses could reproduce the same amplitude and period of the microlensing signal. We assume that the light intensity profile of the quasar's accretion disk is represented by a non-relativistic thin-disk profile (Shakura & Sunyaev 1973) such that

$$I_0(R) \propto \frac{1}{\exp(\xi(R)) - 1}, \tag{6}$$

where

$$\xi(R) = \left(\frac{R}{R_0}\right)^{3/4} \left(1 - \sqrt{\frac{R_{\rm in}}{R}}\right)^{-1/4}. \tag{7}$$

In this last equation, $R_{\rm in}$ corresponds to the radius of inner edge of the accretion disk and R_0 is the scale radius, which can be estimated from the black hole mass, $M_{\rm BH}$:

$$R_0 = 9.7 \times 10^{15}\,{\rm cm} \left(\frac{\lambda_{\rm s}}{\mu{\rm m}}\right)^{4/3} \left(\frac{M_{\rm BH}}{10^9 M_\odot}\right)^{2/3} \left(\frac{L}{\eta L_{\rm E}}\right)^{1/3}, \tag{8}$$

where $\lambda_{\rm s}$ is the observed wavelength in the quasar rest frame, $L_{\rm E}$ is the Eddington luminosity and η is the accretion efficiency. Assuming a typical Eddington ratio $L/L_{\rm E} = 1/3$, accretion efficiency of 10% ($\eta = 0.1$), and a black hole mass of $M_{\rm BH} = 1.6 \times 10^8 M_\odot$ based on Mg II line width measurement (~0.35 dex uncertainties, Peng et al. 2006), we derive a characteristic scale of the accretion disk of $R_0 = 7.9 \times 10^{14}$ cm at 650 nm in the observer frame, corresponding to $\lambda_{\rm s} = 650\,{\rm nm}/(1+z_{\rm s}) = 284$ nm in the quasar rest frame. This corresponds to 0.3 light-days. R_0 is related to the half light radius of the profile through the simple relation $R_{1/2} = 2.44 R_0$. Finally, we fixed

$$R_{\rm in} = 6 r_{\rm g}, \tag{9}$$

where $r_{\rm g} = G M_{\rm BH}/c^2$ is the gravitational radius. $R_{\rm in}$ corresponds the size of the innermost stable circular orbit (ISCO) for a Schwarzschild black hole. We adopted a fiducial macro lens model from Morgan et al. (2008) for a stellar mass fraction $f_{\rm M/L} = 0.9$ ($\kappa = 0.72$, $\gamma = 1.03$, $\kappa_\star/\kappa = 0.92$ for image B). For the population of microlenses used in Sect. 4.3, we made similar assumptions to those by Paic et al. (2022), that is, a Salpeter initial mass function with mean stellar mass $\langle M \rangle = 0.3\,M_\odot$ and a mass ratio of 100 between the heaviest and the lightest

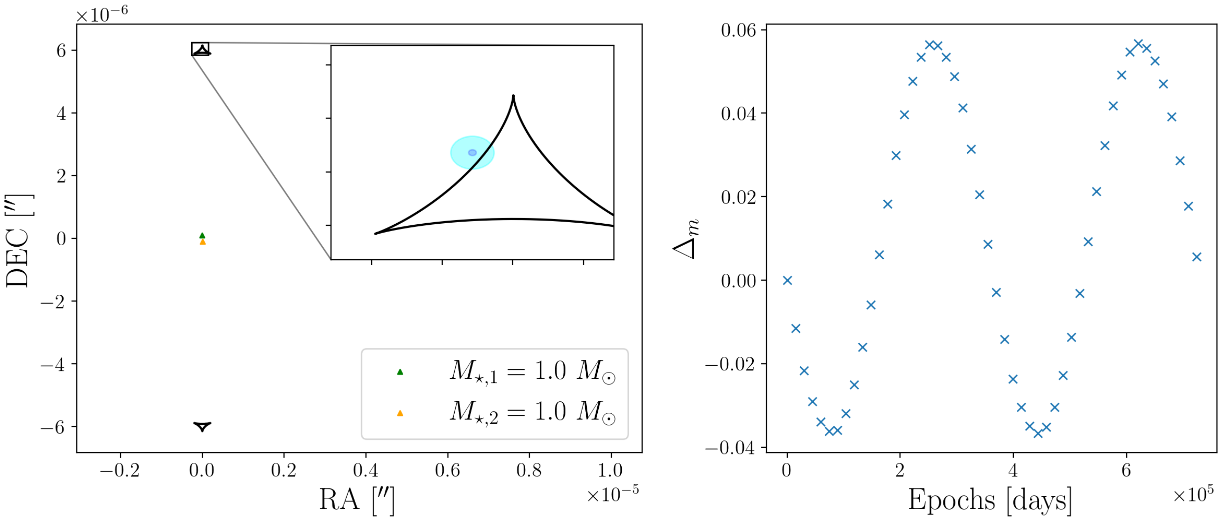

Fig. 5. Simulation of the microlensing effect produced by a binary star. *Left panel*: source plane micro-caustics (black) created by a pair of stars located at the position of image B in the lens plane. The green and orange triangles show the stars' locations, which are separated by 200 AU. The inset panel zooms in onto the position of the accretion disk. The light (dark) blue circle corresponds to the accretion disk size R_0 (size of the ISCO, $R_{\rm ISCO}$). *Right panel*: magnitude change of image B due to the periodic motion of the microlenses. An animated version of this figure is available online.

microlenses. The mean Einstein radius $R_{\rm E}$ of the microlenses, projected into the source plane, is defined as

$$R_{\rm E} = D_s \times \sqrt{\frac{4G\langle M\rangle}{c^2}\frac{D_{ls}}{D_l D_s}}, \tag{10}$$

where D_s, D_l, and D_{ls} are the angular diameter distances to the source, to the lens and between the lens and the source. For $\langle M\rangle = 0.3\,M_\odot$, the Einstein radius is $R_{\rm E} = 3.4 \times 10^{16}$ cm (13.1 light-days). We note that the size of the accretion disk is smaller than the typical Einstein radius of the microlenses ($R_0/R_{\rm E} = 0.023$), which makes this system likely to be affected by large microlensing variations.

4.1. Binary microlenses

In this first scenario, we assume that the periodic variations originate from a stellar binary (or a planetary system) in the lens plane. We aim at estimating the amplitude of the microlensing modulations that such a binary system would produce. First, we fixed the orbital period of the binary system in the lens plane to

$$P_l = 2P_{\rm o}/(1 + z_l), \tag{11}$$

where $P_{\rm o}$ is the measured period in the observer frame and $z_l = 0.317$ is the lens redshift. For the measured $P_{\rm o} = 172.6$ days, this gives $P_l = 262.1$ days. The factor of 2 introduced in Eq. (11) comes from the fact that a binary system produces a modulation of the microlensing signal at half the orbital period. By fixing the period and the masses of the two binary stars, the semi-major axis is imposed through *Kepler*'s second law. Additionally, we assume that the orbital motion is circular and perpendicular to the plane of the sky.

Second, we use the lens modelling software `lenstronomy` (Birrer et al. 2021) to generate the microlensed images of the accretion disk. Our lens model is composed of two point masses (representing the stars) plus external convergence and shear ($\kappa = 0.72$, $\gamma = 1.03$) corresponding to the value of our fiducial macro lens model at the position of image B. We note that, since image B is a saddle point, the caustic produced by the pair of stars is split in two, as can be seen on the left panel of Fig. 5 (see e.g. Schechter & Wambsganss 2002, for a discussion of the properties of microlensing caustics near a macro saddle point).

We assume a thin-disk profile (Eq. (6)) located at a distance $d = 0.5R_0$ from the fold of the caustics in the source plane. We let the system evolve for one full period and compute the total flux of image B at each time step. We compute Δ_m, the maximum peak-to-peak amplitude (in magnitude) of the periodic microlensing signal. It corresponds to the maximal change of microlensing magnification due to the orbital motion of the two stars acting as microlenses.

The choice of $d = 0.5R_0$ maximises the amplitude of the periodic signal for a pair of $1\,M_\odot$ stars. This optimal distance slightly varies with the mass of the microlenses but we fix it to $d = 0.5R_0$ for all microlenses' masses since it does not change Δ_m by more than a factor of 10. Similarly, we chose a location near the caustic's fold that maximises the signal but other choices (e.g. positioning the disk near the caustic's cusp) reduces the amplitude by no more than a factor of 10.

Keeping the same source position relative to the caustic, we repeat the experiment for a pair of compact bodies (stars or planets) with a mass $M_{\star,1}$ and $M_{\star,2}$ in the range 10^{-6}–$10^2\,M_\odot$. The amplitude of the microlensing signal Δ_m produced by such a binary system is shown on the left panel of Fig. 6. We recall that the observed Δ_m for Q J0158−4325 is ~0.2 mag. Even an extremely massive pair of $100\,M_\odot$ stars would not be able to produce a periodic modulation of more than 10^{-5} mag, that is, 4 orders of magnitude smaller than the observed signal.

The right panel of Fig. 6 shows Δ_m as a function of the orbiting radius $r_\star$ of the binary system and its total mass $M_{\star,\rm tot} = M_{\star,1} + M_{\star,2}$, with $M_{\star,1} = M_{\star,2}$. In this case, the orbital period is not forced to match the observed one.

In this last example, we are able to reproduce the observed amplitude but not the correct period. This is highlighted in Fig. 5 for a pair of $1\,M_\odot$ stars. The modulation of the microlensing amplitude can reach 0.1 mag but only when the two stars are separated by 200 astronomical units (AU). This corresponds to a much longer period of 2000 yr. It is therefore not possible to

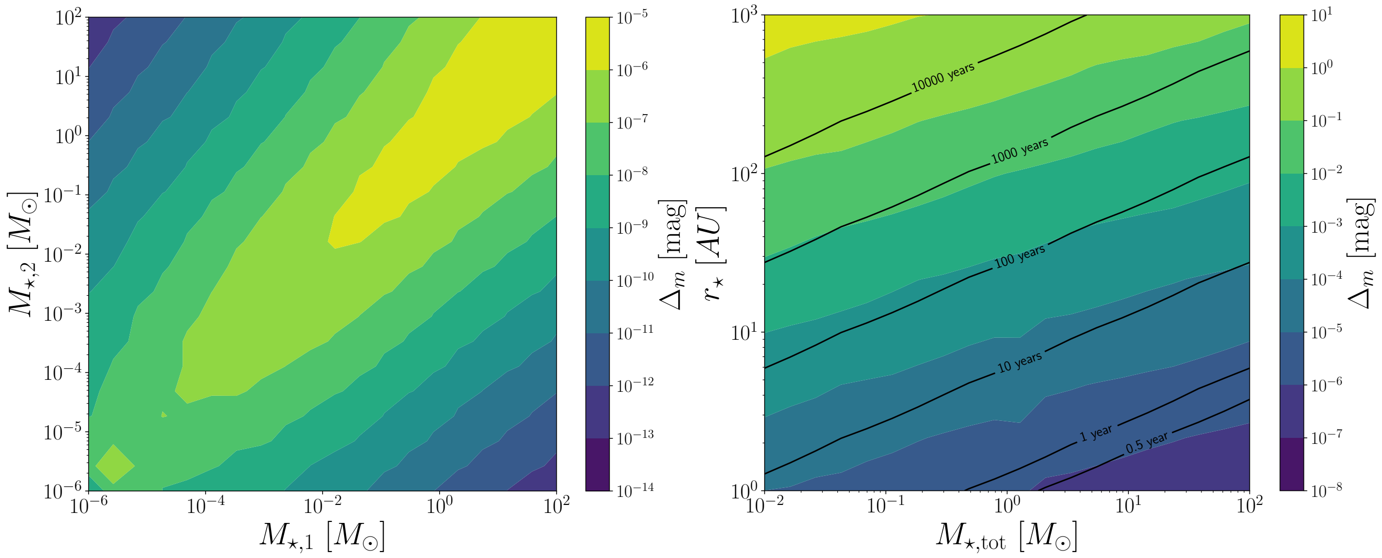

Fig. 6. Maximal amplitude of the periodic signal, Δ_m, for a pair of stars of mass $M_{\star,1}$ and $M_{\star,2}$ (*left panel*). The period is fixed to the observed $P_l = 262$ days, which imposes the separation between the two stars. The *right panel* shows the maximal amplitude of the periodic signal, Δ_m, as a function of the total mass of the binary system, $M_{\star,\mathrm{tot}}$, and the radius of the orbit, $r_\star$. In this case, the orbital period is not fixed and is indicated by the black contours.

reproduce both the period and amplitude of the observed signal. Even when choosing an ideal source position relative to the micro-caustic and extremely massive microlenses the observed signal is at least 4 orders of magnitude larger than our simulations. Moreover, we took a conservatively small value for the accretion disk size, which might in fact be several times larger than predicted by the thin-disk theory (see e.g. Pooley et al. 2007; Morgan et al. 2010; Cornachione & Morgan 2020, or an overview of this issue). A larger disk would further reduce the amplitude of the microlensing signal. It is therefore extremely unlikely that the periodicity observed in the microlensing curve of Q J0158−4325 originates from binary microlenses in the lens plane.

4.2. Supermassive binary black hole

We explore the possibility that the modulation of the microlensing signal originates from a system composed of two gravitationally bound SMBHs. The orbital period in the source plane is $P_s = P_o/(1+z_s) = 75.4$ days. We repeat the experiment presented in Sect. 4.1, but with a single 1 $M_\odot$ star acting as a microlens in the lens plane. This time, the periodic motion is generated by displacing the centre of the thin-disk profile in the source plane around the centre of mass of the binary system.

Similarly to Sect. 4.1, we position the centre of mass of the system at a distance $d = 0.5R_0$ from the fold of the micro-caustic to maximise the microlensing amplitude. However, we do not associate any light emission with the secondary black hole; the modulation of the light profile occurs only because the primary black hole and its accretion disk orbit around the system's centre of mass. Here, we neglect the possibility that the secondary black hole may also have its own accretion disk, or that complex structures such as circumbinary disks and mini-disks may arise from the gravitational interaction of the two systems (see also Sects. 4.3 and 5 for a more detailed discussion of this issue). Several numerical simulations (e.g. Cuadra et al. 2009; D'Orazio et al. 2013; Bowen et al. 2018) predict the formation of a gap between the circumbinary disk and the two spiralling black holes in the centre but the implementation of these profiles is left for future work. Our simple representation is in fact sufficient to reproduce the main features of the microlensing curve, namely the period and the amplitude. Figure 7 shows the maximal peak-to-peak amplitude Δ_m for a secondary black hole's mass in the range 10^3–10^8 $M_\odot$ with the orbital period kept fixed to P_s, and the mass of the main black hole M_1 fixed to the fiducial black hole mass of $1.6 \times 10^8 M_\odot$.

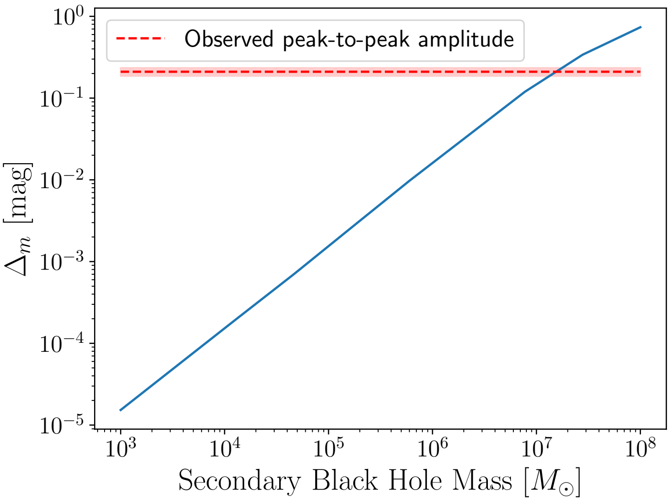

Fig. 7. Maximum amplitude of the periodic signal, Δ_m, as a function of the secondary black hole mass, M_2. The primary black hole mass is fixed to our fiducial black hole mass estimate, $M_{\mathrm{BH}} = 1.6 \times 10^8$ $M_\odot$.

The observed microlensing amplitude is reproduced for a binary companion mass of $M_2 \sim 10^7$ $M_\odot$. This value should rather be considered as a lower limit for M_2 than a proper measurement because we chose an optimal location of the system relative to the micro-caustic and a conservatively small accretion disk size. By changing some of the arbitrarily fixed parameters in the model (such as the mass of the star acting as a microlens or the distance from the caustic), one can easily accommodate bigger masses for the secondary black hole.

Solely based on our simulations, the hypothesis of a binary SMBH is plausible and reproduces well the observed microlensing curve. If we consider that the accretion disk might move away from the caustic due to the relative motion of the source, the star in the lens galaxy, the lens galaxy itself and the observer, the microlensing magnification would be gradually reduced, and the damping of the signal is easily reproduced.

However, such binary systems are thought to be rare because of the rapid decay of their orbit due to GW emission. Neglecting the dynamical friction and considering that the system loses energy only through GW emission, the two black holes will eventually merge on a coalescence timescale that depends on the initial eccentricity and semi-major axis of the orbit. Assuming $M_1 = 1.6\times10^8\,M_\odot$, $M_2 = M_1/10$, and a circular orbit, we obtain an orbiting radius of $r = 9.8\times10^{-4}$ pc from the observed period of 75.4 days in the source frame. The coalescence time of such a close binary system reads (Peters 1964)

$$t_{\mathrm{coal}} = \frac{5}{256}\frac{a^4c^5}{G^3M_1M_2(M_1+M_2)} \tag{12}$$

and is thus estimated to be $t_{\mathrm{coal}} \sim 10^3$ yr. This timescale is extremely small compared to the age of the quasar at redshift $z_\mathrm{s} = 1.29$, which is about 4 yr if the quasar was formed around redshift 7. The probability of observing this system in the last ~1000 yr before merging is approximately 2.6×10^{-7}. If we consider that the black hole could have encountered several merger events during its lifetime, this probability can be increased by a factor of a few but remains very small. Merger rates of SMBBHs are yet to be constrained by observations and depend on the existence of primordial black holes (Auclair et al. 2022, see also Erickcek et al. 2006 for an estimation of SMBH merger rates observable with the Laser Interferometer Space Antenna).

Nevertheless, it is quite surprising, given the ~30 lensed quasars of the COSMOGRAIL sample, that we observe such a system. However, if the mass of the black hole turns out to be overestimated by a factor of 10, which is possible given that black hole mass estimates based on broad line-width measurements are notoriously uncertain, the coalescence time would be much larger. Uncertainties on the black hole mass are typically of the order of 0.3–0.4 dex from the intrinsic scatter of the virial relationships (e.g. Peterson et al. 2004; Mejía-Restrepo et al. 2016) but several biases may affect the measurements, especially if the black hole is a binary. If the mass of the primary black hole is rather of the order of $M_1 = 1.6\times10^7 M_\odot$, the same mass ratio would also reproduce both the amplitude and period of the signal. In this case, we find a larger coalescence time of 5×10^4 yr, under the same assumptions. The probability of observing this system would still be small (of the order of 10^{-5}) and reaches 3×10^{-4}, if we consider the 30 light curves of the COSMOGRAIL sample.

In summary, the scenario of a SMBBH is appealing to explain the observed signal in the light curve but it hardly accommodates for the very short lifetime of these systems when the decay of the orbit is dominated by GW emission. The probability of observing this system in its final stage before merging is small unless the black hole mass of Q J0158−4325 is largely overestimated, or if the merging is delayed by the gravitational interaction of a gaseous circumbinary disk (this issue is discussed in more detail in Sect. 5). In this case, detecting such a signal would be rare but not completely excluded.

Assuming that the emission closest to the larger black hole is not disrupted by the merger process, a possible observational signature would be periodic Doppler shifts of the electromagnetic emission. This would be observed at X-ray wavelengths, by measuring the 6.4 keV Fe-Kα line shift. The Keplerian velocity of the system is ~27 000 km s^{-1}, but for a mass ratio of $q \sim 10$, the line-of-sight velocity of the primary black hole is up to 2700 km s^{-1}, depending on the inclination angle. Line energy variations, both intrinsic and extrinsic (Bhatiani et al. 2019), are typically larger than the 5% level, making such a periodic spectroscopic detection difficult. For this reason, we cannot convincingly conclude that the Fe-Kα line shift seen in the X-ray monitoring data obtained for this system by Chartas et al. (2017) is due to a secondary black hole. Continued photometric monitoring at optical wavelengths, however, should clearly reveal the periodic signal during a microlensing event in either image, under the SMBBH hypothesis.

4.3. Inhomogeneities in the accretion disk around the ISCO

In our third scenario, we explore the possibility of a small inhomogeneity in the accretion disk, differentially amplified due to microlensing magnification of image B. In this case, the bright ‘hotspot’ may periodically approach a micro-caustic, hence modulating the magnification of this region of the disk. To test this scenario, we generate microlensing magnification maps by inverse ray-shooting with the GPU-D software (Vernardos et al. 2014). The size of the maps is $20R_\mathrm{E}\times20R_\mathrm{E}$.

First, we searched for trajectories in the magnification maps that correspond to the long-term trend observed in the microlensing curve. This is performed in a similar way to the Monte-Carlo method presented in Kochanek (2004), except that we are not aiming to measure the accretion disk size of the quasars, which is degenerate with the total relative velocity between the quasar, the microlenses and the observer. Here, we fix the accretion disk size to its thin-disk predicted value, $R_0 = 7.9\times10^{14}$ cm (0.3 light-days). We generate 10^6 random trajectories through the magnification maps assuming a total transverse velocity V, in the range [0–2000] km s^{-1}. We compute the flux ratios between image A and image B along these trajectories, assuming that A is unaffected by microlensing. We compare these simulations to observational data by taking the weighted mean of the observed flux ratios in each season. The five best-fit trajectories are shown in Fig. 8.

Several combinations of total transverse velocity and location relative to the micro-caustics offer a good fit to the global microlensing trend with a $\chi^2_{\mathrm{red}} < 1$. However, those trajectories cannot reproduce the periodic features observed between 2005 and 2010. Therefore, we propose here a more detailed model of the microlensing curve with an accretion disk including a hotspot orbiting the central black hole. A Gaussian profile is added to a standard thin-disk profile to represent the hotspot, with its width fixed to 2 pixels full width half maximum. This corresponds to a physical size of 1.7×10^{14} cm (0.07 light-days). The period, P, the luminosity ratio $L_{\mathrm{ratio}} = L_{\mathrm{disk}}/L_{\mathrm{hotspot}}$, the initial phase of the orbit θ_0 and the accretion disk size R_0 are left as free parameters. The radius of the orbit is determined by the period and the black hole mass, which is kept fixed to $M_{\mathrm{BH}} = 1.6\times10^8 M_\odot$. To limit the number of free parameters, we assume that the hotspot is on a perfectly circular orbit, perpendicular to the plane of the sky in a face-on disk, but our results can be easily generalised to elliptical orbits and inclined accretion disks. We adopted flat priors: $P_\mathrm{o} \in [0, 300]$ days, $L_{\mathrm{ratio}} \in [0, 10]$, $\theta_0 \in [0, 2\pi]$, and $\log_{10}(R_0/\mathrm{cm}) \in [14, 17]$. We then computed the flux ratio along the pre-defined trajectory and compare it with the entire observed Euler light curve. We restrict our analysis to a smaller cutout of the magnification map, encompassing

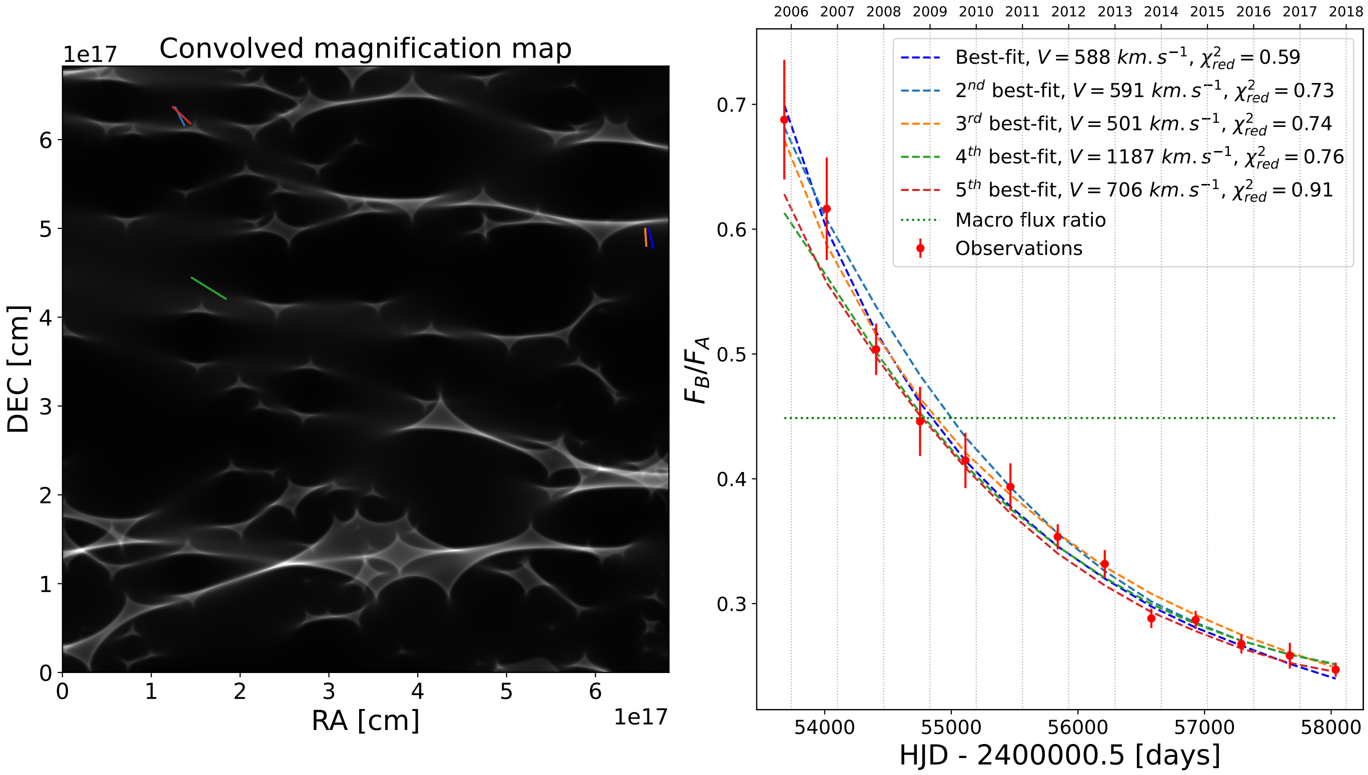

Fig. 8. Modelling of the long-term flux ratio variations from realistic microlensing simulations. *Left panel*: magnification map, convolved by a thin-disk light profile with $R_0 = 7.9 \times 10^{14}$ cm (0.3 light-days). The five best-fit trajectories are shown in colours. *Right panel*: observed flux ratios F_B/F_A of the two lensed images. The observations are averaged by season in order to fit only the long-term variations, attributed to the displacement of the quasar through the micro-caustic network. The five best-fit trajectories are shown as dashed lines. The horizontal dotted line corresponds to the flux ratio expected from the macro lens model. The legend indicates the total transverse velocity, V, corresponding to the selected trajectory as well as the associated reduced χ^2 of the fit.

the best-fit trajectory, in order to keep the computational time manageable.

We used the Python nested sampling package `DYNESTY` and the auto-differentiation package `JAX` (Bradbury et al. 2018) for the likelihood evaluation to make a Bayesian inference possible in a reasonable time on a single GPU. Figure 9 shows the trajectory in the magnification map, the microlensed accretion disk profile, and the best-fit simulated light curve. The posterior distributions of the free parameters are shown in Fig. 10.

This model reproduces well the main features of the light curve but the amplitude of the oscillations is not always matched. Our goal is not to exactly reproduce the data as this would require finding the ensemble of tracks that are compatible and simultaneously account for the unknown complexity of the source. Considering the various hypotheses to be tested and the numerical complexity of such a fit, we do not attempt to perfectly model all the features seen in the microlensing curve. Still, with this simple physical model, we recover a similar value of the period ($P_o = 172.69^{+0.08}_{-0.06}$ days) as our purely empirical model presented in Sect. 3. Interestingly, the luminosity ratio between the main accretion disk and the hotspot is constrained to $L_{\rm ratio} = 4.8^{+0.2}_{-0.2}$. Although R_0 is left as a free parameter, we have an implicit prior on the accretion disk size coming from the pre-selected trajectory, chosen to fit the long-term trend of the microlensing curve. We nevertheless recover a similar luminosity ratio by selecting trajectories with $0.5R_0$ and $2R_0$ and repeating the experiment.

The black hole mass estimates from Peng et al. (2006) and the observed period constrain the distance of the hotspot from the central black hole, which is localised relatively far from the centre ($120r_g$). If we remove our assumption on the black hole mass, we can compute the relation between the black hole mass and the semi-major axis of the orbit for a fixed period of 75.4 days. This is shown in Fig. 11.

We have not yet discussed what could be the emission mechanism at play in this hypothetical hotspot, producing around 20% of the total UV flux. A first explanation would be that it is powered by accretion onto a secondary smaller black hole, which would be similar to our second scenario. Alternatively, one can imagine that a compact region of the disk is significantly hotter than the rest of the accretion disk. To produce 20% of the UV flux, this hotspot would preferably be located close to the ISCO, which would require the mass of the black hole to be largely underestimated. Bringing the hotspot to the ISCO would require an extremely large black hole mass of the order of $10^{10} M_\odot$. Although accretion disks are thought to be inhomogeneous at some level, the model of inhomogeneous accretion proposed by Dexter & Agol (2011) rather produces small temperature fluctuations everywhere in the disk rather than in one single, hot, UV-emitting region. Models predicting numerous small inhomogeneities in the accretion disk would not produce the periodicity observed in the data.

In addition, if the hotspot is powered by a mechanism other than accretion and is not bound by gravity, we would expect that the local inhomogeneity in the disk is rapidly disrupted by Keplerian shear. This is a similar argument made by Eracleous et al. (1995), who estimated that inhomogeneities

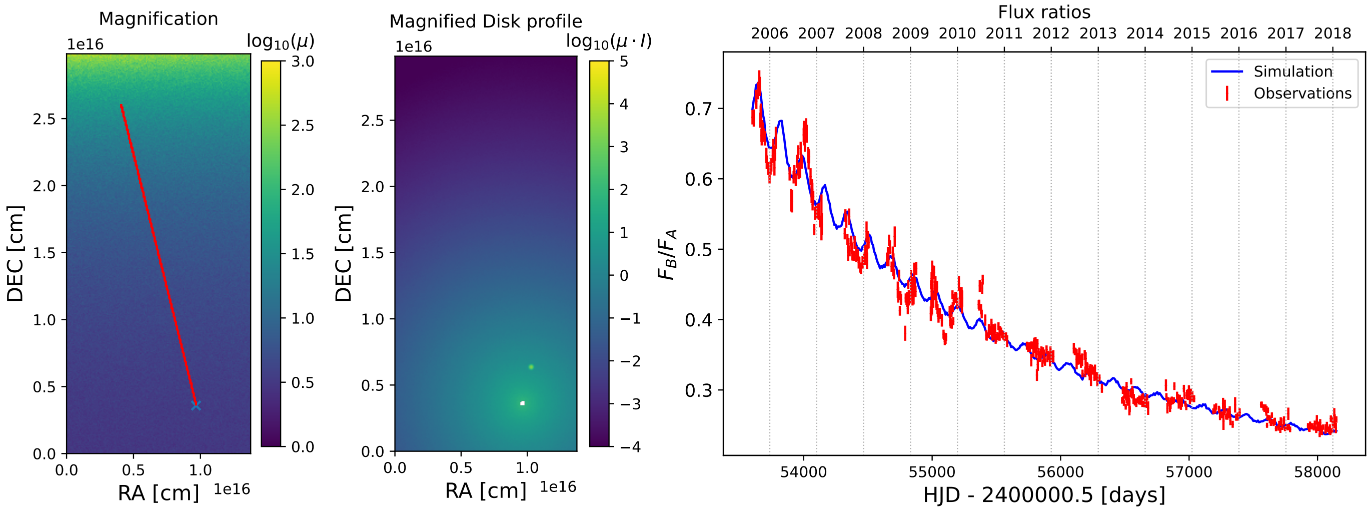

Fig. 9. Inhomogeneous accretion disk simulations. *Left panel*: microlensing magnification map. The red line shows the trajectory that best fits the long-term microlensing trend (see Fig. 8). *Middle panel*: microlensing magnified accretion disk profile, including a Gaussian hotspot orbiting the central black hole. The radius of the circular orbit is determined by the period, which is a free parameter, and the black hole mass, fixed to $1.6 \times 10^8\ M_{\odot}$. *Right panel*: observed (red) and simulated (blue) flux ratios for the best-fit parameters. An animated version of this figure is available online.

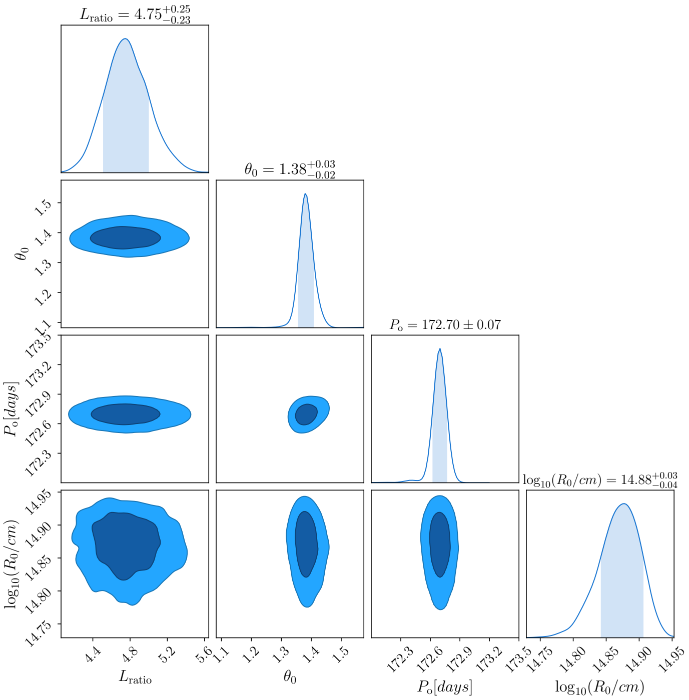

Fig. 10. Posterior distributions of the model parameters. $L_{\rm ratio}$ is the luminosity ratio between the luminosity of the hotspot and the total luminosity of the disk, θ_0 is the initial position angle of the hotspot, $P_{\rm o}$ is the orbital period, and R_0 is the accretion disk size. The mass of the black hole is kept fixed to $1.6 \times 10^8\ M_{\odot}$.

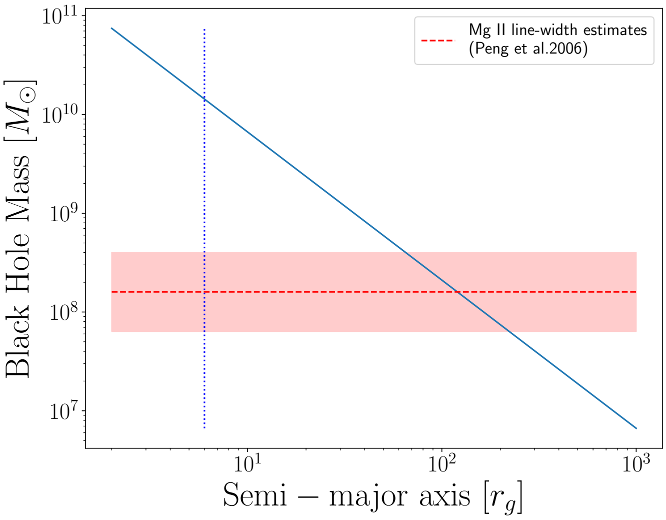

Fig. 11. Black hole mass as a function of the semi-major axis of the hotspot's orbit. The orbital period is fixed to the observed one, P_s = 75.4 days. Peng et al. (2006) estimates of the black hole mass imply that the emission region of the disk at the origin of the periodic signal is located at around $120 r_g$ from the central black hole. The vertical blue line indicates the ISCO for a Schwarzschild black hole.

would dissipate on a timescale of order

$$\tau_{\rm shear} \approx \frac{2 r P_{\rm Kep}}{3h}, \tag{13}$$

where r is the radius of the orbit, $P_{\rm Kep}$ is the Keplerian period and h is the radial extent of the inhomogeneity. Considering that the inhomogeneity is approximately the size of the local height of the disk we obtain (Veilleux & Zheng 1991; Eracleous et al. 1995)

$$\tau_{\rm shear} \sim 7 \left(\frac{M_{\rm BH}}{10^8 M_{\odot}}\right)\left(\frac{r}{100 r_{\rm g}}\right)\left(\frac{T}{10^5 K}\right)^{-1/2} \text{yr}, \tag{14}$$

where T is the local temperature of the disk. This means that a hotspot localised at ~120 gravitational radii from a central black hole of $M_{\rm BH} = 1.6 \times 10^8 M_{\odot}$ will dissipate in about 13 yr because of Keplerian shear. This timescale is indeed longer than our observational baseline. The fact that such an extremely bright hotspot has appeared exactly during the high magnification event of image B would imply that they are much more common than expected. This is at odds with the observations of other lensed quasar microlensing events. The last possibility is that the same region of the disk is constantly heated, regenerating the hotspot on a timescale smaller than τ_{shear}. To our knowledge, no such mechanism is capable of producing one-fifth of the quasar luminosity on a single small region of the disk. In the same vein, obscuring a part of the disk (as proposed by e.g. Wyithe & Loeb 2002) could introduce the observed periodicity but to match the amplitude it would require masking one quarter of the total quasar luminosity, and thus would also quickly be disrupted by Keplerian shear.

Overall, accretion onto a secondary black hole seems the most plausible, if not the only, mechanism capable of producing the required amount of UV flux, while keeping the emission region sufficiently small to be significantly amplified by microlensing.

4.4. Precessing accretion disk

Eccentric accretion disk models were originally proposed to account for asymmetric double-peaked emission lines seen in quasar spectra (Eracleous et al. 1995; Strateva et al. 2003). Two main mechanisms were put forward to explain their formation: (1) a perturbation of the disk by tidal forces induced by a smaller black hole and (2) elliptical accretion of the debris resulting from the disruption of a star. In the case of Q J0158−4325, the black hole seems too massive to provoke a tidal disruption event. A star approaching the black hole would be swallowed without being disrupted (Rees 1988).

Regardless of the formation channel, eccentric disks precess due to the advance of the orbit's pericentre in a Schwarzschild potential. The precession angle per revolution is given by

$$\delta\phi = \frac{6\pi G M_{\text{BH}}}{c^2 a(1-e^2)}, \tag{15}$$

where a is the semi-major axis of the orbit and e its eccentricity. This implies a precession period of (e.g. Eracleous et al. 1995; Storchi-Bergmann et al. 2003)

$$P_{\text{prec}} \sim 3.29 \left(\frac{M_{\text{BH}}}{10^8 M_{\odot}}\right)\left(\frac{r}{100 r_{\text{g}}}\right)^{5/2} \text{yr}, \tag{16}$$

where r is the pericentre distance of the orbit. Fixing P_{prec} to the observed period in the source plane, $P_s = 75$ days, we obtain from Eq. (16) an estimate of the orbit radius of the emitting region in precession:

$$r_{\text{prec}} \sim 27 r_{\text{g}}. \tag{17}$$

Following the argument of Eracleous et al. (1995), the timescale on which an orbit will circularise due to differential precession can be estimated as

$$\tau_{\text{circ}} \sim 2\times10^4 \left(\frac{M_{\text{BH}}}{10^8 M_{\odot}}\right)\left(\frac{r}{100 r_{\text{g}}}\right)^{2}(1+e)\left(\frac{T}{10^5 K}\right)^{-1/2} \text{yr}. \tag{18}$$

If we assume a local temperature of the UV emission region of ~5000 K, the circularisation timescale at r_{prec} is $\tau_{\text{circ}} \sim 2600$ yr. This timescale is to be compared with the local viscous timescale to determine if the disk can remain eccentric for a sufficiently long time. The local viscous timescale is given by (Frank et al. 1992):

$$\tau_{\text{visc}} \sim 3150\,\alpha^{-4/5}\dot{m}^{-3/10}\left(\frac{M_{\text{BH}}}{10^8 M_{\odot}}\right)^{3/2}\left(\frac{r}{100 r_{\text{g}}}\right)^{5/4} \text{yr}, \tag{19}$$

where α is the viscosity parameter as defined by Shakura & Sunyaev (1973), and $\dot{m}$ is the accretion rate in $M_{\odot}\cdot\text{yr}^{-1}$. Assuming a typical value for α of 0.2 and a typical accretion rate of 1 $M_{\odot}\cdot\text{yr}^{-1}$, the viscous timescale of the precessing region can be roughly estimated to $\tau_{\text{visc}} \sim 4500$ yr. The two timescales are comparable, which indicates that the differential precession plays an important role in the circularisation of the disk. As discussed in Eracleous et al. (1995), only the outer part of the disk ($r > 100 r_{\text{g}}$) could maintain a significant eccentricity. This would, however, lead to a much longer precession period, of the order of ~1000 yr, hence impossible to detect. This scenario seems therefore improbable unless the eccentricity has developed recently or is maintained by tidal forces.

We finally propose that a detached disk is in precession; not because of its eccentricity but because it would be subject to Lense & Thirring (1918) differential torques if the disk is not aligned with the black hole spin (Bardeen & Petterson 1975). The disk might break into several rings, which precess at different rates (Nixon & King 2012; Nealon et al. 2015). In this scenario, the orientation of the disk relative to the line of sight might change periodically, hence modulating the luminosity. Alternatively, the detached disk might also shadow periodically the central source. The precession period is given by

$$P_{\text{LT}} = \pi \frac{c^3 a^3 (1-e^2)^{3/2}}{G^2 M_{\text{BH}}^2 \chi}, \tag{20}$$

where χ is the dimensionless black hole spin parameter. Assuming no eccentricity, and black hole spin in the range $\chi = 0.1{-}0.9$, we estimate the radius of the detached ring in the range $8{-}17 r_{\text{g}}$ to match the observed period, assuming that the modulation of the signal occurs at twice the precession frequency. This result is difficult to accommodate with theoretical expectations, which predict that the inner disk ($r \lesssim 100 r_{\text{g}}$) should align rapidly with the black hole spin because of the differential Lense & Thirring (1918) torques (see e.g. Natarajan & Pringle 1998; King et al. 2005; Nixon & King 2012, and references therein). However, recent general-relativistic magnetohydrodynamic simulations by Liska et al. (2021) have shown that the alignment radius might be as small as 5–10 gravitational radii in the case of thin, highly tilted disks around rapidly rotating black holes. Although it cannot be completely excluded, this scenario of an accretion disk in rapid precession would face a second difficulty; if a detached disk is obscuring periodically the central source, it should also leave an imprint in image A, which is not observed. We did not detect any significant power in the Lomb-Scargle periodogram of image A at this frequency. Even in the case of a strong micromagnification gradient across the accretion disk in image B, it is difficult to imagine a configuration where a detached precessing disk would absorb up to 20% of the flux of image B while staying unnoticed in image A.

5. Discussion

Q J0158−4325 has now been monitored in the optical for 15 yr, thus allowing us to obtain a robust measurement of the time delay. Given the time delay, it is now obvious that image B has encountered a high magnification event during the period 2003–2008, with a possible caustic crossing between 2003 and 2006. The quasar has moved away from the caustic and is now de-magnified by microlensing. Over the period 2005–2018, the long-term microlensing trend is typical of a system exiting a micro-caustic and is well reproduced in our simulation (see Fig. 8). It is however not clear why the microlensing amplitude has a maximum in the middle of the season 2003, decreases in 2004 and reaches a second maximum of similar amplitude in 2006. It is possible that this double peak is the signature of double caustic crossing with the quasar entering and exiting the caustic 2 yr apart. However, we could not find any trajectories matching both the long-term trend over the period 2005–2018 and the double peak in 2003 and 2005 for a single disk size. We speculate that a more complex source-size effect plays an important role during the high magnification event between 2003 and 2005, and a simple thin disk model following a rectilinear trajectory through the microlensing magnification pattern is not sufficient to represent our data.

Thus, for the rest of the analysis, we focused only on the Euler data, covering the period 2005–2018, which contain another key feature of the microlensing curve; periodic oscillations of the image flux ratio. These oscillations are detected at a period of 172.6 days during the high magnification event. The amplitude of this signal decreases concomitantly with the microlensing magnification of image B. We note that this period of 172.6 days also matches with the peak observed in the first season in 2003, providing supporting evidence that this peak has the same physical origin as the rest of the oscillations. This feature in the first season of the SMARTS data corroborates the hypothesis that the periodic signal originates from a substructure (possibly a secondary black hole) orbiting the quasar.

The scenario of a binary black hole as the origin of this periodicity is appealing as it naturally explains both the amplitude and period of the signal, whether or not the secondary black hole has its own accretion disk and associated UV emission. Our simple model shows that the motion of the main accretion disk in the source plane around the centre of mass of the system would be sufficient to reproduce the observed signal with a modest mass ratio ($q \lesssim 10$), commonly observed in numerical simulations (e.g. Volonteri et al. 2003, 2009). Similarly, if the secondary black hole has its own light emission and its orbit moves it periodically into higher and lower magnification regions of the microlensing map, only a modest luminosity ratio of ~5 is required to fit our data. Assuming a rough scaling relation $M \propto L^{0.7}$ (Woo & Urry 2002), this leads to a mass ratio of $q \sim 3$, similar to that expected from a companion causing oscillations of the primary disk. These numbers are derived under simplifying assumptions: that the quasar disk is seen face-on and the orbital motion is circular and perpendicular to the line of sight. Including all the orbital degrees of freedom might be necessary to fully explain the shape of the oscillation seen in the microlensing light curve but this is left for future work. We also assumed that the light profile of the quasar follows a simple thin-disk model or a Gaussian profile. Including a more realistic light profile of the interacting accretion disk might also better reproduce the observed data. Finally, there is a possibility that the two black holes have similar UV brightness. We did not fit the mass and luminosity ratios at the same time because these two quantities are degenerate and it did not allow us to obtain meaningful constraints. However, in this scenario, the microlensing light curve is modulated at half the orbital period. This would only change the orbital parameters marginally ($r = 1.6 \times 10^{-3}$ pc) but leave the rest of our conclusions unchanged. This last possibility would qualitatively explain the second harmonic peak at 342 days seen in the periodogram, although it could also be explained by the amplitude of the signal decreasing over time, which would artificially create power at higher harmonics as well.

The main issue of the SMBBH scenario is the short lifetime of these systems, due to the rapid decay of their orbit through GW emission. This problem is in fact far from being insurmountable. Several simulations (Tang et al. 2017; Moody et al. 2019; Muñoz et al. 2019, 2020; Bortolas et al. 2021) have demonstrated that, in some cases, the torques induced by circumbinary disks could counteract the GW-induced torques and slow down the decay of the orbit (see e.g. Sect. 2.2.2.2 of Amaro-Seoane et al. 2022, for a review of this issue). This mechanism could delay significantly the merger of the two black holes, or even cause the two black holes to out-spiral. In this case, close binaries separated by a few hundred r_g to a thousand r_g would be much more common.

Finally, we estimate the characteristic strain and frequency of the GW that could be observed from this system and compare with the sensitivity curves of current and future PTA experiments. For simplicity, we treat the two images separately and ignore interferences although these can be used to break the mass-sheet degeneracy (Cremonese et al. 2021). This is enough to get an order of magnitude of the characteristic strain. The GW frequency, $f_{\rm gw}$, corresponds to twice the observed frequency. We assume the latter to match the orbital frequency, such that $f_{\rm gw} = 2/P_o = 1.34 \times 10^{-7}$ Hz, which falls in the PTA band $[10^{-9}, 10^{-6}]$ Hz. We note that this corresponds to a wavelength of $\lambda_{\rm gw} = 0.072$ pc, which is comparable to the Schwarzschild radius of the lens galaxy, for which wave effects (Çalışkan et al. 2022) and polarisation distortions (Dalang et al. 2022) can be at play[5].

We assume the total mass of the system to be fixed $M_{\rm tot} = M_1 + M_2 = 1.6 \cdot 10^8 M_\odot$ and let the mass ratio $q \equiv M_1/M_2 \in [1, 10]$ such that $M_2(q) = M_{\rm tot}/(1+q)$ and $M_1(q) = q \cdot M_2(q)$. The time evolution of the observed GW frequency for a binary system in quasi-circular orbit that is slowly losing energy to GWs is given by (see e.g. Maggiore 2007)

$$\dot{f}_{\rm gw}(q) = \frac{96}{5}\pi^{8/3}\left(\frac{G\mathcal{M}_z(q)}{c^3}\right)^{5/3} f_{\rm gw}^{11/3}, \tag{21}$$

where the ‘redshifted chirp mass’ is defined as

$$\mathcal{M}_z(q) = (1+z)\frac{[M_1(q)M_2(q)]^{3/5}}{(M_1(q)+M_2(q))^{1/5}}. \tag{22}$$

A PTA experiment is sensitive to a linear combination of the plus and cross polarisations $h(t) = F_+ h_+(t) + F_\times h_\times(t)$, where the factors F_+ and $F_\times$ are combinations of trigonometric functions that depend on the geometry of the pulsar array and satisfy $F_+, F_\times \in [-1, 1]$ (Moore et al. 2015). The two independent and magnified polarisations of a GW emitted by a binary system in quasi-circular orbit, expressed in terms of observed quantities, read (Maggiore 2007; Schneider et al. 1992)

$$h_+(t) = \sqrt{|\mu|}\mathcal{A}_o(q)\left(\frac{1+\cos^2(\iota)}{2}\right)\cos[\Phi(t)] \tag{23}$$

$$h_\times(t) = \sqrt{|\mu|}\mathcal{A}_o(q)\cos\iota\,\sin[\Phi(t)], \tag{24}$$

where $\cos\iota = \hat{\boldsymbol{L}} \cdot \hat{\boldsymbol{n}}$ is the cosine of the angle between the orbital plane $\hat{\boldsymbol{L}}$ and the line of sight $\hat{\boldsymbol{n}}$, μ is the magnification of the considered image, $\Phi(t)$ is the phase of the GW and $\mathcal{A}_o(q)$ is the amplitude of the unlensed GW at the observer, which reads

$$\mathcal{A}_o(q) = \frac{4\left(\frac{G\mathcal{M}_z(q)}{c^2}\right)^{5/3}\left(\frac{\pi f_{\rm gw}}{c}\right)^{2/3}}{D_L(z_s)}. \tag{25}$$

The luminosity distance at redshift $z_s = 1.29$ can be computed using a flat ΛCDM cosmology and we find $D_L(z_s) = 9.3$ Gpc.

---

[5] Since the wavelength is of the order of the Schwarzschild radius of the lens galaxy and therefore much larger than the Schwarzschild radius of the microlens, we do not expect microlensing to affect the GW.

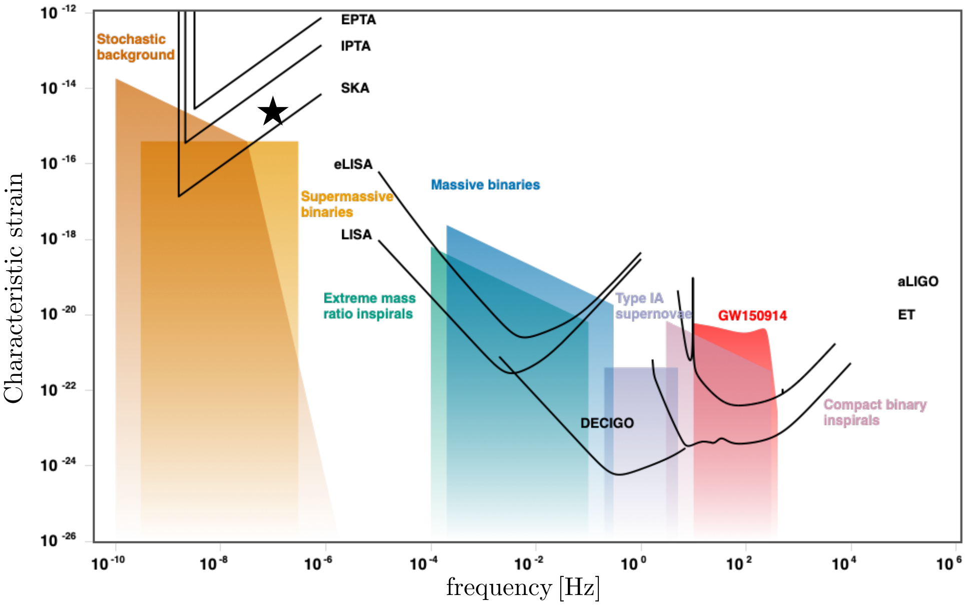

Fig. 12. Adapted from Moore et al. (2015). The approximate characteristic strain of the GW signal is depicted by the star at $f_{\mathrm{gw}} \simeq 1.34 \cdot 10^{-7}$ [Hz], falling in the PTA band $[10^{-9}, 10^{-6}]$ [Hz], and lying above the approximate sensitivity curve of SKA but below that of European PTA (EPTA) and International PTA (IPTA). The detectability with SKA will depend on the exact details of the pulsar array.

The (squared) characteristic strain is defined as (Moore et al. 2015)

$$[h_{\mathrm{c}}(f)]^2 \equiv 4 f^2 \left|\tilde{h}(f)\right|^2 . \tag{26}$$

For a binary in quasi-circular motion, the GW is nearly monochromatic, such that the Fourier transform $\tilde{h}(f)$ of $h(t)$ can be computed using a saddle point approximation (Finn & Thorne 2000; Moore et al. 2015) and we find

$$\tilde{h}(f) = \sqrt{\frac{|\mu|}{\dot{f}}} \frac{\mathcal{A}_{\mathrm{o}}(q)}{2} \left(F_{+} \frac{1+\cos^2(\iota)}{2} + F_{\times} \cos(\iota) \right), \tag{27}$$

where each term inside the brackets belongs to the interval $[-1, 1]$. Therefore, we estimate the characteristic strain at frequency f_{gw} and mass ratio q to be of order

$$h_{\mathrm{c}}(f_{\mathrm{gw}}, q) \sim \sqrt{\frac{f_{\mathrm{gw}}^2 |\mu|}{\dot{f}_{\mathrm{gw}}}} \mathcal{A}_{\mathrm{o}}(q). \tag{28}$$

For image A with lensing macro-magnification $\mu_A = 2.27$, this implies $h_{\mathrm{c}}(f_{\mathrm{o}}, q) \in [1.4{\times}10^{-15}, 2.5{\times}10^{-15}]$ for $q \in [1, 10]$, which is above the approximate sensitivity curve of the Square Kilometre Array (SKA) and below that of the European Pulsar Timing Array (EPTA). Here, we chose a low estimate of the lensing magnification μ_A from the models of Morgan et al. (2008) but the lensing magnification could be up to five times larger if the stellar mass fraction is rather of the order of $f_{\mathrm{M/L}} = 0.3$ instead of 0.9. The exact details of the pulsar array will be needed to estimate if the signal is observable with the SKA. This prevents a more precise conclusion on the detectability of this GW signal. Figure 12 shows how the frequency and the characteristic strain of the signal compare with estimated sensitivity curves of the current and future PTA experiments.

6. Summary and conclusion

We report the first detection of periodic oscillations in the flux ratios of multiple images of a lensed quasar. These oscillations are visible in the microlensing curve of Q J0158−4325 over the period 2003–2010, corresponding to a high magnification event of image B. Their amplitude decreases as image B is less and less magnified by microlensing. We measure from a simple sinusoidal model a period of 172.6 ± 0.9 days in the observer frame, corresponding to 75.4 ± 0.4 days in the quasar rest frame. The same period is detected in each of the Euler and SMARTS microlensing curves as well as in the joint Euler and SMARTS curve. This period is also confirmed by the Lomb-Scargle analysis, with a large peak at 171 days.

From these observations, we have developed several hypotheses to explain the origin of this periodicity. We rank our hypotheses from the most probable to the least probable:

1. Q J0158−4325 hosts a SMBBH: we have demonstrated from a simple model that a binary black hole naturally reproduces both the amplitude and period of the observed signal if the mass ratio is of the order $q \lesssim 10$. Assuming the black hole mass estimate from Peng et al. (2006), we derive a coalescence time due to GW emission of ~1000 yr, extremely short compared to the age of the quasar. However, the transfer of angular momentum from a circumbinary disk to the binary system could significantly increase the lifetime of such close binaries, making them much more likely to be observed.
2. The accretion disk contains a large inhomogeneity: this scenario also fits our observations but it requires one-fifth of the total UV luminosity to be emitted by a compact, hotter region of the disk. If not bound by gravity, this scenario also faces the problem of Keplerian shear, which would disrupt the hotter region of the accretion disk on short timescales. Accretion seems the only plausible mechanism to produce such an amount of UV flux over a sufficiently compact region to be microlensed. If the hotspot in the disk is powered by accretion, then this hypothesis is similar to our first scenario.
3. The accretion disk is in precession: the short period of the signal means that the inner part ($r < 30 r_{\mathrm{g}}$) of the disk must be in precession. In this scenario the disk would be subject to a strong differential precession, leading to a rapid circularisation of the orbit in the case of an eccentric disk, or to a rapid alignment of the accretion disk with the black hole spin, in the case of Lense-Thirring precession.
4. Microlensing by binary stars: this last scenario is ruled out by the small separation between the stars that is imposed by the observed period. A pair of $1\,M_{\odot}$ would need to be

separated by 1.01 AU to produce the observed period. Such small separations in the lens plane only produce an extremely small motion of the micro-caustic in the source plane, making it impossible to reproduce the amplitude of the observed signal.

In the absence of the zoom-in effect produced by microlensing, these oscillations will likely no longer be observed in photometric light curves, but they might reappear if a high magnification microlensing event reoccurs in either of the two images. Over the ten years of the Rubin Observatory's Legacy Survey of Space and Time, it is likely that this system will again approach a microlensing caustic, opening the possibility to trigger spectroscopic follow-up to confirm or rule out different scenarios. Even in the absence of a strong microlensing magnification, a periodic change in the emission lines' profiles might still be detectable.

Finally, the best way to confirm the presence of a SMBBH might very well be the detection of GWs emitted by this source. We show that the mass of this system should be sufficient to be above the noise level of upcoming PTA experiments. This is speculative for the moment, but it might be possible, in the future, to obtain an extremely precise measurement of the time delay from the GW signal, with strong implications for cosmology. This system might be an extraordinary laboratory to test Einstein's theory of general relativity at the crossroad of two of its most famous predictions: the gravitational lensing effect and the propagation of GWs.

Acknowledgements. The authors would like to thank all the Euler observers as well as the technical staff of the Euler Swiss telescope who made the uninterrupted observation over 15 years possible. M.M. warmly thanks Marta Volonteri, Paul Schechter, Lucio Mayer and Georgios Vernardos for useful comments and informative discussions. COSMOGRAIL is supported by the Swiss National Science Foundation (SNSF) and by the European Research Council (ERC) under the European Union's Horizon 2020 research and innovation programme (COSMICLENS: grant agreement No 787886). M.M. acknowledges support by the SNSF through grant P500PT_203114. This project was conceived during the Lensing Odyssey 2021 conference. This research made use of Astropy, a community-developed core Python package for Astronomy (Astropy Collaboration 2013, 2018), the MCMC chain plotting package ChainConsumer (Hinton 2016), and the 2D graphics environment Matplotlib (Hunter 2007).

References

Abbott, T. M. C., Adamów, M., Aguena, M., et al. 2021, ApJS, 255, 20
Amaro-Seoane, P., Andrews, J., Arca Sedda, M., et al. 2022, Liv. Rev. Rel., submitted [arXiv:2203.06016]
Astropy Collaboration (Robitaille, T. P. et al.) 2013, A&A, 558, A33
Astropy Collaboration (Price-Whelan, A. M., et al.) 2018, AJ, 156, 123
Auclair, P., Bacon, D., Baker, T. et al. 2022, arXiv e-prints [arXiv:2204.05434]
Bardeen, J. M., & Petterson, J. A. 1975, ApJ, 195, L65
Begelman, M. C., Blandford, R. D., & Rees, M. J. 1980, Nature, 287, 307
Bhatiani, S., Dai, X., & Guerras, E. 2019, ApJ, 885, 77
Birrer, S., Shajib, A., Gilman, D., et al. 2021, J. Open Source Softw., 6, 3283
Blackburne, J. A., & Kochanek, C. S. 2010, ApJ, 718, 1079
Bogdanović, T., Smith, B. D., Sigurdsson, S., & Eracleous, M. 2008, ApJS, 174, 455
Bogdanović, T., Eracleous, M., & Sigurdsson, S. 2009, ApJ, 697, 288
Boroson, T. A., & Lauer, T. R. 2009, Nature, 458, 53
Bortolas, E., Franchini, A., Bonetti, M., & Sesana, A. 2021, ApJ, 918, L15
Bowen, D. B., Mewes, V., Campanelli, M., et al. 2018, ApJ, 853, L17
Bradbury, J., Frostig, R., Hawkins, P., et al. 2018, JAX: Composable Transformations of Python+NumPy Programs, Version 0.2, 5
Burud, I., Hjorth, J., Courbin, F., et al. 2002, A&A, 391, 481
Çalışkan, M., Ji, L., Cotesta, R., et al. 2022, arXiv e-prints [arXiv:2206.02803]
Charisi, M., Bartos, I., Haiman, Z., et al. 2016, MNRAS, 463, 2145
Chartas, G., Krawczynski, H., Zalesky, L., et al. 2017, ApJ, 837, 26
Chen, Y.-C., Liu, X., Liao, W.-T., et al. 2020, MNRAS, 499, 2245
Chen, Y.-C., Hwang, H.-C., Shen, Y., et al. 2022a, ApJ, 925, 162
Chen, Y. J., Zhai, S., Liu, J. R., et al. 2022b, MNRAS, submitted [arXiv:2206.11497]
Cornachione, M. A., & Morgan, C. W. 2020, ApJ, 895, 93
Cornachione, M. A., Morgan, C. W., Millon, M., et al. 2020, ApJ, 895, 125
Courbin, F., Eigenbrod, A., Vuissoz, C., Meylan, G., & Magain, P. 2005, in IAU Symp., 225, 297
Cremonese, P., Ezquiaga, J. M., & Salzano, V. 2021, Phys. Rev. D, 104, 023503
Cuadra, J., Armitage, P. J., Alexander, R. D., & Begelman, M. C. 2009, MNRAS, 393, 1423
Czesla, S., Schröter, S., Schneider, C. P., et al. 2019, Astrophysics Source Code Library [record ascl:1906.010]
D'Orazio, D. J., Haiman, Z., & MacFadyen, A. 2013, MNRAS, 436, 2997
Dalang, C., Cusin, G., & Lagos, M. 2022, Phys. Rev. D, 105, 024005
Dexter, J., & Agol, E. 2011, ApJ, 727, L24
Dotti, M., Colpi, M., Haardt, F., & Mayer, L. 2007, MNRAS, 379, 956
Dotti, M., Montuori, C., Decarli, R., et al. 2009, MNRAS, 398, L73
Dotti, M., Bonetti, M., Rigamonti, F., et al. 2022, MNRAS, accepted [arXiv:2205.06275]
Eigenbrod, A., Courbin, F., Meylan, G., et al. 2008, A&A, 490, 933
Eracleous, M., Livio, M., Halpern, J. P., & Storchi-Bergmann, T. 1995, ApJ, 438, 610
Eracleous, M., Boroson, T. A., Halpern, J. P., & Liu, J. 2012, ApJS, 201, 23
Erickcek, A. L., Kamionkowski, M., & Benson, A. J. 2006, MNRAS, 371, 1992
Faure, C., Anguita, T., Eigenbrod, A., et al. 2009, A&A, 496, 361
Finn, L. S., & Thorne, K. S. 2000, Phys. Rev. D, 62, 124021
Frank, J., King, A., & Raine, D. 1992, Accretion Power in Astrophysics (Cambridge: Cambridge University Press), 21
Goicoechea, L. J., Artamonov, B. P., Shalyapin, V. N., et al. 2020, A&A, 637, A89
Gould, A., & Miralda-Escudé, J. 1997, ApJ, 483, L13
Graham, M. J., Djorgovski, S. G., Stern, D., et al. 2015, MNRAS, 453, 1562
Gültekin, K., & Miller, J. M. 2012, ApJ, 761, 90
Haehnelt, M. G., & Kauffmann, G. 2002, MNRAS, 336, L61
Hinton, S. R. 2016, J. Open Source Softw., 1, 00045
Hjorth, J., Burud, I., Jaunsen, A. O., et al. 2002, ApJ, 572, L11
Hunter, J. D. 2007, Comput. Sci. Eng., 9, 90
Hutsemékers, D., Sluse, D., & Kumar, P. 2020, A&A, 633, A101
Irwin, M. J., Webster, R. L., Hewett, P. C., Corrigan, R. T., & Jedrzejewski, R. I. 1989, AJ, 98, 1989
Jiang, N., Yang, H., Wang, T., et al. 2022, arXiv e-prints [arXiv:2201.11633]
Kelly, B. C., Bechtold, J., & Siemiginowska, A. 2009, ApJ, 698, 895
King, A. R., Lubow, S. H., Ogilvie, G. I., & Pringle, J. E. 2005, MNRAS, 363, 49
Kochanek, C. S. 2004, ApJ, 605, 58
Lemon, C., Millon, M., Sluse, D., et al. 2022, A&A, 657, A113
Lense, J., & Thirring, H. 1918, Physikalische Z., 19, 156
Liska, M., Hesp, C., Tchekhovskoy, A., et al. 2021, MNRAS, 507, 983
Liu, T., Gezari, S., Burgett, W., et al. 2016, ApJ, 833, 6
Lomb, N. R. 1976, Ap&SS, 39, 447
MacLeod, C. L., Ivezić, Ž., Kochanek, C. S., et al. 2010, ApJ, 721, 1014
Magain, P., Courbin, F., & Sohy, S. 1998, ApJ, 494, 472
Maggiore, M. 2007, in Gravitational Waves. Vol. 1: Theory and Experiments (Oxford: Oxford University Press)
Mejía-Restrepo, J. E., Trakhtenbrot, B., Lira, P., Netzer, H., & Capellupo, D. M. 2016, MNRAS, 460, 187
Merritt, D. 2006, ApJ, 648, 976
Millon, M., Courbin, F., Bonvin, V., et al. 2020a, A&A, 640, A105
Millon, M., Courbin, F., Bonvin, V., et al. 2020b, A&A, 642, A193
Millon, M., Tewes, M., Bonvin, V., Lengen, B., & Courbin, F. 2020c, J. Open Source Softw., 5, 2654
Montuori, C., Dotti, M., Colpi, M., Decarli, R., & Haardt, F. 2011, MNRAS, 412, 26
Moody, M. S. L., Shi, J.-M., & Stone, J. M. 2019, ApJ, 875, 66
Moore, C. J., Cole, R. H., & Berry, C. P. L. 2015, CQG, 32, 015014
Morgan, C. W., Eyler, M. E., Kochanek, C. S., et al. 2008, ApJ, 676, 80
Morgan, C. W., Kochanek, C. S., Morgan, N. D., & Falco, E. E. 2010, ApJ, 712, 1129
Morgan, C. W., Hainline, L. J., Chen, B., et al. 2012, ApJ, 756, 52
Morgan, C. W., Hyer, G. E., Bonvin, V., et al. 2018, ApJ, 869, 106
Morgan, N. D., Dressler, A., Maza, J., Schechter, P. L., & Winn, J. N. 1999, AJ, 118, 1444
Mosquera, A. M., & Kochanek, C. S. 2011, ApJ, 738, 96
Muñoz, D. J., Miranda, R., & Lai, D. 2019, ApJ, 871, 84
Muñoz, D. J., Lai, D., Kratter, K., & Miranda, R. 2020, ApJ, 889, 114
Natarajan, P., & Pringle, J. E. 1998, ApJ, 506, L97
Nealon, R., Price, D. J., & Nixon, C. J. 2015, MNRAS, 448, 1526
Nixon, C. J., & King, A. R. 2012, MNRAS, 421, 1201
O'Neill, S., Kiehlmann, S., Readhead, A. C. S., et al. 2022, ApJ, 926, L35

Paic, E., Vernardos, G., Sluse, D., et al. 2022, A&A, 659, A21
Peng, C. Y., Impey, C. D., Ho, L. C., Barton, E. J., & Rix, H.-W. 2006, ApJ, 640, 114
Peters, P. C. 1964, Phys. Rev., 136, 1224
Peterson, B. M., Ferrarese, L., Gilbert, K. M., et al. 2004, ApJ, 613, 682
Poindexter, S., Morgan, N., Kochanek, C. S., & Falco, E. E. 2007, ApJ, 660, 146
Pooley, D., Blackburne, J. A., Rappaport, S., & Schechter, P. L. 2007, ApJ, 661, 19
Rees, M. J. 1988, Nature, 333, 523
Rodriguez, C., Taylor, G. B., Zavala, R. T., et al. 2006, ApJ, 646, 49
Scargle, J. D. 1982, ApJ, 263, 835
Schechter, P. L., & Wambsganss, J. 2002, ApJ, 580, 685
Schechter, P. L., Udalski, A., Szymański, M., et al. 2003, ApJ, 584, 657
Schild, R. E. 1996, ApJ, 464, 125
Schneider, P., Ehlers, J., & Falco, E. E. 1992, Gravitational Lenses (Berlin-Heidelberg-New York: Springer-Verlag)
Shakura, N. I., & Sunyaev, R. A. 1973, A&A, 24, 337
Shen, Y., & Loeb, A. 2010, ApJ, 725, 249
Sluse, D., & Tewes, M. 2014, A&A, 571, A60
Sluse, D., Hutsemékers, D., Anguita, T., Braibant, L., & Riaud, P. 2015, A&A, 582, A109
Speagle, J. S. 2020, MNRAS, 493, 3132
Storchi-Bergmann, T., Nemmen da Silva, R., Eracleous, M., et al. 2003, ApJ, 598, 956
Strateva, I. V., Strauss, M. A., Hao, L., et al. 2003, AJ, 126, 1720
Tang, S., Silverman, J. D., Ding, X., et al. 2021, ApJ, 922, 83
Tang, Y., MacFadyen, A., & Haiman, Z. 2017, MNRAS, 469, 4258
Tewes, M., Courbin, F., Meylan, G., et al. 2013, A&A, 556, A22
Valtonen, M. J., Lehto, H. J., Nilsson, K., et al. 2008, Nature, 452, 851
Vaughan, S., Uttley, P., Markowitz, A. G., et al. 2016, MNRAS, 461, 3145
Veilleux, S., & Zheng, W. 1991, ApJ, 377, 89
Vernardos, G., Fluke, C. J., Bate, N. F., & Croton, D. 2014, ApJS, 211, 16
Volonteri, M., Haardt, F., & Madau, P. 2003, ApJ, 582, 559
Volonteri, M., Miller, J. M., & Dotti, M. 2009, ApJ, 703, L86
Woo, J.-H., & Urry, C. M. 2002, ApJ, 579, 530
Wyithe, J. S. B., & Loeb, A. 2002, ApJ, 577, 615
Yan, C.-S., Lu, Y., Yu, Q., Mao, S., & Wambsganss, J. 2014, ApJ, 784, 100
Zechmeister, M., & Kürster, M. 2009, A&A, 496, 577
Zu, Y., Kochanek, C. S., Kozlowski, S., & Udalski, A. 2013, ApJ, 765, 106

Appendix A: Reverberated signal in the microlensing curve

Sluse & Tewes (2014) have suggested that, in the presence of microlensing, a deformed imprint of the intrinsic variability signal could appear in the difference light curve of a pair of lensed images because emission arising from differently microlensed regions are mixed in a given observing filter. The two main sources of differentially microlensed emission present in the R band are the power-law continuum emission, and the emission arising from the broad emission lines. The continuum emission region is smaller than a microlens Einstein radius, and is therefore most prone to microlensing, while the emission from the broad line is much less microlensed. As explained in Paic et al. (2022), the spectra of Q J0158−4325 observed by Faure et al. (2009) indicate that ∼ 40% of the R−band flux arises from the BLR (Fig. A.1). Based on this estimate of the fraction of non-microlensed flux in the R band, we generated mock light curves of the lensed images and evaluated the amplitude of the flickering introduced by the above effect. Following Paic et al. (2022), we emulated the continuum signal F_c using a DRW model (Kelly et al. 2009; MacLeod et al. 2010), and added to it a reverberated BLR signal responding to the intrinsic variations with a lag of $\tau = 65$ days through a top-hat transfer function $\Psi(t, \tau)$. Following this procedure, the flux of image i (i.e. A or B), already corrected from the cosmological time delay, can be written as

$$F_i(t) = M_i \mu_i(t) F_c(t) + M_i f_{BLR} [\psi(t, \tau) * F_c(t)], \tag{A.1}$$

where M_i is the absolute value of the macro-magnification of the image, $\mu_i(t)$ the time variable microlensing magnification and f_{BLR} is the fraction of reverberated flux. We consider a constant microlensing amplification of image B fixed to the maximal micro-magnification observed in 2005 (i.e. $\mu_B(t) = 2$), and we assume that A is unaffected by microlensing by fixing $\mu_A(t) = 1$. We also fix the non-microlensed flux ratio to the macro model prediction, $M_B/M_A = 0.44$. We use this physically motivated model to generate 5000 microlensing curves from different DRW realisations, with the same sampling and the same photometric noise as the real data. The mean flux level of $F_c(t)$ is arbitrarily fixed to 100 and the DRW timescale parameter, $\tau_{\rm DRW} = 817$ days, is obtained by fitting the light curve of image A with JAVELIN (Zu et al. 2013). The amplitude of the DRW, $\sigma_{\rm DRW} = 20$ (in flux units), is adjusted so that the variations of the total (i.e. reverberated + continuum) flux in image A matches the observed variations. An example of light curves generated from this model is shown in Fig. A.2.

First, we find a maximum peak to peak amplitude of the flickering of, at most, 0.10 mag. This corresponds to half of the observed amplitude of the observed periodic signal. We note that the detailed structure of the BLR signal does not matter much. For instance, a similar signal is observed if we assume a constant BLR contribution with time. The scattered emission from the continuum (e.g. Sluse et al. 2015; Hutsemékers et al. 2020), would produce a similar effect as long as it arises from a region large enough to remain non microlensed. This simulation shows that, even under conservative assumptions, the signal arising from a larger region than the continuum, may produce red-noise with too low amplitude to mimic the observed signal.

Second, we compute the GLS periodogram over a frequency range $[20^{-1} - 1000^{-1}]$ days^{-1} for each of the simulated light curves and compare the power of the highest peak in the periodogram with that of the observed data. Here, we restrict our analysis over the period 2005-2011, where the periodic signal is clearly seen in the data. The results of this test are shown on Fig. A.3.

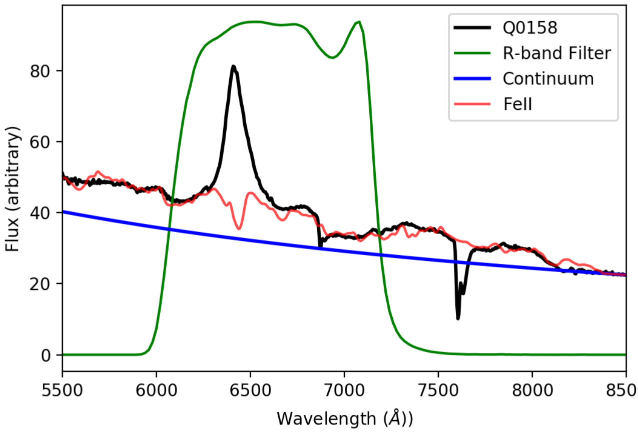

Fig. A.1. Spectrum of image A of Q J0158−4325 (black). The blue and red curve correspond to the best fitted model of continuum and Fe II emission. The green curve shows the transmission curve of the Euler R−band filter.

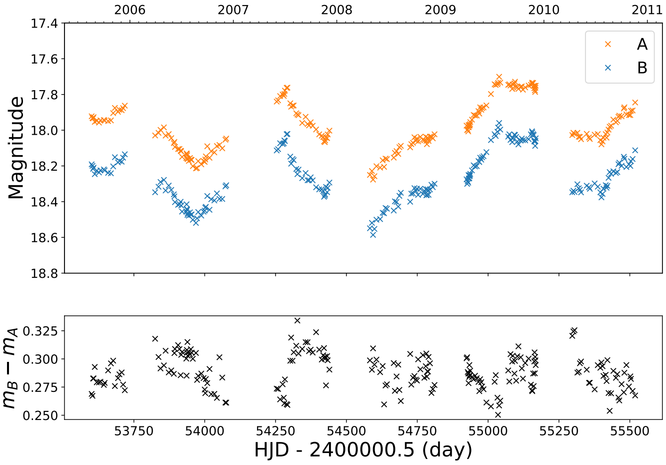

Fig. A.2. Simulated light curves generated from a DRW realisation, including the echoed signal of the BLR (top panel) and difference light curve between image B and image A (bottom panel).

As discussed in O'Neill et al. (2022), peaks at any frequencies should be considered since we have no a priori reason to select the particular frequency observed in the real data. We thus conclude from these simulations that a spurious detection of the periodicity due to the intrinsic variability of the quasar echoed in the microlensing curve is rejected at 99.4% confidence level (3.7σ).

Finally, we test alternative micro and macro-magnification models, selected to match approximately the minimum magnitude difference between image A and image B, $m_B - m_a \sim$ 0.3mag, as observed in 2005. These models are rejected with a significance ranging from 1.9 to 6σ as summarised in Table A.1. We also consider different sizes of the BLR by varying the lag τ from 35 to 130 days. Although the model with a longer lag can only be excluded at 1.2σ when all light curves are considered, this model cannot explain the short observed period as none of the simulated curves with a highest peak period below 200 days have more power at these frequencies than the observed data. Considering only the curves with a highest peak period within the range 165–175 days, this model is excluded at 7.2σ.

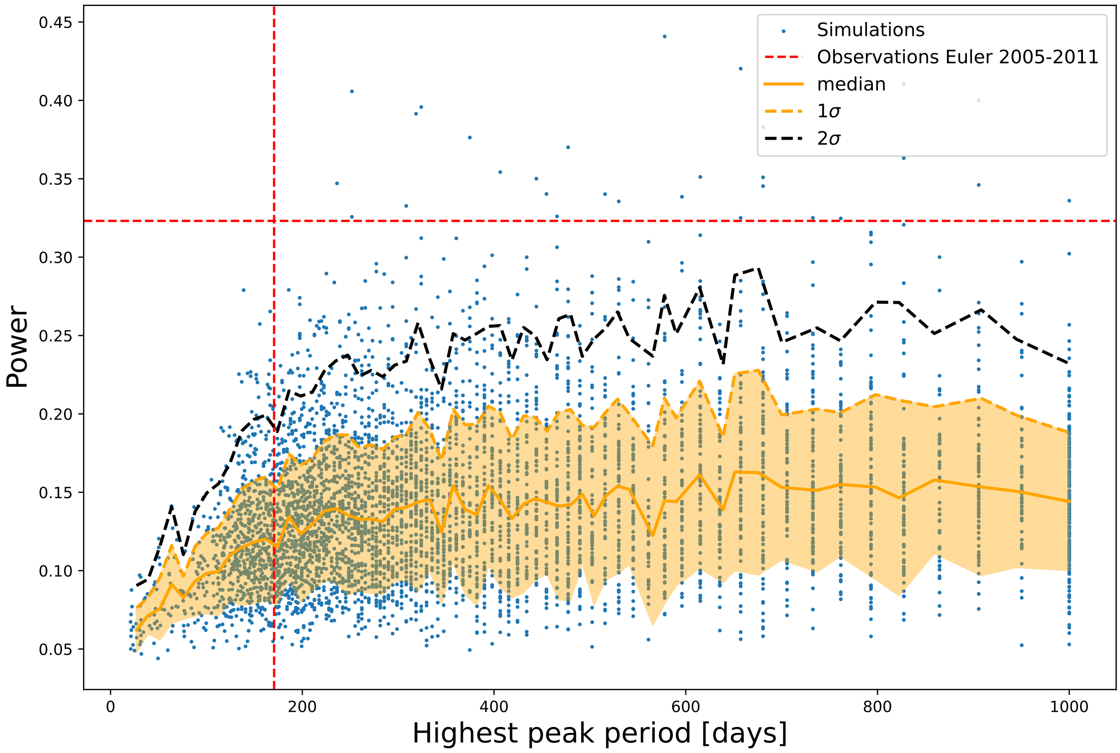

Fig. A.3. Power of the highest peak in the GLS periodogram as a function of the peak period for 5000 simulated microlensing curves. The highest peak power and the period observed in the Euler data over the period 2005-2011 are indicated as dashed red lines. The 1σ (dashed orange line) and 2σ level (dashed black line) are computed in 80 different period bins of width 18.5 days.

Table A.1. Rejection significance, $\sigma_{\rm r}$, for alternative magnification and reverberation models. Model parameters, f_{BLR}, τ, M_A, M_B, μ_A, and μ_B, are defined in Appendix A. They are selected to match approximately the minimal magnitude difference, $m_B - m_A$, observed in 2005. The last column detail the rejection significance $\sigma_{\rm r,165-175}$ when considering only the simulated light curves with highest peak period within the range 165-175 days.

Model	f_{BLR}	τ [days]	M_A	M_B	μ_A	μ_B	$m_B - m_A$ [mag]	$\sigma_{\rm r}$	$\sigma_{\rm r,165-175}$
fiducial	0.4	65	2.26	1.01	1.0	2.0	0.29	3.7σ	5.2σ
alternative micro-model	0.4	65	2.26	1.01	0.5	1.1	0.32	2.4σ	3.3σ
alternative micro-model	0.4	65	2.26	1.01	1.5	2.8	0.34	6.0σ	8.0σ
alternative macro-model	0.4	65	5.00	1.01	1.0	4.8	0.31	1.9σ	2.7σ
alternative reverberation model	0.4	130	2.26	1.01	1.0	2.0	0.29	1.2σ	7.2σ
alternative reverberation model	0.4	35	2.26	1.01	1.0	2.0	0.29	8.6σ	8.0σ

2.4 Forecast of microlensing events in the incoming wide field monitoring surveys.

As discussed in Section 2.1, microlensing light curves give valuable constraints on the mass distribution of stars in the lensing galaxy and the size of the quasar accretion disk. In addition, the original works presented in this thesis show that it is possible also to measure the size of the Broad Line Region and detect SMBBH. Increased sampling of the parts of the light curve where a microlensing event is happening, as well as follow-up observations such as X-ray, UV or multiple optical waveband, would significantly improve the constraints obtained. These supplementary data are even more crucial at the peak of the microlensing event where, as shown by Fig. 2.6, the light curve is the most impacted by the shape of the source and by the physics of the accretion disk (e.g., Vernardos & Tsagkatakis 2019; Best et al. 2022). The probability of observing microlensing events in a given system depends on its stellar convergence κ_*. So far, in the most furnished microlensing light curves data set released by COSMOGRAIL (~ 30 decade-long microlensing light curves Millon et al. 2020b), only three microlensing light curves display microlensing events with a magnitude higher than 1 mag.

The advent of wide-field monitoring surveys such as the Rubin-LSST will multiply this sample 10-fold as it will simultaneously monitor hundreds to thousands of strongly lensed quasars (as forecasted by Oguri & Marshall 2010) in six wavebands (*ugrizy*) covering the optical spectrum from 320 nm to 1080 nm. According to Neira et al. (in prep.), 10 to 20% of these quasars should undergo microlensing events of more than $1 mag$ within the first ten years of the survey. Depending on the observing strategy chosen, the cadence of each band can go from 3 days in the most accessible r and g band to 15 days in the u band. Even though the science cases previously mentioned necessitate a daily cadence, these light curves still allow us to detect the characteristic steady rise of a microlensing event occurring years before the peak as displayed in Fig. 2.7. Moreover, the fact that the apparent size of the disk is smaller in blue bands than in red bands makes the corresponding light curves consistently intercept before the peak of an event, as shown in Fig. 2.10, which gives a constraint on the time at which a peak is reached given the size of the source R_S and its effective velocity $\mathbf{v}_e$. While the first can be roughly estimated based on the flux and strong assumptions on the accretion disk light profile, the latter can be constrained statistically but not measured independently for every light curve. Therefore, this project aims to create a neural network able to predict if a microlensing event will reach a peak in the near future using the multiband microlensing light curves of LSST. This tool will be crucial to optimize follow-up observation of such events.

I lead this project with Favio Neira, Joshua Fagin and Henri Best. Together with FN, we created a realistic training set of microlensing light curves corresponding to the Rubin-LSST observing characteristics, including non-microlensing phenomena that alter their shape and smoothness. JF and HB elaborated a Recurrent Neural Network architecture to predict based on a 1000-day part of a light curve if a microlensing event peak was reached within the next 150 days.

2.4.1 Training set

As described in Section 2.1.2, the microlensing properties of a system are set by the mass model of the lens (κ, γ, κ_*, IMF), the light profile of the source (R_S) and the effective velocity of the microlenses $\mathbf{v}_e$. For the aim of this project, we generate a microlensing light curve using the parameters of three pairs of images in systems knowingly prone to microlensing events based on previous studies and their COSMOGRAIL light curves: images B and C of Q2237+030 (the "Einstein cross" Anguita et al. 2008), images C and D of RXJ1131−1231 (Sluse et al. 2007) and images A and C of HE0435−1223 (Millon et al. 2020b). The

Parameter	Q2237+030	RXJ1131−1231	HE0435−1223
z_l	0.034	0.52	0.454
z_s	1.695	0.658	1.693
$[\kappa_1,\kappa_2]$	[0.38, 0.73]	[0.44, 0.95]	[0.45, 0.44]
$[\gamma_1,\gamma_2]$	[0.39, 0.72]	[0.46,1.02]	[0.38, 0.40]
$[\mathcal{M}_1,\mathcal{M}_2]$	[4.3, 2.2]	[16.7, 0.97]	[6.2,6.5]
R_S $^r[10^{14}$cm]	10.4	2.1	93.1

Table 2.1: Physical parameters used to generate the microlensing light curves. The mass parameter are taken respectively from Pooley et al. (2012), Chen et al. (2019) and Wong et al. (2017). We use the size of the accretion disk measured in r-band by Mosquera & Kochanek (2011).

physical parameters are shown in Table 2.1. Because of the differences in microlensing properties, the events are not equally discernable in each image pair. For example, the HE0435 has a larger source; hence, consecutive microlensing events are more likely to blend than in other systems. To minimize the blending of events, we compute κ_* in each image, assuming that $\kappa_*/\kappa = 0.1$. Using the magnification maps with appropriate κ, γ and κ_*, and Salpeter IMF from the `GERLUMPH` database (Vernardos & Fluke 2014), we apply the tool presented in Neira et al. (2020) to generate simulated multi-waveband microlensing light curves of these systems. Assuming that the accretion disk follows the thin disk model presented in Section 1.2, we compute the apparent size of the disk in the *ugrizy* LSST wave bands using Eq. 1.31. We refer to Section 3.3 of Neira et al. (2020) for the derivation of the model, set by the redshift and sky coordinates of the system, from which $\mathbf{v}_e$ is drawn.

We have generated 10 000 light curves for each pair of images in the six photometric bands of the LSST; an example is shown in Fig. 2.10.

These light curves are then subtracted by pair to match real observation conditions.

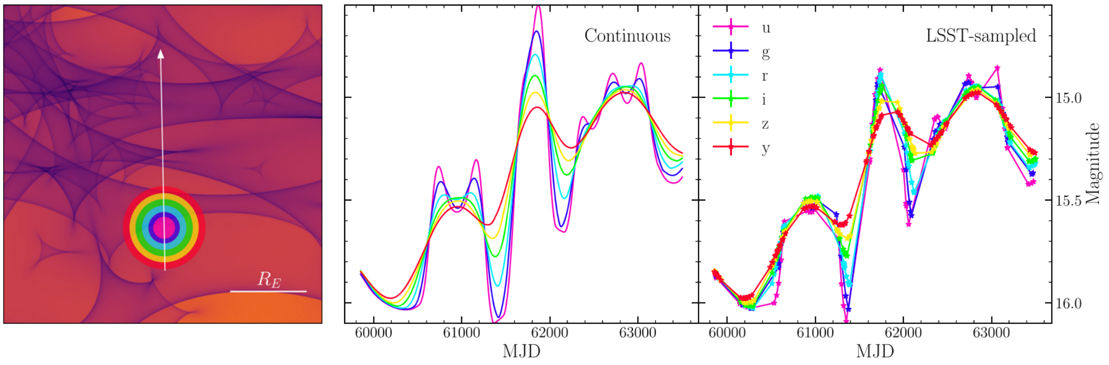

Figure 2.10: Example of a microlensing light curve generated for image A of Q2237. ***Left panel:*** Part of the magnification map and trajectory of the source used. Dedicated colours highlight the apparent size of the source in each band. ***Middle panel:*** Light curve continuously sampled. ***Right panel:*** Light curve as sampled by Rubin-LSST. We note that no photometric noise was added in this simulation. Adapted from Neira et al. (2020)

In addition, we identify the micro magnification events by computing the inflexion points in the light curve. If two consecutive inflexion points are separated by more than 0.3 mag, we mark the enclosed maximum as the position of the microlensing event's peak. We then set the label curve of any simulated microlensing light curve as a time series with the same length as the light curve, which is equal to 1 if the center of the

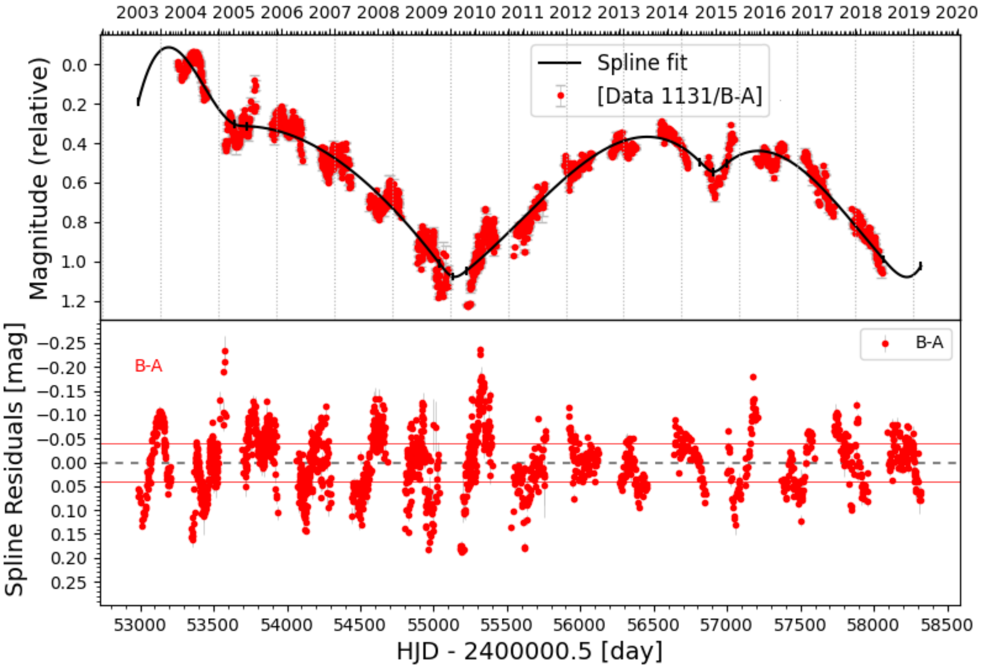

Figure 2.11: ***Top panel:*** : COSMOGRAIL r band microlensing light curve RXJ 1131−1231 over a period of 18 years computed by subtracting B from A after shifting it by the time delay Δt_{AB}= 2.8 days (Millon et al. 2020b). A spline fit is done with η = 300 days. ***Bottom panel:*** : Residuals of the spline fits to the microlensing light curve. The correlated noise present in the light curve appears clearly.

source is within range of the peak position in the u-band and 0 on the contrary case.

Red noise generation As demonstrated in Section 2.2, the reverberation of the continuum by the BLR with a time lag induces an echo of the intrinsic variability within the observed light curve. If a broad emission line falls in the observed waveband and the microlensing is not identical in both images, this echo will appear in the microlensing light curve. The frequency and amplitude of this imprint are characterized by the BLR's size and the continuum's stochastic variability. Additionally, the variability of the light curve can be affected by observational effects such as the seasonal change of airmass and contamination by the lensed arc or the lensing galaxy when measuring the photometry of the images. Since these effects all require precise knowledge about the physical properties of the lens system, we choose to assimilate the combination of those to red noise that is added to the immaculate microlensing light curve.

We quantify this physically agnostic red noise on each system's observed COSMOGRAIL light curves to add statistically similar realizations to LSST-like light curves.

We present the method applied to the RXJ1131 microlensing light curve. As shown by Fig. 2.11, the microlensing light curve is first fitted with a free-knot spline using the PyCS package (see Millon et al. 2020b, for details of the implementation). These piece-wise polynomials allow for a smooth fit of a targeted time scale of variation by constraining the distance η between two consecutive knots.

Since microlensing events are supposed to occur on times scales longer than several years (e.g. Mosquera

& Kochanek 2011), we choose η = 300 days to prevent the spline from fitting intra-season features while recovering the microlensing variations, the fit obtained is displayed in the top panel of Fig. 2.11. The residuals, which we consider as the observed correlated noise, are shown on the lower panel. As shown in Fig. 2.12, the data's power spectrum and the spline fit are identical for frequencies below $1/200$ days^{-1}, which sets the boundary between high and low frequencies. At higher frequencies, the power spectrum of the data is identical to the residual one. The change in slope of the power spectrum of the residual above $1/10$ days^{-1} is likely due to the power spectrum reaching the sampling limit of the light curve (3 to 10 days between 2 points). We aim to generate time series with the same power spectrum as the residuals to add it to the simulated microlensing light curves. We use the red noise generator implemented in `PyCS` to fit the slope β and amplitude σ of the residuals' power spectrum. The addition of a generated red noise to the spline fit is shown in the left panel of Fig. 2.12 and has a power spectrum compatible with original data in the high-frequency range. As shown in the right panel of Fig. 2.12, the same parameters are then used to add red noise to the simulated microlensing light curve in every band.

Dependance of the red noise on the band As stated previously, the presence of red noise and its characteristics depend on the observed band. In this work, the evaluation of the red noise relies on RG-band (equivalent to LSST's *r*-band) data, which represents the longest part of the monitoring. The analysis of the spectrum of the quasar (Fig 2 of Sluse et al. 2003) reveals that the BLR contribution BLR should be heavier in the bluer *u* and *g* bands dominated by the Mg II emission while it should be similar in the *i*, *z* and *y* bands. Moreover, the contribution of the lensed arc (i.e the host galaxy) as well as the lensing galaxy should differ for each band. However, as we are limited by the available data, we use the same noise parameters for each band. We expect that since the *r* and *i* bands have a higher cadence than the blue bands, this assumption does not significantly hinder the subsequent machine learning predictions made.

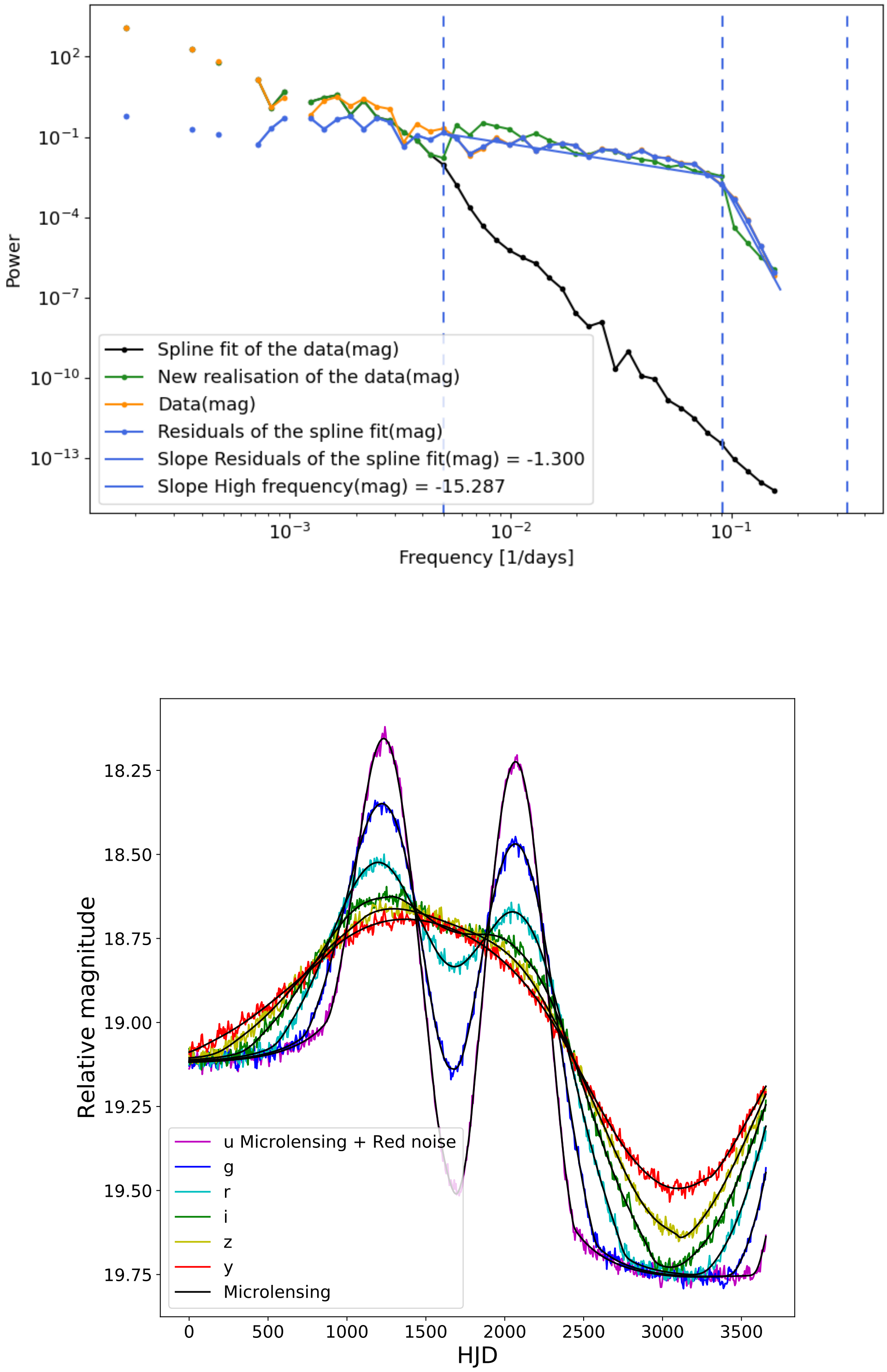

Figure 2.12: ***Left panel:*** Power spectrum fitting of the data. Vertical dashed lines at $1/200$ days^{-1} and $1/10$ days^{-1} delimit the frequency range on which the red noise is added. Adding residual-like noise to the spline fit creates a new realization of the data with the same power spectrum. ***Right panel:*** When adding noise with the same power spectrum as the residuals of the left panel to a simulated microlensing light curve, we obtain realistic light curves for each wave band.

2.4.2 Machine learning algorithm

The first application of machine learning to microlensed quasar light curves was conducted by Vernardos & Tsagkatakis (2019) to assess accretion disk structure. They employed a one-dimensional convolutional neural network (CNN) to categorize accretion disk size and wavelength power law. In this study, we employ a recurrent neural network (RNN) for binary classification to detect caustic crossings. Contrary to Vernardos & Tsagkatakis (2019), we use an RNN due to the presence of season gaps in our light curves, a limitation that a standard CNN cannot address. Our network is trained on a 1000-days subset of the overall light curve. Specifically, it predicts microlensing events within a 150-day window around the last time step in the light curve subset. The normalization process involves subtracting the minimum value across all bands at the first time step. As caustic crossings are infrequent in light curves, we balance the training set by focusing on subsections with positive labels. From a pool of 500,000 light curves, we extract 2,500,000 subsections, of which approximately 20% hold positive labels while 80% are marked negative.

The architecture of the RNN is depicted in Table 2.2. The RNN's input encompasses the relative brightness at each time step, covering all six LSST-like bands. The neural network's design commences with a masking layer to emulate the actual LSST sampling of a given light curve, which is affected by weather conditions and season gaps. Subsequently, two layers of gated recurrent units (GRU; Chung et al. 2014) are employed, which are a type of recurrent neural network layer akin to long short-term memory layers(LSTM; Hochreiter & Schmidhuber 1997). Each GRU layer comprises 128 units and operates with a hyperbolic tangent (tanh) activation function.

The GRU layers are known for their capability to retain memory over long sequences and are hence crucial for modelling the temporal patterns and dependencies present in microlensing light curves.

Following each GRU layer, a dropout layer with a 10% dropout rate is applied. Dropout is a regularization technique that randomly sets a fraction of the input units to zero during training, helping to prevent overfitting and improving the network's generalization ability.

The network continues with batch normalization (Ioffe & Szegedy 2015) and two fully-connected layers, each consisting of 128 units. A 10% dropout layer, ReLU activation function (Nair & Hinton 2010), and batch normalization are applied before each fully-connected layer. Batch normalization helps stabilize and accelerate the training process by normalizing the activations of the previous layer.

At each time step, the network outputs both is the probability of a microlensing event being observed and not being observed in the next 150 days and using a soft-max activation to ensure that the two outputs represent the probabilities summing up to 1.

The network is trained using a binary cross-entropy loss function given by:

$$\mathcal{L}(y, \hat{y}) = -\frac{1}{N} \sum_{\mathrm{i}=1}^{N} y_{\mathrm{i}} \log(\hat{y}) + (1 - y_{\mathrm{i}}) \log(1 - \hat{y}_{\mathrm{i}}), \tag{2.16}$$

where y_{i} is the training label, $\hat{y}_i$ is the prediction of the network, and N is the number of training examples. We minimize the loss function using an Adam optimizer (Kingma & Ba 2014) with a batch size of 1,024 and a learning rate of 0.001. We train the network for 20 epochs, i.e., the number of times the network processed the whole training set. The evolution of Loss and accuracy with epoch displayed in Fig. 2.13 shows that more epochs would be required for the network to converge, but the overall accuracy is good.

Table 2.2: Architecture of the RNN.

Type	Output shape	Number of Trainable parameters
Input	(142,6)	-
Masking	(142,6)	-
GRU	(142,128)	52224
tanh	(142,128)	-
Dropout	(142,128)	-
GRU	128	99072
tanh	128	-
Dropout	128	-
Batch Norm	128	-
Fully Connected	128	16512
Batch Norm	128	-
ReLU	128	-
Dropout	128	-
Fully Connected	128	16512
Batch Norm	128	-
ReLU	128	-
Dropout	128	-
Fully Connected	2	258
Soft-max	2	-
Total		185,346

However, we should recall that positive and negative labels are not represented equally, hence a constant negative prediction would already be 80% accurate.

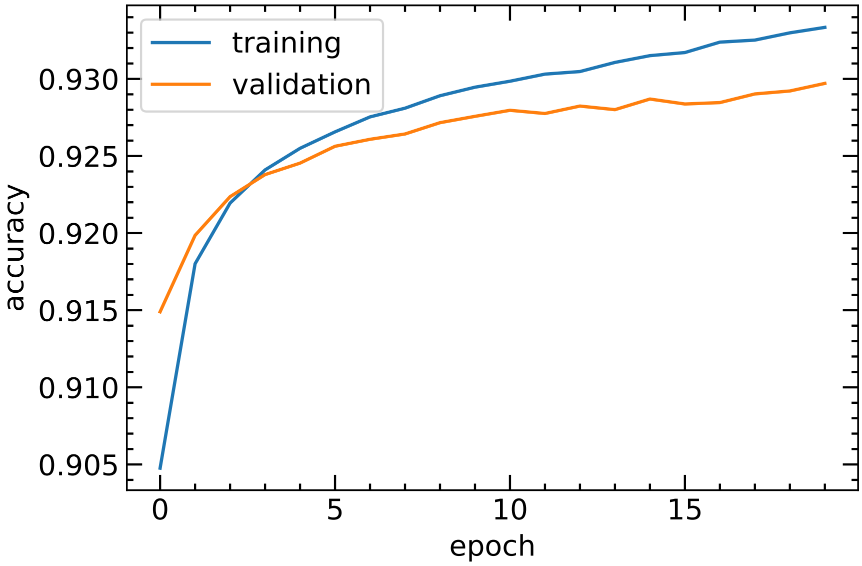

Figure 2.13: Loss and accuracy of the RNN as a function of epoch. Those are evaluated both on the training set and the validation set unknown to the network during the training. Figure credits: Josh Fagin

Application to light curves

We introduce a three-stage triggering mechanism to facilitate swift follow-up actions upon microlensing event forecasts. To establish a positive prediction, we assess whether the mean prediction value minus two times the standard deviation of its uncertainty surpasses the 0.5 threshold. These triggers are colour-coded in order of escalating alert levels: green, yellow, and red.

As shown in Fig. 2.14, the green alert is activated upon any positive prediction from the network. Subsequently, the yellow alert is engaged if a green alert persists consecutively for 50 days. The red alert is initiated when a yellow alert lasts 50 consecutive days. This tiered structure ensures a cautious approach to minimize false positive predictions, especially in scenarios where the uncertainty is notably high. Continuous positive predictions across multiple weeks are vital to maintain the validity of alerts and avoid unnecessary alerts triggered by temporary fluctuations.

We hence get an alternate metric of the network by counting an event as correctly predicted if the red trigger is activated within the label. This metric shows that 55% of the events and 98% of non-events are correctly predicted while 2% of false positives are reported and 45% of th events are missed.

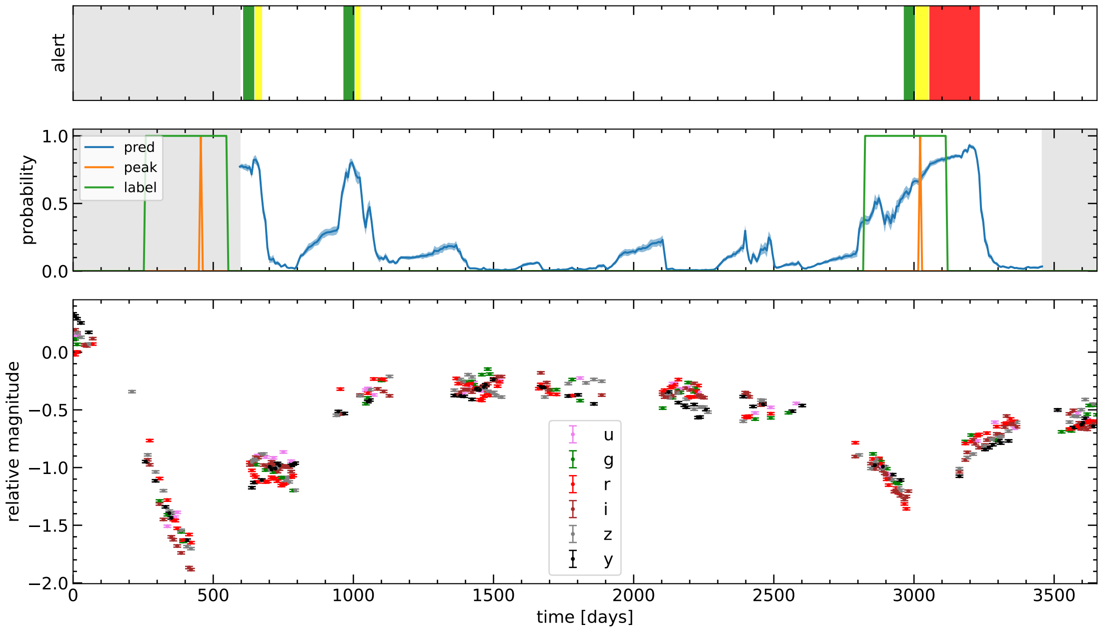

Figure 2.14: Example prediction with three staged triggering systems on a realistic LSST-like microlensing light curve. ***Top panel:*** Activated trigger as a function of time. ***Middle panel:*** Predicted probability as a function of time, the first 600 days are shaded because the preceding light curve is too short for the network to predict. The "peak" curve highlights the position of the microlensing event maximum in the input light curve. ***Bottom panel:*** Input 6 waveband microlensing light curve. Figure credits: Josh Fagin

Additionnal tests

The network's performance is primarily influenced by the hyperparameters used in constructing the training set. For example, the threshold employed to classify a magnitude difference between successive inflexion points as an event determines the training set's completeness. We adopt a threshold of 0.3 mag, excluding events where correlated noise could overshadow the microlensing event and lead to false positives. We will also explore the impact of higher thresholds on the accuracy metrics.

The selection of image pairs aimed to create a versatile training set encompassing a broad spectrum of source sizes, lens convergence, and microlens velocity. This strategy ensures the network's adaptability, which we will test by facing it with unfamiliar systems' light curves.

The trigger threshold of 0.5 was set to limit the False positive rate and maximize the True positive rate. We will investigate how increasing this threshold can focus the prediction on only the highest microlensing peak which are the most physically interesting. This adjustment is unlikely to increase the false positive rate but it will surely decrease the completeness of the prediction.

Although the network might not surpass expert visual inspection in terms of performance, the high rate of True negative prediction demonstrates the network's robustness to noise. It will help to significantly reduce the number of microlensing event candidates necessitating visual examination before triggering follow-up observations.

2.5 Summary

This chapter showcases advanced techniques for studying quasar structures. After reviewing conventional approaches to assess accretion disk size through reverberation mapping and microlensing light curves, we introduce two innovative methods to extract insights from microlensing light curves.

In Paic et al. (2022), we detect for the first time that high-frequency fluctuations in microlensing light curves can arise from accretion disk light reverberation within the Broad Line Region, an aspect often overlooked by standard time-domain fitting techniques (Kochanek 2004). Instead, we match data to simulated light curves using power spectra in the frequency domain, recovering the overall light curve behaviour. We apply this to QJ 0158−4325's microlensing light curve, accurately measuring R_{BLR}, the BLR size. Additionally, we highlight that previous microlensing measurements likely skew towards high values incompatible with the thin-disk model due to neglecting these high-frequency traits.

In Millon et al. (2023), we scrutinize the 2006-2012 segment of the same microlensing light curve, attributing visible periodic oscillations to a Super Massive Binary Black Hole. This hypothesis awaits confirmation from independent observations such as spectroscopic monitoring, potentially revealing periodic Doppler shifting of emission lines. Eventually, the upcoming Pulsar Timing array with the Square Kilometer Array will be sensitive enough to detect the gravitational waves of this SMBBH. If confirmed, this discovery would give unprecedented insights into how SMBBH systems can quickly reach the third stage of their evolution. Moreover, it also could mean that the models underestimate the coalescence time of such systems, and unknown mechanisms are at play.

Both methods will find extensive application with Rubin-LSST's abundance of microlensing light curves, potentially unveiling BLR reverberation or periodic oscillations. These approaches will span various quasar luminosities and redshifts, thoroughly investigating the luminosity-R_{BLR} relation and Super Massive Binary Black Hole populations.

During microlensing events, these phenomena and features of the source light profile become more visible, especially when the micro magnification reaches its maximum. To improve our understanding of these events, I have led the development of a neural network that can identify lensed quasar images that are likely to undergo microlensing and forecast the time at which the micromagnification peaks. This tool uses multi-waveband light curves from Rubin-LSST and will aid in optimized follow-up observations, allowing for better extraction of physical constraints and a deeper understanding of the underlying processes.

3 Time Delay Cosmography

3.1 Overview of the technique

3.1.1 A long list of ingredients

The determination of H_0 using the time delay Δt_{AB}observable between two images A and B of a strong lens system was first suggested by Refsdal (1964) and further developed by Schneider et al. (1992).

It relies on the measurement of the time delay distance $D_{\Delta t} \propto H_0^{-1}$ which, as presented in Section 1.3, can be measured using Δt_{AB}, the redshifts of the source and the lens and the lens potential materialized by the Fermat potential difference $\Delta\phi$.

As pointed out by Falco et al. (1985), the observables of a strong lensing system, such as the image positions, are invariant under the mass-sheet transform (MST). This transformation of the convergence $\kappa(\theta)$ and the source plane coordinates β can be written as:

$$\kappa_\lambda(\theta) = \lambda\kappa(\theta) + 1 - \lambda, \tag{3.1}$$

$$\beta_\lambda = \lambda\beta. \tag{3.2}$$

This mass-sheet degeneracy (MSD), however, impacts the Fermat potential difference and time delay:

$$\Delta\phi_{\mathrm{AB},\lambda} = \lambda\phi_{\mathrm{AB}}, \tag{3.3}$$

$$\Delta t_{\mathrm{AB},\lambda} = \lambda\Delta t_{\mathrm{AB}}, \tag{3.4}$$

$$\tag{3.5}$$

which in turn impacts the inference of $D_{\Delta t}$and H_0:

$$D_{\Delta t,\lambda} = \lambda^{-1} D_{\Delta t}, \tag{3.6}$$

$$H_{0,\lambda} = \lambda H_0, \tag{3.7}$$

In practice, there are two main components to the mass sheet in a lensing system: 1- the mass of the deflectors along the line of sight (LOS) other than the main lens treated as equivalent to a mass sheet with a density κ_{ext} at the position of the lens and 2- the change of the shape of the lens mass profile referred as internal mass sheet which affects the radial profile of the convergence materialized by the $\lambda_{\rm int}$. The MST λ parameter can therefore be expressed as

$$\lambda = (1 - \kappa_{\rm ext})\lambda_{\rm int}. \tag{3.8}$$

As introduced by Birrer et al. (2020), the relation between the angular diameter distance along specific line-of-sights affected by LOS structures ($D_{\rm lensed}$) and the corresponding unperturbed background angular diameter distances ($D_{\rm bkg}$) can be expressed using convergence terms as follows:

$$D^{\ell}_{\rm lensed} = (1 - \kappa_{\rm d})D^{\ell}_{\rm bkg}, \tag{3.9}$$

$$D^{\rm s}_{\rm lensed} = (1 - \kappa_{\rm s})D^{\rm s}_{\rm bkg}, \tag{3.10}$$

$$D^{\ell{\rm s}}_{\rm lensed} = (1 - \kappa_{\rm ds})D^{\ell{\rm s}}_{\rm bkg} \tag{3.11}$$

Here, κ_{ℓ}, $\kappa_{\rm s}$, and $\kappa_{\ell{\rm s}}$ represent the external convergence terms for the specific line-of-sight distances.

From which we can express the total external convergence as:

$$1 - \kappa_{\rm ext} = \frac{(1 - \kappa_{\ell})(1 - \kappa_{\rm s})}{1 - \kappa_{\ell{\rm s}}}. \tag{3.12}$$

Therefore, we can generalize the computation of the time delay given in Eq. 1.60 as:

$$\Delta t_{\rm AB} = (1 - \kappa_{\rm ext})\lambda_{\rm int}\frac{D_{\Delta t}}{c}\Delta\phi_{\rm AB}, \tag{3.13}$$

and the modelled time delay distance $D_{\Delta t}$' is then corrected, giving the final:

$$D_{\Delta t} = \frac{D_{\Delta t}'}{1 - \kappa_{\rm ext}}. \tag{3.14}$$

As presented later in this section, the kinematics of the lens galaxy $\sigma_{\rm LOS}$ give a lensing-independent constrain on its 3D mass, i.e. the deprojected convergence (e.g. Sonnenfeld et al. 2012; Cappellari 2020; Shajib et al. 2020, 2023) and therefore contribute to lifting the MSD within the main deflector.

We now see all the required ingredients to measure H_0 using a strongly lensed quasar:

- The redshift of the source $z_{\rm s}$ and the lens $z_{\rm l}$,
- The time delay between each image $\Delta t_{\rm AB}$,
- The mass model of the lens to determine $\Delta\phi_{\rm AB}$,
- The kinematic analysis to measure $\sigma_{\rm LOS}$,
- The line of sight analyses to obtain $\kappa_{\rm ext}$.

Redshifts

The spectroscopic redshift of the quasar source, z_s, is commonly obtained using the frequent emission lines present in quasars, for instance C III, C IV or Mg II. Accurately measuring z_l requires high signal-to-noise ratio spectra taken under optimal seeing conditions to effectively separate the lensing galaxy from the quasar and identify absorption or emission lines which massive elliptical galaxies generally have few of.

Time delay

Time delay cosmography is only applicable to strong lensing systems with a luminosity-varying source. Even though Sjur Refsdal dream was to measure H_0 using a strongly lensed Supernova, the unfolding of gravitational lens discoveries (around 300 known systems to this day, e.g. Lemon et al. 2018, 2020; Chan et al. 2022; Lemon et al. 2023) put quasars on the forefront of time delay cosmography applications. Following the main goal of this work, we will mainly discuss how the time delay is measured in strongly lensed quasars but it is interesting to note that important efforts are put towards the precise measurement of time delays of strongly lensed supernovae (e.g. Pierel & Rodney 2019; Bayer et al. 2021; Huber et al. 2022).

Typically found in the redshift range $z_s \sim 1$ - 3, quasars are lensed by massive early-type galaxies situated at redshifts $z_l \sim 0.2$ - 0.8. This lensing configuration typically generates multiple quasar images separated by a few arcseconds, which can be resolved with small ground-based telescopes. In any light curve, the measurement of the time delay relies on the identification of features that can be matched in all individual image light curves. This task is, however, complicated by various astrophysical, observational, and instrumental factors:

- Photometric accuracy: Variations of about 0.2 mag are common within one visibility season, requiring accuracy within a few milli-mags to identify critical inflexion points in the light curves. Achieving such precision is challenging as quasar images are often blended with extended sources like gravitational arcs or the lens galaxy, necessitating careful PSF reconstruction and handling of contaminating light.
- Monitoring cadence and duration: The monitoring cadence should match the timescale of the targeted variations, and the campaign's total duration must cover the lensing time delays. Additionally, enough quasar variations must be recorded for multiple images at different relative delayed times. Such light curves necessitate continuous telescope access for at least one visibility season, typically lasting 6 to 8 months.
- Seasonal gaps are common in optical light curves as only circumpolar targets remain observable throughout the year. These gaps can introduce windowing effects, requiring careful consideration when using cross-correlation techniques for time delay measurements. Removing or accounting for the periodic signal from missing data is essential. Additionally, correlated noise, resulting from uncertainties in flux assignment from different quasar images, must be addressed. If variations cannot be unambiguously matched in both light curves, statistical methods are unlikely to measure a time delay robustly.
- Extrinsic variations: As presented in Chapter 2, microlensing of individual images independently alters the observed luminosity of each image and may incorporate reverberated continuum emission in the light curve. While these effects present a great opportunity to study the source and the lens, they deform the shape of the light curves and their inflexion points, which are critical to measuring

the time delay. As Vernardos (2022) showed, they can significantly hinder the time delay precision when not appropriately modelled.

Over the past two decades, significant progress has been made in addressing these challenges. Advancements in photometric instrumentation in the late 1990s allowed for accurate light curves, leading to robust time-delay measurements (e.g. Kundić et al. 1997; Burud et al. 2000; Hjorth et al. 2002; Kochanek et al. 2006).

These early measurements with ∼ 10-15% errors, prompted systematic monitoring by the COSmological MOnitoring of GRAvItationnal Lenses (COSMOGRAIL) program, designed to measure time delays of the brightest objects within five years thanks to regular cadence over long periods (Eigenbrod et al. 2005; Courbin et al. 2011). However, obtaining time delays for less variable and fainter targets required more than a decade of monitoring (Millon et al. 2020b) with a 1-m class telescope. As a result, about 40 lensed quasars now have known time delays, albeit with varying precision.

With an increasing number of lensed quasars being discovered annually, time-delay cosmography faces a new phase where rapid measurements are essential to utilize these systems as cosmological constraints. Using high signal-to-noise ratio (SNR) and daily cadence light curves obtained with a larger 2-m class telescope, Courbin et al. (2018) demonstrated the possibility of accurate time-delay measurements within a single monitoring season, thanks to small amplitude variations of quasars, typically 10 to 50 millimag, occurring over weeks or months, faster than microlensing variability. Detecting these variations at sufficient SNR allows easier disentangling of intrinsic and microlensing variability, reducing the need for long light curves. This new strategy has enabled the measurement of 6 new time delays in a single season (Millon et al. 2020a).

While some methods rely on the light-curve cross-correlations to give a direct measure of the time delay without modelling the extrinsic variations (e.g. Pelt et al. 1996; Aghamousa & Shafieloo 2015), various curve-shifting algorithms have been proposed to separately fit the intrinsic variation of the quasar and the extrinsic variation of the microlensing. As mentioned in Section 1.2, the intrinsic variations can be modelled by a DRW (e.g., Kelly & Siemiginowska 2009), or CARMA processes (e.g., Kelly et al. 2014) with microlensing variations modelled by an additive polynomial (e.g. Tak et al. 2016; Meyer et al. 2023). It is also possible to use flexible tools such as splines (PyCS, Tewes et al. 2013) or Gaussian regressions (e.g. Hojjati et al. 2013) to marginalize over a range of possible fits.

The "Time Delay Challenge" (TDC Dobler et al. 2015) aimed at evaluating the precision and accuracy of each technique by handing simulated but realistic blind data to different teams. The detailed results and conclusions were presented in Liao et al. (2015) and other individual papers (e.g. Bonvin et al. 2016). The challenge proved to be more complex than anticipated, with many participating teams failing to meet the precision and accuracy requirements in the first and simplest stages. However, among the qualified teams for the more advanced stages of the TDC, the aforementioned techniques demonstrated overall good performance considering the actual data quality. Nevertheless, further investigations are needed to determine if this performance level remains valid when more realistic accretion disk emission mechanisms and source-size effects are incorporated into the simulations.

For example, the microlensing time delay described by Tie & Kochanek (2017), poses a subtle challenge as a potential nuisance for time delay measurements. While it has not been directly detected in lensed quasar light curves yet (Bonvin et al. 2018), this effect arises when different emission regions of the accretion disk experience varying magnification due to microlensing.

Lens modeling

As presented in Section 1.3, the Fermat potential difference needed in time delay cosmography is determined by the mass distribution of the lens galaxy. The modelling of the mass is done simultaneously with the modelling of the source shape and position. By mapping the source to the image plane with the lens equation (Eq. 1.33), we aim to reproduce the observed image of the strong lens system along with the lens's light. Understanding all the phenomena that alter the imaging of strong lens systems is necessary to do so. Both the telescope's internal structure and Earth's atmosphere blur the observation, which is equivalent to the convolution of the image with a point spread function (PSF) of the observation. Furthermore, the discretization of the simulated image and the addition of noise accounts for the pixelized nature of CCD camera observations. As illustrated in Fig. 3.1, a simulated model is hence expressed as a series of linear operations:

$$d = \boldsymbol{RB}\left[\boldsymbol{L}_{\psi} s + l\right] + n \tag{3.15}$$

where d represents the data, ψ the lens potential, s the unlensed source light, and l the lens light. The lensing operator L_ψ is based on the lens potential and generates the lensed source when applied to the source model. The blurring operator **B** models seeing effects involving a convolution operation with the PSF. The binning operator **R** models the pixel discretization on the detector, and sources of noise are accounted for by the term n.

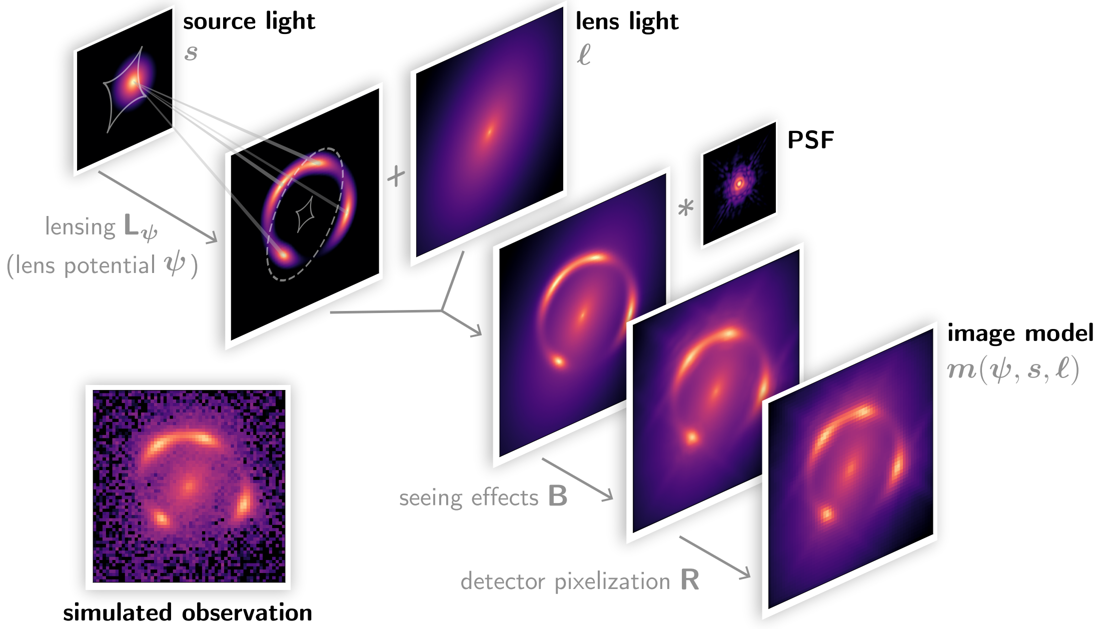

Figure 3.1: Example of the simulation of a strongly lensed system observation starting from an unlensed source light profile s, the potential of the lens galaxy ψ distorts the source through the operator L_ψ. The result is then blurred and pixelized with the operators **B** and **R**. Illustration taken from Aymeric Galan's thesis

Therefore, modelling a strong lens system consists in sampling the posterior probability of the mass and light parameters ξ_{light} and ξ_{mass} by maximizing their likelihood. Following the Bayes theorem, we have:

$$\mathcal{P}(\xi_{\rm light}, \xi_{\rm mass} \mid {\rm Data}) \propto \mathcal{L}(Data \mid \xi_{\rm light}, \xi_{\rm mass}) p(\xi_{\rm light}, \xi_{\rm mass}), \tag{3.16}$$

where $\mathcal{L}(Data \mid \xi_{\rm light}, \xi_{\rm mass})$ is the likelihood of the parameters given the data and $p(\xi_{\rm light}, \xi_{\rm mass})$ is the prior on the parameters. The data used to constrain the posterior are the imaging data (Img) in as many bands as possible and, if available, the time delay, $\Delta t_{\rm AB}$. The likelihood maximized by the sampling is therefore computed with:

$$\mathcal{L}(Data \mid \xi_{\rm light}, \xi_{\rm mass}) = \mathcal{L}({\rm Img} \mid \xi_{\rm light}, \xi_{\rm mass}) + \mathcal{L}(\Delta t_{\rm AB} \mid \xi_{\rm light}, \xi_{\rm mass}) \tag{3.17}$$

$$= \sum_{\rm i}^{N_{\rm pix}} \frac{(D_{\rm Img,i} - M_{\rm Img,i})^2}{\sigma_{\rm i}^2} + \frac{1}{2} \frac{(\Delta t_{\rm AB} - M_{\Delta t_{\rm AB}})^2}{\sigma_{\Delta t_{\rm AB}}}, \tag{3.18}$$

where $D_{\rm Img,i}$ and $M_{\rm Img,i}$ are the observed and modelled image, $\sigma_{\rm i}$ is the pixels's noise and $\sigma_{\Delta t_{\rm AB}}$ the uncertainty on the time delay.

Imaging modelling is primarily conducted using high-resolution data from space-based instruments like the Hubble Space Telescope (HST) (e.g. Wong et al. 2017; Shajib et al. 2019; Birrer et al. 2019) or ground-based adaptive optics (AO) systems (e.g. Chen et al. 2019). As shown by Eq. 3.15, the shape of the source and the lens potential are degenerate when it comes to reproducing the shape of the observed distorted source. Therefore, the difficulty of accurate lens modelling resides in the parametrization of the lens mass and source and lens light profiles. Typically, the modelling process starts with a simple model and progressively increases the complexity of different model components until a satisfactory fit to the data is achieved. Criteria such as the Bayesian Information Criteria (BIC) (e.g., Birrer et al. 2019) and the Bayesian Evidence (e.g., Shajib et al. 2020) are used to assess the goodness of fit during this iterative process.

In the following paragraphs, we will present some of the common choices to parameterize the different light and mass components that will be used in this work.

PSF characterization is an essential step of any modelling endeavour as it fixes the astrometric position of the time-variable source images, i.e. the part of the convergence profile probed to compute $\Delta\phi_{\rm AB}$ (e.g., Birrer & Treu 2019). It also allows the modelling of the extended source structure without contamination from bright quasar images. Current methods for obtaining a precise PSF model involve a first guess based on stars of the field (e.g., Suyu et al. 2014; Birrer et al. 2016, 2022a; Michalewicz et al. 2023) followed by iterative procedures during the model fitting process to extract improved constraints of the PSF directly from the data (Birrer et al. 2016). As shown by Ertl et al. (2022) and Shajib et al. (2022), different treatments of the PSF modelling can significantly change the best fit found, such as the slope of the convergence radial profile, hence impacting the cosmographic inferences.

Lens light: Elliptical galaxies are commonly described by the elliptical Sersic profile, which gives the light intensity at the position (θ_1, θ_2) following:

$$I_{\rm sersic}\,(\theta_1, \theta_2) = I_{\rm eff} \left[-b_{\rm n} \left[\left(\frac{\sqrt{\theta_1^2 + \theta_2^2/q^2}}{\theta_{\rm eff}} \right)^{1/{\rm n}} - 1 \right] \right] \tag{3.19}$$

with $\theta_{\rm eff}$ the effective radius, also defined as the half-light radius thanks to the normalizing factor $b_{\rm n}$, $I_{\rm eff}$ the intensity at $\theta_{\rm eff}$. q is its axis ratio and n the sersic index.

Setting $n = 1$ gives an exponential profile while $n = 4$ falls back on the De Vaucouleur profile, which is particularly effective in fitting the light distribution of galaxies with a smooth and extended structure.

The chameleon profile can also model the light profile of a galaxy (e.g., Suyu et al. 2014) as the difference between two non-singular isothermal ellipsoid (NIE) profiles:

$$I_{\rm Chm}(\theta_1,\theta_2) = \frac{I_{\rm eff}}{1+q}\left[\frac{1}{\sqrt{\theta_1^2+\theta_2^2/q^2+4w_c^2/(1+q)^2}} - \frac{1}{\sqrt{\theta_1^2+\theta_2^2/q^2+4w_{\rm t}^2/(1+q)^2}}\right] \tag{3.20}$$

where q is the axis ratio and w_c and $w_{\rm t}$ are sizes of the cores of the two NIE with $w_{\rm t} > w_{\rm q}$.

Source light: Given its compactness, the quasar remains unresolved and is parametrized as a Dirac profile added to the light profile of its host galaxy. In practice, the amplitude of each Dirac profile is fitted independently on each quasar image and is not linked to the lens mass predicted flux ratio (see Eq. 1.47). In the same way as the lens light, the host galaxy can be modelled with a Sersic profile. However, various reconstruction techniques such as regularized pixelated grid (e.g. Warren & Dye 2003; Treu & Koopmans 2004; Suyu & Blandford 2006; Vernardos 2022; Galan et al. 2022), basis functions like shapelets (e.g. Birrer & Amara 2018) or wavelets (Galan et al. 2021) have been developed to account for potentially complex morphology.

Lens mass: The total mass of the massive elliptical galaxy can be modelled with a power-law elliptical mass distribution (PEMD) for which the convergence at the position (θ_1, θ_2) in the frame aligned with the major and minor axis of the deflector is given by:

$$\kappa_{\rm PL}\left(\theta_1,\theta_2\right) = \frac{3-\gamma_{\rm PL}}{2}\left[\frac{\theta_{\rm E}}{\sqrt{q_{\rm m}\theta_1^2+\theta_2^2/q_{\rm m}}}\right]^{\gamma_{\rm PL}-1}, \tag{3.21}$$

where $\theta_{\rm E}$ is the Einstein radius, γ the slope of the profile and $q_{\rm m}$ its axis ratio. This convergence map is then rotated by the position angle $\phi_{\rm m}$ to belong to the on-sky coordinate frame.

Simpler parametrization fixes the slope of such power law to $\gamma = 2$ to obtain a Single Isothermal Ellipsoids (SIE). By forcing the sphericity of the model, it is possible to simplify further the parametrization now denominated Single Isothermal Spheroids (SIS).

Alternatively, the mass of an elliptical galaxy can be decomposed into its baryonic and dark matter components to create a **composite profile**. In this case, the chameleon profile models the baryonic mass (see Eq. 3.20 Suyu et al. 2014) and the dark matter component follows a Navarro-Frenck-White (NFW) profile whose volumic density is given by:

$$\rho(r) = \frac{\rho_0}{\left(\frac{r}{R_{\rm s}}\right)\left(1+\frac{r}{R_{\rm s}}\right)^2} \tag{3.22}$$

where ρ_0 is a normalization and R_s is the scale radius.

To incorporate the effects of external perturbers on the observed characteristics of the lensing system, we extend the lens mass model by introducing two supplementary parameters. These parameters are the magnitude denoted as $\gamma_{\rm ext}$ and the direction represented by $\psi_{\rm ext}$. These additions are essential for quantifying and considering the influence of external perturbing factors within the context of the lensing model.

Even though a pure mass sheet along the lens plane is unphysical, the potential existence of a dark matter core can cause similar effects. Blum et al. (2020) proposed the following parameterization of such core:

$$\kappa_c(\theta) = \frac{\theta_c^2}{\theta_c^2 + \theta^2}, \tag{3.23}$$

with θ_c the size of the core at which $\kappa_c(\theta)$ drops from $1 - \lambda_c$ to 0. It induces the following MST:

$$\kappa_{\lambda_c} = \lambda_c \kappa(\theta) + (1 - \lambda_c)\kappa_c(\theta). \tag{3.24}$$

λ_c embodies the mathematical internal MST parameter $\lambda_{\rm int}$ associated to an infinite mass sheet. This formulation of the MST tends toward an infinite mass sheet for $\theta_c \to \infty$, but it ensures that the MST convergence κ_{λ_c} converges to 0 as we go away from the lens when θ_c is finite.

Examples of the various light and mass profiles presented are shown in Fig. 3.2.

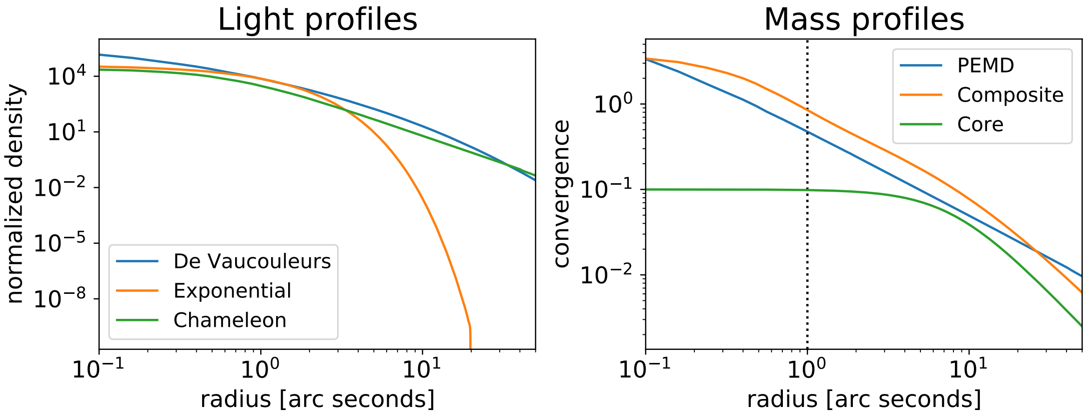

Figure 3.2: ***Left panel:*** Examples of the De Vaucouleurs, exponential and chameleon light profiles expressed in Eqs 3.19 and 3.20 with $\theta_{\rm eff} = 1''$. ***Right panel:*** Examples of a PEMD profile with $\gamma = 2$ and a composite profile, sum of the NFW and Chameleon profile with $\theta_{\rm E} = 1''$, highlighted by the dotted line. An example of a core with $\theta_c = 8''$ is also shown.

In practice, the imaging data puts direct constraints on the Einstein radius $\theta_{\rm E}$ and the following ratio, which is invariant under the MST (Kochanek 2002):

$$\xi_{\rm rad} \equiv \frac{\theta_{\rm E}\alpha''_{\rm E}}{(1 - \alpha'_{\rm E})} \propto \frac{\theta_{\rm E}\alpha''_{\rm E}}{(1 - \kappa_{\rm E})}, \tag{3.25}$$

where $\alpha'_{\rm E}$ and $\alpha''_{\rm E}$ are the first and second derivatives of the deflection angle at the Einstein radius $\theta_{\rm E}$ and $\kappa_{\rm E}$ is the corresponding convergence. When assuming that a given lens follows a power-law profile, this ratio tightly constrains its slope $\gamma_{\mathrm{PL}} = \xi_{\mathrm{rad}} + 2$ and therefore the Fermat potential difference, which depends on the convergence of the lens at the position of the image (see Eq. 1.41). However, when including a core to the model to consider the MST, the radial profile significantly deviates from the power law as shown by the left panel of Fig. 3.3. Since ξ_{rad} is invariant under the MST, the slope inferred by a simple power-law will ignore the core, and the Fermat potential difference will be biased (e.g., Kochanek 2020; Blum et al. 2020). Fortunately, the right panel of Fig. 3.3 shows that the velocity dispersion depends on MST parameter λ_c, hence offering a way to break the MSD by independently measuring σ_{LOS}.

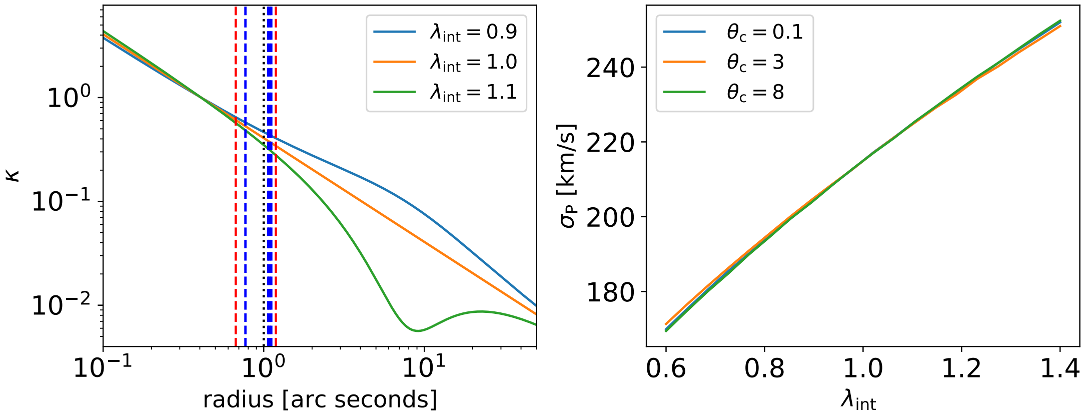

Figure 3.3: ***Left panel:*** Effect of adding a core on a PEMD profile with varying λ_c, following Eq. 3.24. Vertical dotted lines show positions of the image of fiducial source positions, creating two images (in red) or four images (in blue), and the black dashed line highlights the Einstein radius of the uncored PEMD. ***Right panel:*** Central velocity dispersion of the lens dependence on λ_c. The core size, however, does not impact the velocity dispersion. (Reproduced from Birrer et al. 2020)

Kinematic modelling

As shown by Fig. 3.3, the assumptions made about the radial density profile of the primary lensing galaxy to constrain the internal MSD can lead to biases, and kinematic modelling of the stars inside the galaxy is a powerful way to avoid these bias. The observable kinematic parameter is the luminosity-weighted line-of-sight stellar velocity dispersion, denoted as σ_{LOS}. It is measured by targeting stellar absorption lines and quantifying their width with high-resolution spectra.

Following Binney & Tremaine (1987), the orbital distribution $f(\mathbf{x}, \mathbf{v})$ of position and velocity, of the stars in 3D motion in the galactic potential Φ is described by the steady-state collisionless Boltzmann equation:

$$\sum_{\mathrm{i}=1}^{3} \left(v_{\mathrm{i}} \frac{\partial f}{\partial x_{\mathrm{i}}} - \frac{\partial \Phi}{\partial x_{\mathrm{i}}} \frac{\partial f}{\partial v_{\mathrm{i}}} \right) = 0. \tag{3.26}$$

While the actual mass distribution may not be perfectly spherical, assuming spherical symmetry ($\frac{\partial \Phi}{\partial \phi} = \frac{\partial f}{\partial \phi} = \frac{\partial \Phi}{\partial r} = \frac{\partial f}{\partial r} = 0$) is not oversimplifying with ~ 10% uncertainty in kinematic measurement (Sonnenfeld et al. 2012). We then obtain a single spherical Jeans equation:

$$\frac{\partial(\rho_*(r)\sigma_{\mathrm{r}}(r))}{\partial r} + \frac{2\beta_{\mathrm{ani}}(r)\rho_*(r)\sigma_{\mathrm{r}}^2(r)}{r} = -\rho_* \frac{\partial \Phi(r)}{\partial r}, \tag{3.27}$$

with $\rho_*(r)$ the stellar density distribution and $\beta_{\rm ani}$ the orbital anisotropy, defined as the ratio of radial to tangential velocity dispersion components, $\sigma_{\rm r}$ and $\sigma_{\rm t}$:

$$\beta_{\rm ani} \equiv 1 - \frac{\sigma_{\rm t}^2}{\sigma_{\rm r}^2}. \tag{3.28}$$

Given $\sigma_{\rm LOS}$, the values of $\sigma_{\rm r}$ and $\sigma_{\rm t}$ are totally degenerate, leaving $\beta_{\rm ani}$ unconstrained. This introduces a degeneracy between $\sigma_{\rm LOS}$ and the 3D mass profile known as the mass-anisotropy degeneracy (MAD) (Binney & Mamon 1982; Merritt 1985).

Therefore, a prior assumption is often made on the anisotropy profile, such as isotropic or Osipkov-Merritt profiles. The Osipkov-Merritt profile allows the anisotropy to be isotropic near the center ($\beta_{\rm ani} = 0$) and gradually more radial away from the center ($\beta_{\rm ani} = 1$), based on observed properties of stellar orbits in local elliptical galaxies (Osipkov 1979; Merritt 1985):

$$\beta_{\rm ani}(r) = \frac{r^2}{r_{\rm ani}^2 + r^2}, \tag{3.29}$$

with $r_{\rm eff}$ is the half-light radius of the deflector and $r_{\rm ani}$ is the anisotropy scale radius.

A solution of Eq. 3.27 is given by:

$$\sigma_{\rm r}(r) = \frac{G}{\rho_*(r)} \int_{\rm r}^{\infty} \frac{M(s)\rho_*(s)}{s^2} J_\beta(r, s) ds, \tag{3.30}$$

with $M(r)$ the mass enclosed within the radius r and $J_\beta(r, s) = exp\left(\int_{\rm r}^{\rm s} 2\beta_{\rm ani}(r')\frac{dr'}{r'}\right)$.

We then get the modelled velocity dispersion along the LOS, ${\sigma_{\rm LOS}}^{\rm model}$ with:

$$\sigma_{\rm LOS}^{\rm model^2} = \frac{2}{\Sigma_*(R)} \int_{\rm R}^{\infty} \left(1 - \beta_{\rm ani}(r)\frac{R^2}{r^2}\right) \frac{\rho_*(r)\sigma_{\rm r}^2(r)}{\sqrt{r^2 - R^2}} rdr, \tag{3.31}$$

with R the projected radius and Σ_* the enclosed surface stellar density, which can be constrained from the luminosity profile of the lens $I(R)$ assuming a constant mass-to-light ratio $f_{\rm M/L}$ $\Sigma_*(R) = f_{\rm M/L} I(R)$.

To compare this with the observed velocity dispersion along the LOS, $\sigma_{\rm LOS}$, we weigh $\sigma_{\rm LOS}^{\rm model}$ with PSF convolved light profile of the lens:

$$\sigma_{\rm LOS} = \frac{\int_{\rm A} I(R)\sigma_{\rm LOS}^{\rm model^2} * PSFdA}{I(R) * PSFdA} \tag{3.32}$$

The prediction of the observed line-of-sight velocity dispersion from any model, irrespective of the approach, can be decomposed into a cosmology-dependent and a cosmology-independent part:

$$\sigma_{\rm LOS}^2 = \frac{D_{\rm s}}{D_{\ell {\rm s}}} \frac{c^2}{J(\xi_{\rm lens}, \xi_{\rm light}, \beta_{\rm ani})}, \tag{3.33}$$

where the dimensionless quantity J relies on the deflector model parameters ($\xi_{\rm lens}$ and $\xi_{\rm light}$) and $\beta_{\rm ani}$. Moreover, J considers observational conditions and luminosity-weighting within the dispersion measurement aperture, as previously demonstrated in studies like Binney & Mamon (1982) and Treu & Koopmans

(2004). When including $\lambda_{\rm int}$ in the mass-model, we can approximate (Teodori et al. 2022):

$$J(\xi_{\rm lens}, \xi_{\rm light}, \beta_{\rm ani}, \lambda_{\rm int}) = \lambda_{\rm int} J(\xi_{\rm lens}, \xi_{\rm light}, \beta_{\rm ani}). \tag{3.34}$$

Therefore, by combining kinematic and lensing constraints with Eqs. 3.13 and 3.33, we yield constraints on the angular diameter distance of the lens (e.g. Birrer et al. 2019):

$$D_\ell = \frac{1}{1-\kappa_{\rm d}} \frac{\Delta t_{\rm AB} c}{\sigma^2_{\rm LOS}} \frac{\lambda_{\rm int}}{J(\xi_{\rm lens}, \xi_{\rm light}, \beta_{\rm ani}, \lambda_{\rm int})} \tag{3.35}$$

The specific choice of functional model and the adopted priors on parameters like the anisotropy scale radius, $r_{\rm ani}$, can significantly impact the kinematics prediction (Shajib et al. 2018; Birrer et al. 2020). Various forms of the radial anisotropy distribution exist, and the specific choice of the functional model can significantly influence the outcomes, along with the priors adopted. To address this degeneracy, a potential solution is to acquire spatially resolved velocity dispersion measurements with IFU instruments rather than relying on unresolved (or integrated) velocity dispersion measurements with slit instruments (Shajib et al. 2018; Yıldırım et al. 2020). As shown by Fig. 3.4, this approach can help disentangle the degeneracy and provide more accurate estimates of the mass and anisotropy profiles by offering detailed kinematic information across different spatial regions.

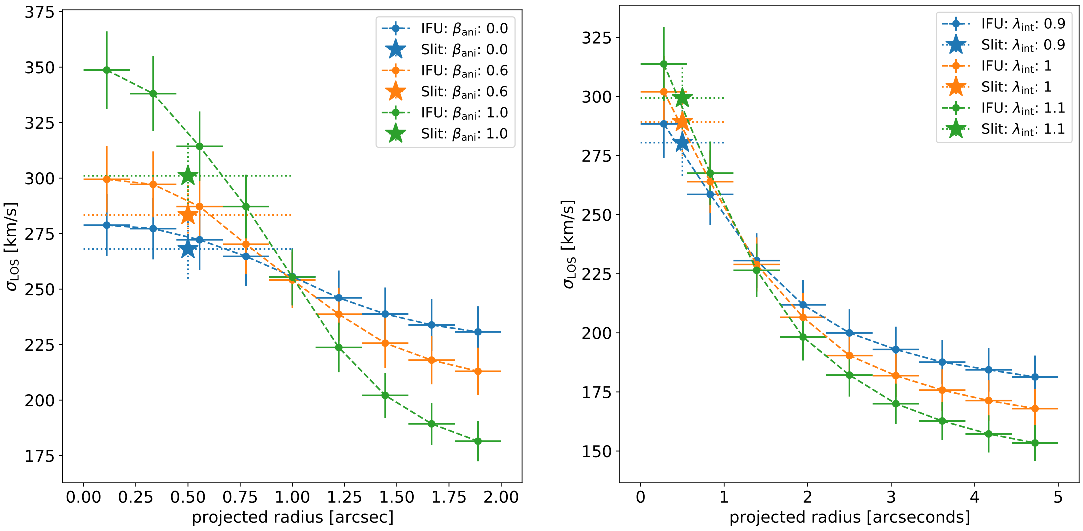

Figure 3.4: Simulated $\sigma_{\rm LOS}$ radial profile measurements with slit and IFU spectrographs. In both simulations, the PEMD fiducial lens model was done with $\gamma = 2$, $\theta_{\rm E} = 1.5''$, and a 5% error was assumed in both cases. The dashed lines show the analytical profiles. ***Left panel:*** Changes in the anisotropy profile are not distinguished by the single aperture measurement whereas the spatially resolved ones give good constraints. In this case we fixed $\lambda_{\rm int}$= 1 ***Right panel:*** Similarly, spatially resolved kinematics give better constraint on $\lambda_{\rm int}$ than single aperture ones. In this case we fixed $\beta_{\rm ani}$= 0.6.

Line-Of-Sight (LOS) analysis

The impact of mass density fluctuations along the line of sight on the lensed source is typically a few per cent, often remaining below 10% of the total lens convergence. While this might seem small, it becomes significant when estimating the Hubble parameter with percent-level accuracy. The constant effective contribution from the LOS can be represented as an external mass-sheet $\kappa_{\rm ext}$ presented by Eq. 3.12.

The specific influence of line-of-sight objects depends on whether the dominant-lens approximation holds, indicating that the critical density of these objects is much smaller than that of the primary deflector. The flexion shift was introduced by McCully et al. (2017) to determine which line-of-sight galaxies should be explicitly included in the lens modelling and which ones should be implicitly accounted for through the computation of $\kappa_{\rm ext}$. The difference in lens image position induced by a given nearby galaxy is given by:

$$\Delta_3 x = f(\beta) \frac{\left(\theta_{\rm E,lens} \cdot \theta_{\rm E,pert}\right)^2}{\theta^3}, \tag{3.36}$$

with $\theta_{\rm E,lens}$ and $\theta_{\rm E,pert}$ the lens and perturber einstein radii, θ the angular separation on the between them and $f(\beta)$ is determined by:

$$f(\beta) = \begin{cases} (1-\beta)^2 & \text{if the perturber is behind the lens} \\ 1 & \text{otherwise} \end{cases} \tag{3.37}$$

$$\beta = \frac{D_{\ell \rm p} D_{\rm os}}{D_{\rm op} D_{\ell \rm s}}, \tag{3.38}$$

with $D_{\rm ij}$ the angular distance between the lens (ℓ), perturber (p), observer (o), and source (s), which are calculated assuming $H_0 = 70$ km s^{-1}Mpc^{-1}. The lens modelling explicitly includes perturbers with a flexion shift above 10^{-4}. Such cases often involve solving the multi-plane lens equation (e.g. Wong et al. 2020; Shajib et al. 2020).

Below this threshold, line-of-sight objects can be treated as small perturbations that introduce nearly constant convergence across the lensed system $\kappa_{\rm ext}$, a statistical treatment suffices (e.g., Sluse et al. 2017; Buckley-Geer et al. 2020; Wells et al. 2023).

However, computing the value of $\kappa_{\rm ext}$ is challenging because direct information on the total matter distribution in the universe at the relevant scales is limited. While McCully et al. (2017) showed that an explicit mass model of all perturbers is possible, it requires extensive spectroscopic observation of the considered field of view, which is very costly. Therefore, the two main measurement techniques, number counts and weak lensing, rely on assumptions about how mass traces light, which is well-motivated by large-scale structure probes but validated only statistically.

Number counts involves measuring the galaxy number density near the lens as a summary statistic and comparing it to reference fields. This comparison helps determine whether the line of sight is over- or under-dense compared to the average background (e.g. Fassnacht et al. 2011; Greene et al. 2013; Wells et al. 2023). It can be summed up in 4 main steps:

- Lines of sight (typically several arcminutes wide squares) are drawn from a large comparison field and compared to the LOS of the lens. Modern survey datasets covering hundreds to thousands of square degrees ensure a sufficiently large comparison field to avoid sampling bias. The photometric catalogues of the fields are cleared from objects more distant than the lensed source and fainter than the used magnitude cut on the i < 24 (e.g., Fassnacht et al. 2011). This cut is designed to consider only object with a reliable photometry.

- The weight value of a given LOS W_i is then computed as the ratio of the weighted number counts for galaxies in the lens field to the same statistic in the reference field.

$$W_\mathrm{i} = \frac{\Sigma_\mathrm{j} w_\mathrm{j,lens}}{\Sigma_\mathrm{j} w_\mathrm{j,i}} \tag{3.39}$$

  where j indexes the galaxies in a given LOS and w is the weight of a galaxy. Different types of weights can be considered (e.g., Greene et al. 2013; Rusu et al. 2017; Wells et al. 2023) such as the galaxy's distance to the center ($1/r_\mathrm{j}$), its potential ($m_\mathrm{j}/r_\mathrm{j}$), its redshift ($z_\mathrm{j}(z_\mathrm{s} - z_\mathrm{j})$) or simply be the same for each galaxy ($w_\mathrm{j} = 1$). The weight value obtained, therefore act as a tracer of the external convergence of the lens LOS.

- Similar weight values are computed in simulated fields with known κ_ext. Previous work, such as Rusu et al. (2017), has shown that using the Millennium Simulation yields a reliable estimate of κ_ext because it provides catalogues of galaxies for several values of the external convergence at sufficient points to represent the Universe accurately. Since the weight value relies on ratios, many dependencies on the simulation's underlying cosmological parameters are expected to cancel out.

- The posterior probability of κ_ext can hence be computed as follows:

$$p(\kappa_\mathrm{ext}|d) = \int p_\mathrm{sim}(\kappa_\mathrm{ext}|W) p(W|d) \Pi_\mathrm{i} dW_\mathrm{i}. \tag{3.40}$$

  Here, $p(W|d)$ represents the probability distribution of the weighting scheme W given the data, and $p_\mathrm{sim}(\kappa_\mathrm{ext}|W)$ denotes the probability distribution of $\kappa_\mathrm{ext}$in the simulated dataset, conditioned on a specific value of the weight W. Greene et al. (2013) showed that the combination of multiple evaluation relying on different weights and on the external shear γ_ext measured by the lens modelling (while adequately taking into account covariances between estimates) significantly improves the precision and robustness of the measurement.

Weak lensing causes shape distortion of background galaxies due to foreground structures (see Section 1.3), providing a direct probe of the line of sight (LOS) structure. At first order, cosmic shear measurements can be translated to convergence, offering a unique mapping without relying on priors from numerical simulations (Kaiser & Squires 1993). Nevertheless, this method is limited to an angular scale determined by the density of lensed sources. While it effectively characterizes large-scale cosmic density distributions, it is not well-suited for capturing smaller-scale density perturbations, such as those on the order of arc seconds. Furthermore, differences in redshift between the weak lensing source population and the strongly lensed source require the translation of the weak lensing convergence map to a different lensing kernel and adds sources of uncertainties (Kuhn et al. 2021). Recent studies on quadruply lensed quasars HE0435-1223 and B1608+656 (Tihhonova et al. 2018, 2020) use weak lensing techniques in combination with HST imaging to reconstruct convergence maps and found estimates with a comparable precision with the number count approach of (Rusu et al. 2017).

3.1.2 Current status

TDCOSMO sample: 7 fully analyzed systems

In the last 15 years, breakthroughs in lens modelling allowed by flexible parametrizations and Bayesian Inference (e.g. Suyu et al. 2009; Birrer & Amara 2018) along with long monitoring of dozens of strongly lensed quasars by the COSMOGRAIL program (Eigenbrod et al. 2005; Courbin et al. 2005) allowed the H_0 Lenses in COsmograil's Wellspring (H0LiCOW) collaboration to conduct analyses of six lensed quasar systems (Suyu et al. 2010, 2014; Wong et al. 2017; Birrer et al. 2019; Chen et al. 2019; Rusu et al. 2020). As displayed in Fig. 3.5, merging with the STRong lensing Insight into the Dark Energy Survey (STRIDES) collaboration estimate (Shajib et al. 2019), the Time-Delay COSMOgraphy (TDCOSMO) sample inferred a 2% precision Hubble constant measurement of $H_0 = 73.7 \pm 1.5$ km s^{-1}Mpc^{-1}. This measurement was obtained using parametric mass density profiles for the deflector, represented by both a power-law (Eq. 3.21) or stars with constant mass-to-light ratio (Eq. 3.20), along with dark matter halos following an NFW profile (Eq. 3.22) with priors based on galaxy population studies (Gavazzi et al. 2007).

Main critics of this measurement regarded the rigidity of the radial profile of the lens mass parametrization used, which implicitly breaks the internal MST (Kochanek 2020). In the presence of a dark matter core in the lens, these assumptions on the radial profile could significantly bias the measurement of the Fermat potential difference and H_0. To quantify the sensitivity of the TDCOSMO method to this problem, Millon et al. (2020c) simulated systems either with a power law, a cored power law or a composite and modelled them with power laws and composites. The results showed that a simple power law can not perfectly model the presence of a core. The goodness of fit metric used, such as the BIC and predicted velocity dispersion, would guide the modeller toward more complex models. Moreover, this experiment showed that agreement between composite and power-law models of a given lens ensures an accurate measurement of H_0. This agreement is observed in the seven TDCOSMO lenses and attributed to the "bulge-halo conspiracy". It states that even though stars and dark matter exhibit distinct density profiles, which differ significantly from an isothermal profile, they appear to conspire in generating a combined density profile that closely resembles an isothermal one (i.e. a power law) (Treu & Koopmans 2004; Dutton & Treu 2014).

Other investigations of Millon et al. (2020c) showed that bias in the measurement of the lens velocity dispersion, $\sigma_{\rm LOS}$ potentially caused by the MAD does not bias the H_0 inference at the population level. Similarly, the treatment of the external convergence $\kappa_{\rm ext}$ contribution is accurate. Additionally, Van de Vyvere et al. (2022a,b) showed that multipoles, twists and other expected azimuthal deformation of the mass distribution do not affect the TDCOSMO measurement of H_0.

Relaxing assumptions

"Extraordinary claims require extraordinary evidence". To be able to confirm the H_0-tension unambiguously, the TDCOSMO collaboration decided to work toward relaxing most assumptions regarding the radial profile of the lens mass model by adding a core component to the mass model as suggested by Blum et al. (2020) (see Eq. 3.23). To compensate for the expected loss in precision, two extensions to the TDCOSMO methodology were implemented: the hierarchical analysis using a large population of galaxies and spatially resolved kinematics.

The hierarchical analysis performed by Birrer et al. (2020) aimed at simultaneously fitting $\lambda_{\rm int}$ and $r_{\rm ani}$ in a large sample of galaxies by assuming that they are drawn from the same parent population. Indeed,

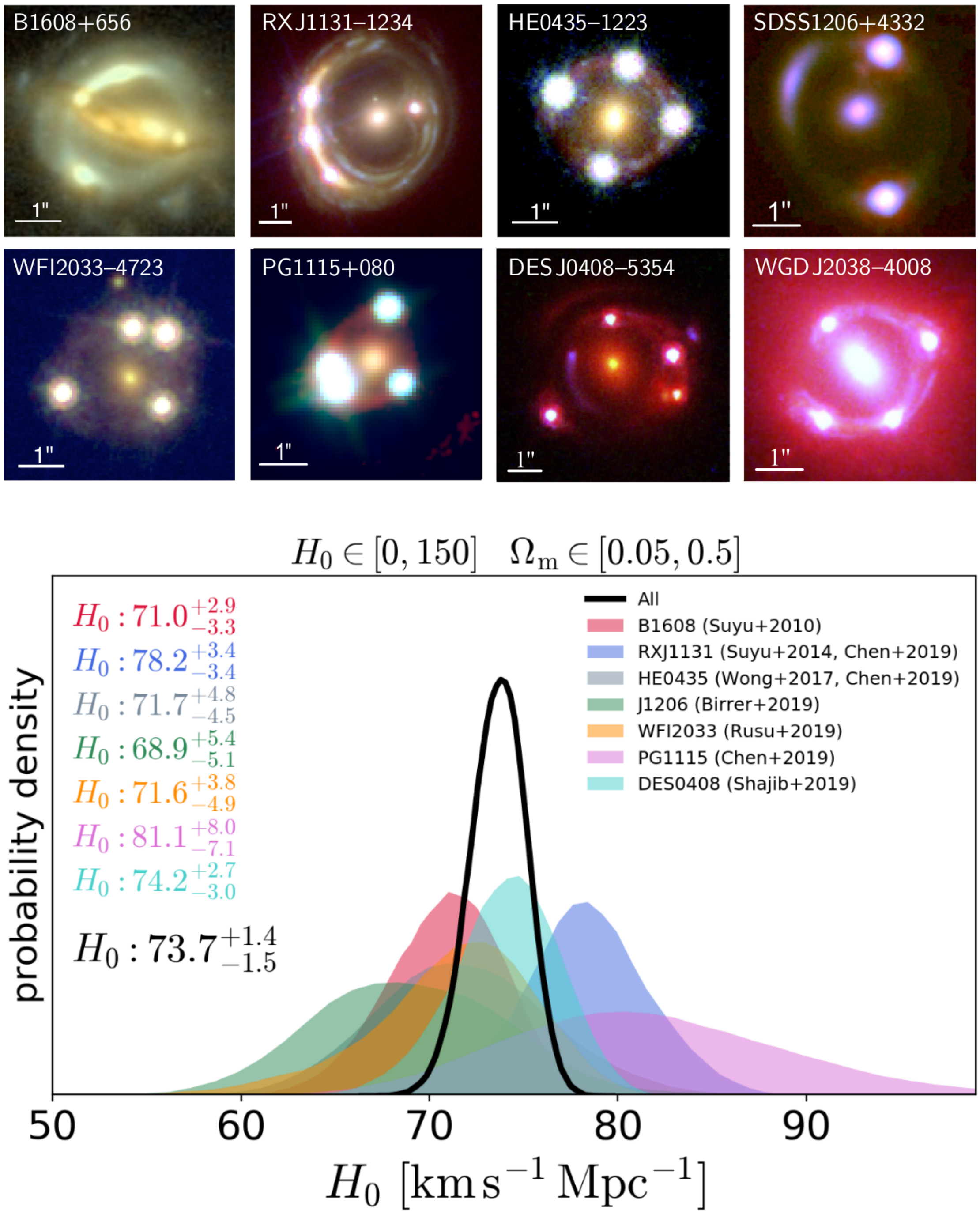

Figure 3.5: ***Top panel:*** HST imaging of the current sample of fully analyzed strongly lensed quasars systems. WGD J2038-4008 is the only system for which the time delay is not yet available hence without an H_0 inference. (Reproduced from Aymeric Galan's thesis) ***Bottom panel:*** Current state of the H_0 measurement with strongly lensed quasars, adapted from Wong et al. (2020).

as shown by the right panel of Fig. 3.3, a 5 to 10% precision on the velocity dispersion measurement is insufficient to constrain $\lambda_{\rm int}$ on a single lens. Moreover, the MAD prevents the fitting of $r_{\rm ani}$, which further dilutes the constraining power of a single central $\sigma_{\rm LOS}$ measurement.

Therefore, the use of a large sample of galaxies is necessary. To do so, the MST and r_{ani} parameters are adapted to each lens galaxy through their effective and Einstein radius θ_{eff} and θ_{E}:

$$\lambda_{\mathrm{int}}(\theta_{\mathrm{eff}}, \theta_{\mathrm{E}}) = \lambda_{\mathrm{int},0} + \alpha_{\lambda}\left(\frac{\theta_{\mathrm{eff}}}{\theta_{\mathrm{E}}} - 1\right), \tag{3.41}$$

$$r_{\mathrm{ani}}(\theta_{\mathrm{eff}}) = a_{\mathrm{ani}}\theta_{\mathrm{eff}}, \tag{3.42}$$

with α_{λ} and a_{ani} the slope of the scaling relations.

By combining the lensing and kinematic constraints of the 7 TDCOSMO systems, $\lambda_{\mathrm{int}} = 1.02 \pm 0.09$ was obtained, which is compatible with the absence of a core as presumed by the use of power law and composite models. While the median value of H_0 inferred did not change, the precision dropped to 8%. To compensate, the sample of galaxies was enlarged using 42 galaxy-galaxy lenses from the Sloan Lens ACS (SLACS) survey, which, by nature, do not have a time delay but for which mass models are available (Auger et al. 2010; Shajib et al. 2021) along with central (33 galaxies) or resolved (9 galaxies) σ_{LOS} measurements. This enhanced sample inferred $\lambda_{\mathrm{int}} = 0.91 \pm 0.04$, which, following Eq. 3.7, induced a 9% shift of the $H_0 = 67.4^{4.1}_{-3.2}$km s^{-1}Mpc^{-1}. While in agreement with previous inferences of the TDCOSMO collaboration, this new measurement is not in tension with early Universe measurements (presented in Section 1.4). It is important to note that this shift in H_0 may be real or due to differences between the TDCOSMO and SLACS samples. While Gomer et al. (2022) showed that redshift disparities between both samples do not bias the hierarchical inference, some undetected selection effects can still be at play between the two samples.

Spatially resolved kinematics of a the lens are able to constraint β_{ani} and by extension λ_{int} (Yıldırım et al. 2020). Using high signal-to-noise ratio IFU data obtained with the Keck telescope, Shajib et al. (2023) was able to measure σ_{LOS} in 41 separate spatial bins, dividing the radius of the lens into at least 7 bins. This allowed to measure $\lambda_{\mathrm{int}} = 1.01^{+0.05}_{0.2}$, which is in agreement with the hierarchical analysis on the TDCOSMO sample and results in a 9.4% measurement $H_0 = 77.1^{7.3}_{-7.1}$km s^{-1}Mpc^{-1} with a single lens. As shown by Fig. 3.6, the different strategies to mitigate the MSD agree.

Future prospects

Following the methodology of the hierarchical analysis and spatially resolved kinematics, Birrer & Treu (2021) showed that adding the spatial kinematics of each lens of the current TDCOSMO sample would yield a 3% precision. Eventually, an extended sample of 40 TDCOSMO-type lenses combined with 200 non-time-delay lenses (i.e. galaxy-galaxy) will allow a precision of 1.2%. The recent launch of the Euclid space telescope and the Rubin-LSST survey at the beginning of 2024 will facilitate the discovery of hundreds of new strongly lensed quasars and galaxies (Oguri & Marshall 2010). Moreover, the efforts to reduce the computational and human-time costs of modelling a system (Ertl et al. 2022; Schmidt et al. 2023) will allow a quick increase of the sample. Alternatively, new modelling techniques relying on free-form lens potential and source light regularized with wavelets (Galan et al. 2021, 2022) or Gaussian process regression (Vernardos 2022) could open new efficient ways to deal with the MSD but still need to be tested on real data.

Finally, the upcoming wide-field surveys such as LSST will also discover hundreds on strongly lensed supernovae (Oguri & Marshall 2010; Goldstein et al. 2019; Wojtak et al. 2019). In particular, strongly lensed Type Ia supernovae provide two extra information that alleviate the MSD and improve the lens

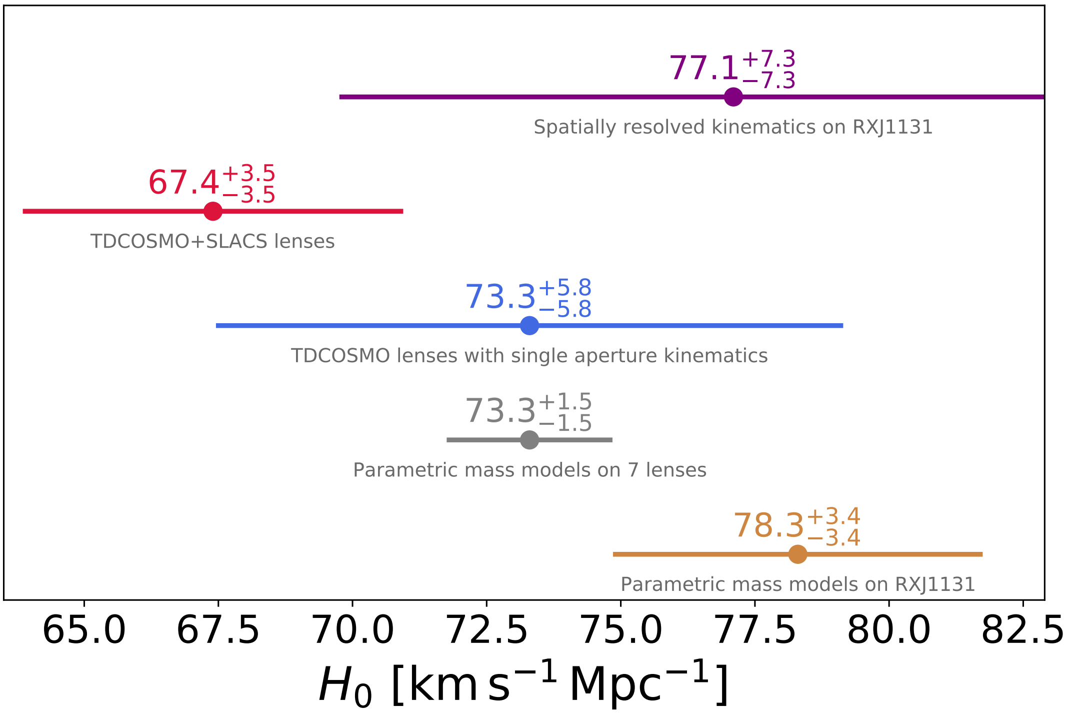

Figure 3.6: Comparison of the different techniques used to break the MSD. From top to bottom, the measurements were given by Shajib et al. (2023), Birrer et al. (2020) (hierarchical analysis using TDCOSMO+SLACS and TDCOSMO with single aperture kinematics samples), Wong et al. (2020) and Chen et al. (2019). With an equally flexible mass parameterization as in the hierarchical analysis of Birrer et al. (2020), spatially resolved kinematics achieve the same precision with a single lens as single aperture do with seven combined lenses. We also see that, for this system, PEMD and composite models of Chen et al. (2019) are self-consistent.

model precision: 1) with proper treatment of the potential micro magnification, the known intrinsic luminosity of the source allows us to constrain the macro-magnification of each image which breaks the MSD (Birrer et al. 2022b), and 2) the fading of the SN provides a clear picture of the lensed host Einstein ring (otherwise partially masked by the bright images).

Until now, only 6 strongly lensed supernovae have been discovered so far in configurations that are not favourable to a time delay cosmography analysis either because the time delay is near 0 (e.g. Goobar et al. 2022) or because the lens is a galaxy cluster which amplifies the MSD problem (Kelly et al. 2023). State-of-the-art forecasts anticipate that 10 strongly lensed SNIa suitable for TDC analysis should be discovered yearly with LSST (Sainz de Murieta et al. 2023). Thanks to this significant boost, strongly lensed supernovae will soon become the most fruitful probe of time delay cosmography (Suyu et al. 2023).

3.2 COSMOGRAIL lightcurves

As mentioned earlier, the COSMOGRAIL collaboration has been overseen by the Laboratory of Astrophysics of EPFL (LASTRO) since 2003 and coordinates the monitoring of strongly lensed quasars to measure precise time delay. Since 2020, it is a core element of the TDCOSMO collaboration, which uses the time delays measured to determine H_0 with Time delay Cosmography.

Initially, the program used 4 telescopes worldwide: Leonhard Euler 1.2m Swiss Telescope [I], Himalayan Chandra Telescope[II], Mercator Telescope[III] and the Liverpool Robotic Telescope [IV].

During this PhD I participated in the effort of data reduction to compile 18 years of monitoring into decade-long light-curves[V] which led to the measurement of time delays in 18 systems published in Millon et al. (2020b) (see Fig. 3.7).

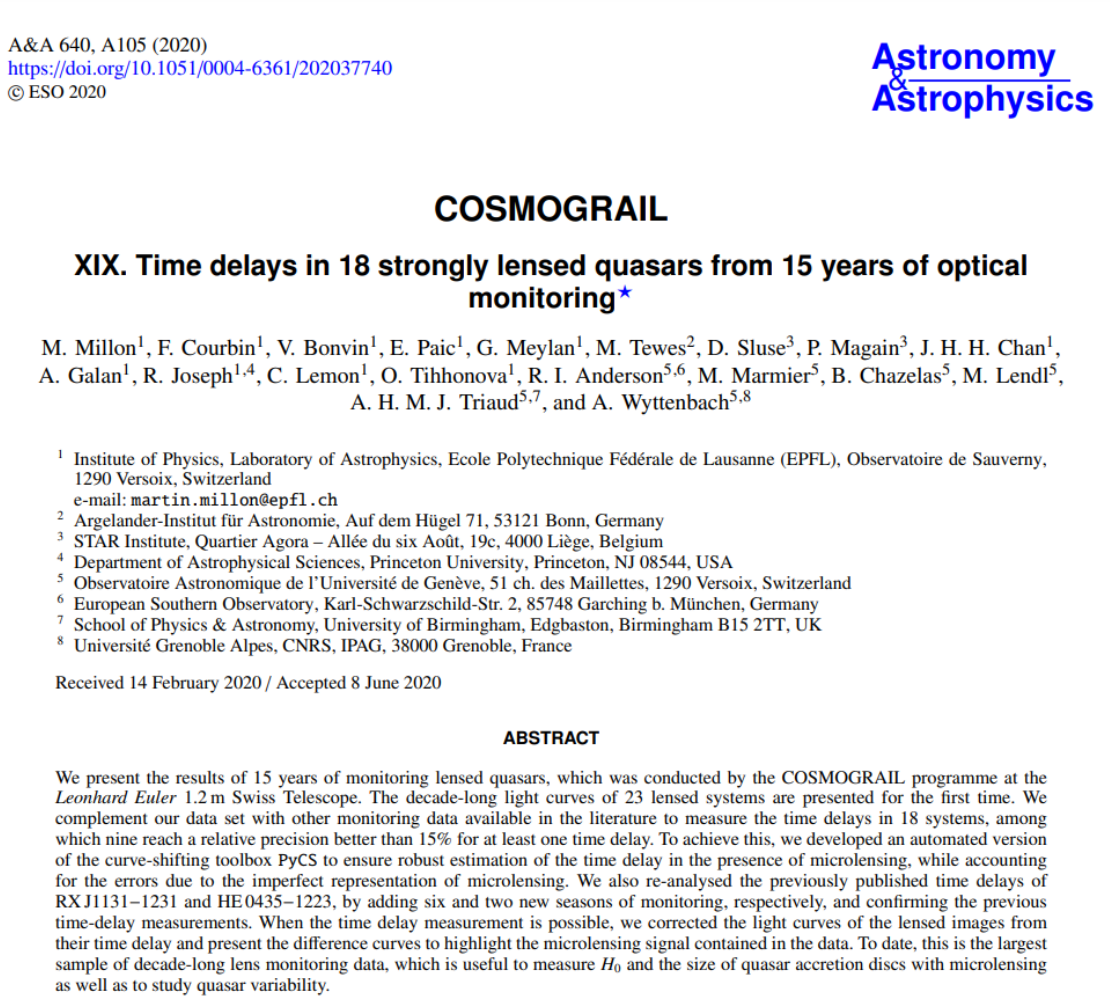

A&A 640, A105 (2020)
https://doi.org/10.1051/0004-6361/202037740
© ESO 2020

Astronomy & Astrophysics

COSMOGRAIL

XIX. Time delays in 18 strongly lensed quasars from 15 years of optical monitoring*

M. Millon[1], F. Courbin[1], V. Bonvin[1], E. Paic[1], G. Meylan[1], M. Tewes[2], D. Sluse[3], P. Magain[3], J. H. H. Chan[1], A. Galan[1], R. Joseph[1,4], C. Lemon[1], O. Tihhonova[1], R. I. Anderson[5,6], M. Marmier[5], B. Chazelas[5], M. Lendl[5], A. H. M. J. Triaud[5,7], and A. Wyttenbach[5,8]

[1] Institute of Physics, Laboratory of Astrophysics, Ecole Polytechnique Fédérale de Lausanne (EPFL), Observatoire de Sauverny, 1290 Versoix, Switzerland
e-mail: `martin.millon@epfl.ch`
[2] Argelander-Institut für Astronomie, Auf dem Hügel 71, 53121 Bonn, Germany
[3] STAR Institute, Quartier Agora – Allée du six Août, 19c, 4000 Liège, Belgium
[4] Department of Astrophysical Sciences, Princeton University, Princeton, NJ 08544, USA
[5] Observatoire Astronomique de l'Université de Genève, 51 ch. des Maillettes, 1290 Versoix, Switzerland
[6] European Southern Observatory, Karl-Schwarzschild-Str. 2, 85748 Garching b. München, Germany
[7] School of Physics & Astronomy, University of Birmingham, Edgbaston, Birmingham B15 2TT, UK
[8] Université Grenoble Alpes, CNRS, IPAG, 38000 Grenoble, France

Received 14 February 2020 / Accepted 8 June 2020

ABSTRACT

We present the results of 15 years of monitoring lensed quasars, which was conducted by the COSMOGRAIL programme at the *Leonhard Euler* 1.2 m Swiss Telescope. The decade-long light curves of 23 lensed systems are presented for the first time. We complement our data set with other monitoring data available in the literature to measure the time delays in 18 systems, among which nine reach a relative precision better than 15% for at least one time delay. To achieve this, we developed an automated version of the curve-shifting toolbox PyCS to ensure robust estimation of the time delay in the presence of microlensing, while accounting for the errors due to the imperfect representation of microlensing. We also re-analysed the previously published time delays of RX J1131−1231 and HE 0435−1223, by adding six and two new seasons of monitoring, respectively, and confirming the previous time-delay measurements. When the time delay measurement is possible, we corrected the light curves of the lensed images from their time delay and present the difference curves to highlight the microlensing signal contained in the data. To date, this is the largest sample of decade-long lens monitoring data, which is useful to measure H_0 and the size of quasar accretion discs with microlensing as well as to study quasar variability.

Figure 3.7: Cover page of Millon et al. (2020b), the largest COSMOGRAIL public data release.

With the advent of telescopes such as Gaia and PanSTARRs, able to map wide portions of the sky, the number of strongly lensed quasar discoveries increased dramatically (e.g., Lemon et al. 2018, 2023) reaching now a few hundred known instances. The recent launch of the Euclid telescope together with the

---

[I] https://www.eso.org/public/teles-instr/lasilla/swiss/
[II] https://www.iiap.res.in/iao/cycle.html
[III] https://www.mercator.iac.es/
[IV] https://telescope.livjm.ac.uk/
[V] These light curves are publicly accessible on https://obswww.unige.ch/~millon/d3cs/COSMOGRAIL_public/

incoming LSST, will bring this number to the thousands. It became clear that COSMOGRAIL needed to change its monitoring strategy to turn all the newly discovered systems into cosmological probes.

Following its initial success (Millon et al. 2020a), the high cadence program was extended with the addition of two 2m class telescopes: the Nordic Optical Telescope (NOT) [VI] and the VLT Survey Telescope (VST) [VII]. During this thesis I managed the target selection and data collection of both facilities and performed the data reduction for the NOT data.

3.2.1 Target selection

To focus the monitoring effort on strongly lensed quasars, we select the systems according to their suitability to Time Delay Cosmography:

- Visibility of the lensed arc and number of images: as discussed in Section 1.3, the deformed image of the lensed source offers valuable constraints on the mass model. For a similar reason, quadruply-imaged quasars are prioritized over doubly lensed ones.
- Image separation: the photometric measurement requires deblending the quasar images from the lensing galaxy and the extended source arc. We select targets with more than 1″separation to ease this process.
- Brightness of the images should be above 21 mag to ensure high SNR observations with a minimal exposure time.
- Ancillary data: we prioritize targets for which high-resolution imaging or spectroscopic data are secured.

Following this precepts, five targets were selected for the Nordic Optical Telescope: two quadruple lenses J1817+2729 and J2145+6345, two doubles SDSS 0806+2006, SDSSJ0921+2854 and the first discovered case of a lensed dual quasar PSJ1721+8842. The latter is particularly powerful for cosmographic inferences but also opens a new way to study high redshift dual quasars (Lemon et al. 2022). The length of an observational season is set by the time of the year when a given object is observable with an airmass of less than 1.5, and it depends on its declination.

3.2.2 Photometric measurement

We primarily gather data in the R-band due to its balanced advantages: quasar variability is more pronounced in bluer bands MacLeod et al. (2010), while the sky brightness is lower compared to bluer optical bands, particularly when the moon is present. Our typical approach involves capturing 4 or 5 dithered exposures per epoch, each lasting 300 or 360 seconds. This strategy prevents saturation of calibration stars and addresses camera defects such as cosmic rays and bad pixels.

The data reduction follows the standard approach detailed in Tewes et al. (2013) and Millon et al. (2020b). The bias and flat are corrected, and the sky is subtracted using the `SEXTRACTOR` software (Bertin & Arnouts 1996). Then, each exposure's Point Spread Function (PSF) is modelled thanks to a simultaneous Moffat

---

[VI] https://www.not.iac.es/

[VII] https://www.eso.org/sci/facilities/paranal/telescopes/vst.html

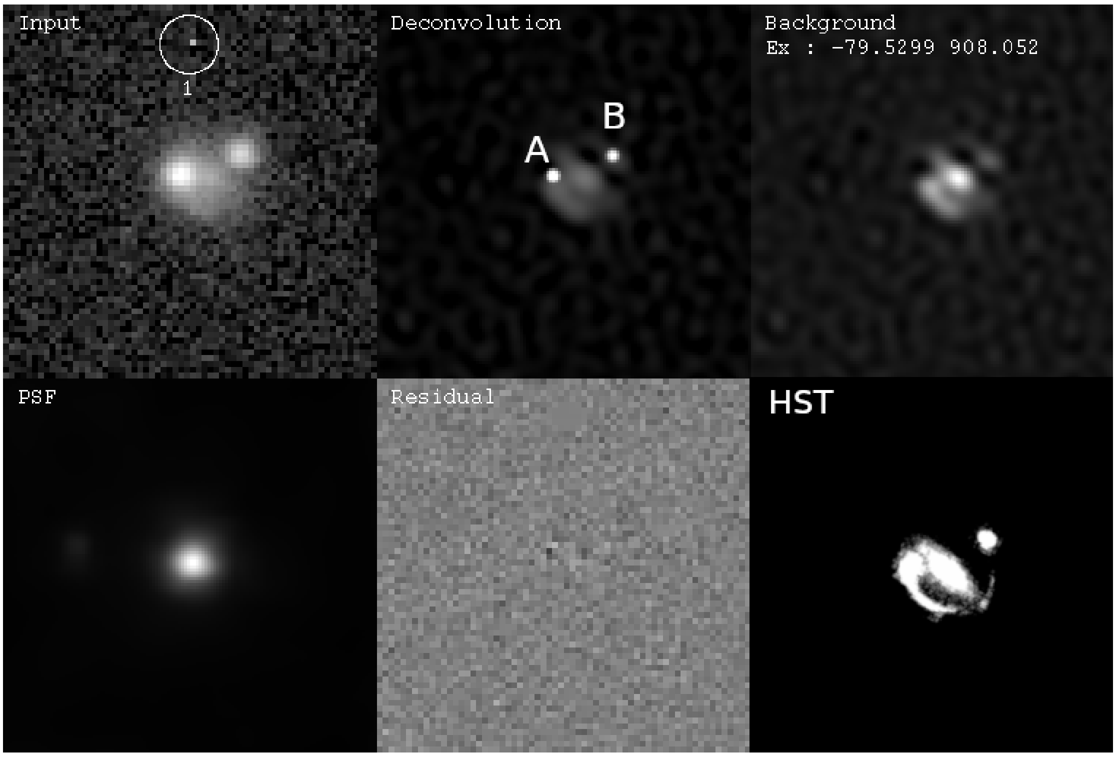

Figure 3.8: Exemple of the MCS deconvolution applied to Nordical Optical Telescope observation of SDSSJ0921+2854, a doubly lensed quasar monitored at the NOT. The top row displays the raw image, the deconvolved point sources, the modeled lens and extended source light. The bottom row displays the PSF modeled using stars of the field, the residuals of the fit and the high-resolution HST imaging of the system, which shows that the extended source and lens are modeled accurately.

profile combined with regularized pixel adjustments fit of ∼ 6 stars with similar luminosity as the lens in the field. The MCS deconvolution algorithm (Magain et al. 1998) is then applied to the lensed images in order to deblend the flux of an image from its counterpart, the lensing galaxy and the arc. As shown in Fig 3.8, the MCS algorithm produces a model consisting of an improved resolution Gaussian point sources for each image and a "pixel channel" containing extended features like the lens galaxy and the lensed host galaxy. The process fixes the pixel channel and relative astrometry of the quasar images for all exposures, allowing variations in image intensities to yield the photometry of each exposure.

The median and standard deviation of the photometry computed from the several exposures at a given epoch gives us the value of the photometry of the lensed images or this epoch.

Finally, a deconvolution of reference stars is carried out using the previously built PSF. Stars displaying the most photometric stability are chosen to calculate a median photometric normalization coefficient for each exposure. This step helps to correct image-to-image systematics resulting from PSF variations across epochs. The resulting light curves are shown for the 5 targets monitored at the NOT, which configurations are shown in Fig. 3.9

These light curves have a mean photometric error of 10 milli-mag, an example of measurement that is comparable to the precision of the 2.2m telescope. The apparent features in J1817, J2145 and PSJ1721 will allow the determination of the time delays using the `PyCS` method. A time-delay measurement example is

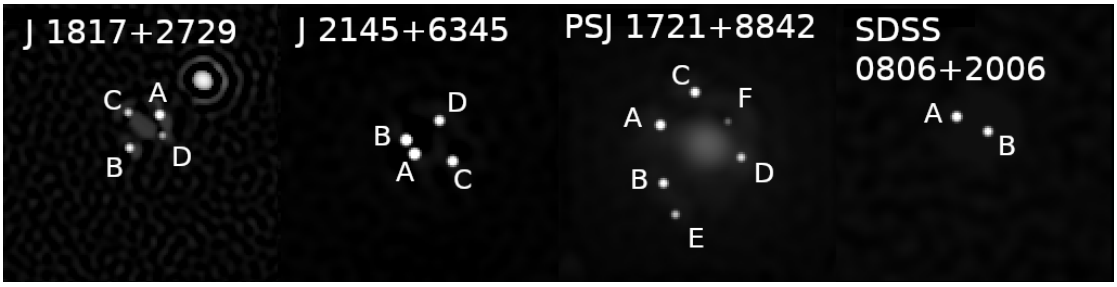
J 1817+2729
C
A
B
D
J 2145+6345
D
B
A
C
PSJ 1721+8842
C
F
A
B
D
E
SDSS
0806+2006
A
B

Figure 3.9: Deconvolved images of the NOT targets.

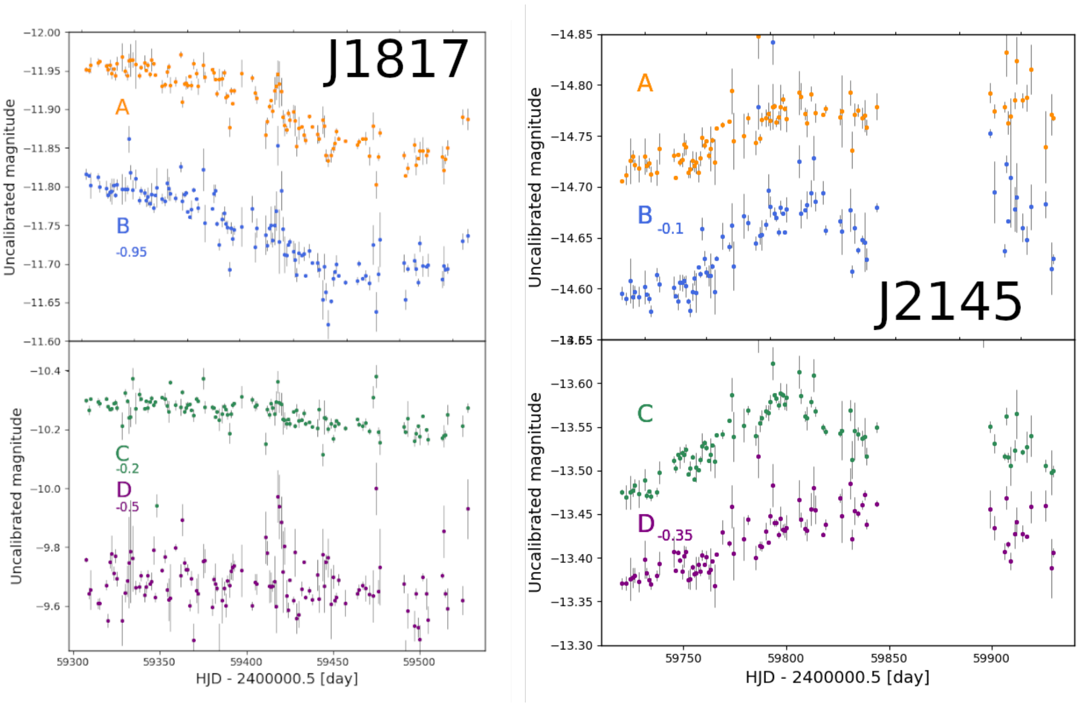

Figure 3.10: NOT light curves of ***Left panel:*** J1817+2729, ***Right panel:*** J2145+6345.

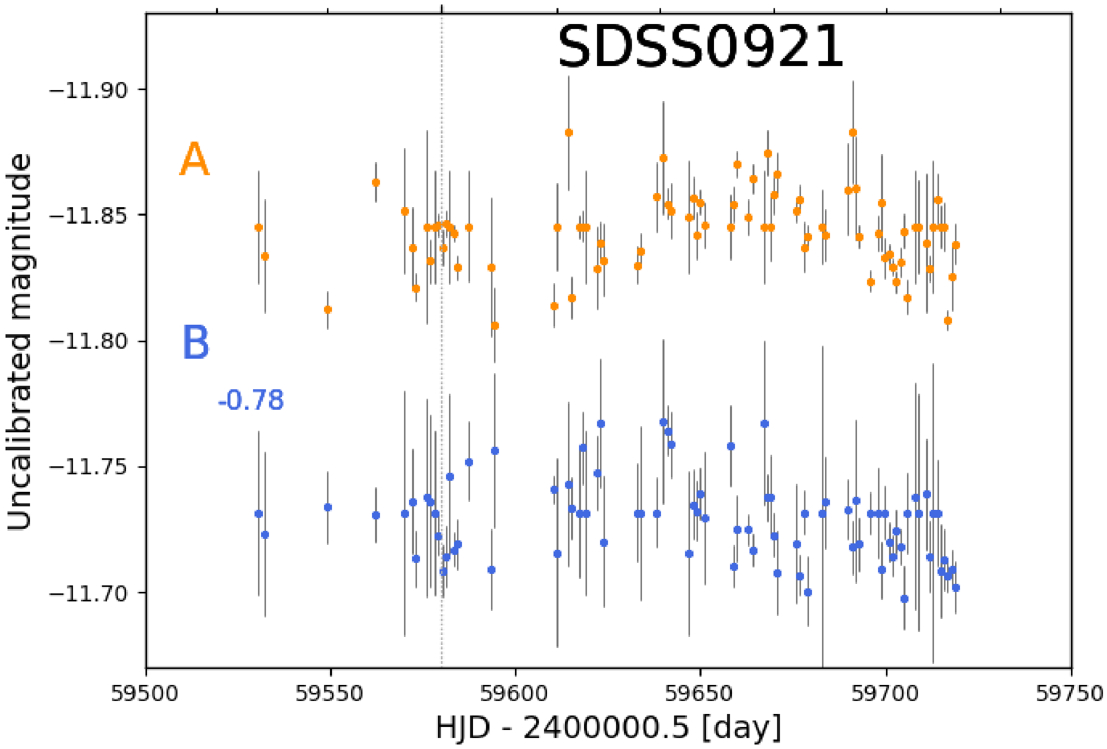

Figure 3.11: NOT light curves of SDSSJ0921+2854.

thoroughly presented in Section 3.3.2.

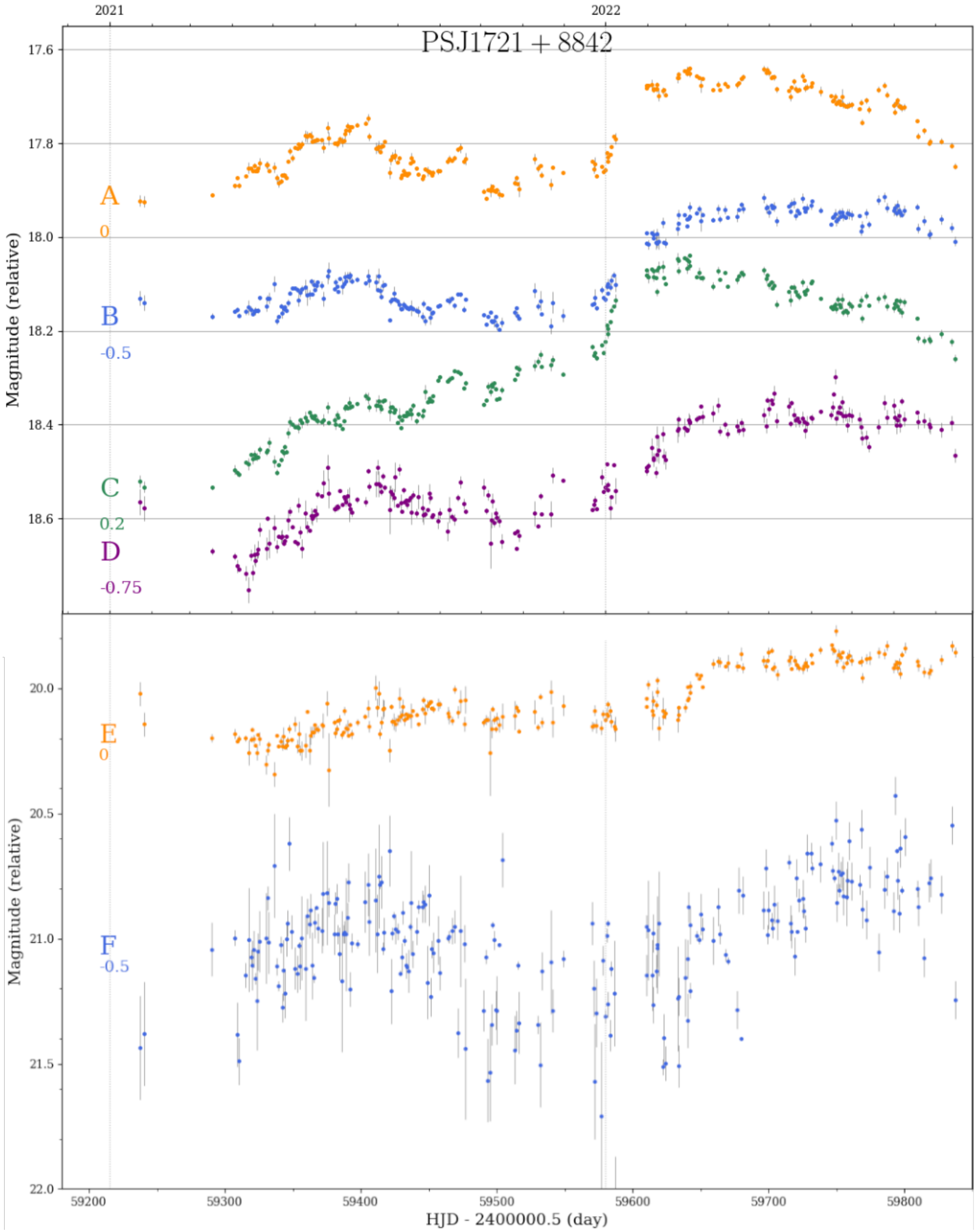

Figure 3.12: NOT light curves of PSJ1721+8842. The rapid rise of C suggests an undergoing fast microlensing event. Figure credits: Frédéric Dux

3.3 Measurement of H_0 with the doubly lensed quasar HE 1104−1805

As shown by Fig. 3.3, since doubly lensed quasars are likely to be more asymmetric and have wider separations than quadruply lensed ones, they probe different regions of the radial convergence profile. In light of the mass sheet degeneracy, doubles provide a complementary test of mitigation strategies mentioned in Section 3.1. Furthermore, for a given source position, two or four images can be created depending on the morphology of the lens (ellipticity, azimuthal structures) or the impact of additional perturbers (external shear). Quadruply imaged quasars offer more constraints on the lens mass model, yield more precise measurements of H_0 and have therefore been the focus of previous time-delay cosmography studies (see Fig. 3.5). Nevertheless, restraining the TDCOSMO sample to quads may expose the H_0 measurement to unknown selection biases related to the morphology or environment of the lens galaxy. Building a sample of fully analyzed doubly-lensed quasar offers a way to unveil and mitigate such biases.

Whether or not a bias is discovered, doubles are far more abundant than quads [VIII]; the extension of the TDCOSMO sample to reach the 1% precision will hence rely on the joint use of doubles and quads. So far, only one H_0-measurement was done with a double (Birrer et al. 2019). Using the SDSS 1206+4332 system it yielded $H_0 = 68.8^{+5.4}_{-5.1}$km s^{-1}Mpc^{-1} using parametric models to break the MSD. During this thesis, I implemented the first time-delay cosmography inference of H_0 with the double HE 1104−1805 while using spatially resolved kinematics to break the MSD. While Lidman et al. (2000) gave a first estimate of H_0 with this double using a time delay based on sparse light curves and oversimplified models, I here present a new measurement of the time delay based on 15 years of monitoring, a new modelling of the lens mass model using state-of-the-art modelling tools to which I add the measurement of $\kappa_{\rm ext}$and $\sigma_{\rm LOS}$.

3.3.1 Lens redshift

HE 1104−1805 is a doubly imaged quasar discovered by Wisotzki et al. (1993) who determined the redshift of the source $z_s = 2.32$ whereas the main lens one was more challenging to determine. First measurements by Wisotzki et al. (1993) and Courbin et al. (1998) relied on a damped Lyα (DLA) system at $z = 1.66$, but the first time delay estimate by Wisotzki et al. (1998) proved that the lens redshift could not be above 1, hence discarding this first measurement. Eventually, Lidman et al. (2000) measured $z_l = 0.729$, and a detailed comparison of the metallicity and ionisation of the DLA in A and B by Lopez et al. (1999) concluded that a protogalaxy lies in the line of sight between the source and the main lens. As this protogalaxy is not visible in the imaging of the system (see Fig. 3.26), it will not be included in the modelling.

3.3.2 Time Delay measurement

Light curve

As one of the first discovered strongly lensed quasars, multiple attempts at measuring its time-delay with different observations have emerged. First, Wisotzki et al. (1998) published 18 spectroscopic observations with the 3.6m ESO telescope spanning over 5 years and estimated that the time delay between images A and B, Δt_{AB}, should be within [109-292]days. Re-analysis of these data by Gil-Merino et al. (2002) and Pelt et al. (2002) show that this sampling is insufficient for a precise delay. With a better sampling of the

---

[VIII] For now, about 56 quads and 164 doubles are listed on the publicly available database https://research.ast.cam.ac.uk/lensedquasars/index.html

R-band photometry between 1997 and 2006 with the OGLE and SMARTS programs [IX], Poindexter et al. (2007) estimated $\Delta t_{\mathrm{AB}} = 152 \pm 3$ days using a Legendre-polynomial fit technique. Later, Morgan et al. (2008) re-estimated to $\Delta t_{\mathrm{AB}} = 162.2 \pm 6.1$ days by jointly fitting the time delay and accretion disk size with the Monte Carlo microlensing fitting method presented in Section 2.1.2. However, this method depends on physical assumptions such as the size of the source or mass-profile of the lens (i.e all parameters related to microlensing described in Section 2.1.2) that could bias the measurement if incorrect.

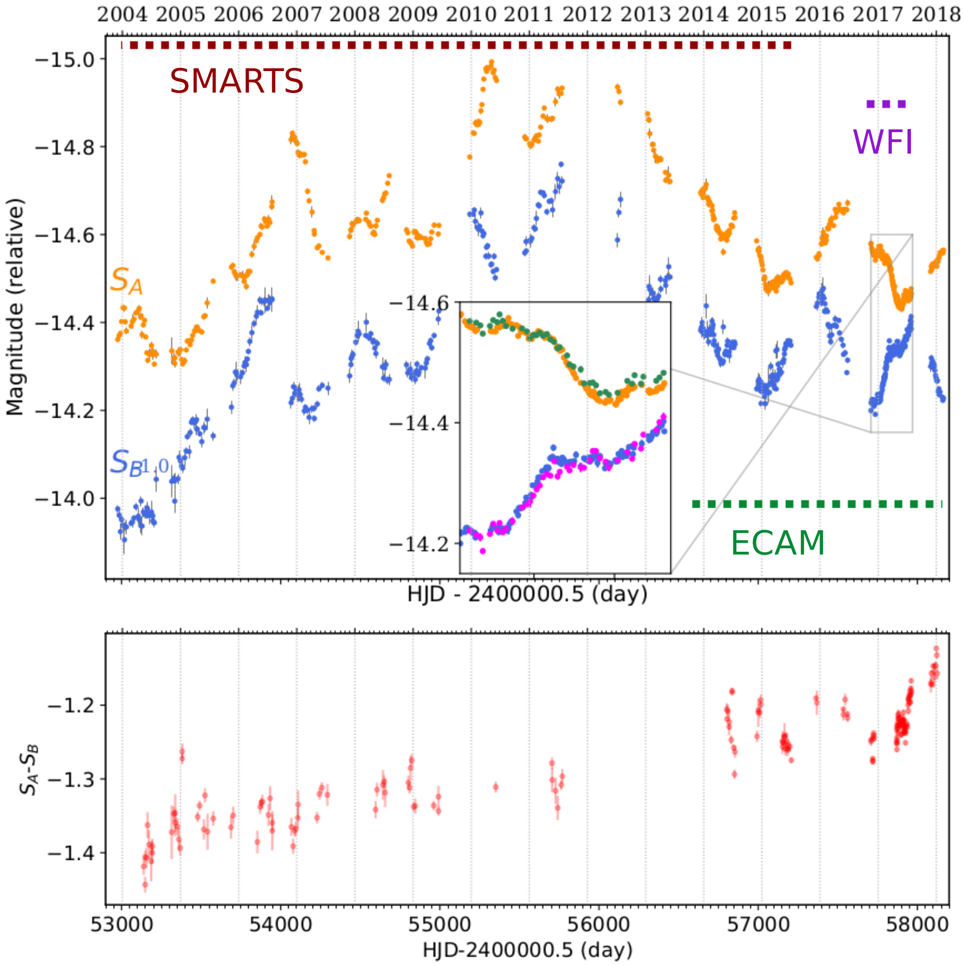

Figure 3.13: ***Top panel:*** HE 1104−1805 R-band light curve obtained by joining three datasets: SMARTS, ECAM and WFI whose time spans are highlighted by dashed lines. For clarity, the light curve of B was shifted by -1 mag. The inset zooms on the WFI dataset (orange and blue), showcasing its superior sampling to the ECAM dataset (green and magenta). ***Bottom panel:*** Microlensing light curve obtained by shifting the B light curve by $\Delta t_{\mathrm{AB}} = 178.7$ days and subtracting B to A where the observed light curves overlap.

In this work, we use 3 new unpublished datasets and apply the established PyCS spline-fitting method to re-estimate the time delay of HE 1104−1805. The first dataset is provided by The SMARTS program, which monitored it from 2003 to 2016 with a ~ weekly cadence. Next, the COSMOGRAIL program (Courbin et al. 2005) observed it every ~ 4 days with ECAM at the Leonhard Euler 1.2m Swiss Telescope from 2013 to 2018 and during the 2017 season with WFI at the MPG/ESO 2.2m Telescope every ~ 2 days. These three data sets will be called SMARTS, ECAM and WFI. The light curve shown in the upper panel

---

[IX] http://www.astro.yale.edu/smarts/

of Fig. 3.13 was obtained with the same methodology as in Millon et al. (2020a) and described in Section 3.2.

The three monitoring datasets presented are merged into a single light curve by fitting for eventual magnitude and flux shifts between instruments that could cause disparities in the level and shape of the light curves. The resulting dataset will be referred to as "ECAM+SMARTS+WFI".

Δt_{AB} measurement

The time delay was computed using the method described extensively in Millon et al. (2020b) relying on free knot spline fitting implemented in the PyCS python package (Millon et al. 2020d). Free-knot splines are piecewise polynomials where the mean number of days between two consecutive knots is controlled by the parameter η which filters out variation with shorter time scales. A single free-knot spline is used to model the intrinsic variability of the quasar visible in both light curves meanwhile an additional spline per light curve (parametrized respectively by η_{ml} and η_{intr}) models the extrinsic variability caused mainly by microlensing. A simultaneous fit of these three components with the time shift needed to match the curves is done using a visual first guess of the time delay as a starting point [X]. Fig. 3.14 shows an example of such fit, giving us a point estimate of the time delay.

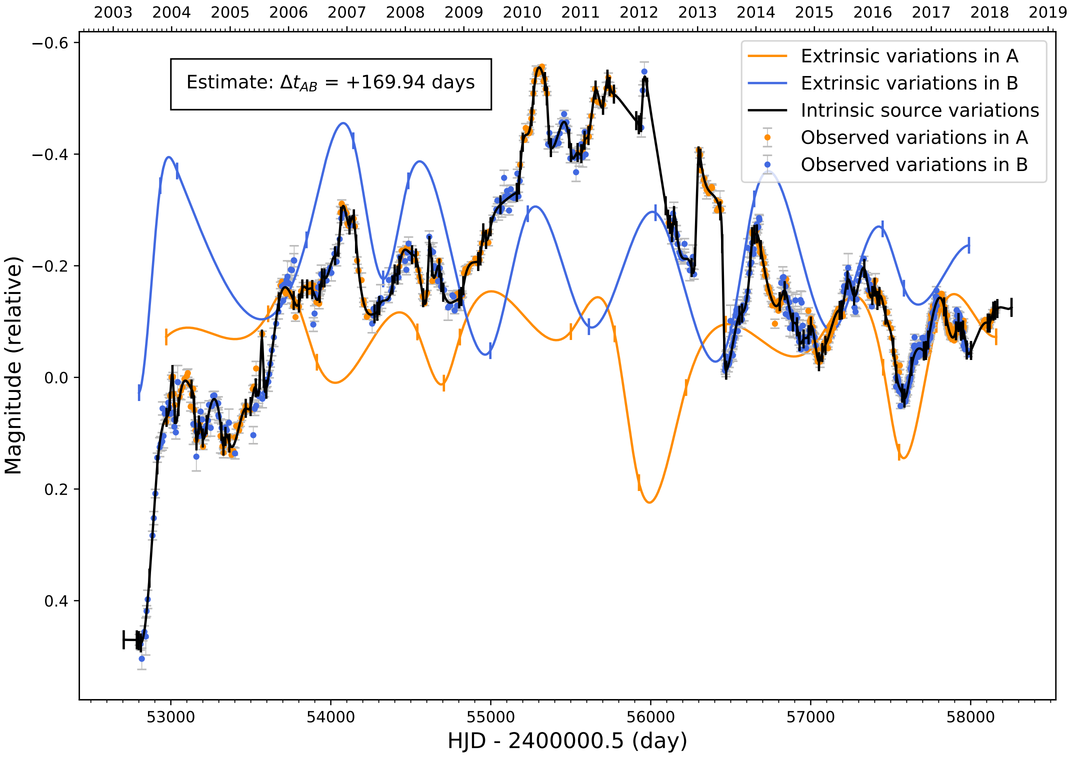

Figure 3.14: Example of a simultaneous fit of an intrinsic lightcurve with η_{intr} = 35 days and η_{ml} = 300 days. The time shift obtained by this fit gives a point estimate of the system's time delay.

It is important to note that since the three variability components are degenerate and not physically

---

[X] This is done on the publicly available D3CS tool: https://obswww.unige.ch/ millon/d3cs/COSMOGRAIL_public/

informed, the resulting splines can not be interpreted as the true source and microlensing variations. However, a visual inspection shows that the magnitude scales of the extrinsic variations are below 0.5 mag over several years, consistent with expected microlensing behaviour (see Section 2.1.2). We, however, note that the number of features in the extrinsic splines is higher than in most systems, which hints toward a more complex microlensing behaviour, such as noticed by Schechter et al. (2003) already suggested with previously published lightcurves, making the extrinsic fit sensitive to hyper-parameter changes.

This fit is then used as a generative model to create a set of mock light curve pairs with the same noise properties as the data and the same time delay. After running the time delay estimation on a set of light curves with starting points randomized uniformly around the first guess value, we take the median value as the final time delay value for a given ($\eta_{\rm ml}$, $\eta_{\rm intr}$).

To assess the uncertainty of this measurement in a data-driven way, a set of mock light curves is generated with built-in time delays uniformly drawn in an interval of ±20days around the median value obtained previously. The distribution of the difference between the measurement and the truth for each of the mocks gives an estimation of the systematic error (mean of the distribution) and the random error (standard deviation) of the time delay estimation. The final uncertainty of the time delay estimation is the sum in quadrature of these two sources of errors.

The choice of values for $\eta_{\rm intr}$ and $\eta_{\rm ml}$ is guided by the fact that quasars vary much faster than microlensing (see Section 1.2.3). Moreover, whether a given feature is mathematically attributed to the intrinsic or extrinsic splines depends on the flexibility balance between the splines. We, therefore, reproduce the same measurement for different values of these two hyper-parameters. Following Millon et al. (2020b), we take $\eta_{\rm intr} \in [25, 35, 45, 55]$ days and $\eta_{\rm ml} \in [150, 300, 450, 600]$ days when fitting the SMARTS, ECAM and the merged data sets. In contrast, the microlensing in the much shorter WFI data set is fitted with a spline having either 1 or 2 knots ($\eta_{\rm ml} \in [1, 2]$) since the microlensing variability is expected to alter the light curve on time scales longer than a year.

The top panel of Fig. 3.15 shows the time-delay measurements obtained by each hyper-parameter configuration ($\eta_{\rm intr}$,$\eta_{\rm ml}$) considered. We can note that as $\eta_{\rm ml}$ is decreased, the uncertainty of the time delay measurement is increased as the extrinsic spline becomes flexible enough to fit more The outlier (55,150) can be explained by the unbalanced rigidity of the intrinsic spline and flexibility of the extrinsic ones relative to the time scale each one is designed to address. Apart from this outlier, the measurements obtained are consistent with each other with variable precision. We gradually marginalize the most precise measurement with the others in precision-increasing order until the tension with the rest of the sample is lower than the threshold τ. Following the methodology of Millon et al. (2020b), we use $\tau = 0.5$ (i.e. no individual measurement is in a tension higher than 0.5σ with the final measurement) to have a conservative error estimation without being biased by outlier measurements.

The same experiment is carried out separately with each other dataset. The particular case of WFI is challenging because it covers only 253 days: given the long time delay, the light curves overlap on less than 100 days. Even though distinct features are visible and well-sampled in the WFI data, the complexity of the microlensing noticed previously cannot be adequately modelled with a single season. The bottom panel of Fig. 3.15 demonstrates that when the extrinsic variations are modelled by a single knot, the measurements are bi-modal, whereas allowing more flexibility with a second knot yields more self-consistent measurements. The precision of the combined values with the different subsets reflect this, and we hence chose to use the second subset's value: $\Delta t_{\rm AB}$=$180.2^{+12.0}_{-13.0}$ days, as the final measure with WFI.

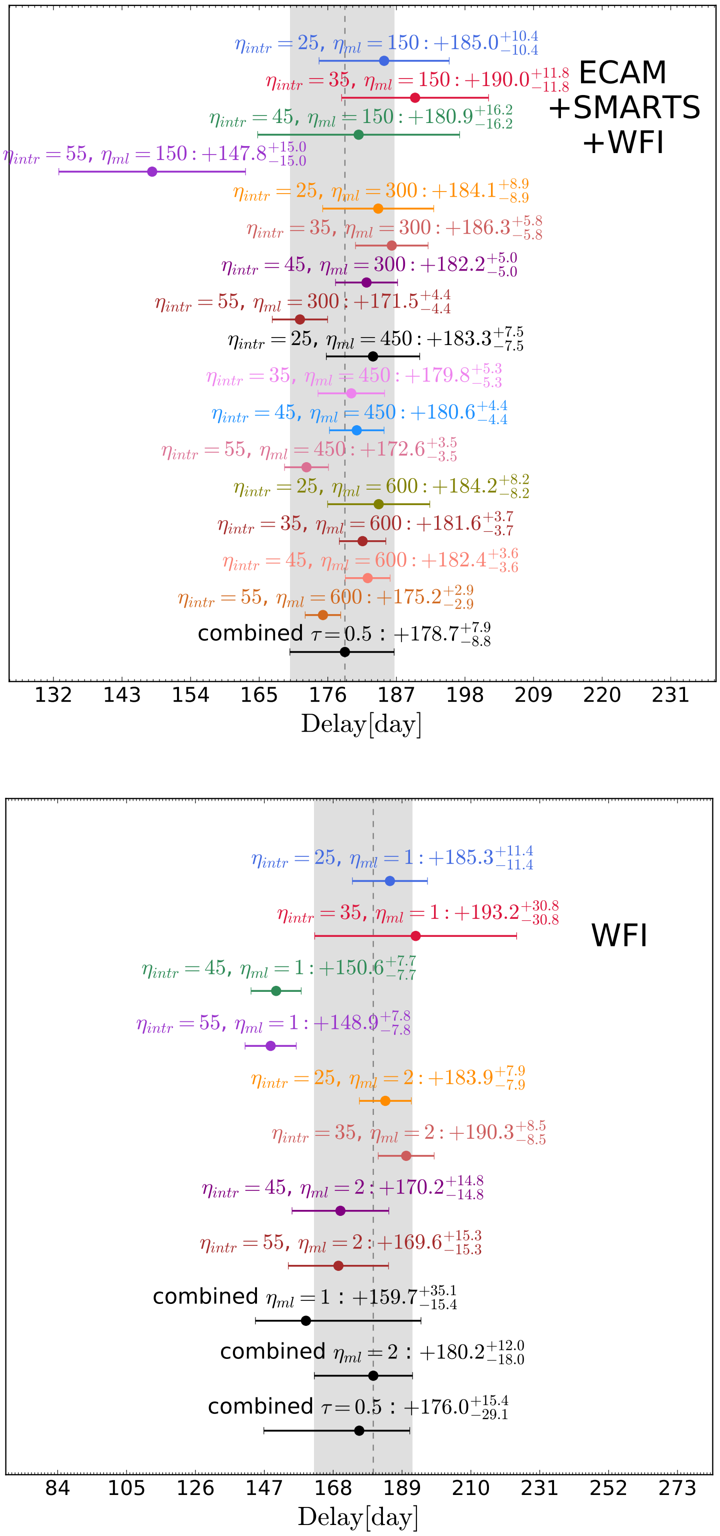

Figure 3.15: ***Top panel:*** Measurements of the time delay for different configurations of ($\eta_{\rm intr}$, $\eta_{\rm ml}$) with the merged ECAM+SMART+WFI dataset. ***Bottom panel:*** Same with the WFI dataset. The difference between the combination over the separate $\eta_{\rm ml}$ showcases the instability of the time-delay measurement with this dataset and the unreliability of the combination over the total set.

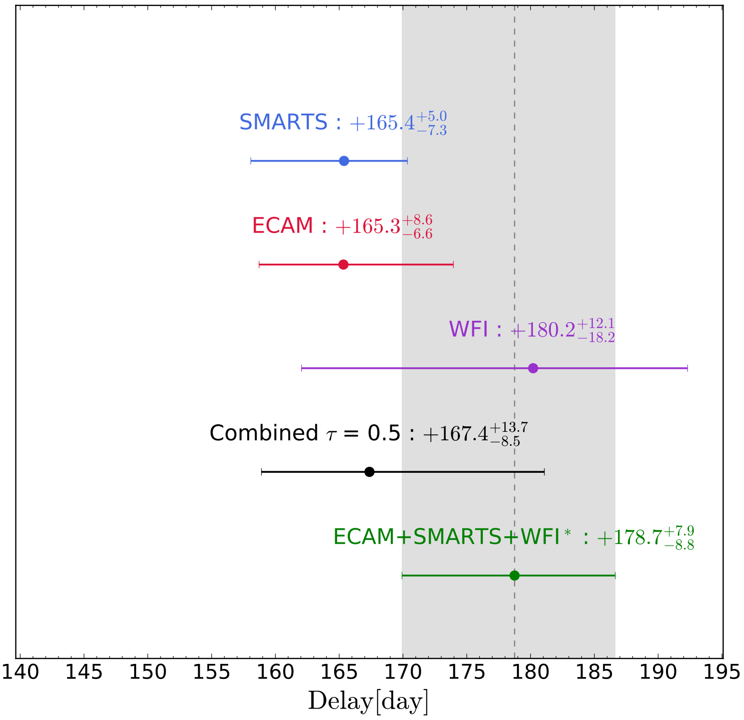

Figure 3.16: Measurement of Δt_{AB} for the different data sets. Since they are not independent of the first three estimates, the estimate with ECAM+SMARTS+WFI in green is not used to compute the marginalized measurement.

Fig. 3.16 shows the time delay measured on the three separate data sets, the combined value, and the measurement on the merged ECAM+SMARTS+WFI data set. The marginalization over the three data sets is relevant if we assume that each dataset is subject to different sources of systematic errors in the photometric measurement. However, the photometry was computed with the same method for each data set, and no discrepancies were observed between time delays measured with ECAM and WFI data on other lens systems (e.g. Millon et al. 2020b,a). As shown by the lower panel of Fig 3.13, the extrinsic variations are particularly complex during the 2017 season. As discussed previously, the WFI dataset cannot properly model the extrinsic and intrinsic variations. The time delay with the WFI data set is, thus, not robust enough for the marginalized time delay value to be trusted. By assuming that the sources of systematic errors in the photometry are equivalent in every dataset, we use the ECAM+SMARTS+WFI dataset, which allows us to use the entire period of the light curve to constrain the microlensing behaviour as well as to take advantage of the high cadence and high signal-to-noise display of the WFI dataset. The time delay measurement on this merged dataset of $\Delta t_{\mathrm{AB}} = 178.7^{+7.9}_{-8.8}$ days will be used in the rest of the cosmography analysis. We do not take into account an eventual microlensing time delay (Tie & Kochanek 2017) because its existence is yet to be observed, and it impacts the time delay only by a day in the worst cases (Bonvin et al. 2018), which is negligible given the length of the time delay.

3.3.3 Resolved kinematics measurement

MUSE Integral Field Unit spectroscopy

An Integral Field Unit (IFU) observation of the system was carried out with the Multi Unit Spectroscopic Explorer (MUSE) instrument on March 13th 2019, in wide field mode with adaptative optics. The observation wavelength ranges from 4700.03 Å to 9351.28 Å with a spectral resolution of R ~ 2500. To have the effective resolution of a spectrum, we need to model the Line Spread Function (LSF), which describes the shape and width of the spectral lines produced by an instrument. To do this, we fit a Gaussian to several sky emission lines found in the spectra of an empty region of the datacube. We find that the observed mean FWHM across the observed (lens rest-frame) wavelength range is 2.89Å (1.67 Å). This range includes the lens redshifted lines Ca H and Ca K lines at 3933Å and 3968Å along with the G-band at 4304Å while 5806Å to 5965 Å wavelengths were cut out due to the notch filter. The integrated cube along wavelength is shown in the top panel of Fig. 3.17. To ease spectral deblending of the quasar images from the lens galaxy, we subtract the point source light at each wavelength of the data cube. To do so, the point sources and lens galaxy light are fitted simultaneously with a Moffat and Sersic profile. As shown on the bottom panel of Fig. 3.17, we first perform the fit on 10 stacked wavelengths to constrain the parameters as a function of wavelength when performing the frame-by-frame fit. The wavelength change of the Moffat index β and the Full-Width-Half-Maximum (FWHM) are consistent with expected MUSE PSF modelling (e.g. Fusco et al. 2020; Weilbacher et al. 2020). The relative instability of the ellipticity of the PSF can be attributed to the abrupt changes in the quasar and lens light shape due to emission and absorption lines. For each wavelength frame, the Moffat part of the fit is then subtracted from the data to obtain the data cube displayed in the inset of Fig. 3.17.

The spectrum of the center of the lens galaxy obtained from this subtracted cube is shown in Fig. 3.18 and displays high SNR observation of the absorption lines Ca H, Ca K and g-band will be used to measure $\sigma_{\rm LOS}$ in Section 3.3.3. This data also contains new high-quality quasar spectra thanks to a small aperture integration on images A and B and the spectra of many of some perturbers annotated on Fig. 3.26 shown in Fig. 3.18.

Finally, we extract the spectra of the two brightest perturbers (P5 and P6) with a high enough SNR to measure the redshift.

$\sigma_{\rm LOS}$ measurement

As shown by the left panel of Fig. 3.19, we mask the pixels from the lens light cube further than 1.8 ″from the center of the galaxy as well as an area of 0.8 ″around the position of images A and B. In order to maximize the number of constraint on the radial velocity profile (see Fig. 3.4), the frame is then divided into three concentric rings of 0.6″width with a minimum signal-to-noise ratio of 15 to allow precise measurement of $\sigma_{\rm LOS}$in these bins. The integrated spectra of each bin is then fitted using the penalized pixel fitting (pPXF) method (Cappellari 2016). This method models the galaxy spectrum with a weighted linear combination of stellar spectra, broadened by a convolution with the galaxy line-of-sight velocity distribution (LOSVD). Additive and multiplicative Legendre polynomials are included in the model to improve the robustness to template mismatch and dust reddening. Any contaminating signal from residuals of the quasar images blended with the galaxy is accounted for by including a scaled quasar spectrum presented in Fig. 3.18.

As shown in Fig. 3.18, the most constraining features of the lens galaxy spectrum for the $\sigma_{\rm LOS}$ measurement

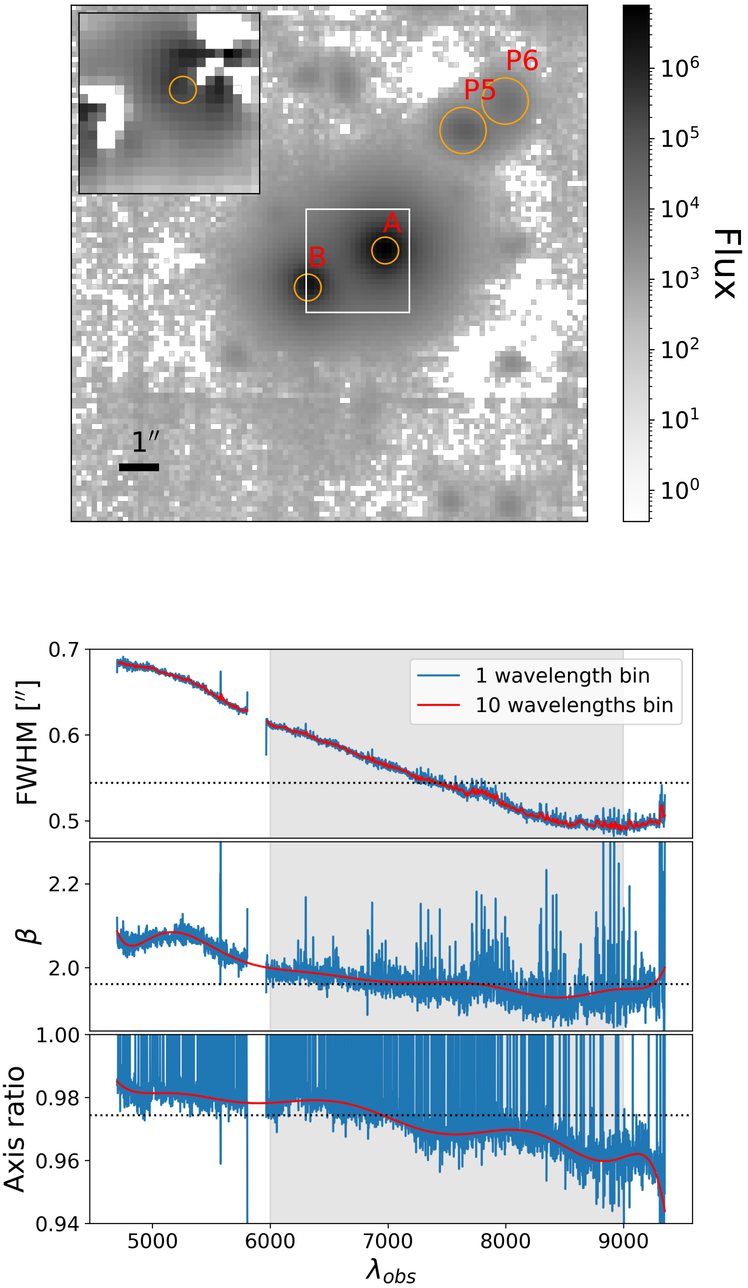

Figure 3.17: ***Top panel:*** MUSE data cube summed over all wavelengths. The apertures used to extract individual spectra of the quasar images, lens center and perturbers shown in Fig. 3.18 are represented by orange circles. The inset displays the point-source subtracted cube revealing the lens galaxy light. ***Bottom panel:*** PSF parameters fitted across wavelength. The values obtained when using stacks of 10 consecutive wavelengths are used as constraining prior for the wavelength-by-wavelength fit. The shaded area indicates the range of wavelength used for the $\sigma_{\rm LOS}$ measurement, and the dotted lines highlight the mean value of the parameters in this range.

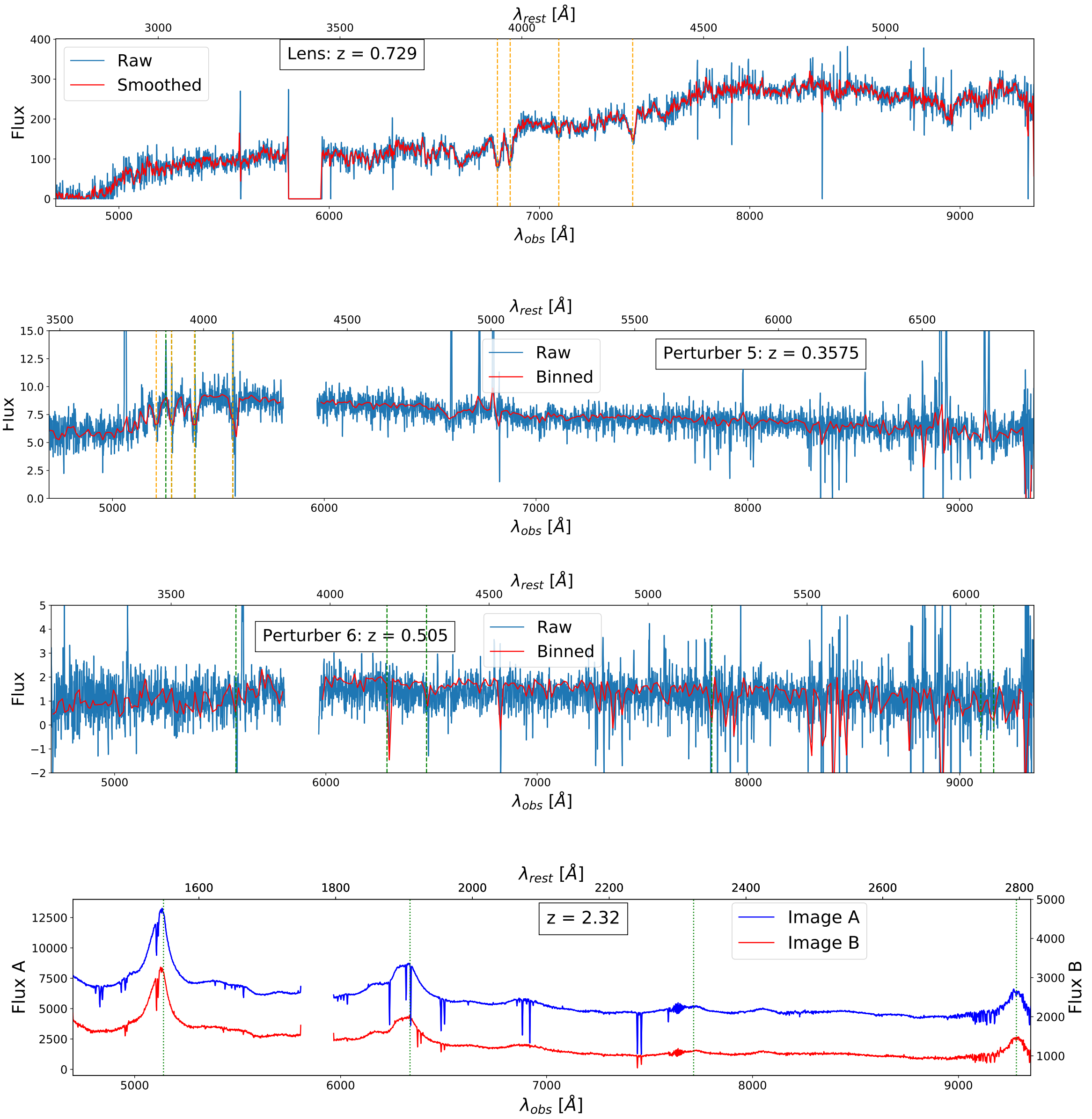

Figure 3.18: Integrated spectra from the MUSE data cube with apertures shown in Fig. 3.17. The binned flux is computed by imposing a minimal SNR of 5 per wavelength bin. From top to bottom, **Lens center:** from left to right the stellar absorption lines Ca H, Ca K, H δ and g-band (orange dashed lines) are consistent with the previously determined $z_l = 0.729$. **P5:** from left to right, the galactic emission lines Ne III, He I, H ϵ and H δ are highlighted with green dashed lines and allow us to measure $z_5 = 0.3575$. We also identify the stellar absorption lines H γ, HE I, Ca H and Ca K allowing a velocity dispersion measurement. **P6:** from left to right the lines Mg I, Ca II O II, H β and O III doublet allow us to measure $z_6 = 0.505$. **Quasar images:** from left to right, we recognize the C IV, C III, C II and Mg II emission lines.

are the Ca H, Ca K and g-band absorption lines identified respectively at 6800 Å, 6828 Å and 7395 Å in the observed frame. To focus the fit on these lines and avoid regions of the spectrum that could be dominated by the C IV and C III emission of the quasars, we restrict the wavelength range to [6000:9000] Å (in the rest-frame [3530:5260]Å).

The stellar templates used for this fit are the high-resolution spectra (R~9700 and FWHM= 0.43 Å) of 628 stars in the UVB range (3000-5560 Å) released as the X-Shooter Spectral Library (Gonneau et al. 2020). To make these templates compatible with the observations, we degrade their resolution with a convolution leading to the same FWHM of the LSF in the galaxy's rest frame.

Following Westfall et al. (2019) we choose an additive polynomial degree of 10, to have sufficient flexibility to fit the data without introducing bias by overfitting it as this study observed when taking higher degrees. To complete the fitting setup, we include the modelling of galactic gas emission lines within the considered range that do not appear in the stellar templates and could bias the measurement. An example of the $\sigma_{\rm LOS}$ estimate in each bin given by a fit with this fiducial setup is shown in Fig. 3.19. However, this arbitrary choice together with the choices of the fitting range and stellar template choice, can significantly bias the estimate (e.g., Westfall et al. 2019; Mozumdar et al. 2023; Shajib et al. 2023).

To estimate systematic and statistical uncertainty of the $\sigma_{\rm LOS}$ measurement in a given bin, we create 50 hyper-parameter configurations with different:

- wavelength ranges, with extreme values uniformly drawn from ([6000,6150]:[8850,9000])Å,
- stellar templates used, following Shajib et al. (2023), 3 different sets of 40 X-shooter spectra are created and used alternatively,
- degree of the additive polynomial, following the recommendation of Westfall et al. (2019), we use degrees between 4 and 10 [XI],

For each fitting setup, we create 50 realizations of Gaussian noise with the same standard deviation as the difference between the observed and binned spectra. The measurement of $\sigma_{\rm LOS}$ is therefore based on 2'500 different estimates of $\sigma_{\rm LOS}$ for a given bin. Additionally, the estimate displayed in the right panel of Fig. 3.19 shows that the depth of observed Ca K and g-band lines can be altered by the presence of sky gas emission lines. To test the robustness of the measurement against this disturbance, we repeat the measurement while masking the Ca K ([6794;6862] Å), g-band ([7361;7430] Å) or both.

The different measurements in each bin are displayed in Fig. 3.20. The final value of $\sigma_{\rm LOS}$ for each bin is marginalized over these four cases and yields $\sigma^1_{\rm LOS} = 282 \pm 21$ km s^{-1}, $\sigma^2_{\rm LOS} = 250 \pm 36$ km s^{-1} and $\sigma^3_{\rm LOS} = 189 \pm 49$ km s^{-1}. Ultimately, the whole set of estimates of the 3 bins $\sigma_{\rm LOS}$ allows us to build the covariance matrix between each bin's velocity measurement.

Furthermore, we apply the same process to the stellar absorption lines identified on the spectrum of P5 shown in Fig. 3.18. In this case, we use the observed wavelength range [(4600,4700):(5600,5700)]ÅÅs shown by the top panel of Fig. 3.21, the absorption lines are not altered by the sky but by galactic gas emission lines. We thus incorporate those in the model without testing different masks. The final value obtained is $\sigma^{P5}_{\rm LOS} = 123 \pm 71$ km s^{-1}.

[XI] For more details, we refer the reader to Fig.14 of this paper.

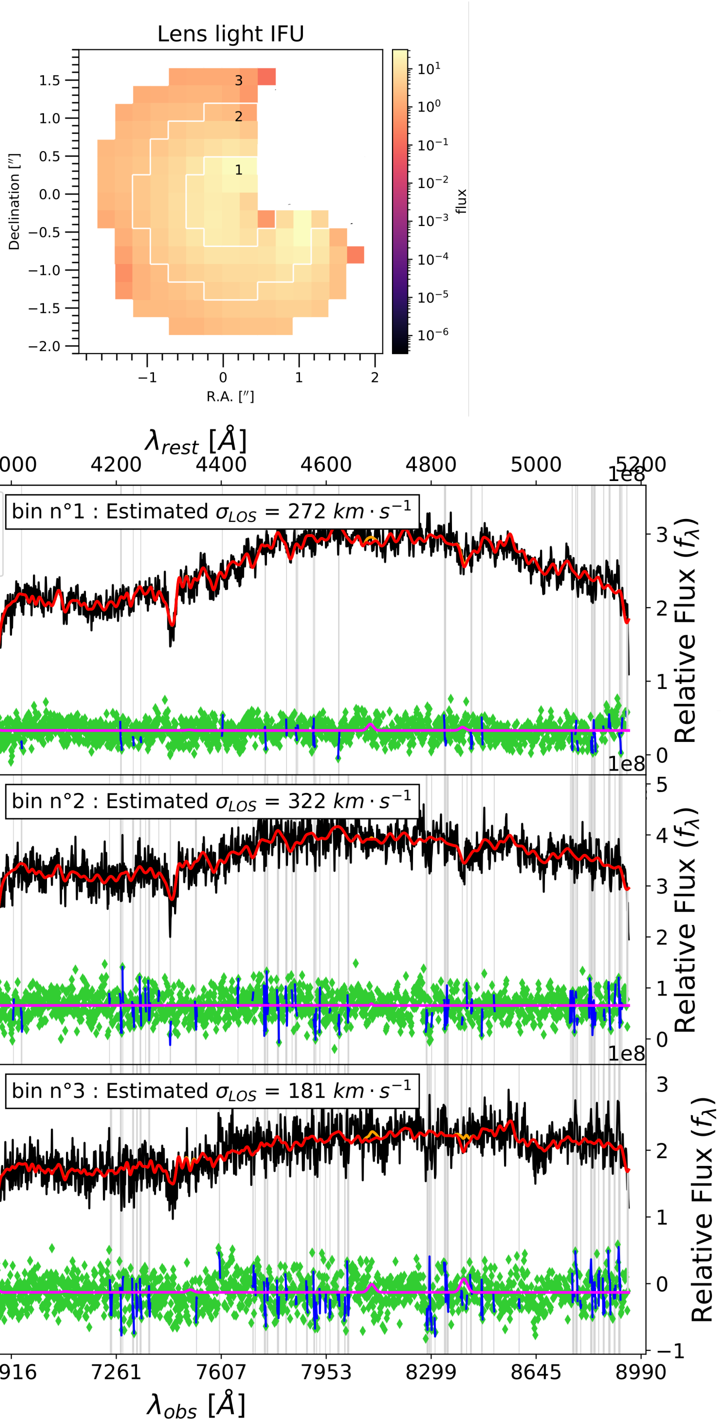

Figure 3.19: Velocity dispersion point-estimate in the 3 radial bins of HE 1104−1805's lens galaxy. ***Top panel:*** Mean of the MUSE data cube after PSF subtraction and masking with overlayed bin numbers and contours. ***Bottom panel:*** Example of a pPXF fit of the integrated spectra of each bin using the fiducial setup, $3-\sigma$ outliers from the binned spectrum marked in grey are apparented to sky emission lines and are therefore masked for the fitting.

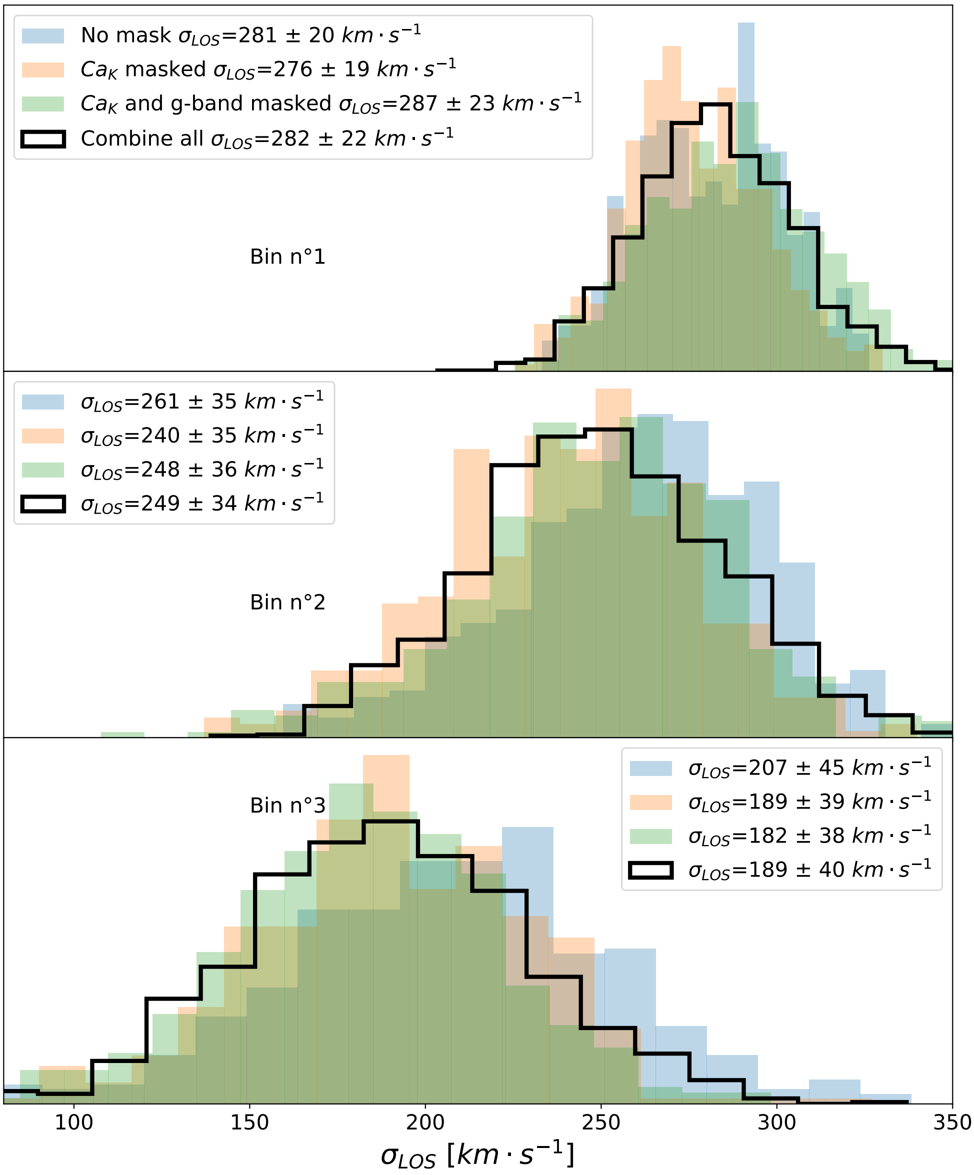

Figure 3.20: Histograms of 2’500 estimates obtained with different ranges of wavelength, realization of the noise, set of stellar template and degree of the additive polynomial used. This experiment was repeated with a mask on the Ca K line, a mask on both Ca K line and g-band and while masking regions of the spectrum affected by sky lines. The marginalization over these four cases gives us our final measurement.

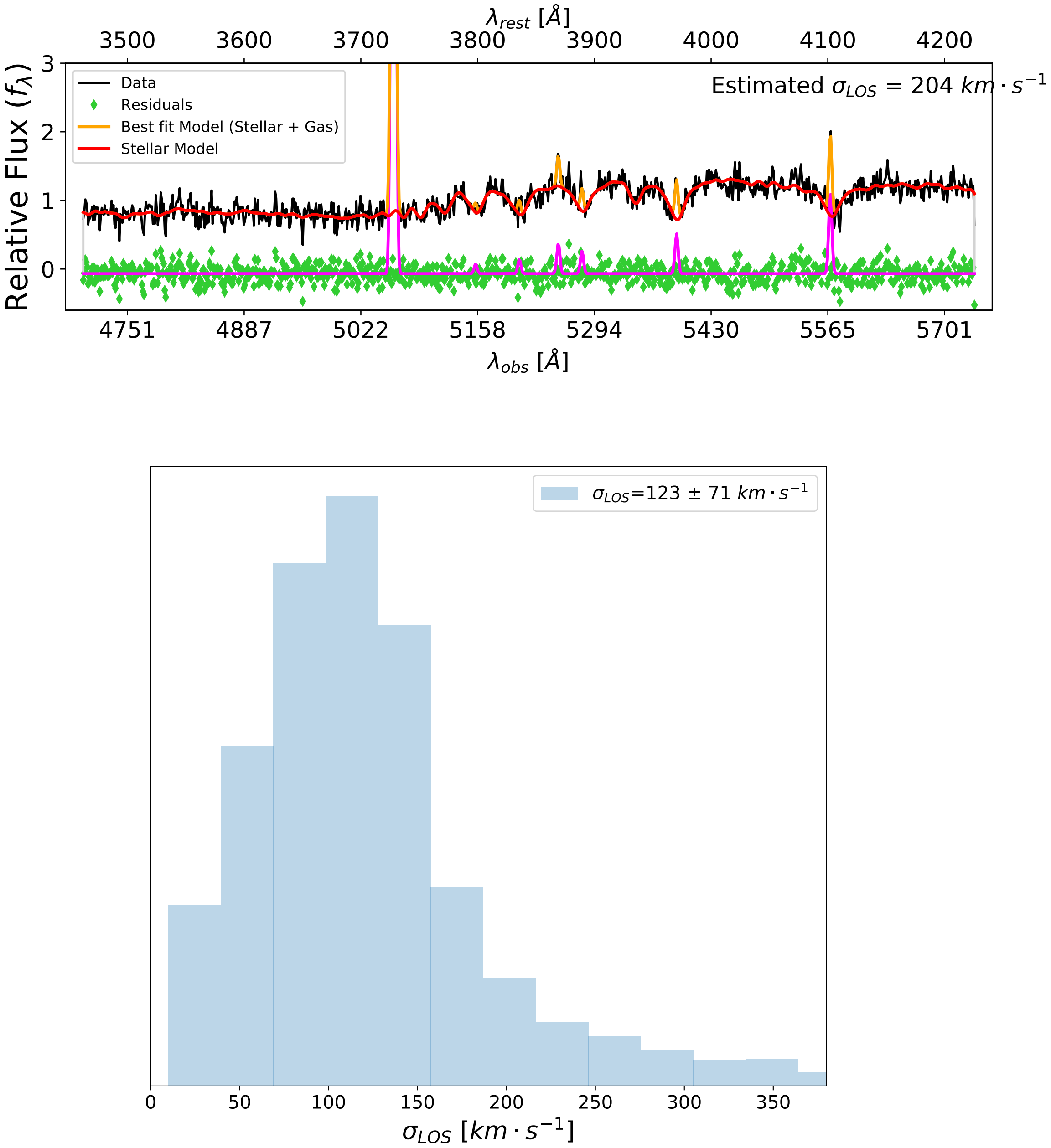

Figure 3.21: Measurement of the P5 stellar kinematics. ***Top panel:*** Point-estimate of $\sigma_{\mathrm{LOS}}{}^{\mathrm{P5}}$ using the fiducial setup with the updated wavelength range. ***Bottom panel:*** Histograms of 2’500 estimates obtained with different ranges of wavelength, realization of the noise, set of stellar template and degree of the additive polynomial used.

3.3.4 Line-Of-Sight analysis

Wide-Field imaging

The area covered by the lens field is encompassed by the Subaru Hyper Suprime-Cam (HSC) Strategic Survey Program region. Fig. 3.22 shows this program's i-band wide-field imaging. In addition, we use the g and r band observation made by the same telescope and the u band imaging made with the Canada France Hawaii Telescope (CFHT). Using the bright star masks and photometric redshift probability density functions furnished by the HSC team, we measure the photometry of each galaxy in the field brighter than 26 mag and with $z \leq z_{\rm source}$. This allows us to create a catalogue of position, magnitude and photometric redshifts for the objects of interest.

Due to the significant presence of nearby perturbers around the lens (as shown in Figure 3.26), our initial step involves identifying the perturbers that are explicitly incorporated into the lens model thanks to the flexion shift criterion, leaving the remaining ones for computation through the external convergence $\kappa_{\rm ext}$.

Perturbers explicitly included in the lens model

We use the $M_* - \sigma_{\rm LOS}$ relation obtained Zahid et al. (2016) on galaxies up to redshift 0.7 to estimate the mass-to-light ratio, M/L, with ${\sigma_{\rm LOS}}^{\rm P5}$ previously measured. The flux determined with a circular aperture around P5 in the F160W band converted into luminosity using a fiducial cosmology with H_0 =70 km s^{-1}Mpc^{-1}and $\Omega_{\rm m} = 0.3$ [XII]. By applying the same M/L ratio to the other perturbers, we estimate their mass and $\sigma_{\rm LOS}$. By approximating their mass distributions with an SIS we compute their Einstein radius, $\theta_{\rm E,SIS}$ with :

$$\theta_{\rm E,SIS} = 4\pi \left(\frac{\sigma_{\rm LOS}}{c}\right)^2 \frac{D_{\rm ps}}{D_{\rm s}} \tag{3.43}$$

with $D_{\rm ps}$ and $D_{\rm s}$ the angular diameter between the source and perturber and between the observer and the source, respectively.

Perturber	Redshift	$\theta_{\rm E,SIS}$ [$''$]	$\log(\Delta_3 x)$
P1	-	$0.2^{+0.5}_{-0.2}$	$-4.2^{+0.5}_{-1.9}$
P2	-	$0.2^{+0.6}_{-0.2}$	$-3.1^{+0.5}_{-1.9}$
P3	-	$0.1^{+0.1}_{-0.1}$	$-4.5^{+0.6}_{-1.4}$
P4	-	$0.3^{+0.3}_{-0.3}$	$-4.1^{+0.4}_{-1.2}$
P5	0.3575	$0.37^{+0.16}_{-0.16}$	$-3.0^{+0.5}_{-0.5}$
P6	0.505	$0.35^{+0.26}_{-0.27}$	$3.3^{+0.4}_{-1.3}$
P7	-	$0.2^{+0.7}_{-0.2}$	$-4.2^{+0.5}_{-1.8}$
P8	-	$0.3^{+0.4}_{-0.3}$	$-3.7^{+0.5}_{-2.0}$

Table 3.1: Estimations of the perturbers' Einstein radii and flexion shifts based on their luminosity and the M/L ratio computed with P5.

Because of the luminosity of the perturbers without a redshift measurement, we assume they lie between the closest perturber P5 and the source. We therefore repeat the computation with redshifts uniformly drawn between z_5 and $z_{\rm s}$ and take the mean and the extreme 0.3 percentiles ($3-\sigma$ in a Gaussian distribution) of the resulting distribution as the final estimate.

[XII] Given the uncertainty of the ${\sigma_{\rm LOS}}^{\rm P5}$ measurement, the uncertainty on the fiducial cosmological parameters can be neglected

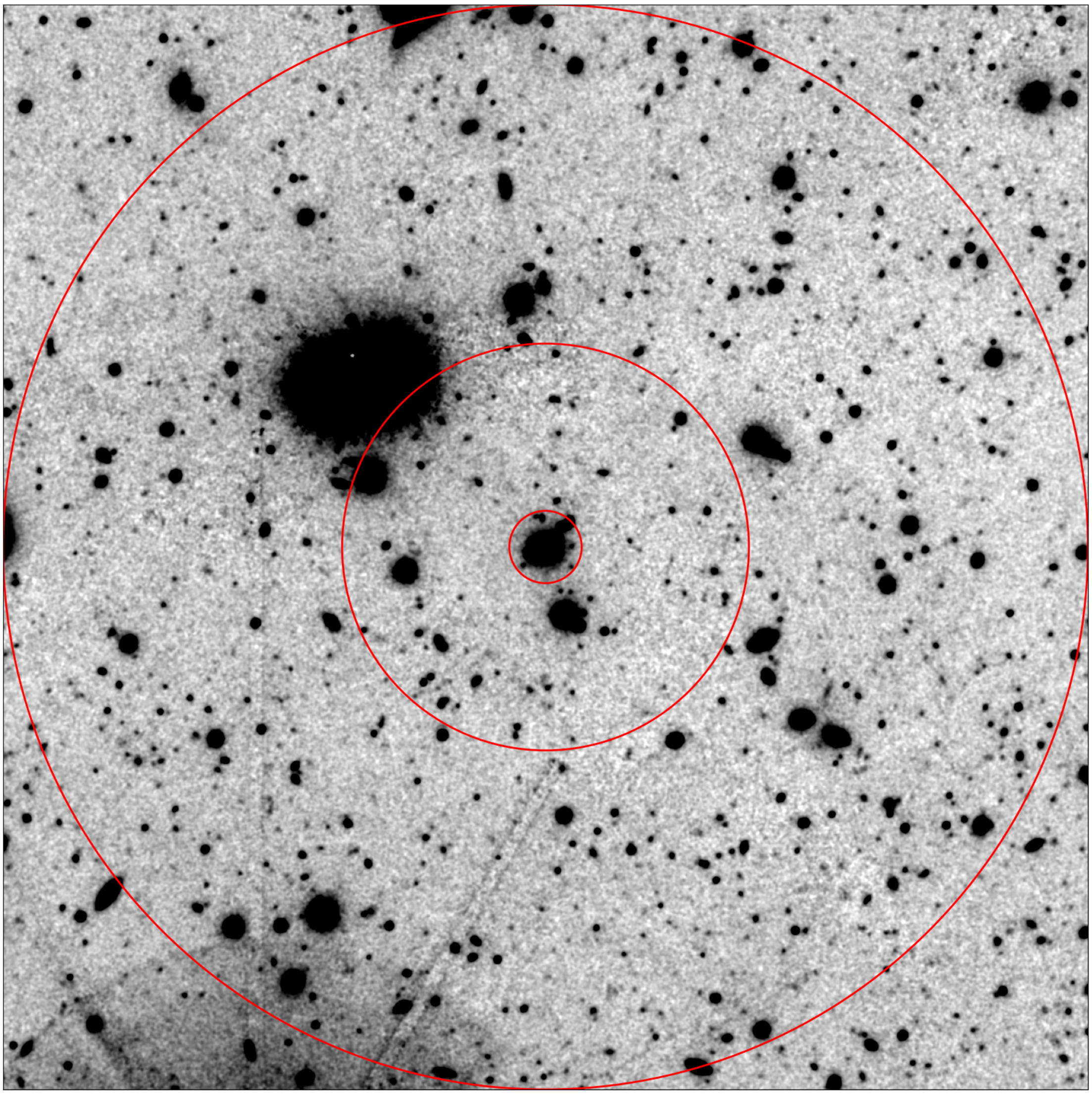

Figure 3.22: Wide-Field Imaging of HE 1104−1805 in the i-band. Red circles denote regions within 8 ″, 45″and 120 ″of the center of the lens.

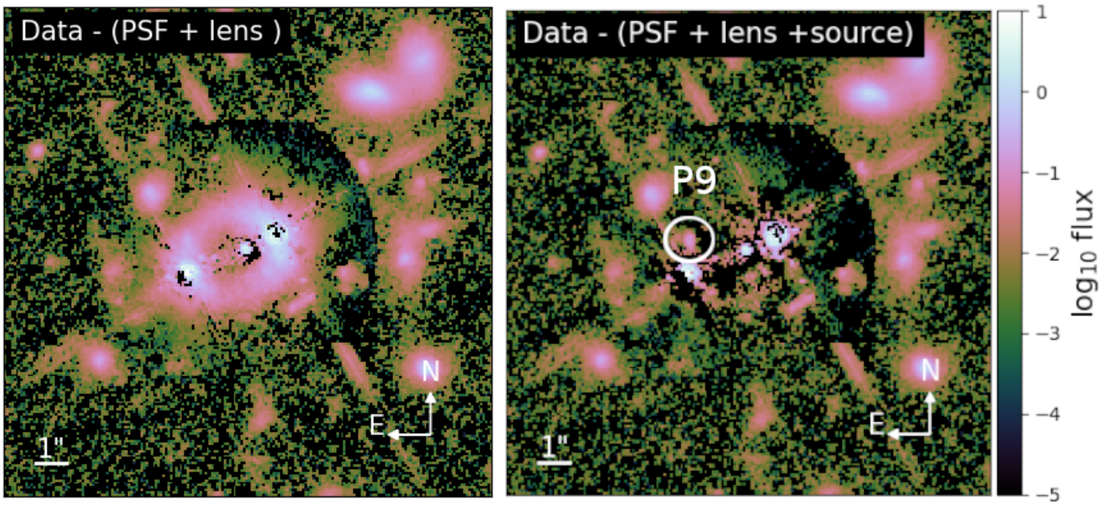

Figure 3.23: Detection of a 9th perturber near image B. ***Left panel:*** F160W band observation with PSF and lens light subtracted. ***Right panel:*** PSF, lens and source light subtracted, the luminous component is circled in white. Because of its proximity with image B ($\sim 0.6\,''$away) and its position within the source light, we include it in the lens light model.

We can then estimate the flexion shift caused by each perturber using Eq. 3.36. The results presented in Table 3.1 show that even when marginalizing on their redshift, the flexion shift of these perturbers are all potentially superior to 10^{-4}. They can therefore significantly influence the image's position and should be included in the mass model.

In addition, the subtraction of the PSF, lens and source light with a preliminary SIE model, shown in Fig. 3.23 revealed the presence of a luminous component $\sim 0.6''$ from image B. Without a counter-image indicating that this feature belongs in the source, we treat this component as a perturber, hereafter P9. Because of its faintness, the spectra of P9 can not be extracted from the MUSE data cube and its mass cannot be estimated with the same technique employed for all other perturbers.

$\kappa_{\rm ext}$ measurement

We use the number count method described in Section 3.1.1. As detailed previously, the treatment of perturbers within 8$''$from the lens is part of the explicit lens model. We, therefore, mask this region from the number counting. Similarly to Wells et al. (2023), the weights used are: the inverse distance $w_{1/r}$, the potential $w_{\rm p}$, the redshift $w_{\rm z}$ and the distance weighted redshift $w_{z/r} = w_{\rm z}/r$. Their computation is displayed in Fig.3.24.

As detailed in Wells et al. (2023), we compare the obtained distribution of weights to similar fields in the `Millenium` simulation (Springel 2005) to determine the relative density of the observed galaxy field. The final measurement $\kappa_{\rm ext} = -0.036^{0.35}_{-0.034}$ is used for the rest of the cosmographic analysis in compliance with the perturber inclusion strategy.

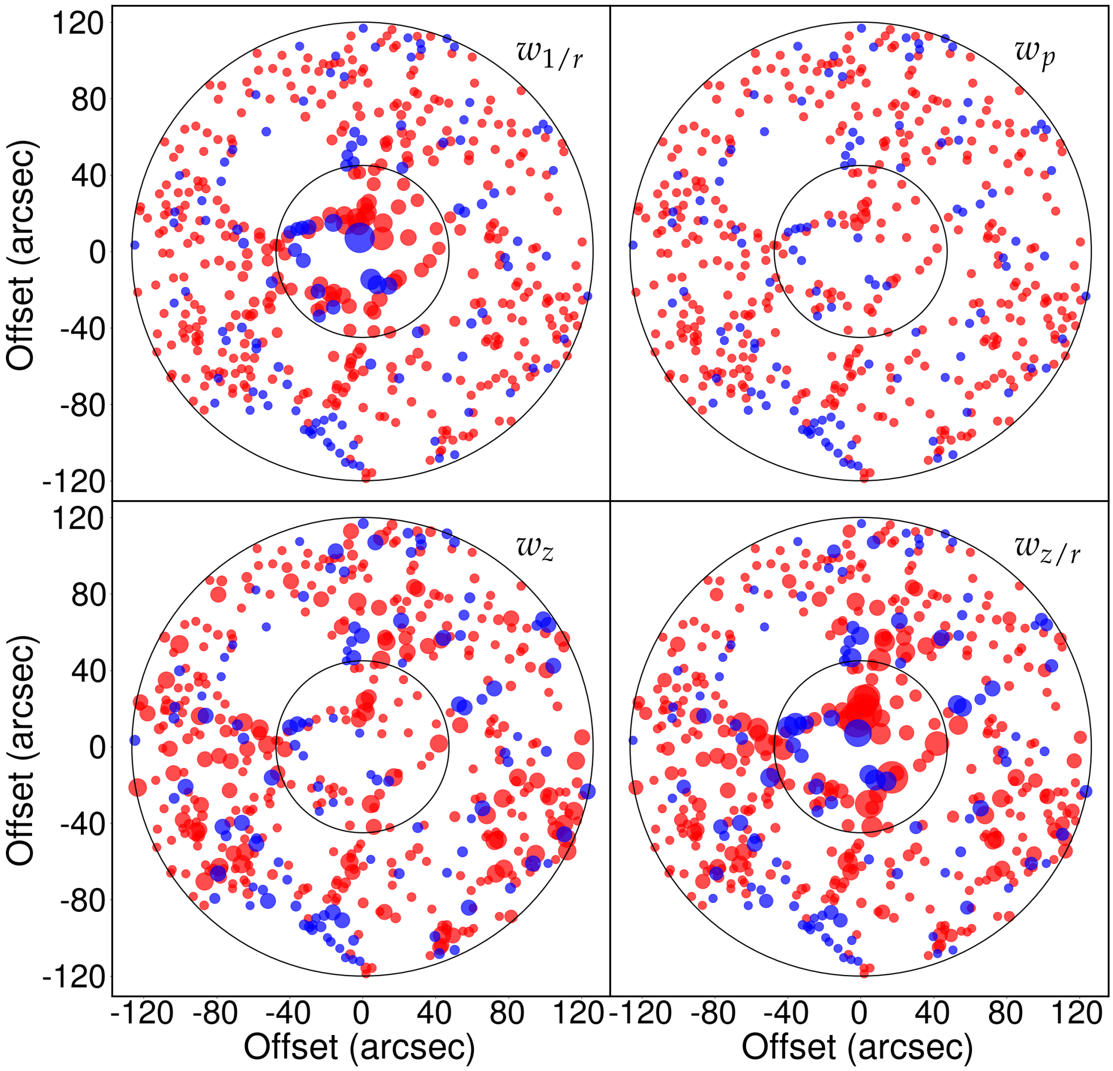

Figure 3.24: Position and weight (size of the dot) of galaxies between us and the source. Black circles indicate the 45″and 120″apertures. Blue dots correspond to objects with i-magnitudes less than 23, while red dots correspond to those with magnitudes between 23 and 24. Figure credit: Patrick Wells

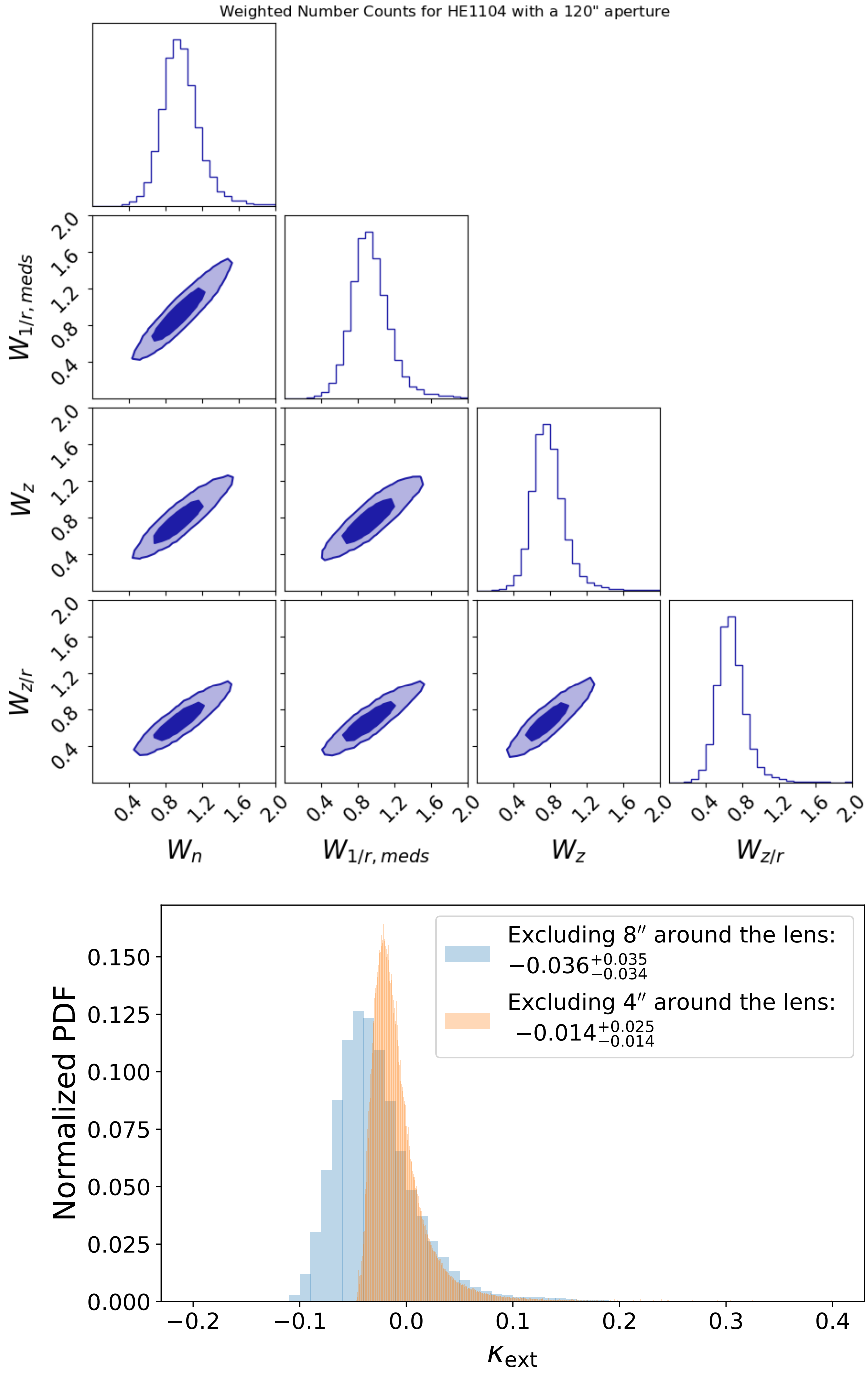

Figure 3.25: ***Left panel:*** Correlation between each weight computed in the observed field. ***Right panel:*** $\kappa_{\rm ext}$ measurement yielded by masking either 4″or 8 ″around the lens. The latter shows that the LOS of HE 1104−1805 is along an underdense region of the Universe. The alternative $\kappa_{\rm ext}$ measurement shows that multiple perturbers near the main lens are coincidental. Figure credit: Patrick Wells

3.3.5 Lens modelling

HST Imaging for mass modeling

As a part of the H0liCOW program (Suyu et al. 2017), Program 12889 (P.I: S.H Suyu) took deep HST data of HE 1104−1805 with Wide Field Camera 3 (WFC3) in bands F160W, F555W and F814W. The infra-red imaging displayed in Fig. 3.26 showcases the main challenges for modelling this system. First, the point source images are particularly bright with the PSF wings of both images aligned with the center of the galaxy; accurate modelling of the PSF is, therefore, crucial to model the lens light correctly. Secondly, the lensing arc is very dim and distinguishable only after proper subtraction of the lens light (see Fig. 3.30). This makes the lens light fitting a primordial and sensitive step to properly reconstruct the shape of the arc, an essential constraint to mass modelling. Thirdly, the system's environment is particularly crowded with 8 luminous galaxies within $15''$ of the main lens. Careful considerations will be given to assess the impact of these companions on the modelled mass of the main lens. The system is also characterized by a large and asymmetric separation of images A and B positions from the lens center of $1.17''$and $2.05''$, respectively.

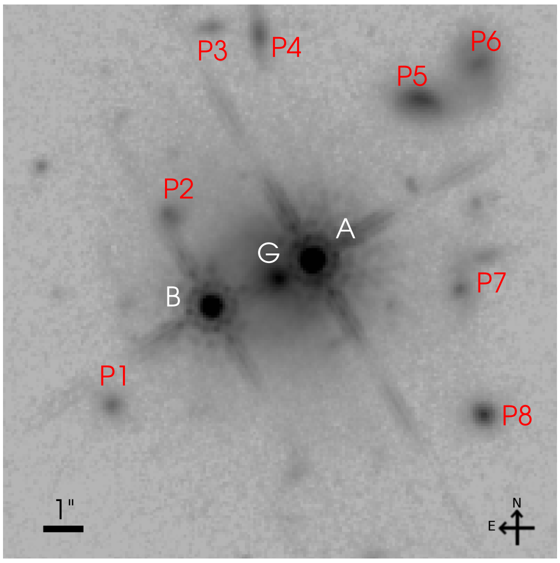

Figure 3.26: HE 1104−1805 imaging in the filter F160W band using HST WFC3. The main lensing galaxy is denoted as G, whereas the main perturbers considered in the analysis are numbered from P1 to P8.

Setup and workflow

Main lens model: Following the recommendation of Millon et al. (2020c) and the methodology of the most recent TDCOSMO lens models (e.g., Shajib et al. 2020, 2022), we model the lens galaxy with two families of models: power law and a composite alternatively. In the first case, the mass is parametrized as a PEMD (Eq. 3.21); the lens light is modelled by a Sersic profile (Eq. 3.19) in the F814W and F555W bands and by a De Vaucouleur profile (i.e. two superposed Sersic with $n = 1$ and $n = 4$ in Eq. 3.19) in the F160W band. The position of the mass component's center is fixed on the light component, which is fit jointly in the three bands.

For the composite, the baryonic mass with a double chameleon profile (i.e. two superposed chameleon profiles presented in Eq. 3.20 with an additional parameter encapsulation the ratio between the two). As in the first case, the lens light is modelled by a Sersic profile (Eq. 3.19) in the F814W and F555W bands. In the F160W, we use a double chameleon profile to model the light, and the fitted parameters fix the parameters of the baryonic mass model. The dark matter halo is modelled with an elliptical NFW profile (Eq. 3.22), whose position is tied to the baryonic mass. Similarly to previous lens modelling with composite works (e.g., Rusu et al. 2017; Wong et al. 2017; Shajib et al. 2022), we constrain the NFW's scale radius $R_s = 58 \pm 8$ kpc based on the measurement of Gavazzi et al. (2007) on galaxies that have a similar $\sigma_{\rm LOS}$ as the one measured in this system.

To simplify the light fitting, we mask pixels further than 5″from the lens in the F814W and F555W bands and 4.3″in the F160 band. We adjust the mask locally to mask the light of all the perturbers and mask the lens's central pixels because the light is not fitted perfectly in this region. Even though this does not physically constrain the mass, the optimizer is tempted to create a central image by creating a core to compensate for the induced residuals.

Source light: The source light is visible only in the F160W band, and we model it with a single Sersic profile in both families of model. No apparent structure in the lensed arc motivates the need for more complex shapes, contrary to previous TDCOSMO studies.

Perturbers model: To include the perturbers in the mass model, we use two strategies:

1. We add an SIS component to the mass model for each perturber considered. Even though we do not fit their light in the final model, an independent sersic fit gives us their position. Since P5 and P6 have different redshifts than the lens, we use the multi lens-plane formalism introduced in Eqs. 1.63 and 1.65. For the other perturbers considered, we assume that they lie in the same plane as the lens. In this scenario, we consider the perturbers P2, P5 and P6 as they have the highest flexion shifts and P9 because of its proximity to image B. We alternatively test the scenario where we include P5; P5 and P6; P5, P6, and P2; P5, P6, P2 and P9.
2. To account for all the perturbers at once without depending on redshift assumptions, we add a flexion term in the lens model. As described in Eqs. 1.45 and 1.46 the flexion $\mathcal{F}$ models the perturbation to the third derivative of the lens potential as a polynomial with four coefficients $f_{\rm xxx}$, $f_{\rm xxy}$, $f_{\rm xyy}$ and $f_{\rm yyy}$. To put a prior on these, we draw a population of perturbers with the same position but different redshifts (except for P5 and P6) and $\theta_{\rm E,SIS}$ within the values shown in Table 3.1 and measure the flexion induced by the combined influence of the eight perturbers at the position of the lens. We repeat this experiment 50'000 times to get a Gaussian prior on the 4 terms displayed in Fig. 3.27.

PSF Modelling: To complete the light model, each component is convolved by the PSF of the corresponding band.

In the optical bands F555W and F814W, the PSF and its noise map were modelled using the only star in the field of the exposure, while in the F160 band, 5 stars of the field were stacked together using the PSFr software (Birrer et al. 2022a).

Since the temperature profile of the stars in the field used for the PSF initial guess do not match the quasar one, we finalize the PSF model with 4 successive repetitions of the following sequence with the Lenstronomy software (Birrer et al. 2016):

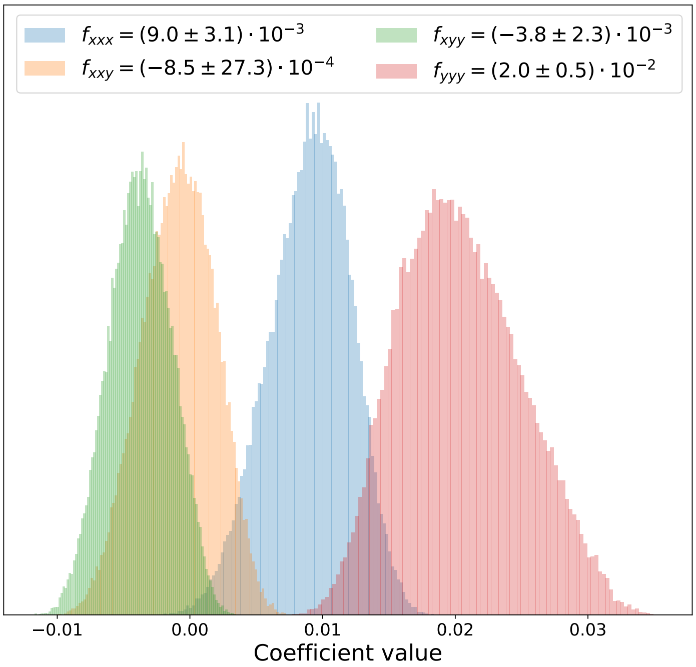

Figure 3.27: Prior on the four flexion coefficients computed using 50’000 different realizations of the 8 perturbers redshift and mass configurations.

1. alignment of the F160W and F555W exposure with the F814W one
2. lens model (mass and light) parameter optimization using the Particle Swarm Optimizer (PSO) routine of COSMOHAMMER (e.g., Eberhart & Kennedy 1995; Birrer & Amara 2018)
3. iterative reconstruction of the PSF on lens and source subtracted residuals. In the latter, we also adjust the PSF noise map in a radius of 0.5″around its center to adapt the constraining power of these pixels.

Posterior sampling and combination of different models: After obtaining a satisfactory PSF, shown in Fig. 3.28, we use the EMCEE software (Foreman-Mackey et al. 2013) to perform an MCMC sampling of the light and mass parameters ($\xi_{\rm light}$ and $\xi_{\rm mass}$) posterior by maximizing the likelihood expressed in Eq.3.18

We use 10 times as many walkers as there are parameters in the model, and we use the last 1 000 out of 20 000 iterations to construct the posterior of a given modelling setup. The best reconstruction of the HST imaging with power-law and composite models shown in Figs. 3.29, 3.30 and 3.32 demonstrate that all relevant features in the light are correctly predicted. Figures 3.31 and 3.33 display the convergence profile and magnification models obtained by each model family in every perturber-inclusion scenario. In both cases, we notice that the convergence of the perturber P5 drops significantly when adding P6 and reaches a much lower value than P6, even though the estimation for the Einstein radii based on the luminosity given in Table 3.1 predict a similar value for both. Nevertheless, since these two perturbers are very close, only

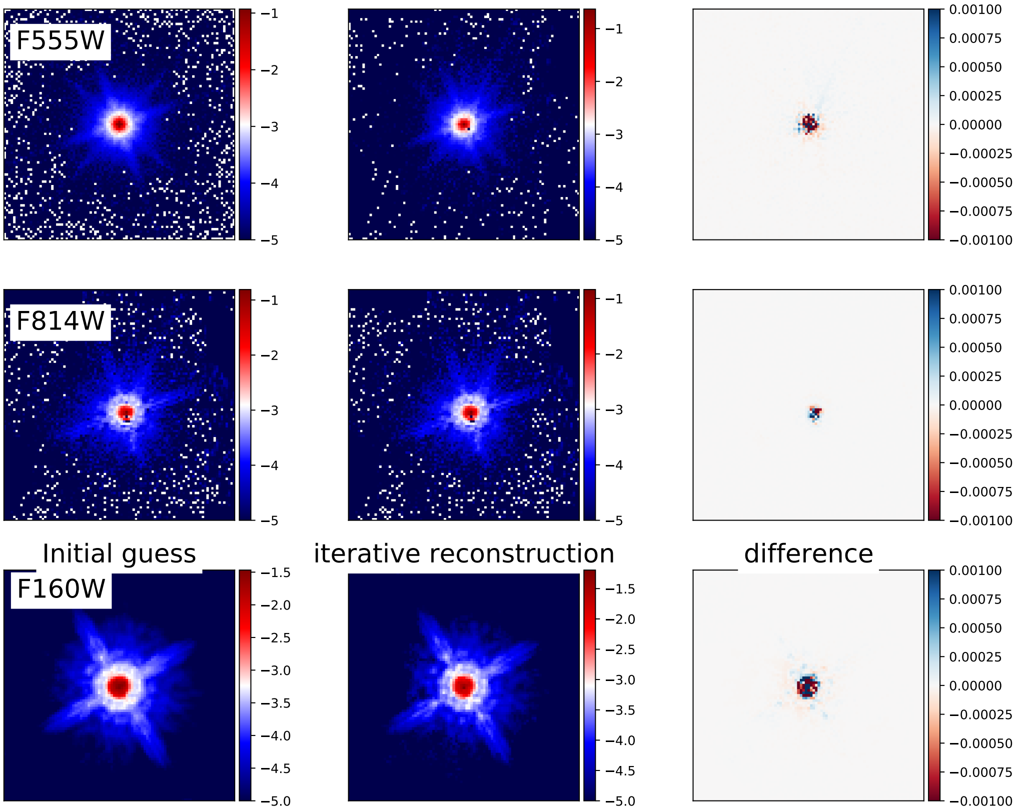

Figure 3.28: From left to right: Initial guess of the PSF from stacked stars in the field, final PSF obtained and the difference between both. We display the results for the band F55W, F814W and F160W from top to bottom.

the combined total convergence impacts the central lens mass, and this quantity is conserved throughout the different scenarios. As flexion does not consider the position of the perturbers and models the third derivative of the lensing potential, the added convergence is smoothly spread over the lens plane, which is unphysical but expected. Still, we note that the added convergence follows the direction of the perturbers P2, P3 and P4 and in a lower measure, the directions of P5 and P6 are also represented which proves the flexion term is a valid way to deal with the perturbers in this system.

The posterior probability of the lens mass model and the induced Fermat potential difference and time delay distance for both families of models are shown in Figs 3.34 and 3.35. In the power-law case, we see that the lens mass is generally compatible with a sphere, which explains the wide range of possible position angles not always in agreement between each scenario. The posterior probability of the other parameters is consistent throughout all configurations. More importantly, thanks to the 4% relative precision on the time delay, we reach a precision of 10% on the time delay distance.

The composite model is not as straightforward; each modelling configuration seems to end up in different local maxima of the likelihood function with precision too high to make different models compatible. This can be explained by the fact that 43 to 46 variables parametrize the composite model, whereas the power-law ones require 37 to 40. The lack of constraint from the imaging (only two images and a dim Einstein ring) cannot sufficiently restrict the number of solutions found. The size of the NFW profiles is

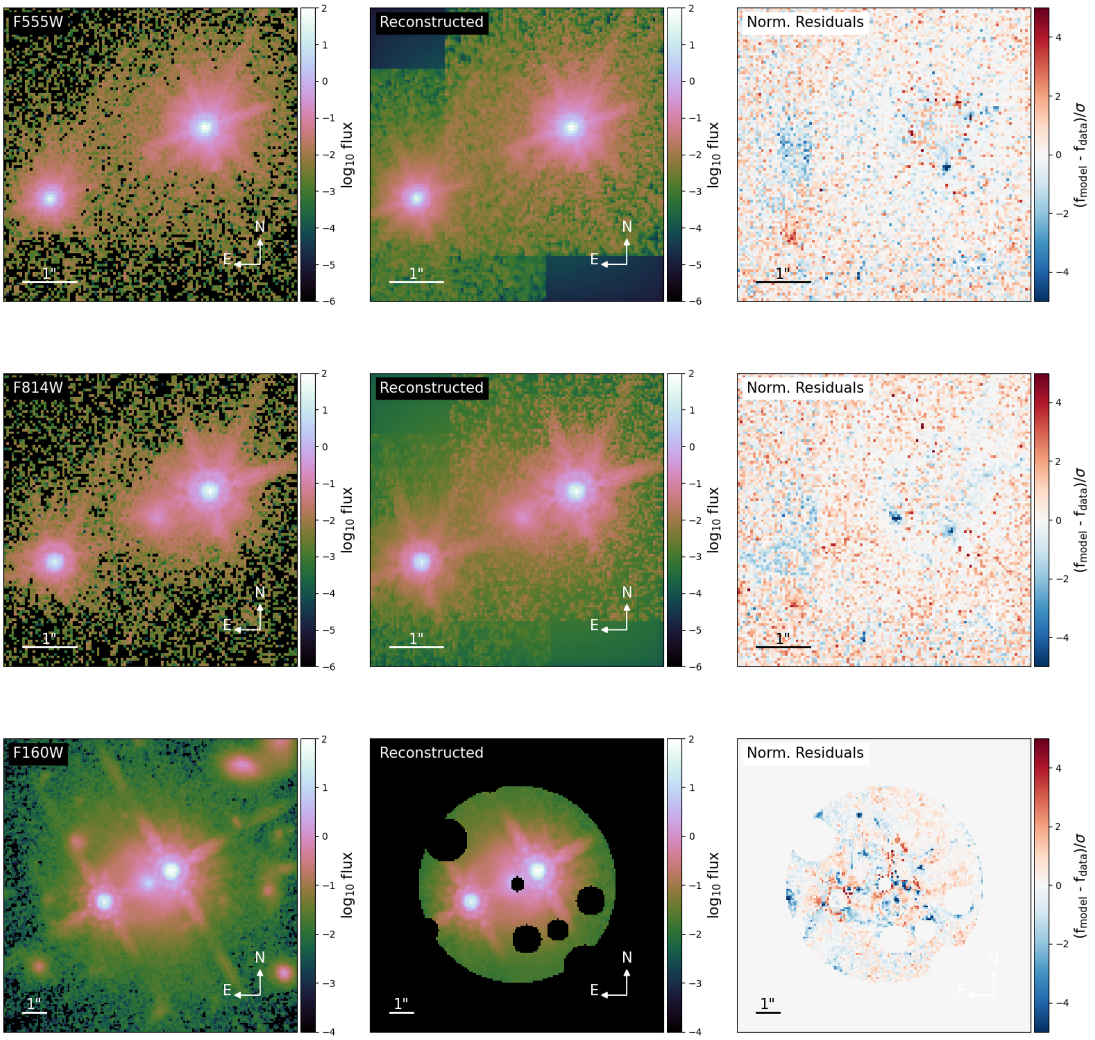

Figure 3.29: Reconstructed image of HE 1104−1805 using the best power-law model (PEMD + Shear + Flexion). From left to right: The imaging data, reconstructed image and normalized residuals are displayed in each HST filter. The residuals show no particular feature and demonstrate a precise image reconstruction.

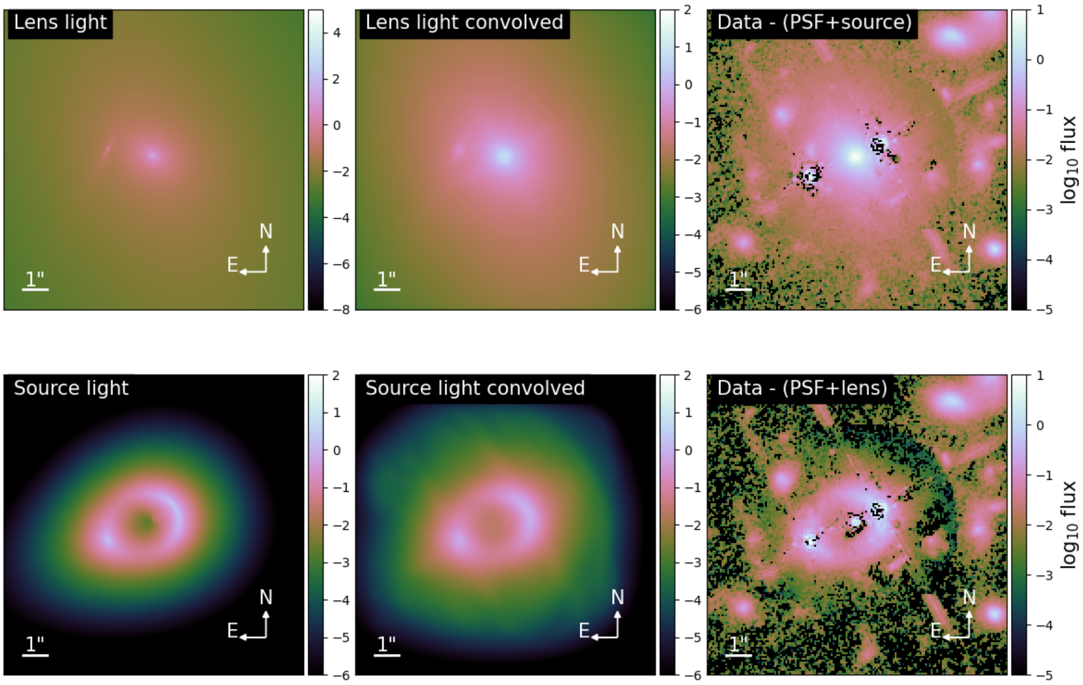

Figure 3.30: HE 1104−1805 reconstructed light component with power-law. From left to right: The light component unconvolved and then convolved with the PSF and its corresponding feature in the imaging data. The top row shows the lens light profile, and the bottom row shows the lensed source light profile. This figure shows that the two light-components model corresponds to expectations based on the observation. The center of the PSF and of the lens are not ideally modelled, which justifies the noise map increase in the first region and the masking of the second region.

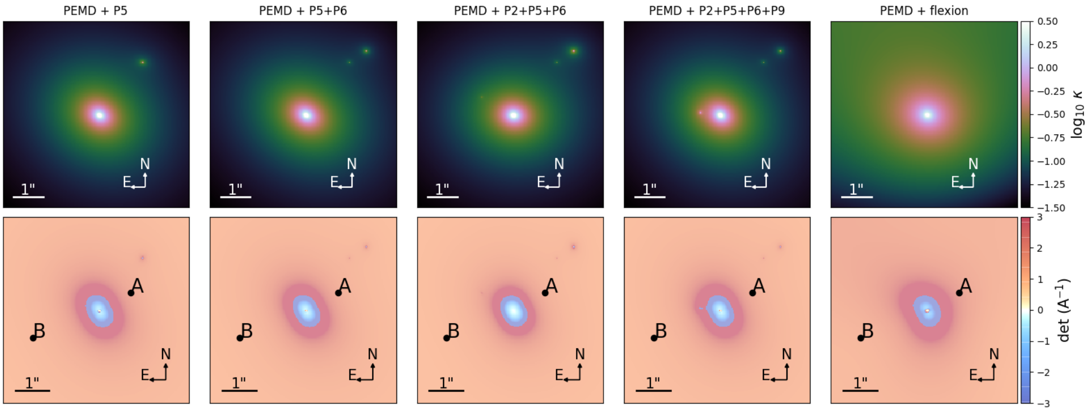

Figure 3.31: HE 1104−1805 modelled potential with power-law and different satellite inclusion strategies. The top row shows the convergence κ, and the bottom row shows the magnification induced by each model. From left to right, we show the models obtained by including P5; P5 and P6; P2, P5 and P6; P2, P5, P6, P9 and flexion.

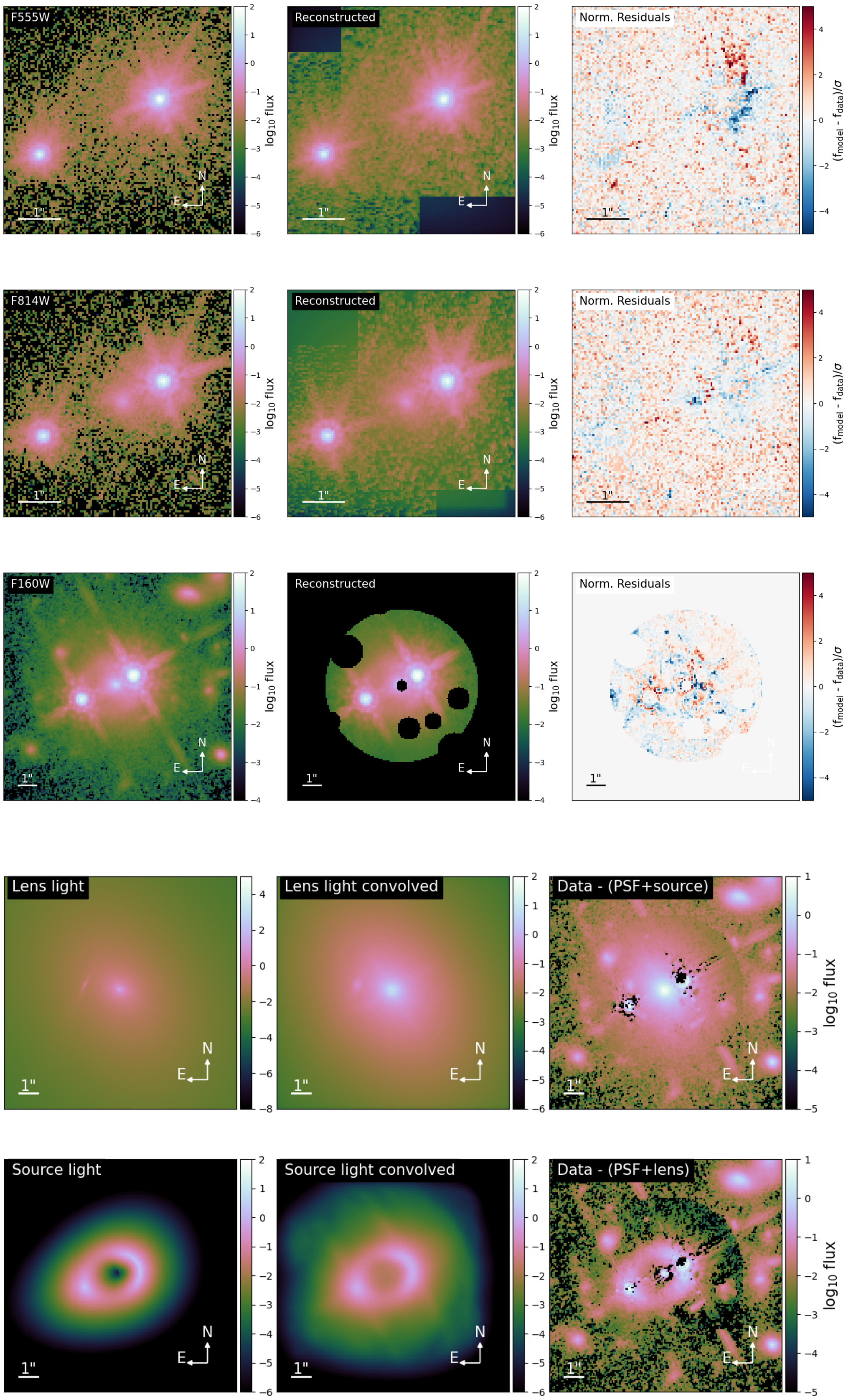
F555W
Reconstructed
Norm. Residuals
F814W
Reconstructed
Norm. Residuals
F160W
Reconstructed
Norm. Residuals
log$_{10}$ flux
$(f_{model} - f_{data})/\sigma$
1"
N
E
2
1
0
−1
−2
−3
−4
−5
−6
4
Lens light
Lens light convolved
Data - (PSF+source)
Source light
Source light convolved
Data - (PSF+lens)
−8

Figure 3.32: Same as Figs. 3.29 and 3.30 with the composite model.

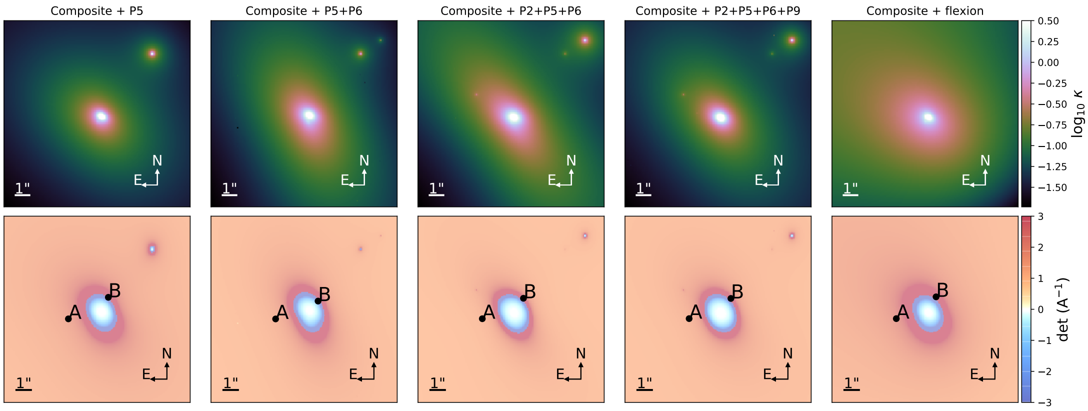

Figure 3.33: Same as Fig.3.31 for the composite model.

consistent with prior established by Gavazzi et al. (2007) but their mass is discrepant from one model to the other with no apparent correlation with the number of perturbers included. Moreover, the two chameleon components are elliptical and anti-aligned ($\Delta\psi_{\rm cham} \approx 60°$). While this allows the central region to appear spherical in the center, it appears that the position angle of the external shear and the second chameleon profile (the most elliptical one) significantly impact the slope of the convergence. As these parameters are naturally affected by the number and position of perturbers, we obtain a bi-modal distribution for γ, reflected in the $\Delta\phi_{\rm AB}$and $D_{\Delta t}$ posterior distributions. Finally, the positional offset is around 0.1 $''$between the baryonic and dark matter profiles, confirming that the "bulge-halo conspiracy" holds also in this system.

The Bayesian Information Criterion (BIC, Schwarz 1978) allows us to compare two models with different parametrizations; it is defined as:

$$BIC = k \cdot ln(n_{\rm Data}) - 2ln(\hat{L}), \tag{3.44}$$

where $\hat{L}$ is the maximized value of the likelihood function of the model M, i.e. $\hat{L} = p(Data \mid \xi_{\rm max})$, where $\widehat{\xi_{\rm max}}$ are the parameter values that maximize the likelihood function, $n_{\rm Data}$ is the number of data points (i.e. the number of unmasked pixels across the three bands + 1 for the time delay), k is the number of parameters in the model.

The BIC values computed with the maximal likelihood of each model are presented in Table 3.2. The variance of the BIC within one family of models is $\sigma_{\Delta\rm BIC} = 14$.

Similarly to Birrer et al. (2019) and Shajib et al. (2022), we determine the weight of each posterior distribution following:

$$W = \frac{1}{\sqrt{2\pi}\sigma_{\Delta\rm BIC}} \int_{-\infty}^{\infty} f(x) \exp\left(-\frac{(\rm BIC - x)^2}{2\sigma_{\Delta\rm BIC}}\right) \rm dx, \tag{3.45}$$

where f(x) is the evidence ratio function given by:

$$f(x) \equiv \begin{cases} 1 & \text{if x} < \text{BIC}_{\rm min}, \\ \exp(\text{BIC}_{\rm min} - \text{x}) & \text{if x} > \text{BIC}_{\rm min}, \end{cases} \tag{3.46}$$

$$\tag{3.47}$$

with BIC$_{\rm min}$ the BIC of the reference model.

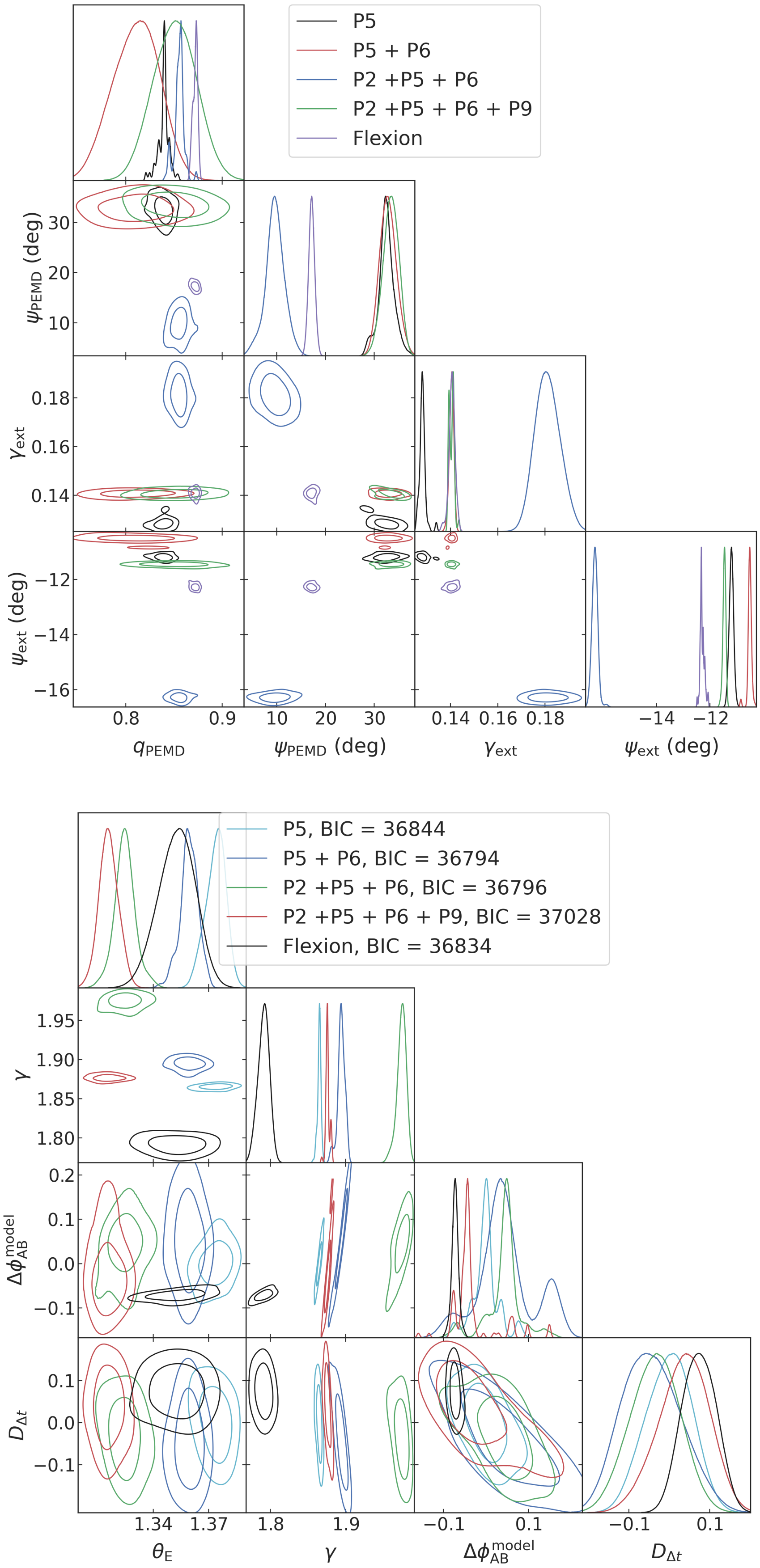

Figure 3.34: ***Top panel:*** Posterior distribution of the ellipticity parameters, axis ratio q and position angle ψ of the PEMD component along with the magnitude and position angle of the external shear $\gamma_{\rm ext}$and $\psi_{\rm ext}$. Following `Lenstronomy`'s convention, the position angle origin is defined along the North axis and increases clockwise. ***Bottom panel:*** Posterior distribution of the Einstein radius $\theta_{\rm E}$, convergence profile slope γ, induced Fermat potential difference $\Delta\phi_{\rm AB}$and time delay distance $D_{\Delta{\rm t}}$. The last two parameters are blinded until all investigations are complete.

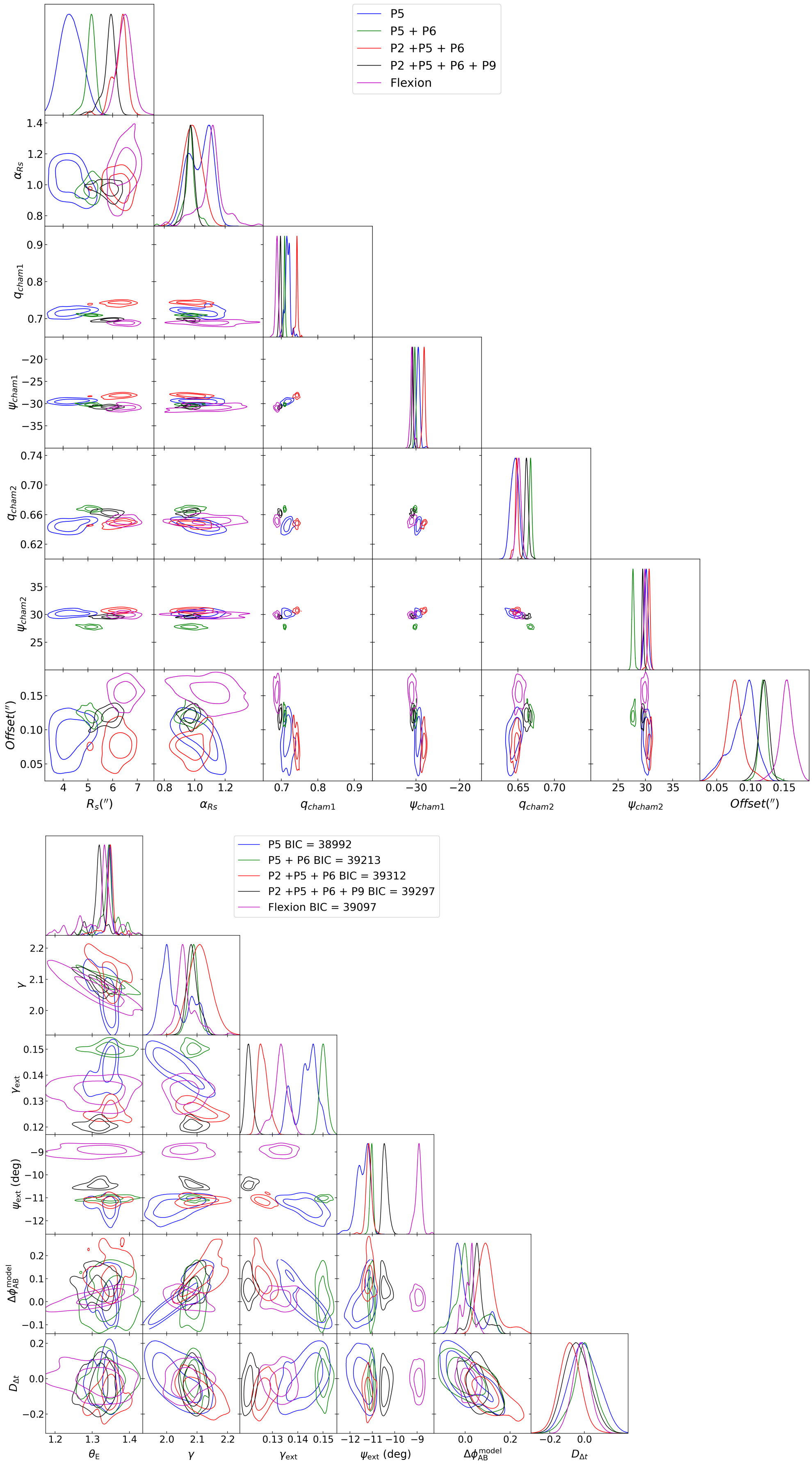

Figure 3.35: Same as Fig. 3.34 for the composite model. The normalization of the NFW profile, ρ_0, is computed with the deflection angle at scale radius of the core $R_{\rm s}$, $\alpha_{\rm Rs}$ with $\rho_0 = \frac{\alpha_{\rm Rs}}{4R_{\rm s}^2(1+ln(1/2))}$. We also display the offset between the center of the NFW and the chameleon profile.

Table 3.2: Every modelling scenario considered and their weight in the final posterior.

Lens model	Perturbers included	BIC	Relative Weight
Power-law	P_5	36844	0.80
Power-law	P_5, P_6	36794	1.
Power-law	P_5, P_6, P_2	36796	0.99
Power-law	P_5, P_6, P_2, P_9	37028	0.24
Power-law	Flexion	36834	0.84
Composite	P_5	39097	0.76
Composite	P_5, P_6	39297	0.38
Composite	P_5, P_6, P_2	39312	0.356
Composite	P_5, P_6, P_2, P_9	38992	1.0
Composite	Flexion	39213	0.52

To create a single posterior out of N multiple models, we sum all the posteriors using their normalized weight:

$$\sum_{\mathrm{n}} \frac{W_{\mathrm{n}}}{max(W_{\mathrm{n}})} p(\xi_{\mathrm{light}}, \xi_{\mathrm{mass}} \mid Data). \tag{3.48}$$

This procedure is done separately for the composite and power law models, and we compare the results in Fig. 3.36. The disparities between the two families on γ induce a 29% shift of the Fermat potential and 22% for the time delay distance between the two families. The external shear is higher than all the other TDCOSMO lenses but agrees with previous estimates from Wisotzki et al. (1998) and Courbin et al. (2000). Etherington et al. (2023), suggests that in power-law + shear models, the external shear is overestimated and aligned or anti-aligned with the main lens mass to compensate for the lack of flexibility of the model. While we indeed observe a decrease in the external shear when using the more flexible composite models, we do not observe a particular alignment of the PEMD mass with the external shear in the most rigid models (P5, P5 + P6 and P5+P6+P2) and conclude that the values of γ_{ext}found are physically motivated.

3.3.6 Combining lensing, kinematics and external convergence for cosmographic inference

Following the methodology of Shajib et al. (2023), we use the spatially resolved kinematics measured in Section 3.3.3 to mitigate the mass sheet degeneracy. To do so, we sample the posterior distribution of the lens model, $\xi_{\mathrm{light}}, \xi_{\mathrm{mass}}$, MST coefficient λ_{int}, and cosmological distances D_ℓ and $D_{\Delta\mathrm{t}}$ given all the observables: imaging, the time-delay Δt_{AB}, the radial bins of the velocity dispersion ${\sigma_{\mathrm{LOS}}}^{1,2,3}$ and the external convergence κ_{ext} measured:

$$\mathcal{P}(\xi_{\mathrm{light}}, \xi_{\mathrm{mass}}, \lambda_{\mathrm{int}}, D_\ell, D_{\Delta\mathrm{t}} \mid \mathrm{Img}, \Delta t_{\mathrm{AB}}, \sigma_{\mathrm{LOS}}, \kappa_{\mathrm{ext}}) \propto \mathcal{L}(\sigma_{\mathrm{LOS}} \mid \sigma_{\mathrm{LOS}}^{\mathrm{modeled}}) p(\lambda_{\mathrm{int}}, \kappa_{\mathrm{ext}}) \tag{3.49}$$

The likelihood of the modelled 3-bin velocity dispersion is computed with the following:

$$\mathcal{L}(\sigma_{\mathrm{LOS}} \mid \sigma_{\mathrm{LOS}}^{\mathrm{modeled}}) \propto exp\left(-\frac{1}{2}(\sigma_{\mathrm{LOS}} - \sigma_{\mathrm{LOS}}^{\mathrm{modeled}})^{\mathrm{T}} \Sigma (\sigma_{\mathrm{LOS}} - \sigma_{\mathrm{LOS}}^{\mathrm{modeled}})\right), \tag{3.50}$$

where $\sigma_{\mathrm{LOS}}^{modeled}$ is the 3-bins velocity-dispersion computed with the `JamPy` package through Eqs. 3.31 and

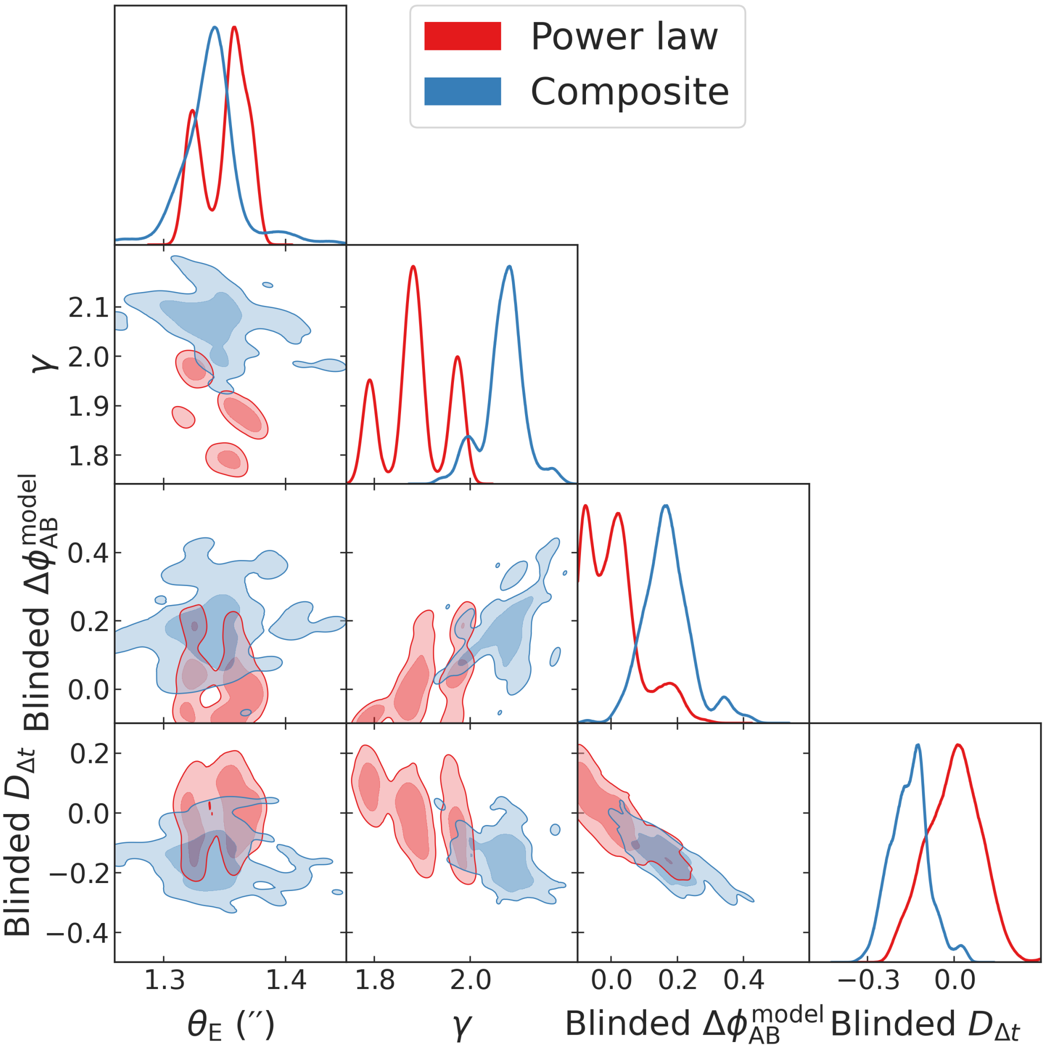

Figure 3.36: BIC weighted comparison of the power-law and composite models. We obtain $\theta_E^{\rm PL} = 1.35 \pm 0.01$, $\gamma^{\rm PL} = 1.93 \pm 0.02$, $\gamma_{\rm ext}^{\rm PL} = 0.14 \pm 0.01$, $\theta_E^{\rm Comp} = 1.35 \pm 0.05$, $\gamma^{\rm Comp} = 2.25 \pm 0.11$ and $\gamma_{\rm ext}^{\rm Comp} = 0.10 \pm 0.02$

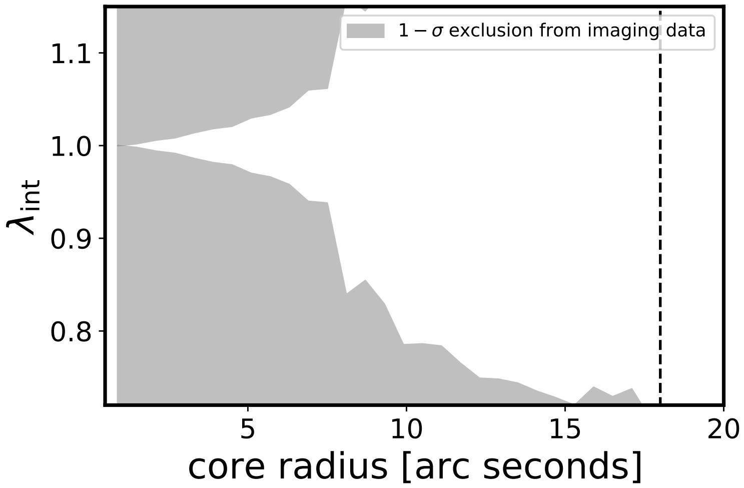

Figure 3.37: Correlation between $\lambda_{\rm int}$ and $\theta_{\rm c}$ in the posterior of a fiducial cored power-law. We used the $\xi_{\rm light}$ and $\xi_{\rm lens}$ with the highest likelihood on top of which a core with $\theta_{\rm c} = 8''$ was added.

3.32. Σ is the covariance matrix between $\sigma_{\rm LOS}$ measured in each bin determined in Section 3.3.3. In practice, the software uses Multi-Gaussian-Expansions (Emsellem et al. 1994, MGE) fits of the mass and light profiles to be able to deproject these surface densities into 3D ones in a straightforward way (Monnet et al. 1992). The light MGE fit is based on the lens light profile corresponding to the $\xi_{\rm light}$ with maximum likelihood. The PSF is modelled as a Moffat with $\beta = 1.96$ and $FWHM = 0.54''$ based on the mean value of these parameters along the wavelength range used for the $\sigma_{\rm LOS}$ measurement (i.e. [6000-9000] Å) that is shown in in the bottom panel of Fig. 3.17.

For each sample, we compute the MST-affected convergence by combining Eqs. 3.8 and 3.24:

$$\kappa_{\lambda}(\theta = (1 - \kappa_{\rm ext})(\lambda_{\rm int} * \kappa(\theta) + (1 - \lambda_{\rm int})\frac{\theta_{\rm c}^2}{\theta_{\rm c}^2 + \theta^2}. \tag{3.51}$$

As this MST is not parametrized in the imaging-based part of the modelling, we need the size of the core $\theta_{\rm c}$ to be large enough so that $\lambda_{\rm int}$ cannot be constrained by the imaging data. To find the minimal value of $\theta_{\rm c}$, we simulate a lensing system with parameters identical to the maximum likelihood system without the perturbers (i.e. a PEMD with external shear) and add a core with a fiducial size of $\theta_{\rm c} = 8''$which we fit using only imaging and time delay data. The correlation between $\lambda_{\rm int}$ and $\theta_{\rm c}$ in the obtained posterior distribution displayed in Fig. 3.37 shows us that for cores larger than $18''$, $\lambda_{\rm int}$ is unconstrained. We therefore use $\theta_{\rm c} = 18\ ''$. A uniform prior $\mathcal{U}(0.5, 1.13)$ on $\lambda_{\rm int}$ ensures that the MST transformed mass model is monotonic; this is necessary to allow an accurate MGE representation (Shajib 2019). We also use the measurement of $\kappa_{\rm ext}$ presented in Section 3.1.1 as prior to disentangle the internal from the external MSTs expressed in Eq.3.8. The anisotropy is modelled with the Osipkov-Merritt parametrization (see Eq 3.29) where we compute the anisotropy scale radius with a uniform prior $\mathcal{U}(0.1, 5)$ on $a_{\rm ani}$ as it is a standard choice in previous studies (e.g., Birrer et al. 2016; Shajib et al. 2022). The resulting posterior distribution for these parameters based on the power-law and composite models is shown in Fig. 3.38. In both families of model we obtain a $\lambda_{\rm int}$ compatible with 1. However, given the $\sim 10\%$ precision on this measurement, meaning that the MST does not have a strong effect on this system. Because the anisotropy scale $a_{\rm ani}$ is better constrained by the composite model, we obtain a more precise value for $\mathrm{D}_{\ell}^{\rm Comp}$ than for

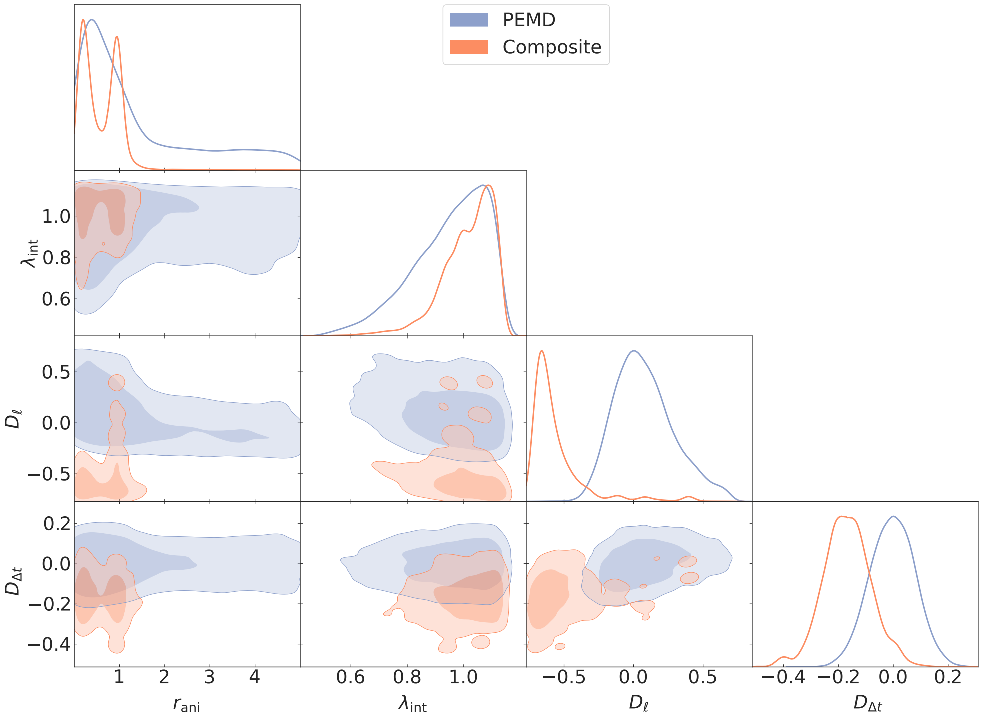

Figure 3.38: Posterior of $\lambda_{\rm int}$, $D_{\Delta t}$ and D_ℓ using kinematics based on the power-law and composite mass models. We measure ${\lambda_{\rm int}}^{\rm PL} = 0.97^{+0.11}_{-0.16}$, and ${\lambda_{\rm int}}^{\rm Comp} = 1.03^{+0.07}_{-0.10}$. The precision on the cosmological distance are $\frac{\Delta D_{\Delta t}}{D_{\Delta t}}^{\rm PL} = 8\%$, $\frac{\Delta D_\ell}{D_\ell}^{\rm PL} = 21\%$, $\frac{\Delta D_{\Delta t}}{D_{\Delta t}}^{\rm Comp} = 9\%$ and $\frac{\Delta D_\ell}{D_\ell}^{\rm PL} = 16\%$. We observe a 16% relative difference between $D_{\Delta t}^{\rm PL}$ and $D_{\Delta t}^{\rm Comp}$, and 67% between $\mathrm{D}_\ell^{\rm PL}$ and $\mathrm{D}_\ell^{\rm Comp}$.

$\mathrm{D}_\ell^{\rm PL}$ with a tension of nearly 2-σ. While the precision on $D_{\Delta t}$ did not change, the prediction of the two families are in agreement within 1-σ

Using the posterior distribution of D_ℓ and $D_{\Delta t}$ we then infer H_0 in a flat-ΛCDM cosmology with a uniform prior $\mathcal{U}(0, 150)$km s^{-1}Mpc^{-1} and for $\Omega_{\rm m} = \mathcal{U}(0.05, 0.5)$. These prior are voluntarily conservative and follow the current cosmological paradigm described in Section 1.1. The resulting posterior distributions obtained for both models are displayed in Fig. 3.39. As the more precise $D_{\Delta t}$ measurement dominates the likelihood of this sampling, we obtain H_0 measurement with both families compatible within 1-σ. We combine both measurement by weighting the posterior of each family prediction by their kinematic likelihood and see that the power-law model dominates the result. We hence obtain an 11% precision on H_0. As discussed in Section 1.4, the angular diameter distances are sensitive to $\Omega_{\rm m}$ only to the second order; it is therefore expected to not yield any constraint on this parameter through Time Delay Cosmography alone.

3.3.7 Discussion and conclusion

The Table 3.3 regroups all the cosmography-related measurements achieved for HE 1104−1805.

The measurement of the time delay, even though higher than previous estimates (e.g. Poindexter et al.

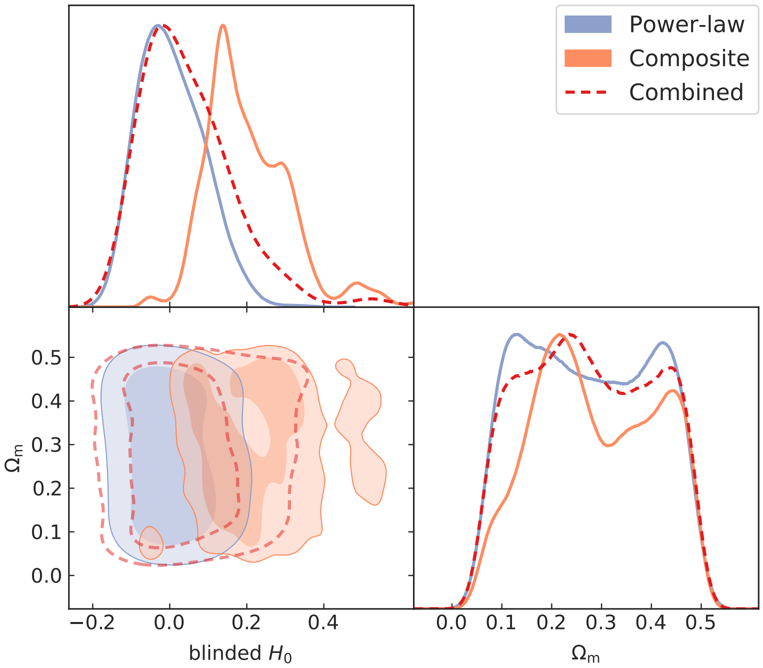

Figure 3.39: H_0 measurement with HE 1104−1805 obtained with the powerlaw and composite models. The precision of the different measurements of H_0 are $\frac{\Delta H_0}{H_0}^{\rm PL} = 8\%$, $\frac{\Delta H_0}{H_0}^{\rm Comp} = 9\%$ and $\frac{\Delta H_0}{H_0}^{\rm Combined} = 11\%$.

Table 3.3: Summary of all the relevant measurements on HE 1104−1805. The relative difference was computed using regarding the power-law model.

Lens modelling measurements

	Power-law	Composite	Relative difference [%]
$\theta_{\rm E}$	1.35 ± 0.01	1.35 ± 0.05	0
γ	1.93 ± 0.02	2.25 ± 0.11	16
$\gamma_{\rm ext}$	0.14 ± 0.01	0.10 ± 0.02	28
$\lambda_{\rm int}$	0.99 ± 0.13	1.06 ± 0.08	6
$\frac{\Delta D_{\Delta t}}{D_{\Delta t}}$	7%	9%	13
$\frac{\Delta D_{\ell}}{D_{\ell}}$	20%	12%	67

Ancillary measurements

$\Delta t_{\rm AB}$	$178.7^{+7.9}_{-8.8}$ days
$\kappa_{\rm ext}$	$-0.036^{0.35}_{-0.034}$
$\sigma^1_{\rm LOS}, \sigma^2_{\rm LOS}, \sigma^3_{\rm LOS}$	$282 \pm 21, 250 \pm 36, 189 \pm 49$ km s^{-1}

2007; Morgan et al. 2008), relies on the longest and best-sampled data. It was estimated with a data-driven algorithm whose accuracy was assessed on multiple simulated and observed light curves, which is crucial as we saw that the extrinsic variability is particularly challenging to model in this system. Physical constraints could introduce bias to the measurement. We are, therefore, ensured to have the most robust estimate for this object.

The measurements of the velocity dispersion $\sigma_{\rm LOS}{}^{1,2,3}$ and the external convergence $\kappa_{\rm ext}$ are robust to the systematic checks and are therefore accurate.

The lens mass modelling was performed with the two main parametrization families: power-law and composite. The nearby perturbers were accounted for both individually with successive addition of SIS models and globally using the flexion term. The power-law models are robust to the different perturber configurations and yield an 7% precision on $D_{\Delta t}$, 20% precision on D_{ℓ} and 10% on H_0. Similarly, the composite model yields a 9% precision on $D_{\Delta t}$ and 12% on D_{ℓ}. We however note a discrepancy between the two families of model of 13% $\sim 1.1\,\sigma$ distributions between $D_{\Delta t}$predicted by the two model families. Such discrepancy was already observed in modelling the quadruply lensed quasar WGD 2038−4008 (Shajib et al. 2022) because the system's compactness only allowed to probe the inner regions of the mass profile. In our case, the fact that we have only two images and a dim arc does not provide enough containing power to completely lift the degeneracy created by the multiple perturbers. Nevertheless, as shown by Fig.3.39, the weighted combination of the two H_0 measurements favors the power-law estimate and enables to discriminate between the two families and yields a 12% precision on H_0. The complete analysis presented is now under review by the TDCOSMO collaboration. The unblinding of the H_0 value will reveal if the relative difference of 13 % between both measurements makes one measurement agree with the early Universe and the other with the late Universe values of H_0. In any case, despite the challenges raised by the faintness of the lensing arc, the brightness of the PSF and the numerous perturbers near the main lens the most conservative H_0 measurement yields a marginalized precision of 11%. This precision is not as good as with J1206 (8%), the other TDCOSMO double, which displays a brighter arc as shown in Fig. 3.5. Nevertheless, this work is a cornerstone analysis for the upcoming comparison of the H_0 measurement with doubles and quadruples, as it shows that H_0 can be measured in not ideal conditions with reasonable precision.

3.4 Summary

In this chapter, I have presented my contribution to the measurement of H_0 through Time Delay Cosmography. The results of the NOT monitoring campaign have been displayed, which will provide time delay data for six new systems. Additionally, I have showcased the detailed Time delay cosmography analysis of the double-lensed quasar HE 1104−1805, which involved measuring the time delay, the resolved velocity dispersion, external convergence, and the mass model. While the first two measurements are robust, the low number of imaging constraints lead to a discrepancy between the power-law and composite models. Even if this affects the precision of the H_0 measurement, we obtain a final 12% precision. This work has set the stage for the TDCOSMO collaboration to analyze more doubly lensed quasars, as their focus has primarily been on quadruply lensed ones up until now.

Conclusion

In the first part of this work, we fructify the monitoring efforts led by COSMOGRAIL during the last 20 years to obtain high signal-to-noise and well-sampled light curves to unveil new probes of the quasar structure. In Paic et al. (2022), we show that high-frequency features of the QJ 0158−4325 microlensing light-curve can measure the Broad Line Region. This novelty completes the standard light-curve fitting method of Kochanek (2004), which measures the size of the accretion disk, as it exposes sources of systematic bias and opens the possibility of a formalism able to determine the size of the accretion disk and the Broad Line Region with a single light curve. Additionally, Millon et al. (2023) shows that the same microlensing light curve suggests the existence of a small separation Super Massive Binary Black Hole (SMBBH) in QJ 0158−4325. The imminent Rubin-LSST program will simultaneously monitor thousands of lensed quasars with different filters, multiplying the number of observed microlensing light curves 100-fold. To focus the follow-up observations and human resources on the most interesting systems (i.e. the ones undergoing the most intense micro-magnification), I led the development of a neural network able to forecast pairs of lensed quasar images that are likely to reach a micro-magnification peak 150 days in advance.

The next decade of microlensing light curve studies will be the turning point for several outstanding challenges the quasar studies raise. The new techniques presented will allow a large sample study of the accretion disk and BLR size. Our understanding of these components' geometry is still heavily debated and the interaction with the host galaxy is still poorly understood. Moreover, additional discoveries of small separation SMBBH ($\leq$0.01 pc) could question the coalescence time prediction of such systems which are supposed to collapse rapidly.

The past decade saw the transformation of Time delay Cosmography from a convoluted idea requiring large amounts of data to a mature technique aware of its flaws with observational resources to tackle them, making this technique one of the most precise tool to inquire the so-called H_0 tension. In the second part of this work, I contribute to investigating the validity of the H_0-tension by measuring H_0 with the double-lensed quasar HE 1104−1805. To do so, I computed each key component of the Time Delay Cosmography method: the time delay, the lens stellar kinematics, the lens mass model and the external mass contribution. Despite the complexity of the system and the low constraining power of the imaging data we reach a 12% precision on H_0. Even though the unblinded value will not alone infirm or confirm the tension, this study shows that reasonable precision can be attained with doubles. In the quest to reach a 1% precision on the H_0 measurement with this technique, the doubles must be better represented in the TDCOSMO sample. Even though their constraining power is not as high as the quadruples, the population of double is much larger than the quadruples and favouring the latter could lead to selection biases. This endeavour will be supported by the ever-increasing number of strong lenses, which will be discovered by Euclid and Rubin-LSST and enhanced observation, improving each strong lens's accuracy. For instance, the James Webb Telescope will yield high-resolution imaging in redder bands than the currently used Hubble Space Telescope, giving clearer observations of the lensed host galaxy.

The measurement of H_0 and the study of distant quasars have revolutionized our understanding of the Universe multiple times. This work contributes to the future resolution of some of the outstanding questions in cosmology and astrophysics, such as the co-evolution of galaxies with their central SMBH and the existence of dark energy.

Eric Paic

☎ +(41) 78 943 80 20 @ eric.paic@epfl.ch
Rue des charpentiers 4, Morges 1110, Switzerland ℹ 11.11.1994, French

Education

October - 2023 **PhD in astrophysics**
”Strong and microlensing study of distant quasars”, Supervisor : Pr. Courbin, EPFL.

2019 **Master in applied physics**
”Measurement of the radius of lensed quasar QJ0158-4325 using the power spectrum of the microlensing curve”, Supervisor : Pr. Courbin, EPFL.

2017 **Bachelor of Science in physics**, EPFL.

2012 **Scientific Baccalaureate, ”Mention Bien”**, Lycée Notre Dame de la Providence, Vincennes, France.

Work Experience

January 2019 – July 2018 **Research and Development internship, Rolex, Geneva, Switzerland**
Thermal Analysis of metal alloys. Automatizing the establishement of the Time-Temperature-Cooling phase diagrams of new metal alloys to optimize their mechanical treatment.

July 2016 **Internship, LASTRO, EPFL**
Determination of time delays for several gravitational lenses used to compute Hubble’s constant H_0.

July 2015 **Internship, LASTRO, EPFL**
Optimizing the photometric measurement pipeline used to generate COSMOGRAIL light curves.

August 2011 – July 2011 **Internship, ANTARES Experiment, Centre for particle physics of Marseille (CPPM), France**
Calibration of liquid scintillator detectors for the Astronomy with a Neutrino Telescope and Abyss environmental RESearch (ANTARES) project.

July 2010 – August 2010 **Internship, HAWC Experiment, Astrophysical laboratory of Universidad Nacional Autónoma de México (UNAM), Mexico**
Calibration of photomultiplier detectors for the High Altitude Water Cherenkov (HAWC) experiment.

Teaching Experience

Spring 2023 – 2020 **PhD teaching assistant, Astrophysics I, EPFL**

Fall 2022 – 2019 **PhD teaching assistant, Astrophysics Practical works, EPFL**
Python handling of astronomical data.

Spring 2019 – Fall 2016 **Student teaching assistant, Physics Practical works, EPFL**
Hands-on experiment on electro-magnetism.

Fall 2016 – 2014 **Student teaching assistant, Physics I, EPFL**

Fall 2022 **Co-supervisor, Francis Zong Lang, EPFL**
”Microlensing and Internal Structure of HE2149-2745”.

Spring 2021	Co-supervisor, Sophie Stucki, EPFL *"Studying Black Hole accretion disks with Convolutional Neural Networks".*
Spring 2020	Co-supervisor, Soumira Sheeram, EPFL *"Classifying the Source Radius from Microlensing Light Curves using Neural Networks".*
Spring 2020	Co-supervisor, Petra Awad, EPFL *"Improbability of Stellar Distributions as the Cause of Microlensing Signals for Gravitationally Lensed Quasars".*

OUTREACH AND VOLUNTEERING

2022	**Swiss finalist** of the "My thesis in 180 seconds" competition.
2019-2022	**Guide** for public tours of the Geneva Observatory and public night sky observations.
2016,2017, 2021	**Science demonstrator** for "Scientastic", a public outreach science festival at EPFL.

SKILLS

Programming languages : Python (advanced), Matlab (advanced), C/C++ (moderate), LaTeX.

Astronomical softwares : `PyCS3`,`Lenstronomy`, `JAMpy`, `SExtractor`.

Telescope operating : Swiss Euler Telescope (La Silla, Chile), Nordic Optical Telescope (La Palma, Spain).

Languages : French (Native), English (Bilingual), Spanish (Fluent), Croatian (beginner).

OTHERS

Collaboration membership : COSMOGRAIL, TDCOSMO.

Journal referee : The Astrophysical Journal (ApJ).

Captain of the Swiss Team in the International Physics Tournament, 7/90 of the individual ranking.

Publications list

ADS list of publication

2022	**Paic, E.**, Vernardos, G., Sluse, D., Millon, M., Courbin, F., Chan, J. H. and Bonvin, V. ”Constraining quasar structure using high-frequency microlensing variations and continuum reverberation”, A&A, Volume 659, DOI : 10.1051/0004-6361/202141808
2023	Rojas, K., et al. ”The impact of human expert visual inspection on the discovery of strong gravitational lenses”, MNRAS, Volume 523, DOI : 10.1093/mnras/stad1680
2023	Awad, P., Chan, J. H. H., Millon, M., Courbin, F. and **Paic, E.** ”Probing Compact Dark Matter Objects with Microlensing in Gravitationally Lensed Quasars”, A&A, Volume 673, DOI : 10.1051/0004-6361/202245615
2022	Millon, M., Dalang, C., Lemon, C., Sluse, D. , **Paic, E.**, et al. ”Evidence for a milliparsec-separation Supermassive Binary Black Hole with quasar microlensing”, A&A, Volume 668, DOI : 10.1051/0004-6361/202244440
2022	Chan, J. H. H., Lemon, C., Courbin, F., Gavazzi, R., Clément, B., Millon, M., **Paic, E**, et al. ”Discovery of strongly lensed quasars in the Ultraviolet Near Infrared Optical Northern Survey (UNIONS)”, A&A, Volume 659, DOI : 10.1051/0004-6361/202142389
2022	Lemon, C., Millon, M., Sluse, D., Courbin, F., Auger, M., Chan, J. H. H., **Paic, E.**, et al. ”J1721+8842 : a gravitationally lensed binary quasar with a proximate damped Lyman-α absorbed”, A&A, Volume 657, DOI : 10.1051/0004-6361/202142138
2020	M. Millon, F. Courbin, V. Bonvin, E. Buckley-Geer, C. D. Fassnacht, J. Frieman, P. J. Marshall, S. H. Suyu, T. Treu, T. Anguita, V. Motta, A. Agnello, J. H. H. Chan, D. C.-Y. Chao, M. Chijani1, D. Gilman, K. Gilmore, C. Lemon, J. R. Lucey, A. Melo, **E. Paic** et al. ”TDCOSMO. II. Six new time delays in lensed quasars from high-cadence monitoring at the MPIA 2.2 m telescope”, A&A 642, A193, A193. DOI : 10.1051/0004-6361/202038698
2020	Millon, M., Courbin, F., Bonvin, V., **Paic, E.**, et al. Aug. 2020. “COSMO- GRAIL. XIX. Time delays in 18 strongly lensed quasars from 15 years of optical monitoring”, A&A 640, A105. DOI : 10.1051/0004-6361/202037740.
2018	Courbin, F., Bonvin, V., Buckley-Geer, E., Fassnacht, C. D., Frieman, J., Lin, H., Marshall, P. J., Suyu, S. H., Treu, T., Anguita, T., Motta, V., Meylan, G., **Paic, E** et al. ”COSMOGRAIL : the COSmological MOnitoring of GRAvItational Lenses. XVI. Time delays for the quadruply imaged quasar DES J0408-5354 with high-cadence photometric monitoring”, A&A, Volume 609, DOI : 10.1051/0004-6361/201731461
2018	Bonvin, V., Chan, J. H. H., Millon, M., Rojas, K., Courbin, F., Chen, G. C. -F., Fassnacht, C. D., **Paic, E.** et al. ”COSMOGRAIL. XVII. Time delays for the quadruply imaged quasar PG 1115+080”, A&A, Volume 616, DOI : 10.1051/0004-6361/201833287

Conferences

September 2022	Strong Lensing Odyssey Conference, Kouremenos, Crete, Greece
June 2022	Swiss Physical Society annual meeting, Fribourg, Switzerland
February 2021	Time-Domain Cosmology with Strong Gravitational Lensing Conference, IPMU, Tokyo, Japan (online)

Bibliography

Abbott, B. P., Abbott, R., Abbott, T., et al. 2016, Physical review letters, 116, 131103

Abbott, B. P., Abbott, R., Abbott, T. D., et al. 2017, Phys. Rev. Lett., 118, 121102

Abramowicz, M. A., Czerny, B., Lasota, J. P., & Szuszkiewicz, E. 1988, ApJ, 332, 646

Abramowicz, M. A. & Fragile, P. C. 2013, Living Reviews in Relativity, 16, 1

Agazie, G., Anumarlapudi, A., Archibald, A. M., et al. 2023a, ApJ, 951, L8

Agazie, G., Anumarlapudi, A., Archibald, A. M., et al. 2023b, ApJ, 952, L37

Aghamousa, A. & Shafieloo, A. 2015, ApJ, 804, 39

Aiola, S., Calabrese, E., Maurin, L., et al. 2020, J. Cosmology Astropart. Phys., 2020, 047

Akiyama, K., Algaba, J. C., Alberdi, A., et al. 2021, The Astrophysical Journal Letters, 910, L12

Alam, S., Aubert, M., Avila, S., et al. 2021, Phys. Rev. D, 103, 083533

Alpher, R. A., Bethe, H., & Gamow, G. 1948, Phys. Rev., 73, 803

Anderson, R. I., Koblischke, N. W., & Eyer, L. 2023, arXiv e-prints, arXiv:2303.04790

Anguita, T., Schmidt, R. W., Turner, E. L., et al. 2008, A&A, 480, 327

Antonucci, R. 1993, ARA&A, 31, 473

Archidiacono, M. & Gariazzo, S. 2022, Universe, 8, 175

Auger, M. W., Treu, T., Bolton, A. S., et al. 2010, ApJ, 724, 511

Awad, P., Chan, J., Millon, M., Courbin, F., & Paic, E. 2023, arXiv e-prints

Bañados, E., Venemans, B. P., Mazzucchelli, C., et al. 2018, Nature, 553, 473

Baade, W. & Minkowski, R. 1954, ApJ, 119, 206

Bacon, D. J., Refregier, A. R., & Ellis, R. S. 2000, MNRAS, 318, 625

Bailes, M., Berger, B. K., Brady, P., et al. 2021, Nature Reviews Physics, 3, 344

Baldwin, J., Ferland, G., Korista, K., & Verner, D. 1995, ApJ, 455, L119

Bardeen, J. M. 1970, Nature, 226, 64

Bashinsky, S. & Seljak, U. 2004, Phys. Rev. D, 69, 083002

Bate, N. F., Floyd, D. J. E., Webster, R. L., & Wyithe, J. S. B. 2008, MNRAS, 391, 1955

Bate, N. F., Vernardos, G., O'Dowd, M. J., et al. 2018a, MNRAS, 479, 4796

Bate, N. F., Vernardos, G., O'Dowd, M. J., et al. 2018b, MNRAS, 479, 4796

Batiste, M., Bentz, M. C., Raimundo, S. I., Vestergaard, M., & Onken, C. A. 2017, ApJ, 838, L10

Bayer, J., Huber, S., Vogl, C., et al. 2021, A&A, 653, A29

Begelman, M. C., Blandford, R. D., & Rees, M. J. 1980, Nature, 287, 307

Bentz, M. C., Denney, K. D., Grier, C. J., et al. 2013, ApJ, 767, 149

Bentz, M. C., Street, R., Onken, C. A., & Valluri, M. 2021, ApJ, 906, 50

Bentz, M. C., Walsh, J. L., Barth, A. J., et al. 2009, ApJ, 705, 199

Bertin, E. & Arnouts, S. 1996, A&AS, 117, 393

Best, H., Fagin, J., Vernardos, G., & O'Dowd, M. 2022, arXiv e-prints, arXiv:2210.10500

Binney, J. & Mamon, G. A. 1982, MNRAS, 200, 361

Binney, J. & Tremaine, S. 1987, Galactic dynamics

Birrer, S. & Amara, A. 2018, Lenstronomy: Multi-purpose gravitational lens modeling software package, Astrophysics Source Code Library, record ascl:1804.012

Birrer, S., Amara, A., & Refregier, A. 2016, J. Cosmology Astropart. Phys., 2016, 020

Birrer, S., Bhamre, V., Nierenberg, A., Yang, L., & Van de Vyvere, L. 2022a, PSFr: Point Spread Function reconstruction, Astrophysics Source Code Library, record ascl:2210.005

Birrer, S., Dhawan, S., & Shajib, A. J. 2022b, ApJ, 924, 2

Birrer, S., Shajib, A. J., Galan, A., et al. 2020, A&A, 643, A165

Birrer, S. & Treu, T. 2019, MNRAS, 489, 2097

Birrer, S. & Treu, T. 2021, A&A, 649, A61

Birrer, S., Treu, T., Rusu, C. E., et al. 2019, MNRAS, 484, 4726

Blackburne, J. A., Pooley, D., Rappaport, S., & Schechter, P. L. 2011, The Astrophysical Journal, 729, 34

Blakeslee, J. P., Jensen, J. B., Ma, C.-P., Milne, P. A., & Greene, J. E. 2021, ApJ, 911, 65

Blum, K., Castorina, E., & Simonović, M. 2020, ApJ, 892, L27

Bolton, A. S., Burles, S., Koopmans, L. V. E., Treu, T., & Moustakas, L. A. 2006, ApJ, 638, 703

Bolton, A. S., Treu, T., Koopmans, L. V. E., et al. 2008, ApJ, 684, 248

Bolton, J. G., Stanley, G. J., & Slee, O. B. 1949, Nature, 164, 101

Bonanos, A. Z., Stanek, K. Z., Kudritzki, R. P., et al. 2006, ApJ, 652, 313

Bond, I. A., Abe, F., Dodd, R. J., et al. 2001, MNRAS, 327, 868

Bond, J. R. & Efstathiou, G. 1984, ApJ, 285, L45

Bonvin, V., Chan, J. H. H., Millon, M., et al. 2018, A&A, 616, A183

Bonvin, V. & Millon, M. 2020, H0LiCOW H0 tension plotting notebook, Zenodo

Bonvin, V., Tewes, M., Courbin, F., et al. 2016, A&A, 585, A88

Braglia, M., Ballardini, M., Finelli, F., & Koyama, K. 2021, Physical Review D, 103, 043528

Britto, R., Fermi-LAT Collaboration, Böttcher, M., et al. 2017, in 5th Annual Conference on High Energy Astrophysics in Southern Africa, 13

Bromm, V. & Loeb, A. 2003, ApJ, 596, 34

Brust, C., Cui, Y., & Sigurdson, K. 2017, Journal of Cosmology and Astroparticle Physics, 2017, 020

Buckley-Geer, E. J., Lin, H., Rusu, C. E., et al. 2020, MNRAS, 498, 3241

Buen-Abad, M. A., Marques-Tavares, G., & Schmaltz, M. 2015, Physical Review D, 92, 023531

Burke, W. L. 1981, ApJ, 244, L1

Burrows, D. N., Hill, J. E., Nousek, J. A., et al. 2005, Space Sci. Rev., 120, 165

Burud, I., Hjorth, J., Jaunsen, A. O., et al. 2000, ApJ, 544, 117

Cackett, E. M., Bentz, M. C., & Kara, E. 2021, iScience, 24, 102557

Cackett, E. M., Gelbord, J., Li, Y.-R., et al. 2020, ApJ, 896, 1

Cackett, E. M., Horne, K., & Winkler, H. 2007, MNRAS, 380, 669

Caditz, D. 1993, ApJ, 404, 539

Cappellari, M. 2016, ARA&A, 54, 597

Cappellari, M. 2020, MNRAS, 494, 4819

Chabrier, G. 2003, PASP, 115, 763

Chan, J. H. H., Lemon, C., Courbin, F., et al. 2022, A&A, 659, A140

Chan, J. H. H., Rojas, K., Millon, M., et al. 2020, arXiv e-prints, arXiv:2007.14416

Chandrasekhar, S. 1935, MNRAS, 95, 207

Chang, K. & Refsdal, S. 1979, Nature, 282, 561

Chen, G. C. F., Fassnacht, C. D., Suyu, S. H., et al. 2019, MNRAS, 490, 1743

Chevallier, M. & Polarski, D. 2001, International Journal of Modern Physics D, 10, 213

Chung, J., Gulcehre, C., Cho, K., & Bengio, Y. 2014, Empirical Evaluation of Gated Recurrent Neural Networks on Sequence Modeling

Clowe, D., Bradač, M., Gonzalez, A. H., et al. 2006, ApJ, 648, L109

Clowe, D., Gonzalez, A., & Markevitch, M. 2004, ApJ, 604, 596

Collett, T. E. & Auger, M. W. 2014, MNRAS, 443, 969

Combes, F. 2021, Active Galactic Nuclei, 2514-3433 (IOP Publishing)

Copi, C. J., Huterer, D., Schwarz, D. J., & Starkman, G. D. 2006, MNRAS, 367, 79

Cornachione, M. A. & Morgan, C. W. 2020, ApJ, 895, 93

Cornachione, M. A., Morgan, C. W., Burger, H. R., et al. 2020a, ApJ, 905, 7

Cornachione, M. A., Morgan, C. W., Millon, M., et al. 2020b, ApJ, 895, 125

Courbin, F., Bonvin, V., Buckley-Geer, E., et al. 2018, A&A, 609, A71

Courbin, F., Chantry, V., Revaz, Y., et al. 2011, A&A, 536, A53

Courbin, F., Eigenbrod, A., Vuissoz, C., Meylan, G., & Magain, P. 2005, in Gravitational Lensing Impact on Cosmology, ed. Y. Mellier & G. Meylan, Vol. 225, 297–303

Courbin, F., Lidman, C., & Magain, P. 1998, A&A, 330, 57

Courbin, F., Lidman, C., Meylan, G., Kneib, J. P., & Magain, P. 2000, A&A, 360, 853

Dahle, H., Hannestad, S., & Sommer-Larsen, J. 2003, ApJ, 588, L73

Dai, X., Kochanek, C. S., Chartas, G., et al. 2010, ApJ, 709, 278

Dalal, N. & Kochanek, C. S. 2002, ApJ, 572, 25

Dalla Bontà, E., Peterson, B. M., Bentz, M. C., et al. 2020, ApJ, 903, 112

Davies, R. I., Thomas, J., Genzel, R., et al. 2006, ApJ, 646, 754

Dawson, K. S., Schlegel, D. J., Ahn, C. P., et al. 2013, AJ, 145, 10

De Rosa, G. 2015, in IAU General Assembly, Vol. 29, 2257825

de Vaucouleurs, G. & Bollinger, G. 1979, ApJ, 233, 433

Denney, K. D., Peterson, B. M., Pogge, R. W., et al. 2010, ApJ, 721, 715

Dessauges-Zavadsky, M., Richard, J., Combes, F., et al. 2023, Monthly Notices of the Royal Astronomical Society, 519, 6222

Dexter, J. & Agol, E. 2011, ApJ, 727, L24

Di Valentino, E., Mena, O., Pan, S., et al. 2021, Classical and Quantum Gravity, 38, 153001

Ding, X., Silverman, J., Treu, T., et al. 2020, ApJ, 888, 37

Ding, X., Treu, T., Birrer, S., et al. 2021, MNRAS, 501, 269

Dobler, G., Fassnacht, C. D., Treu, T., et al. 2015, ApJ, 799, 168

Dodelson, S. & Widrow, L. M. 1994, Phys. Rev. Lett., 72, 17

Dong, F.-T., Gai, N., Tang, Y., Wang, Y.-F., & Yi, T.-F. 2022, Research in Astronomy and Astrophysics, 22, 115001

Dong, S., Mérand, A., Delplancke-Ströbele, F., et al. 2019, The Astrophysical Journal, 871, 70

Du, P., Hu, C., Lu, K.-X., et al. 2015, ApJ, 806, 22

Dutton, A. A. & Treu, T. 2014, MNRAS, 438, 3594

Dyson, F. W., Eddington, A. S., & Davidson, C. 1920, Philosophical Transactions of the Royal Society of London Series A, 220, 291

Eberhart, R. & Kennedy, J. 1995, in MHS'95. Proceedings of the Sixth International Symposium on Micro Machine and Human Science, 39–43

Edelson, R., Gelbord, J., Cackett, E., et al. 2019, ApJ, 870, 123

Eigenbrod, A., Courbin, F., Meylan, G., et al. 2008a, A&A, 490, 933

Eigenbrod, A., Courbin, F., Sluse, D., Meylan, G., & Agol, E. 2008b, A&A, 480, 647

Eigenbrod, A., Courbin, F., Vuissoz, C., et al. 2005, Astronomy & Astrophysics, 436, 25

Einstein, A. 1905, Annalen der Physik, 322, 132

Einstein, A. 1915, Sitzungsber. preuss.Akad. Wiss, 47, 831

Einstein, A. 1936, Science, 84, 506

Ellis, J., Hagelin, J., Nanopoulos, D., Olive, K., & Srednicki, M. 1984, Nuclear Physics B, 238, 453

Emsellem, E., Monnet, G., Bacon, R., & Nieto, J. L. 1994, A&A, 285, 739

Ertl, S., Schuldt, S., Suyu, S. H., et al. 2022, arXiv e-prints, arXiv:2209.03094

Escudero, M. & Witte, S. J. 2020, The European Physical Journal C, 80, 294

Etherington, A., Nightingale, J. W., Massey, R., et al. 2023, arXiv e-prints, arXiv:2301.05244

Event Horizon Telescope Collaboration, Akiyama, K., Alberdi, A., et al. 2022a, ApJ, 930, L12

Event Horizon Telescope Collaboration, Akiyama, K., Alberdi, A., et al. 2022b, ApJ, 930, L17

Event Horizon Telescope Collaboration, Akiyama, K., Alberdi, A., et al. 2019, ApJ, 875, L1

Fabian, A. C. & Lasenby, A. N. 2019, arXiv e-prints, arXiv:1911.04305

Fagin, J., Park, J. W., Best, H., et al. 2023, arXiv preprint arXiv:2304.04277

Falco, E. E., Gorenstein, M. V., & Shapiro, I. I. 1985, ApJ, 289, L1

Falco, E. E., Impey, C. D., Kochanek, C. S., et al. 1999, ApJ, 523, 617

Farrah, D., Croker, K. S., Zevin, M., et al. 2023, ApJ, 944, L31

Fassnacht, C. D., Koopmans, L. V. E., & Wong, K. C. 2011, MNRAS, 410, 2167

Fath, E. A. 1909, Popular Astronomy, 17, 504

Fausnaugh, M. M., Denney, K. D., Barth, A. J., et al. 2016, ApJ, 821, 56

Floyd, D. J. E., Bate, N. F., & Webster, R. L. 2009, MNRAS, 398, 233

Fonseca Alvarez, G., Trump, J. R., Homayouni, Y., et al. 2020, ApJ, 899, 73

Foreman-Mackey, D., Hogg, D. W., Lang, D., & Goodman, J. 2013, PASP, 125, 306

Fowler, J. W., Acquaviva, V., Ade, P. A. R., et al. 2010, ApJ, 722, 1148

Franchino-Viñas, S. & Mosquera, M. 2021, arXiv preprint arXiv:2107.02243

Freedman, W. L. 1988, AJ, 96, 1248

Freedman, W. L., Madore, B. F., Gibson, B. K., et al. 2001, ApJ, 553, 47

Freedman, W. L., Madore, B. F., Hoyt, T., et al. 2020, ApJ, 891, 57

Fusco, T., Bacon, R., Kamann, S., et al. 2020, A&A, 635, A208

Gaia Collaboration, Brown, A. G. A., Vallenari, A., et al. 2021, A&A, 649, A1

Galan, A., Peel, A., Joseph, R., Courbin, F., & Starck, J. L. 2021, A&A, 647, A176

Galan, A., Vernardos, G., Peel, A., Courbin, F., & Starck, J. L. 2022, A&A, 668, A155

Gardner, E. & Done, C. 2017, MNRAS, 470, 3591

Gaskell, C. M. & Sparke, L. S. 1986, ApJ, 305, 175

Gavazzi, R., Treu, T., Rhodes, J. D., et al. 2007, ApJ, 667, 176

Ghosh, S., Kumar, S., & Tsai, Y. 2021, arXiv preprint arXiv:2107.09076

Gil-Merino, R., Wisotzki, L., & Wambsganss, J. 2002, A&A, 381, 428

Giveon, U., Maoz, D., Kaspi, S., Netzer, H., & Smith, P. S. 1999, MNRAS, 306, 637

Goldberg, D. M. & Natarajan, P. 2002, ApJ, 564, 65

Goldstein, D. A., Nugent, P. E., & Goobar, A. 2019, ApJS, 243, 6

Gomer, M. R., Sluse, D., Van de Vyvere, L., Birrer, S., & Courbin, F. 2022, A&A, 667, A86

Gonneau, A., Lyubenova, M., Lançon, A., et al. 2020, A&A, 634, A133

Goobar, A., Johansson, J., Schulze, S., et al. 2022, arXiv e-prints, arXiv:2211.00656

Gorenstein, M. V., Shapiro, I. I., Rogers, A. E. E., et al. 1984, ApJ, 287, 538

Gould, A., Udalski, A., Shin, I. G., et al. 2014, Science, 345, 46

Graczyk, D., Pietrzyński, G., Thompson, I. B., et al. 2018, ApJ, 860, 1

Graczyk, D., Pietrzyński, G., Thompson, I. B., et al. 2020, ApJ, 904, 13

Gravity Collaboration, Sturm, E., Dexter, J., et al. 2018, Nature, 563, 657

Green, A. M. & Kavanagh, B. J. 2020

Greene, Z. S., Suyu, S. H., Treu, T., et al. 2013, ApJ, 768, 39

Grier, C. J., Martini, P., Watson, L. C., et al. 2013, ApJ, 773, 90

Grier, C. J., Pancoast, A., Barth, A. J., et al. 2017, ApJ, 849, 146

Grier, C. J., Shen, Y., Horne, K., et al. 2019, ApJ, 887, 38

Grillo, C., Suyu, S. H., Rosati, P., et al. 2015, ApJ, 800, 38

Gültekin, K., Richstone, D. O., Gebhardt, K., et al. 2009, ApJ, 698, 198

Gupta, A. C. 2014, Journal of Astrophysics and Astronomy, 35, 307

Gupta, A. C., Srivastava, A., & Wiita, P. J. 2008, The Astrophysical Journal, 690, 216

Guth, A. H. 1981, Phys. Rev. D, 23, 347

Hall, P. B., Sarrouh, G. T., & Horne, K. 2018, ApJ, 854, 93

Harrison, C. M. 2016, Observational Constraints on the Influence of Active Galactic Nuclei on the Evolution of Galaxies

Hawking, S. 1971, MNRAS, 152, 75

Hernández Santisteban, J. V., Edelson, R., Horne, K., et al. 2020, MNRAS, 498, 5399

Hewish, A. & Ryle, M. 1955, MmRAS, 67, 97

Hjorth, J., Burud, I., Jaunsen, A. O., et al. 2002, ApJ, 572, L11

Hochreiter, S. & Schmidhuber, J. 1997, Neural Computation, 9, 1735

Hojjati, A., Kim, A. G., & Linder, E. V. 2013, Phys. Rev. D, 87, 123512

Homayouni, Y., Trump, J. R., Grier, C. J., et al. 2019, ApJ, 880, 126

Hopkins, A. M. 2018, Publications of the Astronomical Society of Australia, 35, e039

Hopkins, P. F., Hernquist, L., Cox, T. J., Robertson, B., & Krause, E. 2007, ApJ, 669, 67

Hotokezaka, K., Nakar, E., Gottlieb, O., et al. 2019, Nature Astronomy, 3, 940

Hubble, E. 1929, Proceedings of the National Academy of Science, 15, 168

Hubble, E. & Humason, M. L. 1931, ApJ, 74, 43

Huber, S., Suyu, S. H., Ghoshdastidar, D., et al. 2022, A&A, 658, A157

Humason, M. L. 1932, PASP, 44, 267

Humason, M. L., Mayall, N. U., & Sandage, A. R. 1956, AJ, 61, 97

Humphreys, E. M. L., Reid, M. J., Moran, J. M., Greenhill, L. J., & Argon, A. L. 2013, ApJ, 775, 13

Ioffe, S. & Szegedy, C. 2015, Batch Normalization: Accelerating Deep Network Training by Reducing Internal Covariate Shift

Irwin, M. J., Webster, R. L., Hewett, P. C., Corrigan, R. T., & Jedrzejewski, R. I. 1989, AJ, 98, 1989

Ivezić, Ž. & MacLeod, C. 2014, in Multiwavelength AGN Surveys and Studies, ed. A. M. Mickaelian & D. B. Sanders, Vol. 304, 395–398

Iwasawa, M., Funato, Y., & Makino, J. 2006, ApJ, 651, 1059

Jedamzik, K. & Abel, T. 2013, Journal of Cosmology and Astroparticle Physics, 2013, 050

Jiang, Y.-F., Green, P. J., Greene, J. E., et al. 2017, ApJ, 836, 186

Jiménez-Vicente, J. & Mediavilla, E. 2019, ApJ, 885, 75

Jiménez-Vicente, J. & Mediavilla, E. 2022, ApJ, 941, 80

Kaiser, N. 2000, ApJ, 537, 555

Kaiser, N. & Squires, G. 1993, ApJ, 404, 441

Kamionkowski, M. & Riess, A. G. 2022, arXiv preprint arXiv:2211.04492

Kammoun, E. S., Dovčiak, M., Papadakis, I. E., Caballero-García, M. D., & Karas, V. 2021, ApJ, 907, 20

Karwal, T. & Kamionkowski, M. 2016, Physical Review D, 94, 103523

Kaspi, S., Brandt, W. N., Maoz, D., et al. 2021, arXiv e-prints, arXiv:2106.00691

Kaspi, S., Maoz, D., Netzer, H., et al. 2005, ApJ, 629, 61

Kaspi, S., Smith, P. S., Netzer, H., et al. 2000, ApJ, 533, 631

Kayser, R., Refsdal, S., & Stabell, R. 1986, A&A, 166, 36

Kellermann, K. I., Condon, J. J., Kimball, A. E., Perley, R. A., & Ivezić, Ž. 2016, ApJ, 831, 168

Kelly, B. C., Becker, A. C., Sobolewska, M., Siemiginowska, A., & Uttley, P. 2014, ApJ, 788, 33

Kelly, B. C. & Siemiginowska, A. 2009, The Astrophysical Journal, 698, 895

Kelly, P. L., Rodney, S., Treu, T., et al. 2023, Science, 380, abh1322

Kenworthy, W. D., Scolnic, D., & Riess, A. 2019, ApJ, 875, 145

Kerr, R. P. 1963, Phys. Rev. Lett., 11, 237

Khan, F. M., Holley-Bockelmann, K., Berczik, P., & Just, A. 2013, The Astrophysical Journal, 773, 100

Khetan, N., Izzo, L., Branchesi, M., et al. 2021, A&A, 647, A72

Kingma, D. P. & Ba, J. 2014, Adam: A Method for Stochastic Optimization

Kochanek, C. S. 2002, ApJ, 578, 25

Kochanek, C. S. 2004, The Astrophysical Journal, 605, 58

Kochanek, C. S. 2020, MNRAS, 493, 1725

Kochanek, C. S., Dai, X., Morgan, C., et al. 2006, arXiv preprint astro-ph/0609112

Kogut, A., Lineweaver, C., Smoot, G. F., et al. 1993, ApJ, 419, 1

Kollatschny, W., Bischoff, K., Robinson, E. L., Welsh, W. F., & Hill, G. J. 2001, A&A, 379, 125

Kormendy, J. & Ho, L. C. 2013, ARA&A, 51, 511

Kosowsky, A. 2003, New A Rev., 47, 939

Kourkchi, E., Tully, R. B., Courtois, H. M., Dupuy, A., & Guinet, D. 2022, Monthly Notices of the Royal Astronomical Society, 511, 6160

Kovačević, A. B., Ilić, D., Popović, L. Č., et al. 2023, Universe, 9, 287

Kreisch, C. D., Cyr-Racine, F.-Y., & Doré, O. 2020, Physical Review D, 101, 123505

Kroupa, P. 2001, MNRAS, 322, 231

Kuhn, F. A., Birrer, S., Bruderer, C., Amara, A., & Refregier, A. 2021, J. Cosmology Astropart. Phys., 2021, 010

Kulier, A., Ostriker, J. P., Natarajan, P., Lackner, C. N., & Cen, R. 2015, ApJ, 799, 178

Kundić, T., Turner, E. L., Colley, W. N., et al. 1997, ApJ, 482, 75

Lagattuta, D. J., Richard, J., Ebeling, H., et al. 2023, MNRAS, 522, 1091

Lam, C. Y., Lu, J. R., Udalski, A., et al. 2022, ApJ, 933, L23

Leavitt, H. S. 1908, Annals of Harvard College Observatory, 60, 87

Lemaître, G. 1927, Annales de la Soci&eacute;t&eacute; Scientifique de Bruxelles, 47, 49

Lemon, C., Anguita, T., Auger-Williams, M. W., et al. 2023, MNRAS, 520, 3305

Lemon, C., Auger, M. W., McMahon, R., et al. 2020, MNRAS, 494, 3491

Lemon, C., Millon, M., Sluse, D., et al. 2022, A&A, 657, A113

Lemon, C. A., Auger, M. W., McMahon, R. G., & Ostrovski, F. 2018, MNRAS, 479, 5060

Li, X. & Shafieloo, A. 2020, The Astrophysical Journal, 902, 58

Liao, K., Treu, T., Marshall, P., et al. 2015, ApJ, 800, 11

Lidman, C., Courbin, F., Kneib, J. P., et al. 2000, A&A, 364, L62

Lin, J. Y.-Y., Pandya, S., Pratap, D., Liu, X., & Kind, M. C. 2020, arXiv preprint arXiv:2011.15095

Lopez, S., Reimers, D., Rauch, M., Sargent, W. L. W., & Smette, A. 1999, ApJ, 513, 598

Lynden-Bell, D. 1969, Nature, 223, 690

Maccarone, T. J., Nelson, T. J., Brown, P. J., et al. 2019, Nature Astronomy, 3, 173

MacLeod, C. L., Ivezić, Ž., Kochanek, C. S., et al. 2010, The Astrophysical Journal, 721, 1014

Magain, P., Courbin, F., & Sohy, S. 1998, The Astrophysical Journal, 494, 472

Martel, A. R., Ford, H. C., Tran, H. D., et al. 2003, AJ, 125, 2964

McConnell, N. J. & Ma, C.-P. 2013, ApJ, 764, 184

McCully, C., Keeton, C. R., Wong, K. C., & Zabludoff, A. I. 2017, ApJ, 836, 141

McHardy, I. M., Cameron, D. T., Dwelly, T., et al. 2014, MNRAS, 444, 1469

Mediavilla, E., Muñoz, J. A., Lopez, P., et al. 2006, ApJ, 653, 942

Mediavilla, E., Muñoz, J., Kochanek, C., et al. 2011, The Astrophysical Journal, 730, 16

Mengistue, S. T., Del Olmo, A., Marziani, P., et al. 2023, MNRAS, 525, 4474

Merritt, D. 1985, AJ, 90, 1027

Meyer, A. D., van Dyk, D. A., Tak, H., & Siemiginowska, A. 2023, ApJ, 950, 37

Michalewicz, K., Millon, M., Dux, F., & Courbin, F. 2023, The Journal of Open Source Software, 8, 5340

Millon, M., Courbin, F., Bonvin, V., et al. 2020a, A&A, 642, A193

Millon, M., Courbin, F., Bonvin, V., et al. 2020b, A&A, 640, A105

Millon, M., Courbin, F., Galan, A., et al. 2023, Nature Astronomy, 7, 959

Millon, M., Galan, A., Courbin, F., et al. 2020c, A&A, 639, A101

Millon, M., Tewes, M., Bonvin, V., Lengen, B., & Courbin, F. 2020d, The Journal of Open Source Software, 5, 2654

Mineur, H. 1944, Annales d'Astrophysique, 7, 160

Monnet, G., Bacon, R., & Emsellem, E. 1992, A&A, 253, 366

Morgan, C. W., Eyler, M. E., Kochanek, C. S., et al. 2008, ApJ, 676, 80

Morgan, C. W., Hainline, L. J., Chen, B., et al. 2012, The Astrophysical Journal, 756, 52

Morgan, C. W., Hyer, G. E., Bonvin, V., et al. 2018, The Astrophysical Journal, 869, 106

Morgan, C. W., Kochanek, C., Morgan, N. D., & Falco, E. E. 2010, The Astrophysical Journal, 712, 1129

Mortonson, M. J., Schechter, P. L., & Wambsganss, J. 2005, The Astrophysical Journal, 628, 594

Mosquera, A. M. & Kochanek, C. S. 2011, The Astrophysical Journal, 738, 96

Motta, V., García-Aspeitia, M. A., Hernández-Almada, A., Magana, J., & Verdugo, T. 2021, Universe, 7, 163

Motta, V., Mediavilla, E., Rojas, K., et al. 2017, The Astrophysical Journal, 835, 132

Mould, J. & Kristian, J. 1986, ApJ, 305, 591

Mozumdar, P., Fassnacht, C. D., Treu, T., Spiniello, C., & Shajib, A. J. 2023, A&A, 672, A20

Mudd, D., Martini, P., Zu, Y., et al. 2018, ApJ, 862, 123

Nagy, D., Dessauges-Zavadsky, M., Richard, J., et al. 2022, A&A, 657, A25

Nair, V. & Hinton, G. E. 2010, in Proceedings of the 27th International Conference on International Conference on Machine Learning, ICML'10 (Madison, WI, USA: Omnipress), 807–814

Narayan, R. 1996, ApJ, 462, 136

Neira, F., Anguita, T., & Vernardos, G. 2020, Monthly Notices of the Royal Astronomical Society, 495, 544

Neira, F., Anguita, T., & Vernardos, G. in prep.

Newman, A. B., Treu, T., Ellis, R. S., & Sand, D. J. 2013, ApJ, 765, 25

Niedermann, F. & Sloth, M. S. 2020, Physical Review D, 102, 063527

Oguri, M. & Marshall, P. J. 2010, MNRAS, 405, 2579

Onken, C. A., Ferrarese, L., Merritt, D., et al. 2004, ApJ, 615, 645

Onken, C. A., Valluri, M., Brown, J. S., et al. 2014, ApJ, 791, 37

Oppenheimer, J. R. & Volkoff, G. M. 1939, Physical Review, 55, 374

Osipkov, L. P. 1979, Soviet Astronomy Letters, 5, 42

O'Neill, S., Kiehlmann, S., Readhead, A. C. S., et al. 2022, The Astrophysical Journal Letters, 926, L35

Pacucci, F. & Loeb, A. 2020, ApJ, 895, 95

Pacucci, F. & Loeb, A. 2021, Monthly Notices of the Royal Astronomical Society, 509, 1885

Paic, E., Vernardos, G., Sluse, D., et al. 2022, A&A, 659, A21

Pancoast, A., Brewer, B. J., & Treu, T. 2011, ApJ, 730, 139

Pancoast, A., Brewer, B. J., Treu, T., et al. 2014, MNRAS, 445, 3073

Papadakis, I. E., Dovčiak, M., & Kammoun, E. S. 2022, A&A, 666, A11

Peccei, R. & Quinn, H. 1977, Phys. Rev. Lett, 1440

Peebles, P. J. E. 1968, ApJ, 153, 1

Peebles, P. J. E. & Ratra, B. 1988, ApJ, 325, L17

Pelt, J., Kayser, R., Refsdal, S., & Schramm, T. 1996, A&A, 305, 97

Pelt, J., Refsdal, S., & Stabell, R. 2002, A&A, 389, L57

Penzias, A. A. & Wilson, R. W. 1965, ApJ, 142, 419

Perlmutter, S., Aldering, G., della Valle, M., et al. 1998, Nature, 391, 51

Pesce, D., Braatz, J., Reid, M., et al. 2020, in $H_0$2020: Assessing Uncertainties in Hubble's Constant Across the Universe, 20

Peterson, B. 2006, The Broad-Line Region in Active Galactic Nuclei, ed. D. Alloin, R. Johnson, & P. Lira (Berlin, Heidelberg: Springer Berlin Heidelberg), 77–100

Peterson, B. M., Ali, B., Horne, K., et al. 1993, ApJ, 402, 469

Peterson, B. M., Ferrarese, L., Gilbert, K. M., et al. 2004, ApJ, 613, 682

Peterson, B. M. & Wandel, A. 1999, ApJ, 521, L95

Philcox, O. H. E. & Ivanov, M. M. 2022, Phys. Rev. D, 105, 043517

Phillips, M. M. 1993, ApJ, 413, L105

Pierel, J. D. R. & Rodney, S. 2019, ApJ, 876, 107

Planck Collaboration, Aghanim, N., Akrami, Y., et al. 2020a, A&A, 641, A1

Planck Collaboration, Aghanim, N., Akrami, Y., et al. 2020b, A&A, 641, A6

Planck Collaboration, Aghanim, N., Akrami, Y., et al. 2020c, A&A, 641, A5

Poindexter, S. & Kochanek, C. S. 2010, ApJ, 712, 668

Poindexter, S., Morgan, N., Kochanek, C. S., & Falco, E. E. 2007, ApJ, 660, 146

Poitevineau, R., Castignani, G., & Combes, F. 2023, Astronomy and Astrophysics, 672, A164

Pooley, D., Rappaport, S., Blackburne, J. A., Schechter, P. L., & Wambsganss, J. 2012, ApJ, 744, 111

Poulin, V., Serpico, P. D., & Lesgourgues, J. 2016, Journal of Cosmology and Astroparticle Physics, 2016, 036

Raichoor, A., de Mattia, A., Ross, A. J., et al. 2021, MNRAS, 500, 3254

Refsdal, S. 1964, Monthly Notices of the Royal Astronomical Society, 128, 307

Reid, M. J., Pesce, D. W., & Riess, A. G. 2019, ApJ, 886, L27

Reynolds, C. S. 2019, Nature Astronomy, 3, 41

Rhee, G. 1991, Nature, 350, 211

Riess, A. G., Casertano, S., Yuan, W., Macri, L. M., & Scolnic, D. 2019, ApJ, 876, 85

Riess, A. G., Filippenko, A. V., Challis, P., et al. 1998, AJ, 116, 1009

Riess, A. G., Yuan, W., Macri, L. M., et al. 2022, ApJ, 934, L7

Risaliti, G., Harrison, F. A., Madsen, K. K., et al. 2013, Nature, 494, 449

Ritondale, E., Vegetti, S., Despali, G., et al. 2019, MNRAS, 485, 2179

Rojas, K., Motta, V., Mediavilla, E., et al. 2014, ApJ, 797, 61

Rojas, K., Motta, V., Mediavilla, E., et al. 2020, The Astrophysical Journal, 890, 3

Rozyczka, M., Thompson, I. B., Dotter, A., et al. 2022, Monthly Notices of the Royal Astronomical Society, 517, 2485

Rubin, V. C., Ford Jr, W. K., & Thonnard, N. 1978, Astrophysical Journal, Part 2-Letters to the Editor, vol. 225, Nov. 1, 1978, p. L107-L111., 225, L107

Rumbaugh, N., Shen, Y., Morganson, E., et al. 2018, ApJ, 854, 160

Rusu, C. E., Fassnacht, C. D., Sluse, D., et al. 2017, MNRAS, 467, 4220

Rusu, C. E., Wong, K. C., Bonvin, V., et al. 2020, MNRAS, 498, 1440

Sainz de Murieta, A., Collett, T. E., Magee, M. R., et al. 2023, arXiv e-prints, arXiv:2307.12881

Salpeter, E. 1964, Publications of Goddard Space Flight Center, 165

Salpeter, E. E. 1955, ApJ, 121, 161

Sandage, A. 1958, ApJ, 127, 513

Sandage, A. & Tammann, G. A. 1976, ApJ, 210, 7

Schechter, P. 1976, ApJ, 203, 297

Schechter, P. L., Udalski, A., Szymański, M., et al. 2003, The Astrophysical Journal, 584, 657

Schmidt, M. 1963, Nature, 197, 1040

Schmidt, R. W. & Wambsganss, J. 2010, General Relativity and Gravitation, 42, 2127

Schmidt, T., Treu, T., Birrer, S., et al. 2023, MNRAS, 518, 1260

Schneider, P., Ehlers, J., & Falco, E. E. 1992, Gravitational Lenses

Schneider, P., Kochanek, C. S., Wambsganss, J., & Schneider, P. 2006, Gravitational Lensing: Strong, Weak and Micro, 1

Schwarz, G. 1978, Annals of Statistics, 6, 461

Schwarzschild, K. 1916, Sitzungsberichte der K&ouml;niglich Preussischen Akademie der Wissenschaften, 189

Schöneberg, N., Abellán, G. F., Sánchez, A. P., et al. 2022, Physics Reports, 984, 1, the H0 Olympics: A fair ranking of proposed models

Sekiguchi, T. & Takahashi, T. 2021, Physical Review D, 103, 083507

Seyfert, C. K. 1943, ApJ, 97, 28

Shajib, A. J. 2019, MNRAS, 488, 1387

Shajib, A. J., Birrer, S., Treu, T., et al. 2020, MNRAS, 494, 6072

Shajib, A. J., Birrer, S., Treu, T., et al. 2019, MNRAS, 483, 5649

Shajib, A. J., Mozumdar, P., Chen, G. C. F., et al. 2023, arXiv e-prints, arXiv:2301.02656

Shajib, A. J., Treu, T., & Agnello, A. 2018, MNRAS, 473, 210

Shajib, A. J., Treu, T., Birrer, S., & Sonnenfeld, A. 2021, MNRAS, 503, 2380

Shajib, A. J., Wong, K. C., Birrer, S., et al. 2022, A&A, 667, A123

Shakura, N. I. & Sunyaev, R. A. 1973, Astronomy and Astrophysics, 24, 337

Shapiro, I. I. 1964, Phys. Rev. Lett., 13, 789

Shappee, B. J., Prieto, J. L., Grupe, D., et al. 2014, ApJ, 788, 48

Sharma, D., Collett, T. E., & Linder, E. V. 2023, J. Cosmology Astropart. Phys., 2023, 001

Shen, Y., Liu, X., Greene, J. E., & Strauss, M. A. 2011, ApJ, 735, 48

Shin, I.-G., Yee, J. C., Hwang, K.-H., et al. 2022, AJ, 163, 254

Sądowski, A. 2009, ApJS, 183, 171

Skowron, J., Jaroszynski, M., Udalski, A., et al. 2007, Acta Astron., 57, 281

Slipher, V. M. 1917, Lowell Observatory Bulletin, 3, 59

Sluse, D., Claeskens, J. F., Hutsemékers, D., & Surdej, J. 2007, A&A, 468, 885

Sluse, D., Sonnenfeld, A., Rumbaugh, N., et al. 2017, MNRAS, 470, 4838

Sluse, D., Surdej, J., Claeskens, J. F., et al. 2003, A&A, 406, L43

Sluse, D. & Tewes, M. 2014, Astronomy & Astrophysics, 571, A60

Smoot, G. F., Bennett, C. L., Kogut, A., et al. 1992, ApJ, 396, L1

Soliman, N. H., Macciò, A. V., & Blank, M. 2023, MNRAS, 525, 12

Sonnenfeld, A., Treu, T., Gavazzi, R., et al. 2012, ApJ, 752, 163

Soszyński, I., Olechowska, A., Ratajczak, M., et al. 2021, ApJ, 911, L22

Spergel, D. N., Verde, L., Peiris, H. V., et al. 2003, ApJS, 148, 175

Springel, V. 2005, MNRAS, 364, 1105

Spruit, H. C. 2010, arXiv e-prints, arXiv:1005.5279

Starkey, D. A., Horne, K., & Villforth, C. 2016, MNRAS, 456, 1960

Suberlak, K. L., Ivezić, Ž., & MacLeod, C. 2021, ApJ, 907, 96

Sun, M., Xue, Y., Guo, H., et al. 2020, ApJ, 902, 7

Suyu, S. H. & Blandford, R. D. 2006, MNRAS, 366, 39

Suyu, S. H., Bonvin, V., Courbin, F., et al. 2017, MNRAS, 468, 2590

Suyu, S. H., Goobar, A., Collett, T., More, A., & Vernardos, G. 2023, arXiv e-prints, arXiv:2301.07729

Suyu, S. H., Marshall, P. J., Auger, M. W., et al. 2010, ApJ, 711, 201

Suyu, S. H., Marshall, P. J., Blandford, R. D., et al. 2009, ApJ, 691, 277

Suyu, S. H., Treu, T., Hilbert, S., et al. 2014, ApJ, 788, L35

Tachibana, Y., Graham, M. J., Kawai, N., et al. 2020, ApJ, 903, 54

Tak, H., Mandel, K., van Dyk, D. A., et al. 2016, arXiv e-prints, arXiv:1602.01462

Tang, J.-J., Wolf, C., & Tonry, J. 2023, Nature Astronomy, 7, 473

Teodori, L., Blum, K., Castorina, E., Simonović, M., & Soreq, Y. 2022, J. Cosmology Astropart. Phys., 2022, 027

Terebizh, V. I. 1980, Astrofizika, 16, 45

Tewes, Courbin, F., Meylan, G., et al. 2013, Astronomy & Astrophysics, 556, A22

Thompson, A. C., Fluke, C. J., Barnes, D. G., & Barsdell, B. R. 2010, New Astronomy, 15, 16

Tie, S. S. & Kochanek, C. S. 2017, Monthly Notices of the Royal Astronomical Society, 473, 80

Tihhonova, O., Courbin, F., Harvey, D., et al. 2020, MNRAS, 498, 1406

Tihhonova, O., Courbin, F., Harvey, D., et al. 2018, MNRAS, 477, 5657

Tonry, J. & Schneider, D. P. 1988, AJ, 96, 807

Treu, T., Auger, M. W., Koopmans, L. V. E., et al. 2010, ApJ, 709, 1195

Treu, T. & Koopmans, L. V. E. 2004, ApJ, 611, 739

Tsujikawa, S. 2013, Classical and Quantum Gravity, 30, 214003

Tully, R. B. & Fisher, J. R. 1977, A&A, 54, 661

Tyson, J. A., Valdes, F., & Wenk, R. A. 1990, ApJ, 349, L1

Udalski, A., Szymanski, M., Kaluzny, J., et al. 1994, Acta Astron., 44, 227

Udalski, A., Szymanski, M. K., Kubiak, M., et al. 2006, Acta Astron., 56, 293

Urry, C. M. & Padovani, P. 1995, PASP, 107, 803

Valtonen, M. J., Nilsson, K., Lehto, H. J., et al. 2008, in AAS/Division of Dynamical Astronomy Meeting, Vol. 39, AAS/Division of Dynamical Astronomy Meeting #39, 15.05

Van de Vyvere, L., Gomer, M. R., Sluse, D., et al. 2022a, A&A, 659, A127

Van de Vyvere, L., Sluse, D., Gomer, M. R., & Mukherjee, S. 2022b, A&A, 663, A179

Van Waerbeke, L., Mellier, Y., Erben, T., et al. 2000, A&A, 358, 30

Vasiliev, E., Antonini, F., & Merritt, D. 2015, ApJ, 810, 49

Vegetti, S., Lagattuta, D. J., McKean, J. P., et al. 2012, Nature, 481, 341

Verde, L., Treu, T., & Riess, A. G. 2019, Nature Astronomy, 3, 891

Vernardos, G. 2022, MNRAS, 511, 4417

Vernardos, G. & Fluke, C. J. 2014, MNRAS, 445, 1223

Vernardos, G. & Tsagkatakis, G. 2019, MNRAS, 486, 1944

Vernardos, G. & Tsagkatakis, G. 2019, Monthly Notices of the Royal Astronomical Society, 486, 1944

Vilardell, F., Ribas, I., Jordi, C., Fitzpatrick, E. L., & Guinan, E. F. 2010, A&A, 509, A70

Walsh, D., Carswell, R. F., & Weymann, R. J. 1979, Nature, 279, 381

Walton, D. J., Harrison, F. A., Grefenstette, B. W., et al. 2014, ApJ, 793, 21

Wambsganss, J. 1999, Journal of Computational and Applied Mathematics, 109, 353

Warren, S. J. & Dye, S. 2003, ApJ, 590, 673

Weedman, D. W. 1976, ApJ, 208, 30

Weilbacher, P. M., Palsa, R., Streicher, O., et al. 2020, A&A, 641, A28

Weinberg, D. H., Mortonson, M. J., Eisenstein, D. J., et al. 2013, Phys. Rep., 530, 87

Wells, P., Fassnacht, C. D., & Rusu, C. E. 2023, arXiv e-prints, arXiv:2302.03176

Westfall, K. B., Cappellari, M., Bershady, M. A., et al. 2019, AJ, 158, 231

White, R. J. & Peterson, B. M. 1994, PASP, 106, 879

Wilkins, D. R. 2019, MNRAS, 489, 1957

Williams, P. R., Treu, T., Dahle, H., et al. 2020, arXiv e-prints, arXiv:2011.02007

Wisotzki, L., Koehler, T., Kayser, R., & Reimers, D. 1993, A&A, 278, L15

Wisotzki, L., Wucknitz, O., Lopez, S., & Sorensen, A. N. 1998, A&A, 339, L73

Wojtak, R., Hjorth, J., & Gall, C. 2019, MNRAS, 487, 3342

Wong, K. C., Suyu, S. H., Auger, M. W., et al. 2017, MNRAS, 465, 4895

Wong, K. C., Suyu, S. H., Chen, G. C. F., et al. 2020, MNRAS, 498, 1420

Woo, J.-H., Le, H. A. N., Karouzos, M., et al. 2018, ApJ, 859, 138

Wu, H.-Y. & Huterer, D. 2017, MNRAS, 471, 4946

Xie, G. Z., Zhou, S. B., & Liang, E. W. 2004, The Astronomical Journal, 127, 53

Yee, J. C., Zang, W., Udalski, A., et al. 2021, AJ, 162, 180

Yıldırım, A., Suyu, S. H., & Halkola, A. 2020, MNRAS, 493, 4783

York, D. G., Adelman, J., Anderson, John E., J., et al. 2000, AJ, 120, 1579

Yu, Z., Martini, P., Davis, T. M., et al. 2020, ApJS, 246, 16

Zahid, H. J., Geller, M. J., Fabricant, D. G., & Hwang, H. S. 2016, ApJ, 832, 203

Zeldovich, Y. 1964, Doklady Akademii Nauk SSSR, 155, 67

Zel'dovich, Y. B. & Novikov, I. D. 1966, AZh, 43, 758

Zhang, J., Zhang, H.-M., Zhu, Y.-K., et al. 2017, The Astrophysical Journal, 849, 42

Zhang, X. 2022a, Monthly Notices of the Royal Astronomical Society, 516, 3650

Zhang, X. 2022b, Monthly Notices of the Royal Astronomical Society, 516, 3650

Zhang, X. 2022c, Monthly Notices of the Royal Astronomical Society, 512, 1003

Zu, Y., Kochanek, C. S., Kozłowski, S., & Udalski, A. 2013, The Astrophysical Journal, 765, 106

Zu, Y., Kochanek, C. S., & Peterson, B. M. 2011, ApJ, 735, 80

Zwicky, F. 1933, Helvetica Physica Acta, 6, 110

Zwicky, F. 1937, Physical Review, 51, 679